Observation of the B_c Meson in 1.8-TeV Proton-Antiproton Collisions

Jun-ichi SUZUKI

A dissertation submitted to the Doctoral Program
in Physics, the University of Tsukuba
in partial fulfillment of the requirements for the
degree of Doctor of Philosophy (Science)

January 1998

Abstract

The B_c meson is the lowest-mass bound state of a bottom anti-quark and a charmed quark. It is the last stable meson predicted by the Standard Model and has not been observed in any experiments yet. The B_c meson mass is well predicted to be in the range 6.25 – 6.29 GeV/c^2 within the framework of the nonrelativistic potential model. On the other hand, the predictions for the B_c lifetime lie in a wide range between 0.4 and 1.4 ps depending on the model assumption of bound state effects.

We report the observation of the B_c meson in proton-antiproton collisions at a center of mass energy of 1.8 TeV. The B_c mesons are found through their semileptonic decays, $B_c^+ \to J/\psi \ell^+ X$, where $\ell^+ = e^+$ or μ^+. The data were collected during the 1992–1995 Tevatron Collider run using the Collider Detector at Fermilab (CDF). The corresponding integrated luminosity is 105 pb^{-1}.

We first search for the $B_c^+ \to J/\psi e^+ X$ events in the $J/\psi \to \mu^+\mu^-$ data set by requiring the three leptons, μ^+, μ^-, and e^+ to form a displaced vertex. We form an invariant mass of the J/ψ and the electron, $m(J/\psi e)$, and calculate the pseudo-proper decay length, x. We find 19 $B_c^+ \to J/\psi e^+ X$ candidate events in the signal mass region $4 < m(J/\psi e) < 6$ GeV/c^2, with the pseudo-proper decay length cut of $x > 60$ μm. We estimate 5.0 ± 1.1 background events in the signal mass region with the $x > 60$ μm cut. The search for the $B_c^+ \to J/\psi \mu^+ X$ mode was performed by other collaborators in CDF. They found 12 $B_c^+ \to J/\psi \mu^+ X$ candidate events in the signal mass region $4 < m(J/\psi \mu) < 6$ GeV/c^2 with the $x > 60$ μm cut, while 7.1 ± 1.5 background events were expected. Then we combine the results from the $B_c^+ \to J/\psi e^+ X$ mode and from the $B_c^+ \to J/\psi \mu^+ X$ mode. The probability that the observed yield is consistent with the background is estimated to be 2.5×10^{-5}. In the wider mass range $3.35 < m(J/\psi \ell)$ < 11 GeV/c^2, we perform a shape-dependent likelihood fit to the mass distribution and find that it requires a B_c signal contribution of $20.4\ ^{+6.2}_{-5.5}$ events. A fit without a B_c contribution is found to be inconsistent with the observed distribution at the probability level of $< 1.1 \times 10^{-5}$.

We extend our analysis to obtain the lifetime of the B_c meson. The lifetime is estimated to be

$$\tau = 0.55\ ^{+0.21}_{-0.19} \pm 0.12 \text{ ps},$$

where the first uncertainty is statistical and the second is systematic.

Finally, we estimate the product of the production cross section times branching ratio for $B_c^+ \to J/\psi \ell^+ X$ at the above value of the lifetime relative to that for $B_u^+ \to J/\psi K^+$. Our estimation for this ratio is:

$$\frac{\sigma_{B_c^+} \mathcal{B}(B_c^+ \to J/\psi \ell^+ X)}{\sigma_{B_u^+} \mathcal{B}(B_u^+ \to J/\psi K^+)} = 0.155\,^{+0.047}_{-0.043} \pm 0.027,$$

where the first uncertainty is statistical and the second is systematic.

Acknowledgements

I would like to thank Professor Koji Takikawa, my thesis advisor, for his guidance and encouragement throughout my graduate years. He has provided me with advice in many phases of my study. I am also grateful for his careful reading of the text and his many criticisms to the point. I would like to thank Professor Kunitaka Kondo, who gave me the opportunity to join the CDF experiment and the support in working on CDF.

I would like to thank Professor Shinhong Kim and Dr. Fumihiko Ukegawa for their supports and encouragements. They provided me a lot of suggestions at crucial points. I learned a great deal from their precise way of thinking. I could not have finished this work without their continuous supports.

Many thanks go to, Dr. Joseph Kroll, Professor Michael Schmidt and members of CDF B physics group, who gave me many useful suggestions and advice for this analysis. I want to thank Dr. Todd Huffman, Dr. Prem Singh, Professor Paul Shepard and Professor Gene Engels, who performed a search for the B_c meson using the $B_c^+ \to J/\psi\mu^+X$ mode and made efforts to combine a result for the $B_c^+ \to J/\psi e^+X$ mode and that for the $B_c^+ \to J/\psi\mu^+X$ mode. I am grateful to Professor Tom Devlin, Dr. Fritz Dejongh and Dr. Jonathan Lewis, who gave us many useful suggestions and helpful advice for the publication.

Discussions on physics and other various things with Yoshihiro Seiya, Ryutaro Oishi, Takashi Asakawa and Luc Demortier were very beneficial for me.

Conversations with Junsuke Iwai, Nobuaki Oshima, Taiji Yamanouchi, Shuichi Kunori, Itsuo Nakano, Takafumi Ohmoto, Takanobu Handa and Hirotoshi Toyoda made my stay at Fermilab unforgettable. I should thank Shin Aota, Hirofumi Ikeda, Toshiharu Uchida, Masakazu Okabe, Toshiaki Kikuchi, Tomoko Kuwabara, Hiroyuki Sato, Tsuyoshi Takada, Takeshi Takano, Koji Terashi, Hosai Nakada, Eiichiro Hayashi and Hiroyuki Minato staying at Fermilab for their help, and I had a very good time with them.

I also wish to thank other members of the Tsukuba high energy physics group for their constant help. They include Kazuhiko Hara, Shigeyuki Miyashita, Kiyoshi Yasuoka and other colleagues.

I thank the Fermilab staffs and the technical staffs of the participating institutions for their vital contributions. I thank many CDF collaborators who have developed the detector and other analysis environment.

I want to express my great appreciation to Carol Picciolo, Kyoko Kunori, Mutsumi Uenishi and Kazuko Kumashiro for their help through their secretary works.

Finally and most importantly I thank my parents and my brothers for their constant support and encouragement.

This work was supported by the U.S. Department of Energy and National Science Foundation; the Italian Istituto Nazionale di Fisica Nucleare; the Ministry of Education, Science and Culture of Japan; the Natural Sciences and Engineering Research Council of Canada; the National Science Council of the Republic of China; and the A. P. Sloan Foundation.

Contents

List of Figures

List of Tables

The CDF Collaboration

F. Abe,[17] H. Akimoto,[38] A. Akopian,[31] M. G. Albrow,[7] S. R. Amendolia,[27] D. Amidei,[20] J. Antos,[33] S. Aota,[36] G. Apollinari,[31] T. Arisawa,[38] T. Asakawa,[36] W. Ashmanskas,[18] M. Atac,[7] F. Azfar,[26] P. Azzi-Bacchetta,[25] N. Bacchetta,[25] W. Badgett,[20] S. Bagdasarov,[31] M. W. Bailey,[22] J. Bao,[40] P. de Barbaro,[30] A. Barbaro-Galtieri,[18] V. E. Barnes,[29] B. A. Barnett,[15] M. Barone,[9] E. Barzi,[9] G. Bauer,[19] T. Baumann,[11] F. Bedeschi,[27] S. Behrends,[3] S. Belforte,[27] G. Bellettini,[27] J. Bellinger,[39] D. Benjamin,[35] J. Benlloch,[19] J. Bensinger,[3] D. Benton,[26] A. Beretvas,[7] J. P. Berge,[7] J. Berryhill,[5] S. Bertolucci,[9] S. Bettelli,[27] B. Bevensee,[26] A. Bhatti,[31] K. Biery,[7] M. Binkley,[7] D. Bisello,[25] R. E. Blair,[1] C. Blocker,[3] S. Blusk,[30] A. Bodek,[30] W. Bokhari,[26] G. Bolla,[29] V. Bolognesi,[2] Y. Bonushkin,[4] D. Bortoletto,[29] J. Boudreau,[28] L. Breccia,[2] C. Bromberg,[21] N. Bruner,[22] E. Buckley-Geer,[7] H. S. Budd,[30] K. Burkett,[20] G. Busetto,[25] A. Byon-Wagner,[7] K. L. Byrum,[1] C. Campagnari,[7] M. Campbell,[20] A. Caner,[27] W. Carithers,[18] D. Carlsmith,[39] J. Cassada,[30] A. Castro,[25] D. Cauz,[27] Y. Cen,[30] A. Cerri,[27] F. Cervelli,[27] P. S. Chang,[33] P. T. Chang,[33] H. Y. Chao,[33] J. Chapman,[20] M. -T. Cheng,[33] M. Chertok,[34] G. Chiarelli,[27] T. Chikamatsu,[36] C. N. Chiou,[33] L. Christofek,[13] S. Cihangir,[7] A. G. Clark,[10] M. Cobal,[27] E. Cocca,[27] M. Contreras,[5] J. Conway,[32] J. Cooper,[7] M. Cordelli,[9] C. Couyoumtzelis,[10] D. Crane,[1] D. Cronin-Hennessy,[6] R. Culbertson,[5] T. Daniels,[19] F. DeJongh,[7] S. Delchamps,[7] S. Dell'Agnello,[27] M. Dell'Orso,[27] R. Demina,[7] L. Demortier,[31] M. Deninno,[2] P. F. Derwent,[7] T. Devlin,[32] J. R. Dittmann,[6] S. Donati,[27] J. Done,[34] T. Dorigo,[25] A. Dunn,[20] N. Eddy,[20] K. Einsweiler,[18] J. E. Elias,[7] R. Ely,[18] E. Engels, Jr.,[28] D. Errede,[13] S. Errede,[13] Q. Fan,[30] G. Feild,[40] Z. Feng,[15] C. Ferretti,[27] I. Fiori,[2] B. Flaugher,[7] G. W. Foster,[7] M. Franklin,[11] M. Frautschi,[35] J. Freeman,[7] J. Friedman,[19] H. Frisch,[5] Y. Fukui,[17] S. Funaki,[36] S. Galeotti,[27] M. Gallinaro,[26] O. Ganel,[35] M. Garcia-Sciveres,[18] A. F. Garfinkel,[29] C. Gay,[11] S. Geer,[7] D. W. Gerdes,[15] P. Giannetti,[27] N. Giokaris,[31] P. Giromini,[9] G. Giusti,[27] L. Gladney,[26] M. Gold,[22] J. Gonzalez,[26] A. Gordon,[11] A. T. Goshaw,[6] Y. Gotra,[25] K. Goulianos,[31] H. Grassmann,[27] L. Groer,[32] C. Grosso-Pilcher,[5] G. Guillian,[20] J. Guimarães,[15] R. S. Guo,[33] C. Haber,[18] E. Hafen,[19] S. R. Hahn,[7] R. Hamilton,[11] R. Handler,[39] R. M. Hans,[40] F. Happacher,[9] K. Hara,[36] A. D. Hardman,[29] B. Harral,[26] R. M. Harris,[7] S. A. Hauger,[6] J. Hauser,[4] C. Hawk,[32]

E. Hayashi,[36] J. Heinrich,[26] B. Hinrichsen,[14] K. D. Hoffman,[29] M. Hohlmann,[5] C. Holck,[26] R. Hollebeek,[26] L. Holloway,[13] S. Hong,[20] G. Houk,[26] P. Hu,[28] B. T. Huffman,[28] R. Hughes,[23] J. Huston,[21] J. Huth,[11] J. Hylen,[7] H. Ikeda,[36] M. Incagli,[27] J. Incandela,[7] G. Introzzi,[27] J. Iwai,[38] Y. Iwata,[12] H. Jensen,[7] U. Joshi,[7] R. W. Kadel,[18] E. Kajfasz,[25] H. Kambara,[10] T. Kamon,[34] T. Kaneko,[36] K. Karr,[37] H. Kasha,[40] Y. Kato,[24] T. A. Keaffaber,[29] K. Kelley,[19] R. D. Kennedy,[7] R. Kephart,[7] P. Kesten,[18] D. Kestenbaum,[11] H. Keutelian,[7] F. Keyvan,[4] B. Kharadia,[13] B. J. Kim,[30] D. H. Kim,[7a] H. S. Kim,[14] S. B. Kim,[20] S. H. Kim,[36] Y. K. Kim,[18] L. Kirsch,[3] P. Koehn,[23] A. Köngeter,[16] K. Kondo,[36] J. Konigsberg,[8] S. Kopp,[5] K. Kordas,[14] A. Korytov,[8] W. Koska,[7] E. Kovacs,[7a] W. Kowald,[6] M. Krasberg,[20] J. Kroll,[7] M. Kruse,[30] S. E. Kuhlmann,[1] E. Kuns,[32] T. Kuwabara,[36] A. T. Laasanen,[29] S. Lami,[27] S. Lammel,[7] J. I. Lamoureux,[3] M. Lancaster,[18] M. Lanzoni,[27] G. Latino,[27] T. LeCompte,[1] S. Leone,[27] J. D. Lewis,[7] P. Limon,[7] M. Lindgren,[4] T. M. Liss,[13] J. B. Liu,[30] Y. C. Liu,[33] N. Lockyer,[26] O. Long,[26] C. Loomis,[32] M. Loreti,[25] J. Lu,[34] D. Lucchesi,[27] P. Lukens,[7] S. Lusin,[39] J. Lys,[18] K. Maeshima,[7] A. Maghakian,[31] P. Maksimovic,[19] M. Mangano,[27] M. Mariotti,[25] J. P. Marriner,[7] A. Martin,[40] J. A. J. Matthews,[22] R. Mattingly,[19] P. Mazzanti,[2] P. McIntyre,[34] P. Melese,[31] A. Menzione,[27] E. Meschi,[27] S. Metzler,[26] C. Miao,[20] T. Miao,[7] G. Michail,[11] R. Miller,[21] H. Minato,[36] S. Miscetti,[9] M. Mishina,[17] H. Mitsushio,[36] T. Miyamoto,[36] S. Miyashita,[36] N. Moggi,[27] Y. Morita,[17] A. Mukherjee,[7] T. Muller,[16] P. Murat,[27] S. Murgia,[21] H. Nakada,[36] I. Nakano,[36] C. Nelson,[7] D. Neuberger,[16] C. Newman-Holmes,[7] C.-Y. P. Ngan,[19] M. Ninomiya,[36] L. Nodulman,[1] S. H. Oh,[6] K. E. Ohl,[40] T. Ohmoto,[12] T. Ohsugi,[12] R. Oishi,[36] M. Okabe,[36] T. Okusawa,[24] R. Oliveira,[26] J. Olsen,[39] C. Pagliarone,[27] R. Paoletti,[27] V. Papadimitriou,[35] S. P. Pappas,[40] N. Parashar,[27] S. Park,[7] A. Parri,[9] J. Patrick,[7] G. Pauletta,[27] M. Paulini,[18] A. Perazzo,[27] L. Pescara,[25] M. D. Peters,[18] T. J. Phillips,[6] G. Piacentino,[27] M. Pillai,[30] K. T. Pitts,[7] R. Plunkett,[7] L. Pondrom,[39] J. Proudfoot,[1] F. Ptohos,[11] G. Punzi,[27] K. Ragan,[14] D. Reher,[18] A. Ribon,[25] F. Rimondi,[2] L. Ristori,[27] W. J. Robertson,[6] T. Rodrigo,[27] S. Rolli,[37] J. Romano,[5] L. Rosenson,[19] R. Roser,[13] T. Saab,[14] W. K. Sakumoto,[30] D. Saltzberg,[4] A. Sansoni,[9] L. Santi,[27] H. Sato,[36] P. Schlabach,[7] E. E. Schmidt,[7] M. P. Schmidt,[40] A. Scott,[4] A. Scribano,[27] S. Segler,[7] S. Seidel,[22] Y. Seiya,[36] F. Semeria,[2] G. Sganos,[14] T. Shah,[19] M. D. Shapiro,[18] N. M. Shaw,[29] Q. Shen,[29] P. F. Shepard,[28] M. Shimojima,[36] M. Shochet,[5] J. Siegrist,[18] A. Sill,[35] P. Sinervo,[14] P. Singh,[13] K. Sliwa,[37] C. Smith,[15] F. D. Snider,[15] T. Song,[20] J. Spalding,[7] T. Speer,[10] P. Sphicas,[19] F. Spinella,[27]

M. Spiropulu,[11] L. Spiegel,[7] L. Stanco,[25] J. Steele,[39] A. Stefanini,[27] J. Strait,[7] R. Ströhmer,[7a] D. Stuart,[7] G. Sullivan,[5] K. Sumorok,[19] J. Suzuki,[36] T. Takada,[36] T. Takahashi,[24] T. Takano,[36] K. Takikawa,[36] N. Tamura,[12] B. Tannenbaum,[22] F. Tartarelli,[27] W. Taylor,[14] P. K. Teng,[33] Y. Teramoto,[24] S. Tether,[19] D. Theriot,[7] T. L. Thomas,[22] R. Thun,[20] R. Thurman-Keup,[1] M. Timko,[37] P. Tipton,[30] A. Titov,[31] S. Tkaczyk,[7] D. Toback,[5] K. Tollefson,[30] A. Tollestrup,[7] H. Toyoda,[24] W. Trischuk,[14] J. F. de Troconiz,[11] S. Truitt,[20] J. Tseng,[19] N. Turini,[27] T. Uchida,[36] N. Uemura,[36] F. Ukegawa,[26] G. Unal,[26] J. Valls,[7a] S. C. van den Brink,[28] S. Vejcik, III,[20] G. Velev,[27] R. Vidal,[7] R. Vilar,[7a] M. Vondracek,[13] D. Vucinic,[19] R. G. Wagner,[1] R. L. Wagner,[7] J. Wahl,[5] N. B. Wallace,[27] A. M. Walsh,[32] C. Wang,[6] C. H. Wang,[33] J. Wang,[5] M. J. Wang,[33] Q. F. Wang,[31] A. Warburton,[14] T. Watts,[32] R. Webb,[34] C. Wei,[6] H. Wei,[35] H. Wenzel,[16] W. C. Wester, III,[7] A. B. Wicklund,[1] E. Wicklund,[7] R. Wilkinson,[26] H. H. Williams,[26] P. Wilson,[5] B. L. Winer,[23] D. Winn,[20] D. Wolinski,[20] J. Wolinski,[21] S. Worm,[22] X. Wu,[10] J. Wyss,[25] A. Yagil,[7] W. Yao,[18] K. Yasuoka,[36] Y. Ye,[14] G. P. Yeh,[7] P. Yeh,[33] M. Yin,[6] J. Yoh,[7] C. Yosef,[21] T. Yoshida,[24] D. Yovanovitch,[7] I. Yu,[7] L. Yu,[22] J. C. Yun,[7] A. Zanetti,[27] F. Zetti,[27] L. Zhang,[39] W. Zhang,[26] and S. Zucchelli[2]

[1] *Argonne National Laboratory, Argonne, Illinois 60439*

[2] *Istituto Nazionale di Fisica Nucleare, University of Bologna, I-40127 Bologna, Italy*

[3] *Brandeis University, Waltham, Massachusetts 02254*

[4] *University of California at Los Angeles, Los Angeles, California 90024*

[5] *University of Chicago, Chicago, Illinois 60637*

[6] *Duke University, Durham, North Carolina 27708*

[7] *Fermi National Accelerator Laboratory, Batavia, Illinois 60510*

[8] *University of Florida, Gainesville, FL 32611*

[9] *Laboratori Nazionali di Frascati, Istituto Nazionale di Fisica Nucleare, I-00044 Frascati, Italy*

[10] *University of Geneva, CH-1211 Geneva 4, Switzerland*

[11] *Harvard University, Cambridge, Massachusetts 02138*

[12] *Hiroshima University, Higashi-Hiroshima 724, Japan*

[13] *University of Illinois, Urbana, Illinois 61801*

[14] *Institute of Particle Physics, McGill University, Montreal H3A 2T8, and University of Toronto, Toronto M5S 1A7, Canada*

[15] *The Johns Hopkins University, Baltimore, Maryland 21218*

[16] *Institut für Experimentelle Kernphysik, Universität Karlsruhe, 76128 Karlsruhe, Germany*

[17] *National Laboratory for High Energy Physics (KEK), Tsukuba, Ibaraki 315, Japan*

[18] *Ernest Orlando Lawrence Berkeley National Laboratory, Berkeley, California 94720*

[19] *Massachusetts Institute of Technology, Cambridge, Massachusetts 02139*

[20] *University of Michigan, Ann Arbor, Michigan 48109*

[21] *Michigan State University, East Lansing, Michigan 48824*

[22] *University of New Mexico, Albuquerque, New Mexico 87131*

[23] *The Ohio State University, Columbus, OH 43210*

[24] *Osaka City University, Osaka 588, Japan*

[25] *Universita di Padova, Istituto Nazionale di Fisica Nucleare, Sezione di Padova, I-36132 Padova, Italy*

[26] *University of Pennsylvania, Philadelphia, Pennsylvania 19104*

[27] *Istituto Nazionale di Fisica Nucleare, University and Scuola Normale Superiore of Pisa, I-56100 Pisa, Italy*

[28] *University of Pittsburgh, Pittsburgh, Pennsylvania 15260*

[29] *Purdue University, West Lafayette, Indiana 47907*

[30] *University of Rochester, Rochester, New York 14627*

[31] *Rockefeller University, New York, New York 10021*

[32] *Rutgers University, Piscataway, New Jersey 08855*

[33] *Academia Sinica, Taipei, Taiwan 11530, Republic of China*

[34] *Texas A&M University, College Station, Texas 77843*

[35] *Texas Tech University, Lubbock, Texas 79409*

[36] *University of Tsukuba, Tsukuba, Ibaraki 315, Japan*

[37] *Tufts University, Medford, Massachusetts 02155*

[38] *Waseda University, Tokyo 169, Japan*

[39] *University of Wisconsin, Madison, Wisconsin 53706*

[40] *Yale University, New Haven, Connecticut 06520*

Chapter 1

Introduction

In 1977, the b – beauty or bottom – quark was discovered [1]. In collisions of 400 GeV/c protons on a Copper or Platinum target at Fermi National Accelerator Laboratory (FNAL), the resonance in the mass region 9-10 GeV/c^2 was observed and was interpreted as a $b\bar{b}$ bound state called the Upsilon Υ. This resonance has been studied in detail at the Doppel RIng Speicher (DORIS) and the Cornell Electron Storage Ring (CESR), where the center of mass energy was ideally matched to this mass range. These e^+e^- experiments [2] observed the four $b\bar{b}$ states, $\Upsilon(1S)$ (9.46 GeV/c^2), $\Upsilon(2S)$ (10.02 GeV/c^2), $\Upsilon(3S)$ (10.36 GeV/c^2) and $\Upsilon(4S)$ (10.58 GeV/c^2). The first three states were all narrow but the $\Upsilon(4S)$ state was significantly wider. The CESR e^+e^- storage ring energy was set to the $\Upsilon(4S)$ and the CLEO experiments found the b-flavored mesons (B^+ and B^0) with exactly expected properties [3]. The B^+ (B^0) meson is a bound state of $\bar{b}u$ ($\bar{b}d$). In the Standard Model, there can exist heavier B mesons, B_s^0 ($\bar{b}s$) and B_c^+ ($\bar{b}c$). The B_s^0 meson was found for the first time at the Large Electron-Positron Collider (LEP) experiments [4]. The mass and the lifetime of the B_s^0 meson have been measured by LEP [4, 5] and the Collider Detector at Fermilab (CDF) [6]. The B_c meson has not been observed yet, though several searches have been performed by LEP and CDF.

1.1 B_c production in proton-antiproton collisions

B mesons, which are made up of a $\bar{b}$ quark and a light flavor quark, are produced through the strong interaction in $p\bar{p}$ collisions. A pair of $b\bar{b}$ is produced by scattering processes between a parton in p and a parton in $\bar{p}$. The lowest order (α_s^2) diagrams $q+\bar{q} \rightarrow b+\bar{b}$ and $g+g \rightarrow b+\bar{b}$, are shown in Figure 1.1. The produced b quark then fragments into a b hadron with a light flavor $\bar{q}$, where the light flavor $q\bar{q}$ pair is created from the vacuum. The B meson transverse momentum (p_T) distribution observed at CDF [7] is shown in Figure 1.2. The theoretical prediction is also shown in Figure 1.2, where the p_T distribution of the b-quark is calculated up to the next-to-leading order (α_s^3) [8] and the Peterson fragmentation model [9] is employed. The data is higher than the theoretical prediction by a factor of two in the low p_T region, but it tends to agree with the theoretical prediction in the high p_T region.

The production mechanism of the B_c meson, which consists of two heavy quarks $\bar{b}$ and c, is different from that of the other B mesons. The reason is that the probability to create a pair of heavy quarks from the vacuum is much smaller than that to create a pair of light quarks. According to the soft fragmentation model described in Ref. [10], the probabilities for the heavy quark pair creation from the vacuum as compared to u- or d-quark pair creation are:

$$u : d : s : c \simeq 1 : 1 : \frac{1}{3} : 10^{-11}. \tag{1.1}$$

Therefore the B_c meson production in which a $\bar{b}$ quark hadronizes into a B_c meson with a c-quark created from the vacuum, in a similar way as in the production of the other B mesons, is highly suppressed. The B_c^+ meson is expected to be produced dominantly by the following mechanism: in a $b\bar{b}$ pair production, a hard virtual gluon is emitted and the gluon fragments into a $c\bar{c}$ pair; the $\bar{b}$ quark forms a bound state with the c quark. This production mechanism is called the "hadronic production" in Refs. [11] – [14]. It is possible to calculate the production cross section with the perturbative Quantum Chromodynamics (QCD). Seven diagrams of $q\bar{q}$ annihilation ($q\bar{q} \rightarrow B_c^+ + b + \bar{c}$) and thirty-six diagrams of gg fusion ($gg \rightarrow B_c^+ + b + \bar{c}$) contribute to the hadronic production at the lowest order of α_s^4. Figure 1.3 shows some examples of the order α_s^4 Feynman diagrams. At $\sqrt{s} = 1.8$ TeV, the gg fusion processes are dominant. Recently, using the full thirty-six diagrams, the production spectra are calculated in Ref. [11] – [14] and their estimations which are approximately consistent with each other are listed in Table 1.1. Figure 1.5 shows the production spectrum of the B_c

	$\sigma(B_c^+)+\sigma(B_c^{*+})$	Note
Ref. [11]	2.0 nb	$p_T > 5$ GeV/c, $\lvert\eta\rvert < 1.5$, 1S state
Ref. [12]	2.0 nb	$p_T > 5$ GeV/c, 1S state
Ref. [13]	3.3 nb	$p_T > 5$ GeV/c, $\lvert\eta\rvert$ <1, 1S and 2S states
Ref. [14]	0.1 nb	$p_T > 10$ GeV/c, $\lvert\eta\rvert$ <1, 1S state

Table 1.1: The predictions for the total cross section of the pseudo scalar B_c^+ (1 ^{1}S$_0$) and the vector B_c^{*+} (1 ^{3}S$_1$) meson calculated at the α_s^4 order. The B_c^{*+} immediately decays into $B_c^+\gamma$.

meson calculated at α_s^4 order in Ref. [11]. In this calculation, the structure function CTEQ3M [16] is used.

The B_c meson production cross section can be alternatively calculated [11], [15] with a fragmentation approximation for $p_T \gg m(B_c)$ using perturbative QCD. A fragmentation function that a $\bar{b}$ quark hadronizes into a B_c meson is evaluated using the $\bar{b} \to \bar{b}c\bar{c}$ diagram as shown in Figure 1.4. The production spectrum of the B_c meson calculated using the fragmentation function is also shown in Figure 1.5. The $\bar{b} \to B_c$ process is more dominant than the $c \to B_c$ process by two orders of magnitude [15].

1.2 B_c mass spectrum

The mass spectrum of the B_c mesons consisting of heavy quarks $\bar{b}$ and c is calculated using the nonrelativistic potential models, in a similar way as the $c\bar{c}$ (ψ) and the $b\bar{b}$ (Υ) states. The nonrelativistic potential models have been studied in detail using both the ψ and the Υ states. The nonrelativistic potential models successfully reproduce the observed mass spectra of the ψ and the Υ families. Although several functional forms for the potential are used, each potential does not depend on the flavor of heavy quarks. Hence the B_c mass can be accurately predicted. In Ref. [17], mass of the B_c^+ meson or $\bar{b}c$ ground ($n\ ^{2S+1}L_J = 1\ ^1S_0$) state is estimated by using four kinds of potentials to lie in the range,

$$6.248 < m(B_c(1\ ^1\mathrm{S}_0)) < 6.266\ \mathrm{GeV}/c^2, \tag{1.2}$$

	$m(B_c^+)$ (in GeV/c^2)	Potential
Ref. [17]	6.264	Buchmüller-Tye potential
	6.248	power-law potential
	6.266	logarithmic potential
	6.254	Cornell potential
	6.258 $\pm$ 0.020	average of above four potential
Ref. [18]	6.27	Cornell potential
Ref. [19]	6.287	dual-QCD potential
Ref. [20]	6.246	power-law potential

Table 1.2: Predictions for the mass of the B_c^+ meson (the $\bar{b}c$ ground state).

and $m(B_c) = 6.258 \pm 0.020$ GeV/c^2 is their best estimate. Many other estimations for $m(B_c)$ are available and some of them are listed in Table 1.2.

The excited states are also calculated within the framework of the nonrelativistic potential models. Figure 1.6 shows the $\bar{b}c$ mass spectrum predicted by Ref. [17] using the Buchmüller-Tye potential. The fifteen excited states below the $\bar{B}D$ threshold, *i.e.*, the states with mass $m < m_B + m_D = 7.1431$ GeV/c^2, decay into the ground state ($1\ {}^1\mathrm{S}_0$) by emitting γ or $\pi\pi$ via electromagnetic or strong interactions. The $2\ {}^1\mathrm{P}_1$ $\bar{b}c$ state decay $B_c^{*+}(2\ {}^1\mathrm{P}_1) \rightarrow B_c^+(1\ {}^1\mathrm{S}_0) + 455$ MeV-γ, which can experimentally be detected, is especially interesting, since the $1\ {}^1\mathrm{P}_1$ $c\bar{c}$ and $b\bar{b}$ states (h_c and h_b) have not been observed yet. The study of $\bar{b}c$ spectroscopy confirms and refines our understanding of the nonrelativistic potential model.

1.3 B_c decays and lifetime

The B_c^+ meson (the $\bar{b}c$ ground state) decays only through the weak interaction. Three processes, shown in Figure 1.7, are expected to dominate the B_c^+ meson decay:

- the c spectator decay: $\bar{b} \rightarrow \bar{c}W^+$. This decay leads to final states such as $B_c^+ \rightarrow J/\psi \ell^+ \nu$, $J/\psi \pi^+$ and so on.

- the $\bar{b}$ spectator decay: $c \rightarrow sW^+$. This decay leads to final states such as $B_c^+ \rightarrow B_s^0 \ell^+ \nu$, $B_s^0 \pi^+$ and so on.

	[21]	[22]	[23]	[24]	[25]
$\Gamma_{\bar{b}\to\bar{c}W^+}$ (ps^{-1})	0.74	0.67	0.39	$\cdots$	0.615
Γ_{PI} (ps^{-1})	$\cdots$	$\cdots$	$\cdots$	$\cdots$	0.124
$\Gamma_{c\to sW^+}$ (ps^{-1})	0.90	1.45	0.07	$\cdots$	1.229
$\Gamma_{\bar{b}c\to W^+}$ (ps^{-1})	0.36	0.38	0.22	$\cdots$	0.194
Γ_{tot} (ps^{-1})	2.0	2.5	0.68	$\cdots$	1.914
$\tau(B_c)$ (ps)	0.50	0.40	1.44	< 1.0	$0.52^{+0.2}_{-0.1}$

Table 1.3: Predictions for the decay width and lifetime of the B_c^+ meson.

- the $\bar{b}c$ weak annihilation into a virtual W^+: $\bar{b}c \to W^+$. This decay leads to final states such as $B_c^+ \to \tau^+\nu$ and so on.

Naively, the total decay width (Γ_{tot}) is written as

$$\Gamma_{\mathrm{tot}} = \Gamma_{\bar{b}\to\bar{c}W^+} + \Gamma_{c\to sW^+} + \Gamma_{\bar{b}c\to W^+}. \tag{1.3}$$

These decay widths are estimated in Refs. [21] – [23] and their predictions are listed in Table 1.3.

The B_c meson lifetime is more precisely investigated in Refs. [24] and [25], within the framework of an operator product expansion in inverse powers of the heavy quark masses and subsequent matching onto nonrelativistic QCD. For the c spectator decay $\bar{b}c \to \bar{c}\bar{s}cc$, an interference between different diagrams providing the same final state, which is often referred to as "Pauli Interference", is taken into consideration in Refs. [24] and [25]. Then the total decay width is modified as

$$\Gamma_{\mathrm{tot}} = \Gamma_{\bar{b}\to\bar{c}W^+} - \Gamma_{\mathrm{PI}} + \Gamma_{c\to sW^+} + \Gamma_{\bar{b}c\to W^+}. \tag{1.4}$$

The lifetime of the B_c meson is obtained from Γ_{tot}:

$$\tau(B_c) = \frac{1}{\Gamma_{\mathrm{tot}}} \tag{1.5}$$

The predictions of Bigi [24] and Beneke and Buchall [25] are also listed in Table 1.3.

The predictions for the B_c meson lifetime lie in a rather wide range, between 0.4 ps and 1.4 ps, as shown in Table 1.3. These predictions depend mainly on the model

	$B_c^+ \to J/\psi\ell^+\nu$		$B_c^+ \to J/\psi\pi^+$	
	Γ (ps^{-1})	$\mathcal{B}$	Γ (ps^{-1})	$\mathcal{B}$
[21] (BSW)	3.3×10^{-2}	1.7%	$\cdots$	$\cdots$
[21] (ISGW)	5.9×10^{-2}	3%	4.0×10^{-3}	0.2%
[22] (NQRM)	5.2×10^{-2}	2.1%	4.8×10^{-3}	0.2%
[23]	1.0×10^{-2}	1.2%	2.7×10^{-3}	0.4%
[26] (ISGW)	4.3×10^{-2}	$\cdots$	$\cdots$	$\cdots$
[27] (ISGW II)	2.5×10^{-2}	$\cdots$	$\cdots$	$\cdots$

Table 1.4: Predictions for the partial decay width Γ and the branching ratio $\mathcal{B}$ for the $B_c^+ \to J/\psi\ell^+\nu$ and $B_c^+ \to J/\psi\pi^+$ decays.

assumption of bound state effects. If a $\bar{b}$ quark and a c quark are tightly bound, the quark mass is reduced by the binding energy $\mu_{\rm BE}$ inside the B_c meson and the B_c decay width is reduced very considerably. Assuming a partial width Γ_Q is proportional to the fifth power of a quark mass m_Q, *i.e.*, $\Gamma_Q \propto m_Q^5$, we find a relative reduction Γ'_Q/Γ_Q:

$$\frac{\Gamma'_Q}{\Gamma_Q} = \frac{(m_Q - \mu_{\rm BE})^5}{m_Q^5} \tag{1.6}$$

For $\mu_{\rm BE} \sim 500$ MeV, we find that the $\Gamma_{\bar{b}\to\bar{c}W^+}$ and $\Gamma_{c\to sW^+}$ are reduced by a factor of 1.7 and 6, assuming that the binding energy is the same for the b and for the c. Therefore, the $\bar{b} \to \bar{c}$ transitions are dominant, and the lifetime is expected to be longer, *i.e.*, $\tau(B_c) > 1$ ps, as described in Ref. [23]. On the other hand, if the $\bar{b}$ and c are free, we may approximate the $\Gamma_{\bar{b}\to\bar{c}W^+}$ by $\Gamma(B^0)$ and the $\Gamma_{c\to sW^+}$ by $\Gamma(D^0)$ and we obtain

$$\Gamma_{\rm tot} \sim \Gamma(B^0) + \Gamma(D^0). \tag{1.7}$$

If Eq. (1.7) were to hold, the $c \to s$ transitions would dominate over the $\bar{b} \to \bar{c}$ transitions, and the B_c lifetime would be rather short, $\tau(B_c) \simeq 0.3$ ps. Thus, the B_c lifetime is sensitive to the model assumption of bound state effects.

The partial widths for exclusive B_c decays are also predicted. Some estimations for the $B_c^+ \to J/\psi\ell^+\nu$ mode and the $B_c^+ \to J/\psi\pi^+$ mode are listed in Table 1.4 (Throughout this thesis a reference to a particular charge state also implies its charge conjugate).

1.4 Review of the previous B_c meson searches

The LEP and CDF experiments have searched for the B_c meson. We briefly describe the results from the previous LEP and CDF experiments and then compare their relative significance.

In the LEP experiments, they use a few million hadronic Z decays and have reported the following results:

- A search for B_c^+ meson decaying into the channels $J/\psi\pi^+$ and $J/\psi\ell^+\nu$ ($\ell = e$ or μ) has been performed by the ALEPH Collaboration, in a sample of 3.9 million hadronic Z decays [28]. They found 0 and 2 candidates in the $J/\psi\pi^+$ and $J/\psi\ell^+\nu$ channels, respectively, while 0.4 and 0.81 background events were expected. Then the 90% confidence level upper limits with respect to the hadronic Z decays are derived:

$$\frac{\mathcal{B}(Z \to B_c^+ X)}{\mathcal{B}(Z \to q\bar{q})}\mathcal{B}(B_c^+ \to J/\psi\pi^+) < 3.6 \times 10^{-5}, \tag{1.8}$$

$$\frac{\mathcal{B}(Z \to B_c^+ X)}{\mathcal{B}(Z \to q\bar{q})}\mathcal{B}(B_c^+ \to J/\psi\ell^+\nu) < 5.2 \times 10^{-5}. \tag{1.9}$$

  An additional $B_c^+ \to J/\psi(\to e^+e^-)\mu^+\nu$ candidate with very low background probability is also reported. This candidate event is found by scanning events with $\psi X^\pm$ system mass above the $B^\pm$ mass, where ψ is J/ψ or $\psi(2S)$ and $X^\pm$ is a single charged track. Since the muon track exists outside the muon chamber coverage, this event was not selected by the previously discussed $B_c^+ \to J/\psi\ell^+\nu$ analysis.

- The DELPHI collaboration looked for the B_c meson with the three decay modes $B_c^+ \to J/\psi\pi^+$, $B_c^+ \to J/\psi\ell^+\nu$ and $B_c^+ \to J/\psi\pi^+\pi^-\pi^+$ in 3.02 million hadronic Z decays [29]. They found one $B_c^+ \to J/\psi\pi^+$ candidate, no $B_c^+ \to J/\psi\ell^+\nu$ candidate and one $B_c^+ \to J/\psi\pi^+\pi^-\pi^+$ candidate, while 1.7, 0.3 and 2.3 background events were expected. The following 90% confidence level upper limits are obtained:

$$\mathcal{B}(Z \to B_c^+ X)\mathcal{B}(B_c^+ \to J/\psi\pi^+) < (1.05\,\text{to}\,0.84) \times 10^{-4}, \tag{1.10}$$

$$\mathcal{B}(Z \to B_c^+ X)\mathcal{B}(B_c^+ \to J/\psi \ell^+ \nu) < (5.8\,\mathrm{to}\,5.0) \times 10^{-5}, \tag{1.11}$$

where the ranges quoted correspond to the assumed range of the B_c^+ lifetime from 0.4 to 1.4 ps, and

$$\mathcal{B}(Z \to B_c^+ X)\mathcal{B}(B_c^+ \to J/\psi \pi^+\pi^-\pi^+) < 1.75 \times 10^{-4}, \tag{1.12}$$

where the limit is constant over the predicted range of the B_c lifetime.

- The OPAL collaboration searched for the B_c meson using the $B_c^+ \to J/\psi\pi^+$, $B_c^+ \to J/\psi a_1^+$, $a_1^+ \to \pi^+\pi^-\pi^+$ and $B_c^+ \to J/\psi\ell^+\nu$ decay modes in 4.2 million hadronic Z decays [30]. Two $B_c^+ \to J/\psi\pi^+$, no $B_c^+ \to J/\psi a_1^+$ and one $B_c^+ \to J/\psi\ell^+\nu$ candidates were found while 0.63 $\pm$ 0.20, 0.82 $\pm$ 0.19 and 1.10 $\pm$ 0.22 background events were expected. Then the following 90% confidence level limits are obtained:

$$\frac{\mathcal{B}(Z \to B_c^+ X)}{\mathcal{B}(Z \to q\bar{q})}\mathcal{B}(B_c^+ \to J/\psi\pi^+) < 1.06 \times 10^{-4}, \tag{1.13}$$

$$\frac{\mathcal{B}(Z \to B_c^+ X)}{\mathcal{B}(Z \to q\bar{q})}\mathcal{B}(B_c^+ \to J/\psi a_1^+) < 5.53 \times 10^{-5}, \tag{1.14}$$

$$\frac{\mathcal{B}(Z \to B_c^+ X)}{\mathcal{B}(Z \to q\bar{q})}\mathcal{B}(B_c^+ \to J/\psi\ell^+\nu) < 6.96 \times 10^{-5}. \tag{1.15}$$

In the Tevatron experiments, only the CDF experiment is able to search for the B_c meson, because the D0 experiment does not have a solenoid magnet and a fine resolution tracking detector. The CDF collaboration searched for the $B_c^+ \to J/\psi\pi^+$ decay [31] in 105 pb^{-1} and reported a 95% confidence level upper limit on the production cross section times the branching ratio with respect to the $B_u^+ \to J/\psi K^+$ decay:

$$\frac{\sigma_{B_c^+}\mathcal{B}(B_c^+ \to J/\psi\pi^+)}{\sigma_{B_u^+}\mathcal{B}(B_u^+ \to J/\psi K^+)} = (0.15\,\mathrm{to}\,0.04), \tag{1.16}$$

where the range quoted corresponds to the assumed range of the B_c lifetime from 0.4 to 1.4 ps.

To compare the relative significance of the four experiments, we convert the limits reported by the LEP experiments to the ratio used by the CDF experiment, *i.e.*, the ratio relative to the production of the B_u^+ followed by the $B_u^+ \to J/\psi K^+$ decay. We naively estimate the relevant quantities in the LEP experiments as follows:

- ALEPH and OPAL

$$\begin{aligned}\frac{\mathcal{B}(Z \to B_u^+ X)}{\mathcal{B}(Z \to q\bar{q})}\mathcal{B}(B_u^+ \to J/\psi K^+) &= \frac{\mathcal{B}(Z \to b\bar{b})}{\mathcal{B}(Z \to q\bar{q})} f(\bar{b} \to B_u^+)\mathcal{B}(B_u^+ \to J/\psi K^+) \\ &= 2. \times \frac{0.1546}{0.6990} \times 0.378 \times 1.01 \times 10^{-3} \\ &= 1.69 \times 10^{-4}, \end{aligned} \tag{1.17}$$

where we use $\mathcal{B}(Z \to b\bar{b}) = 0.1546$, $\mathcal{B}(Z \to q\bar{q}) = 0.6990$, $f(\bar{b} \to B_u^+) = 0.378$ and $\mathcal{B}(B_u^+ \to J/\psi K^+) = 1.01 \times 10^{-3}$ [32]. The factor of "2" in the second line is needed since the limit reported by the ALEPH and the OPAL is for the sum of the two charge conjugate modes.

- DELPHI

$$\begin{aligned}\mathcal{B}(Z \to b\bar{b}) f(\bar{b} \to B_u^+ X)\mathcal{B}(B_u^+ \to J/\psi K^+) &= 2. \times 0.1546 \times 0.378 \times 1.01 \times 10^{-3} \\ &= 1.18 \times 10^{-4}, \end{aligned} \tag{1.18}$$

The factor of "2" is needed due to the same reason for ALEPH and OPAL.

By dividing the ALEPH and OPAL limits by Eq. (1.17) and the DELPHI limits by Eq. (1.18), we obtain the limits on the ratio of the B_c production and decay with respect to the B_u^+ production followed by the $B_u^+ \to J/\psi K^+$ decay. The results are listed in Table 1.5, where the limit reported by the CDF includes uncertainty of the B_u^+ production, while those for the LEP experiments do not include the uncertainty. Table 1.5 shows that the results of the four previous experiments are roughly comparable with each other.

1.5 Outline of this analysis

The CDF Collaboration has searched for the B_c meson using the $B_c^+ \to J/\psi\pi^+$ mode and has reported the 95% confidence level upper limits [31]. Using the data of

Experiment	decay mode	Upper limits
ALEPH	$B_c^+ \to J/\psi\pi^+$	0.2 (90% C.L.)
	$B_c^+ \to J/\psi\ell^+\nu$	0.3 (90% C.L.)
DELPHI	$B_c^+ \to J/\psi\pi^+$	0.9 to 0.7 (90% C.L.)
	$B_c^+ \to J/\psi\ell^+\nu$	0.5 to 0.4 (90% C.L.)
	$B_c^+ \to J/\psi\pi^+\pi^-\pi^+$	1.5 (90% C.L.)
OPAL	$B_c^+ \to J/\psi\pi^+$	0.6 (90% C.L.)
	$B_c^+ \to J/\psi a_1^+$	0.3 (90% C.L.)
	$B_c^+ \to J/\psi\ell^+\nu$	0.4 (90% C.L.)
CDF	$B_c^+ \to J/\psi\pi^+$	0.15 to 0.04 (95% C.L.)

Table 1.5: The results of the previous B_c^+ meson searches. The quoted limit is on the ratio with respect to the B_u^+ production followed by the $B_u^+ \to J/\psi K^+$ decay.

105 pb^{-1} collected with the CDF detector, we search for the B_c meson in a semileptonic decay mode of $B_c^+ \to J/\psi\ell^+X$, where the J/ψ decays into a $\mu^+\mu^-$ pair and $\ell = e$ or μ. The B_c^+ meson can decay into a $\ell^+\nu$ pair and also into a higher mass $c\bar{c}$ state, which in turn can decay into $J/\psi X'$. Hence the X in $B_c^+ \to J/\psi\ell^+X$ includes a neutrino ν in the semileptonic decay and the X' which are the decay products of the higher mass $c\bar{c}$ state.

The event topology of the $B_c^+ \to J/\psi\ell^+X$ mode is fairly simple, as shown in Figure 1.8. The dimuon pair from the J/ψ decay and the third lepton from the semileptonic decay form a common vertex, since the J/ψ immediately decays into $\mu^+\mu^-$. Even if the B_c meson has the shortest lifetime ($\tau(B_c) = 0.4$ ps) allowed by the current predictions, the B_c meson decays at a displaced point from the primary interaction vertex and one can identify the secondary vertex of the B_c meson decay. We first look for an opposite sign dimuon pair with the dimuon invariant mass consistent with the world average J/ψ mass. We select the third lepton and reconstruct a common vertex of the three leptons (μ^+, μ^-, ℓ^+). The final state we are looking at is very clean. The branching ratio for the $B_c^+ \to J/\psi\ell^+X$ mode is three to fifteen times larger than that for the $B_c^+ \to J/\psi\pi^+$ mode, as listed in Table 1.4. A search for the B_c meson using the $B_c^+ \to J/\psi\ell^+X$ mode has these advantages over the previous search using the $B_c^+ \to J/\psi\pi^+$ at the CDF.

In the following chapters, we mainly describe the search using the $B_c^+ \to J/\psi e^+ X$ mode, *i.e.*, using electrons as the third lepton. The experimental setup, the event selection and the background estimation for the $B_c^+ \to J/\psi e^+ X$ mode are described. After that, we combine the results from the $B_c^+ \to J/\psi e^+ X$ mode and the $B_c^+ \to J/\psi \mu^+ X$ mode and estimate the statistical significance. Then we measure the lifetime of the B_c meson. Finally, we obtain the production cross section times the branching ratio for $B_c^+ \to J/\psi \ell^+ X$ at the measured value of the lifetime relative to the cross section times the branching ratio for $B_u^+ \to J/\psi K^+$.

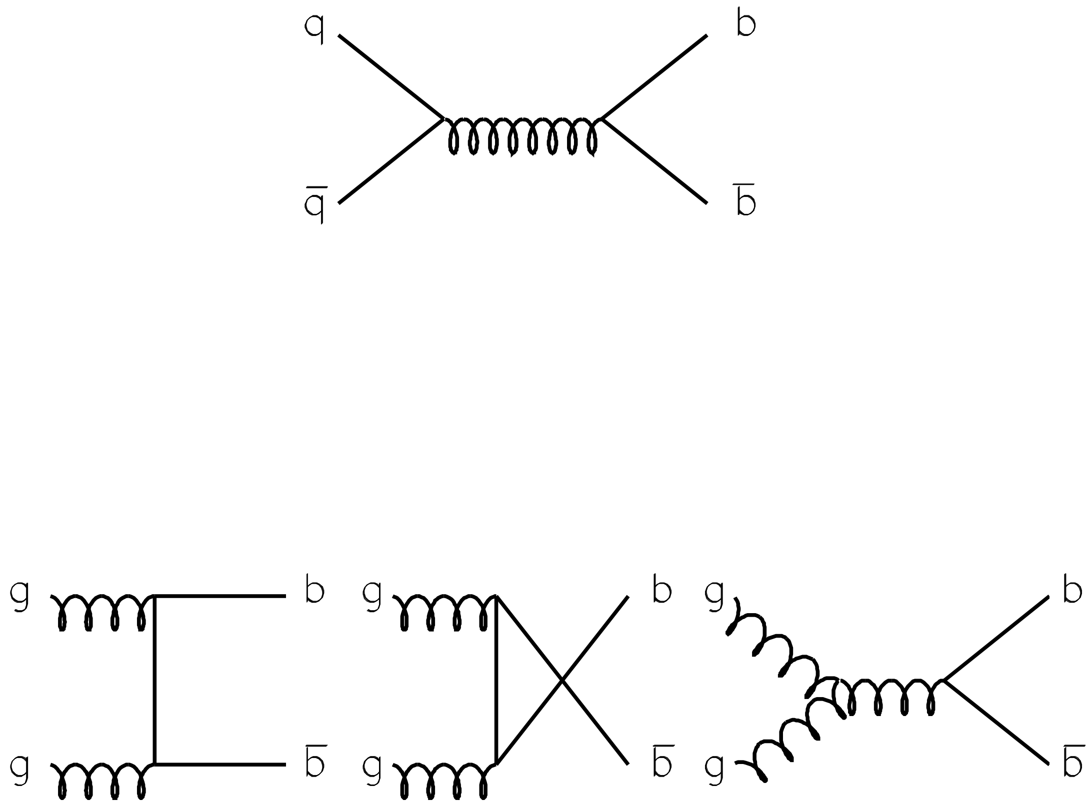

Figure 1.1: The lowest order Feynman diagrams for $b\bar{b}$ production.

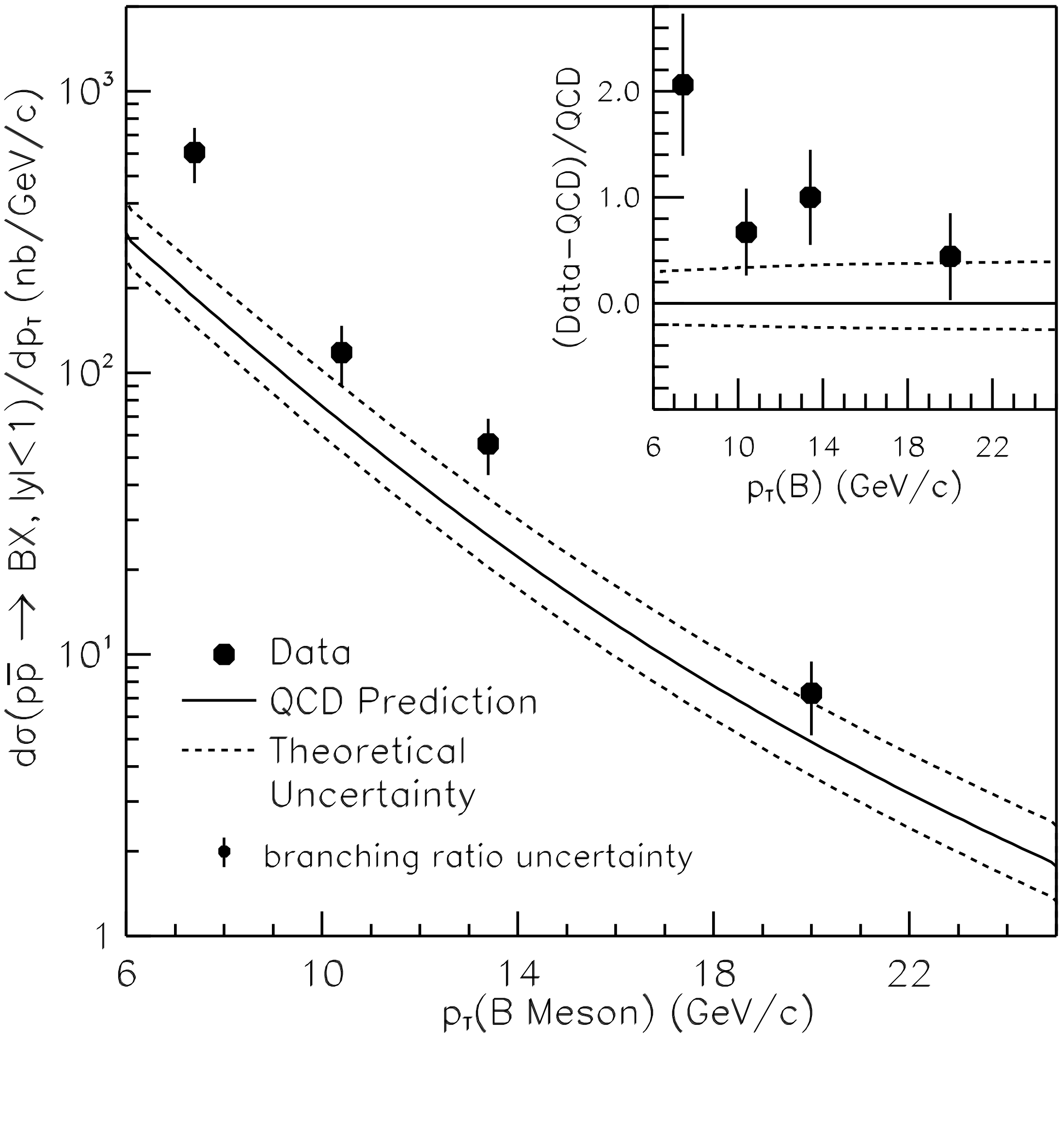

Figure 1.2: The p_T distribution of B mesons observed at CDF using 19 pb^{-1} of data. The B mesons are fully reconstructed using the $B^+ \rightarrow J/\psi K^+$ mode and the $B^0 \rightarrow J/\psi K^*(892)$ mode.

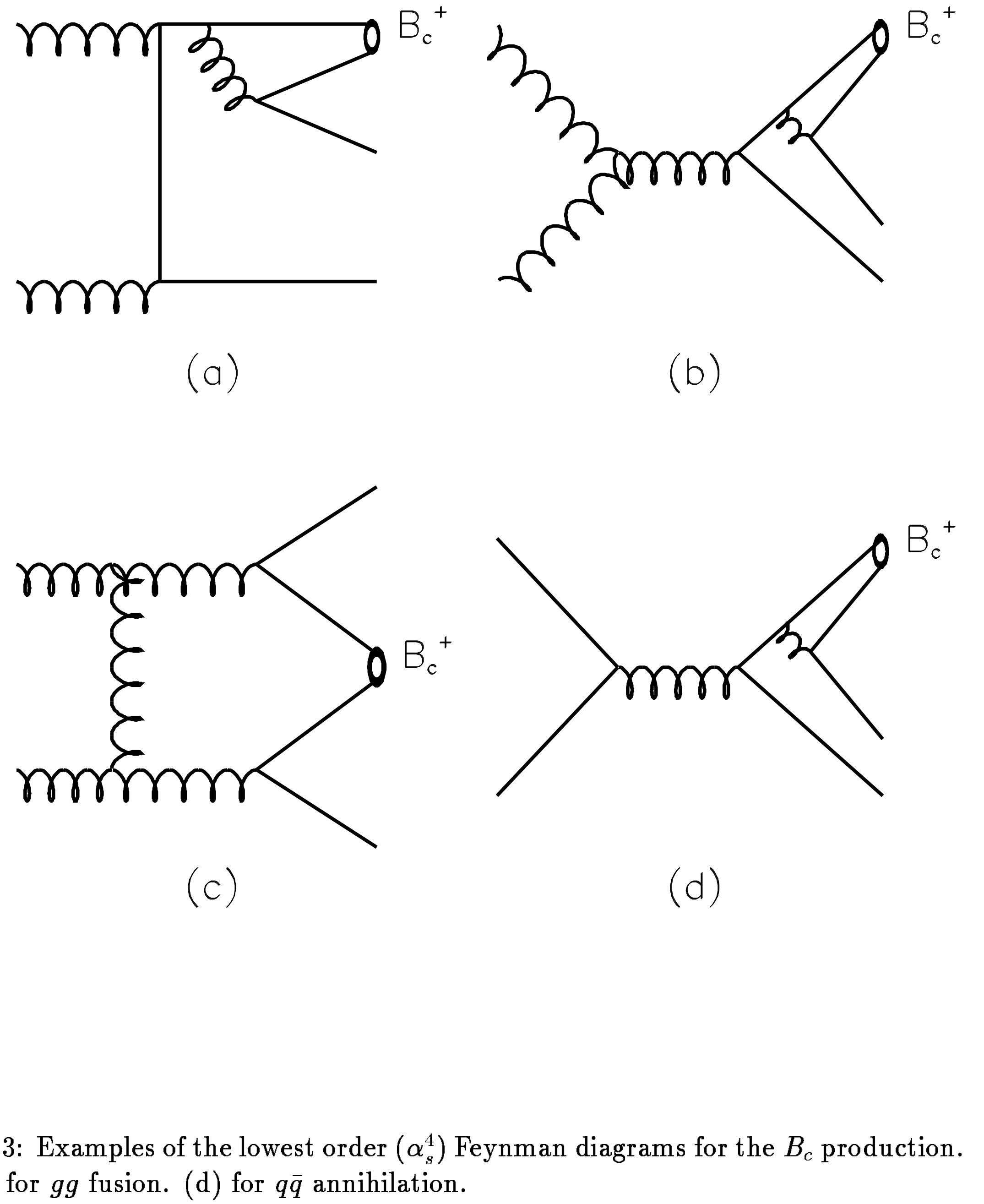

Figure 1.3: Examples of the lowest order (α_s^4) Feynman diagrams for the B_c production. (a) – (c) for gg fusion. (d) for $q\bar{q}$ annihilation.

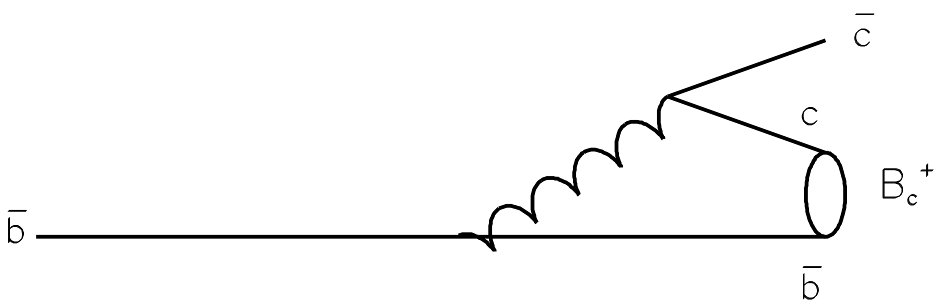

Figure 1.4: An example of the $\bar{b} \to \bar{b}c\bar{c}$ Feynman diagrams which contribute to the fragmentation of $\bar{b}$ into the B_c^+.

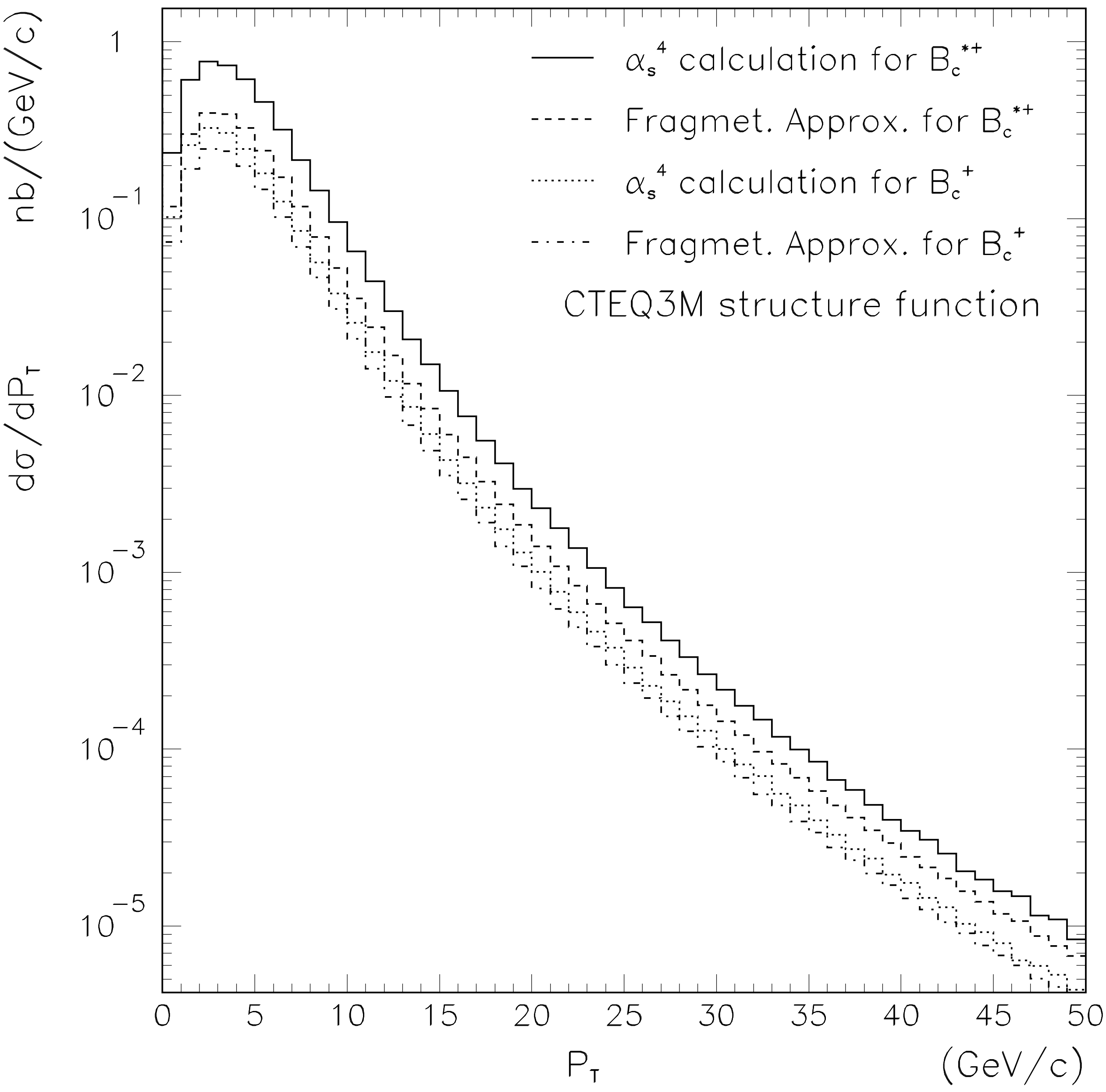

Figure 1.5: The p_T distribution for the pseudo scalar $B_c^+(1\ ^1\mathrm{S}_0)$ and the vector B_c^{*+} $(1\ ^3\mathrm{S}_1)$ meson production calculated by Chang *et. al.* [11].

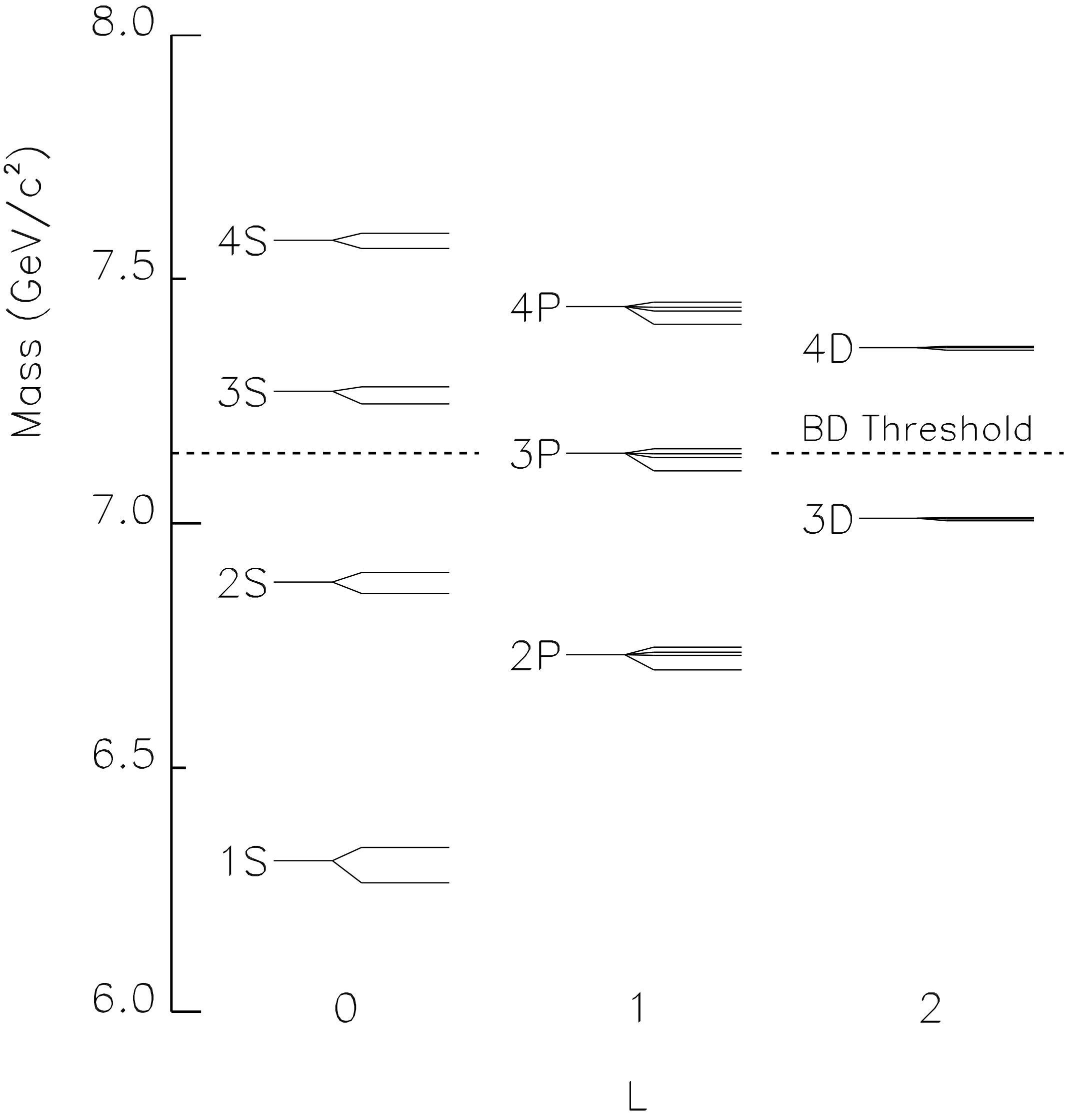

Figure 1.6: The mass spectrum of the $\bar{b}c$ bound states estimated in Ref. [17] using the Buchmüller-Tye potential. The "L" is the orbital angular momentum. The dashed line shows the threshold for the $B_c^{*+} \to \bar{B}D$ decay.

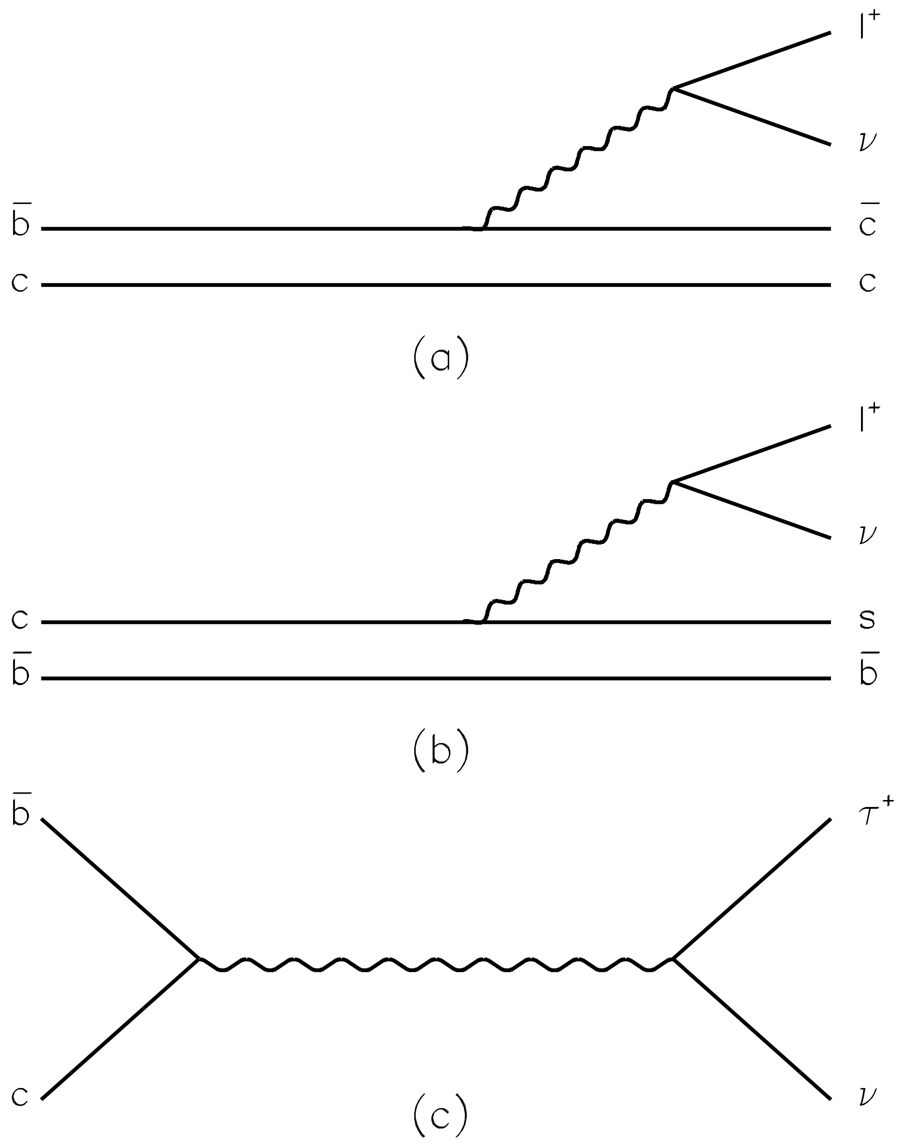

Figure 1.7: The diagrams for the B_c decay: (a) the c spectator decay, (b) the $\bar{b}$ spectator decay and (c) the $\bar{b}c$ weak annihilation.

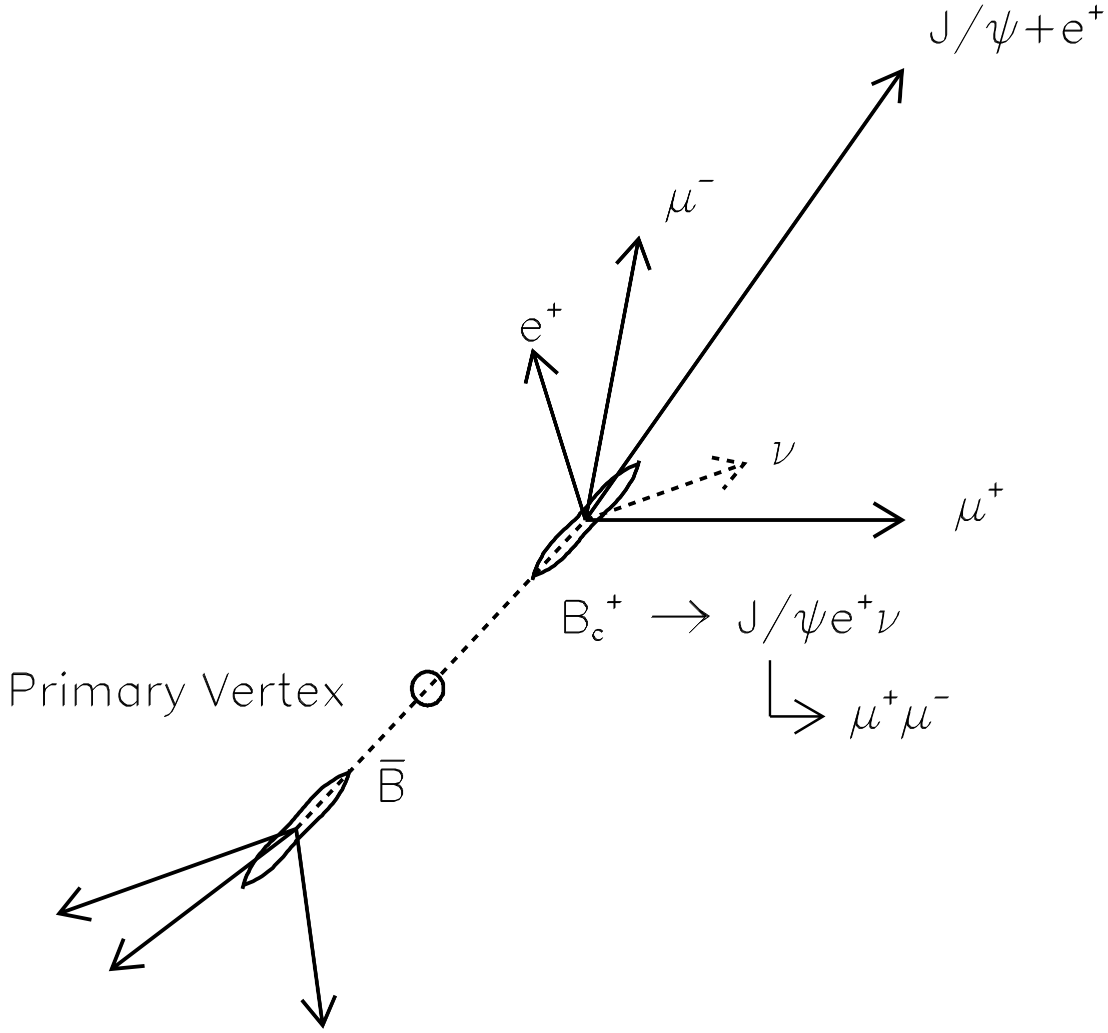

Figure 1.8: A sketch of the $B_c^+ \to J/\psi e^+\nu$ decay.

Chapter 2

Experimental Setup

The data of $p\bar{p}$ collisions at the center of mass energy of 1.8 TeV were collected using the CDF detector during 1992 – 1996. The collider run in this period is called "Run I". Run I consists of two collider runs, Run Ia (1992 – 1993) and Run Ib (1994 – 1996). The data corresponding to 105 pb^{-1} (19 pb^{-1} for Run Ia and 86 pb^{-1} for Run Ib) were collected in Run I. In this chapter, we describe the Fermilab accelerator complex very briefly and the CDF detector with emphasis on detector components which are relevant to this analysis.

2.1 Accelerator complex

The accelerator complex at Fermilab is made up of five accelerators, as shown in Figure 2.1. In the Cockcroft-Walton accelerator, negative hydrogen ions (H^-) are accelerated to an energy of 750 keV by a DC electric field. The second stage of the acceleration process utilizes a 500-foot-long linear accelerator (Linac). The H^- ions are accelerated to 400 MeV in the Linac and injected into the Booster. The Booster is a synchrotron with a diameter of approximately 500 feet, located in a tunnel 20 feet below the ground. At the injection into the Booster, the ions pass through a carbon foil, which strips off the electrons thereby leaving only the protons circulating around the Booster ring. The protons are accelerated by the Booster to 8 GeV and injected into the Main Ring, a synchrotron with a diameter of 2 km. The Main Ring is operated at room temperature in an underground tunnel and is used for two purposes, accelerating protons to 150 GeV for injection into the Tevatron and generating 120 GeV protons for antiproton production.

During antiproton stacking the 120 GeV protons are extracted from the Main Ring onto a tangusten target. Every two seconds, approximately 10^7 antiprotons are produced for 2×10^{15} protons striking the target and are collected in the Debuncher, which is roughly triangular with three straight sections of low dispersion. The Debuncher reduces the momentum spread of the antiprotons and reduces their transverse profile with the stochastic cooling. The antiprotons are then transferred into the Accumulator. The Accumulator ring is located in the same tunnel as the Debuncher. The antiprotons are merged into a single beam, cooled further and stored in the Accumulator. The antiprotons are rebunched and injected into the Main Ring. The Main Ring is used to accelerate the antiprotons to 150 GeV, and injects them into the Tevatron.

The 150 GeV proton and antiproton bunches are accelerated to 900 GeV by the Tevatron. The Tevatron consists of superconducting magnets and is located below the Main Ring. The Tevatron operates with six proton and six antiproton bunches colliding in two luminous regions, B0 and D0. The CDF detector is located at B0. The Tevatron provided an average instantaneous luminosity of 1.0×10^{31} cm^{-2}s^{-1} during Run I.

2.2 The CDF detector

The CDF detector is a large, general purpose detector designed to study $p\bar{p}$ collisions at $\sqrt{s} = 1.8$ TeV. The CDF is approximately 27 meters long, 10 meters high, and weighs about 5000 tons. It covers almost all of the solid angle, 2π in azimuth and the angular region $2^\circ < \theta < 178^\circ$, where θ is the polar angle with respect to the beam direction. The CDF detector consists of three detectors, the central ($10^\circ < \theta < 170^\circ$) and two identical forward ($2^\circ < \theta < 10^\circ$)/backward ($170^\circ < \theta < 178^\circ$) detectors.

A superconducting solenoid of length 4.8 m and radius 1.5 m produces a 1.4 T magnetic field and contains three tracking chambers, a silicon vertex detector (SVX), vertex time projection chambers (VTX) and a central tracking chamber (CTC), which are used to detect charged particles and measure their momenta. Surrounding the solenoid are calorimeter systems used to measure the electromagnetic energy of electrons and photons and the hadronic energy of jets. The calorimeter system consists of three regions, the central, end plug and forward. Each region has an electromagnetic calorimeter in front of a corresponding hadronic calorimeter. The central electromagnetic calorimeter (CEM) is covered with two hadron calorimeter systems, the central hadron (CHA) and the wall hadron calorimeter (WHA), while a single system of the plug hadron (PHA) and the forward hadron (FHA) calorimeter overlaps the plug electromagnetic (PEM) and the forward electromagnetic (FEM) calorimeters, respectively. Outside the calorimeters are drift chambers used for muon detection. A central muon system (CMU), a central muon upgrade (CMP), a central muon extension (CMX) and a forward muon system (FMU) compose the muon detection system. One quarter of the CDF detector is lustrated in Figure 2.2.

The CDF detector is described in detail elsewhere [33]. In the following the emphasis will be on detector components of the central detector which are used in this analysis.

2.2.1 Coordinate system

The CDF coordinate system is a right-handed system with the origin taken at the center of the detector. The z direction is taken along the proton beam, West to East, the y axis points vertically upward, and the x axis points radially outward from the Tevatron ring. The polar angle θ and the azimuthal angle ϕ are defined as follows: θ is measured with respect to the positive z-axis and $\phi = 0$ is along the positive x-axis with ϕ increasing toward the positive y-axis. The polar angle is often expressed in terms of the pseudorapidity η defined by

$$\eta = -\ln\left(\tan\frac{\theta}{2}\right). \tag{2.1}$$

The transverse momentum (p_T) and energy (E_T) are defined as

$$\begin{aligned} p_T &= p\sin\theta, \\ E_T &= E\sin\theta. \end{aligned} \tag{2.2}$$

2.2.2 Tracking detectors

SVX and SVX′

The silicon vertex detector (SVX) [56] is a new device installed in 1992 and provides high precision tracking information in the r–ϕ plane. The SVX is located between the beam pipe and the VTX along with the beam direction. The SVX is made up of two cylindrical modules with a total active length of 51 cm and a gap of 2.15 cm between the modules. This module is referred to as "barrel" and is shown in Figure 2.3. The $p\bar{p}$ interaction region at CDF is roughly Gaussian with standard deviation $\sigma \sim 30$ cm in the z direction. The geometrical acceptance of the SVX is about 60% of the interaction region at CDF.

The SVX barrel consists of four radial layers of single sided silicon strip detectors segmented into twelve 30 degree wedges. The layers of the SVX are labelled $0-3$ in increasing radius from the beam line and their positions are listed in Table 2.1. The pitch of the strips is 60 μm for layers 0–2 and 55 μm for layer 3. The silicon detectors are 8.5 cm long and 300 μm thick with different widths for each layer as listed in Table 2.1. The detectors are bonded to each other along the beam direction in groups of three making a "ladder", as shown in Figure 2.4.

Because of the radiation damage, the SVX was replaced for Run Ib by the SVX′ [35] with the radiation-hard electronics. The geometries of these two detectors are nearly identical. The major difference is the radius of the innermost layer. For the SVX′, the radius of layer 0 is at 2.8612 cm, while it is at 3.0049 cm for the SVX.

The relevant performance numbers of the SVX and SVX′ are the spatial hit resolution of approximately 13 μm and the impact parameter resolution of

$$\sigma_{d_0}(p_T) = 13 \oplus \frac{40}{p_T}\ \mu\text{m}, \tag{2.3}$$

where p_T is a transverse momentum of a track in GeV/c. The symbol "$\oplus$" denotes a quadrature sum, $a \oplus b = \sqrt{a^2 + b^2}$. The SVX and SVX′ have allowed us to detect the displaced vertices from B hadrons.

	SVX	SVX$'$
Channels	46080	
Readout Strips L0	256	
L1	384	
L2	512	
L3	768	
Radius L0	3.0049 cm	2.8612 cm
L1	4.2560 cm	
L2	5.6872 cm	
L3	7.8658 cm	
Length	8.5 cm	
Thickness	300 μm	
Active Area Width L0	15360 μm	
L1	23040 μm	
L2	30720 μm	
L3	42240 μm	
Gain	15 mV/fC	21 mV/fC
Readout time	2.7 μm	2.1 μm
Radiation limit	15–20 Krad	> 1 Mrad
Occupancy typical	7–10%	5%
Occupancy maximum	12–20%	25%

Table 2.1: The basic characteristics of the SVX and SVX$'$.

VTX

The vertex time projection chamber (VTX) is a set of drift chambers that is mounted outside the SVX. It provides tracking information in the r–z plane up to a radius of 21 cm and in the pseudorapidity region $|\eta| < 3.25$. The VTX is used to determine the location of the primary vertex along the z direction. The resolution of the primary vertex in the z direction is about 1 mm.

CTC

The central tracking chamber (CTC) is a large cylindrical drift chamber with excellent spatial and momentum resolutions used to measure charged tracks in the central region ($30^\circ < \theta < 150^\circ$). The CTC is made up of 84 layers of sense wires arranged into 9 superlayers. Five of the superlayers contain 12 sense wires parallel to the beam line. These five axial superlayers are interleaved with four superlayers of stereo wires tilted at $+3^\circ$ or -3° with respect to the beam direction. The stereo angle direction alternates at each stereo superlayer. Each stereo superlayer contains 6 sense wires. Both axial and stereo superlayers are divided into cells so that the maximum drift distance is less than 40 mm, corresponding to a drift time of about 800 ns.

Axial and stereo data are combined to form a three-dimensional track. When the track is constrained to come from the beam, the z resolution is approximately 4 mm and the momentum resolution is

$$\frac{\delta p_T}{p_T} = 0.002 p_T, \tag{2.4}$$

where p_T has units of GeV/c. The momentum resolution for a track which has SVX hits is given by

$$\frac{\delta p_T}{p_T} = 0.0009 p_T \oplus 0.0066, \tag{2.5}$$

where p_T is in GeV/c.

Using wire signals in the superlayers 3 – 8, we can measure the ionization loss (dE/dX) of a charged particle in the CTC [36].

2.2.3 Central preshower chambers

The Central Preshower chambers (CPR) [37] are located in front of the central electromagnetic calorimeter at a radius of 168 cm from the beam line. The CPR samples the electromagnetic showers that begin in the solenoid magnet material of 1.1 radiation lengths (X_0) and is designed to separate a single photon from multiple photons (π^0, $\eta \to \gamma\gamma$) and to help identify of electrons.

The CPR is made up of multiwire proportional chambers that have 2.22 cm wide cells segmented in azimuth and are divided into four segments in η.

2.2.4 Central calorimeters

CEM

The central electromagnetic calorimeter (CEM) surrounds the solenoid and measures the energy of an electron and a photon. The energy resolution of the CEM is

$$\frac{\Delta E_T}{E_T} = \frac{13.7\%}{\sqrt{E_T}} \oplus 2\%, \tag{2.6}$$

where E_T is the transverse energy in GeV. The CEM has a tower geometry and covers the pseudorapidity region $-1.1 < \eta < 1.1$. The tower segmentations are uniform in azimuth and pseudorapidity, and are 15° in ϕ and 0.1 units in η. A wedge is made up of 10 towers along the η and the CEM consists of 48 wedges. Figure 2.5 shows one wedge of the CEM. The CEM is a sampling calorimeter which uses 3.2 mm thick lead sheets interleaved with 5 mm thick polystyrene scintillator as the active detector medium. Plastic light guides transmit the light up to two phototubes per tower. The total thickness of the CEM is $18X_0$ for normal incidence.

The central strip detector (CES) is located $6X_0$ deep in the CEM, near the shower maximum for electromagnetic showers. The CES consists of proportional chambers with cathode strip and anode wire readout and provides shower-position information in both the r–z and r–ϕ views. The CES also measures the energy at the shower maximum.

CHA/WHA

The central and wall hadronic calorimeters (CHA and WHA) overlap the CEM calorimeter and use scintillator sandwiched with steel absorber plates for energy measurement. The CHA consists of 43 layers of 10 mm plastic scintillator interleaved with 32 layers of 25 mm iron. The WHA consists of 15 layers of 10 mm plastic scintillator interleaved with 15 layers of 50 mm iron. The energy resolutions for incident isolated pions are approximately given by

$$\frac{\Delta E_T}{E_T} = \frac{50\%}{\sqrt{E_T}} \oplus 3\%, \tag{2.7}$$

for the CHA, and

$$\frac{\Delta E_T}{E_T} = \frac{75\%}{\sqrt{E_T}} \oplus 4\%, \tag{2.8}$$

for the WHA.

2.2.5 Muon detectors

The muon detection system in the central region ($-1 < \eta < 1$) consists of three detectors, the central muon detection system (CMU), the central muon upgrade (CMP) and the central muon extension (CMX). All of these muon detectors are located outside the central hadronic calorimeter. The η–ϕ coverage of the central muon detector system is shown in Figure 2.6.

CMU

The central muon (CMU) drift chambers cover the η region $-0.6 < \eta < 0.6$ and are located outside the central hadron calorimeter. The CMU identifies muons with p_T > 1.4 GeV/c, since muons must penetrate 4.9 absorption lengths to reach the CMU.

The CMU is segmented into $\Delta\phi = 12.6°$ wedges which fit into the top of each central calorimeter wedge. A wedge has three modules which are made up of four layers of four rectangular drift cells. The typical drift cell configuration of the chamber module is shown in Figure 2.7. The dimensions of the individual cells are 63.5 mm wide $\times$ 26.8 mm high $\times$ 2261 mm long. A stainless steel resistive sense wire 50 μm in diameter is located at the center of the cell. A muon track reconstructed by the CMU which is often referred to as a "stub" in the r–ϕ and in r–z planes. The r–ϕ position resolution is approximately 250 μm, while the z resolution is about 1.2 mm. The CMU provides a rough measurement of the p_T of muons which is used in the level 1 trigger.

CMP

In 1992, a layer of 0.6 m thick steel ($\sim$ 3 absorption lengths) was added behind the CMU system for additional hadron absorption, and additional four layers of drift chambers were added behind the steel to detect muons. This system is referred to as the central muon upgrade (CMP) [38]. The CMP identifies muons with $p_T > 2.5$ GeV/c and provides the muon position only in the r–ϕ plane. The position resolution is approximately 300 μm.

CMX

The central muon extension (CMX) [38] covers the pseudorapidity region $0.6 < |\eta| < 1.0$. The CMX consists of drift chambers which are sandwiched with two scintillation counters called the Central Muon Extension Scintillators (CSX). Particles that scatter off the face of the forward detectors or in the beam pipe between the central and forward detectors can hit the CMX creating a fake muon signal in the CMX. Such a background is rejected by the timing signal from the CSX, since the background comes late after the beam crossing.

2.3 Trigger system

The beam crossing rate at the Tevatron is about 300 kHz (= 1 crossing/3.5 μs). At higher luminosities the average number of $p\bar{p}$ interactions per crossing exceeds one. CDF writes out events at the rate of a few Hz (5–7 Hz), thus keeping the amount of data for offline processing to a manageable level. This requires the use of a trigger system that has a rejection factor of about 5000 to 1.

CDF utilizes the three-level trigger system in order to achieve the above rejection factor. The lowest level trigger (level 1) makes a decision in hardware during the time between beam crossings. The events that pass the level 1 trigger are considered by the level 2 trigger system. The level 2 trigger is also implemented in hardware, but uses microprocessors for some of its work. The level 2 trigger decision requires 25-35 μs and 7-10 beam crossings are lost during this time since the data has not been buffered at this stage. Those events that pass the level 2 requirements are digitized and then read out by scanners into a buffer (taking about 3 ms). Once the event scan is complete, the level 1 and level 2 trigger systems are reenabled and begin to look at a new data from beam crossings again. The buffered events are passed to the level 3 trigger system. The level 3 trigger is entirely based on software. The events that pass the level 3 requirements are written out to 8mm magnetic tape. About 35 million events are recorded onto tape during Run I.

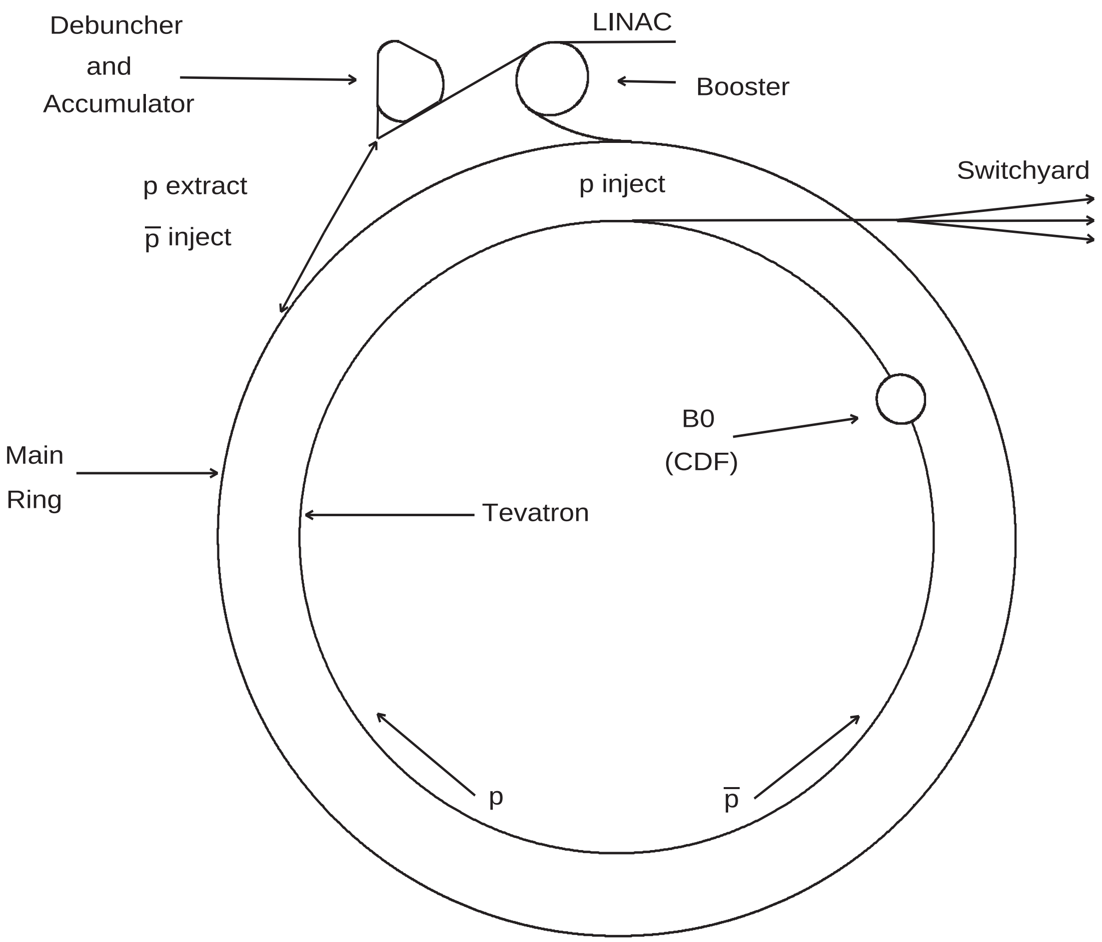

Figure 2.1: The accelerator complex at Fermilab.

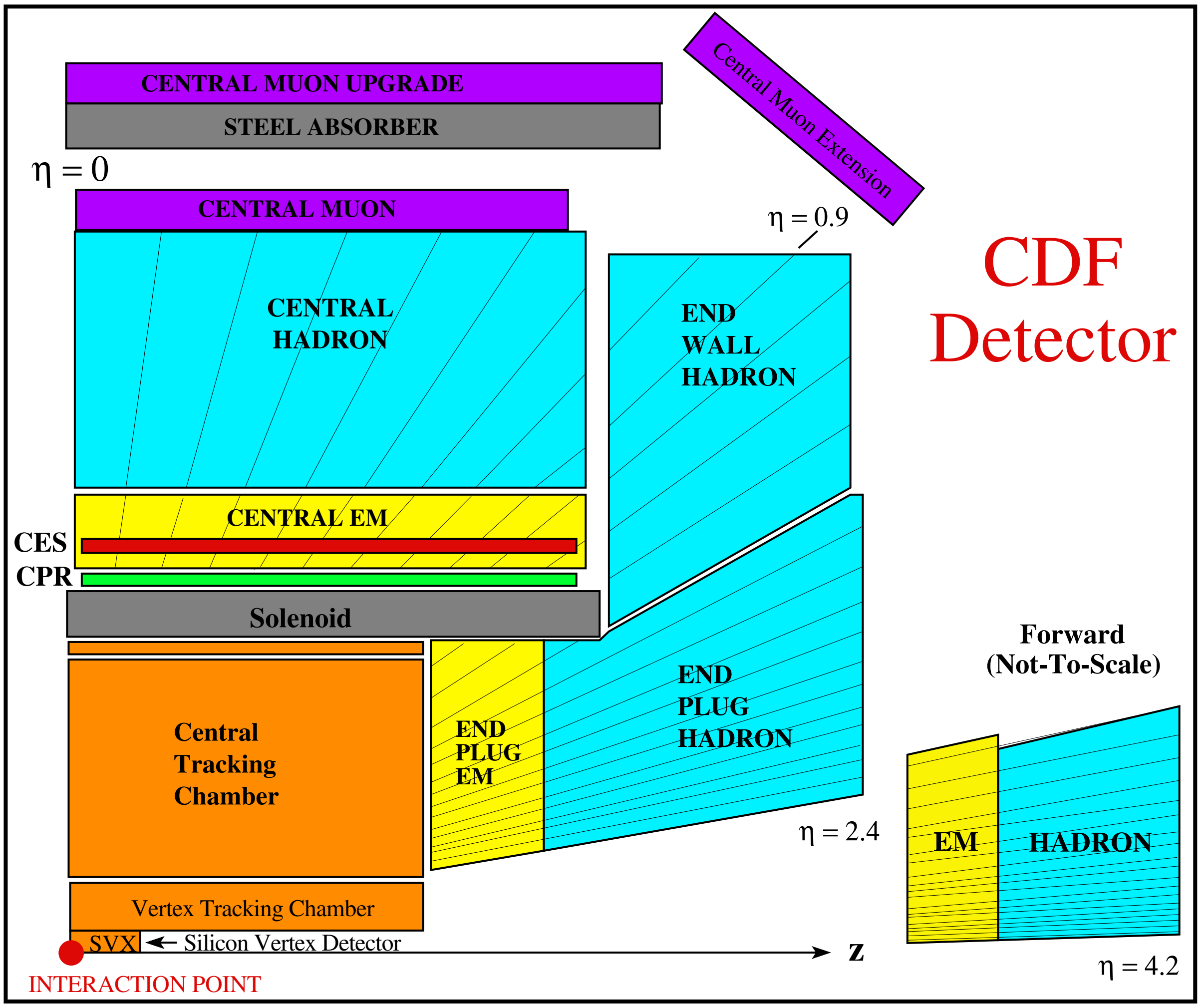

Figure 2.2: One quarter of the CDF detector.

Figure 2.3: A sketch of one of the SVX barrels.

Figure 2.4: A sketch of the SVX ladder.

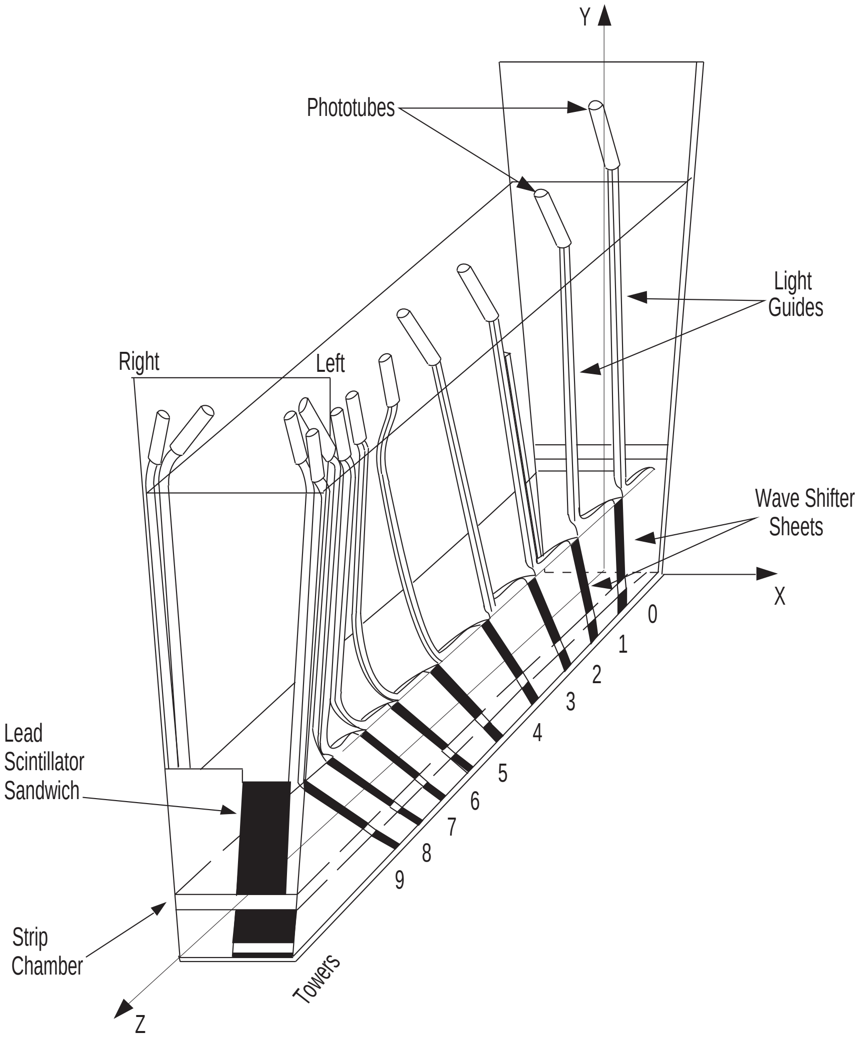

Figure 2.5: Perspective view of one wedge of the CEM with the light-gathering system.

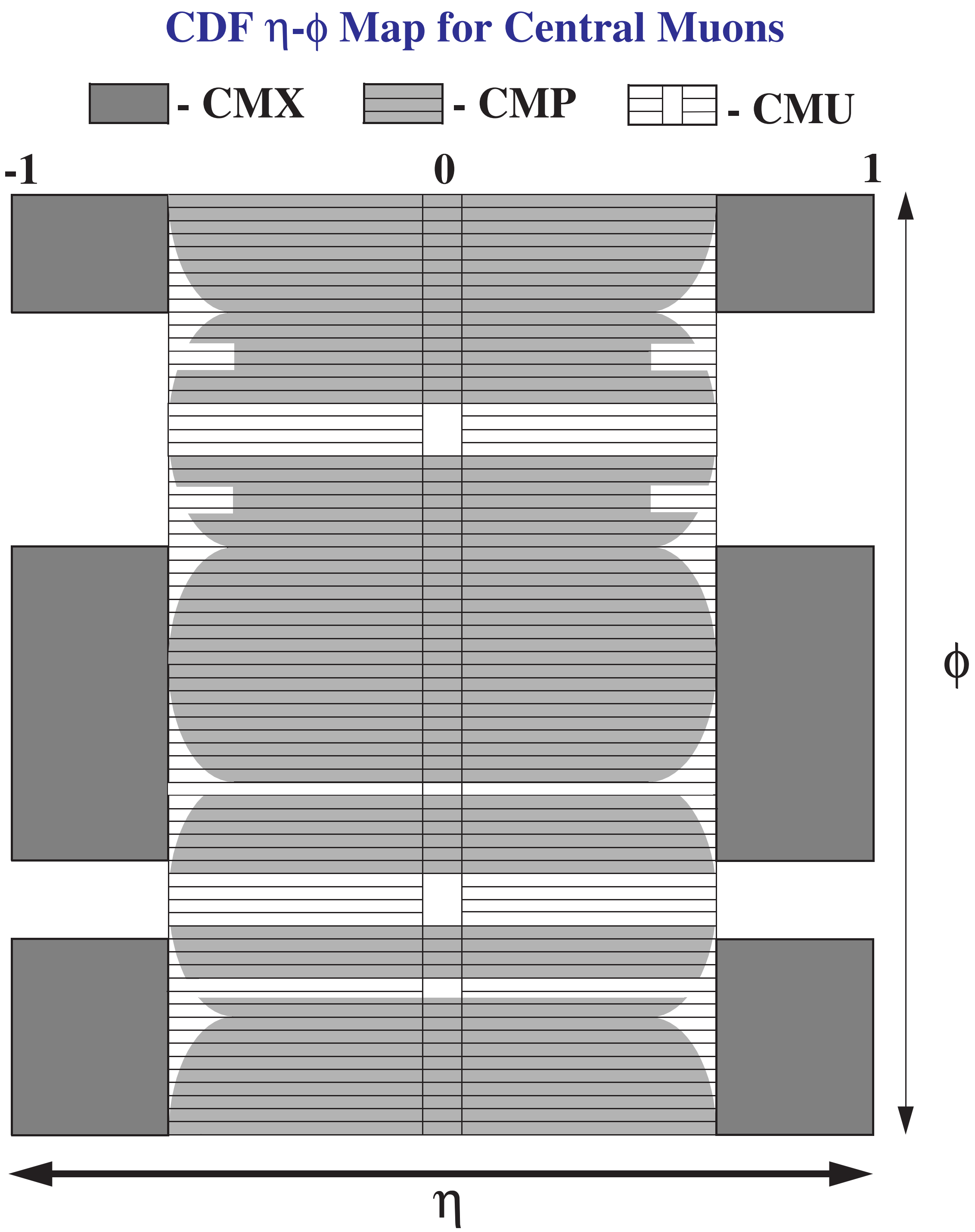

Figure 2.6: The coverage of the central muon detection system in the $\eta - \phi$ plane.

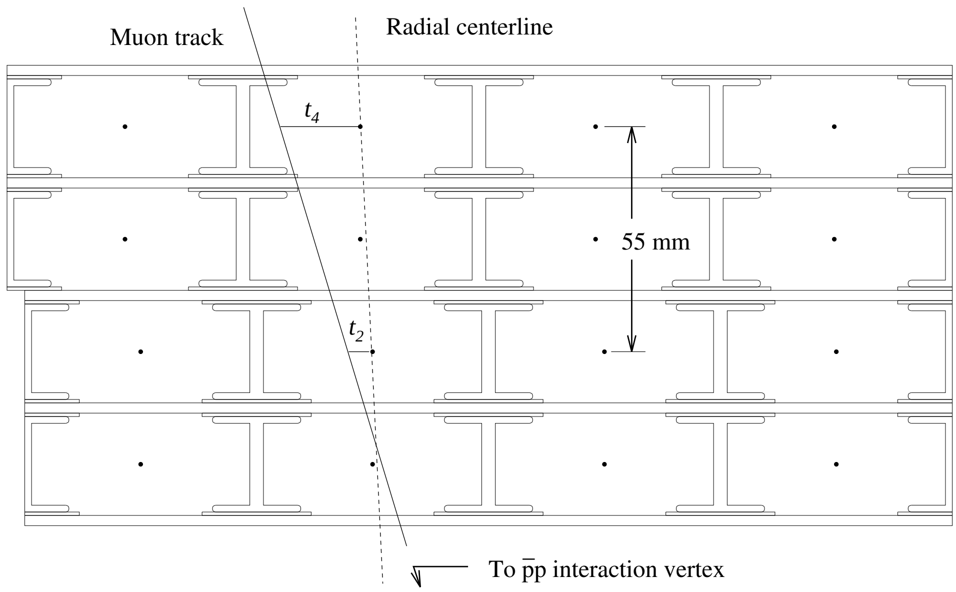

Figure 2.7: The arrangement of the four planes of the central muon chamber module ($\Delta\phi = 4.2°$) in a view along the beam direction. From the difference in drift times, p_T of the muon is estimated and is used in the level 1 trigger.

Chapter 3

Data Set and Event Selection

In this chapter, the J/ψ data set and the event selection at offline are described.

3.1 Dimuon trigger and J/ψ data set

The inclusive b quark production cross section at the Tevatron is a steeply falling function of the b-quark transverse momentum. The transverse momentum cut for b triggers should be very low. The inelastic cross section for $\bar{p}p$ collisions at $\sqrt{s} = 1.8$ TeV is about 50 mb, which is several orders as high as the b quark total production cross section (about 20 μb). Therefore, it requires a distinct signature to trigger on events including b decays without exceeding the capabilities of the data aquisition system. Single leptons and pairs of leptons provide just such a signature. The thresholds for the single lepton and dilepton triggers are set as low as possible within the rate limitations of the CDF trigger system. Dilepton requirements allow the lower p_T trigger thresholds.

The dimuon trigger used to obtain the data is described below. The level 1 trigger requires that two muon stubs are observed in the muon system. In the level 2 trigger, the muon stubs which pass the level 1 trigger requirements are matched to tracks reconstructed in the $r - \phi$ plane by the Central Fast Tracker (CFT) [39]. The CFT is a hardware track finder that uses the axial superlayers in the CTC. The level 3 trigger requires that two reconstructed CTC tracks are matched with two subs in the muon chambers and that the mass of oppositely charged muon pair is between 2.8 and 3.4 GeV/c^2. These events are written to 8 mm tape, reconstructed by the standard CDF

Dimuon Triggers Used	p_T cut on μ
CMU_CMU_ONE_CFT_1A	2.8, 1.65
CMU_CMX_ONE_CFT_1A	2.8, 1.65
CMU_CMU_TWO_CFT_1B	1.9, 1.9
CMU_CMX_TWO_CFT_1B	1.9, 1.9
CMUP_CMX_TWO_CFT_1B	2.4, 1.9
CMX_CMX_TWO_CFT_1B	1.9, 1.9
CMU_CMU_ONE_CFT_1B	3.0, 1.65
CMU_CMX_ONE_CFT_1B	3.0, 1.65
CMUP_CMU_ONE_CFT_1B	3.0, 1.65
CMUP_CMX_ONE_CFT_1B	3.0, 1.65
CMU_CMU_SIX_TOW_1B	1.9, 1.9

Table 3.1: Types of level 2 dimuon trigger and p_T cuts on muons. For example, CMU_CMU means that two muon stubs are in the CMU and TWO_CFT means that two muon stubs are matched to CFT tracks.

reconstruction programs, and split off into a J/ψ data set.

3.2 $J/\psi \to \mu^+\mu^-$ event selection

J/ψ candidates are selected from the J/ψ data set. We use events collected with the level 2 dimuon triggers listed in Table 3.1 [40]. We apply the p_T cut for muons depending on the level 2 trigger type. The muon p_T cuts are listed in Table 3.1.

There are two major sources of muon backgrounds. First, a hadron might decay to a muon in front of the muon detectors, carrying a significant fraction of hadron momentum. Then the muon reaches the muon detector and makes hits in the muon detector. Such a muon is called a "decay-in-flight" background. Second, a hadron might penetrate through the hadron calorimeter and hits the muon detector. This often occurs when a hadron interacts near the back end of the hadron calorimeter. This is called a "punch-through" background. To reduce such backgrounds, we use a χ^2 cut on the position matching. We extrapolate the muon track in the CTC to the muon chambers, and calculate the position difference between the extrapolated track and the muon stub and its uncertainty by correcting for multiple scattering and energy loss which depends on the p_T of the muon [41]. We apply a matching χ^2 cut depending

muon type	in r–ϕ	in r–z
CMU type	$\chi^2(\text{CMU}) < 3\sigma$	$\chi^2(\text{CMU}) < 3.5\sigma$
CMU/CMP type	$\chi^2(\text{CMU}) < 3\sigma$	$\chi^2(\text{CMU}) < 3.5\sigma$
CMX type	$\chi^2(\text{CMX}) < 3\sigma$	$\chi^2(\text{CMX}) < 3.5\sigma$
CMU/CMX type	$\min(\chi^2(\text{CMU}), \chi^2(\text{CMX})) < 3\sigma$	$\min(\chi^2(\text{CMU}), \chi^2(\text{CMX})) < 3.5\sigma$

Table 3.2: The position matching χ^2 cuts. "CMU/CMP (CMU/CMX)" type means that a muon stub is found in both the CMU and the CMP (CMX). σ is an uncertainty of the position difference between the muon stub and the extrapolated track.

on the muon stub. The requirements are listed in Table 3.2.

We also require that the muon track is reconstructed in the SVX, since we look for a displaced vertex of the three leptons.

We perform a vertex constraint fit of the dimuon tracks using the code CTVMFT [42] and reconstruct the dimuon invariant mass. Figure 3.1 shows the dimuon invariant mass distribution. The following events contribute to the background under the mass peak:

- irreducible decay-in-flight and punch-through background,
- a pair of muons produced by the Drell-Yang process,
- double sequential semileptonic decays of b quarks ($b \to \mu^- cX$, $c \to \mu^+ sX'$).

To estimate the number of $J/\psi \to \mu^+\mu^-$ candidates, we parametrize the $\mu^+\mu^-$ mass shape with two Gaussians plus a linear function. We assume the signal shape to be two Gaussians, because of the final state radiation of muons. The linear function represents the background shape. As a result of the fit, we find 191000 $\pm$ 2100 $J/\psi \to \mu^+\mu^-$ events. For the B_c search, the J/ψ signal region is defined $\pm$ 50 MeV/c^2 around the J/ψ world average mass ($m(J/\psi) = 3.0968$ GeV/c^2 [32]). This is referred to as the J/ψ sample. The J/ψ sample contains 186400 $\pm$ 2000 $J/\psi \to \mu^+\mu^-$ events with 17500 $\pm$ 1400 background events.

3.3 Electron identification

For high E_T electrons, an electron identification method based on calorimetry is used in various CDF analyses [43]. This method requires that the E_T of an electron is greater than 5 GeV. On the other hand, a method based on tracks [44] has been developed to tag a low p_T electron coming from the semileptonic decays of b hadrons. We have to look for a low p_T electron, because the electrons produced by the $B_c^+ \to J/\psi e^+ X$ decay has the soft p_T distribution as shown in Figure 3.2. Therefore we use the Soft Lepton Tagging (SLT) method to identify an electron.

3.3.1 Fiducial requirements

All candidate tracks for soft electrons have to satisfy the following requirements:

- $p_T > 2$ GeV/c,
- impact parameter with respect to the primary vertex < 3 mm,
- number of hits in CTC > 10,
- be reconstructed in SVX.

The tracks which satisfy these requirements are extrapolated to the CES (radius = 184 cm) in the CEM. The fiducial tracks are defined as those that are extrapolated to a point at least 2 cm away from the phi edge of a tower (towers are 48 cm wide) and 6 cm away from the z boundary of the arch (an arch is 249 cm long). The "chimney" region of the CEM where there is a gap in the calorimeter coverage that allows for access to the solenoid is also excluded from the fiducial region. Finally, the tracks are extrapolated to the CPR and are required to be away from the edges of the CPR chambers.

3.3.2 CES requirements

The SLT electron candidate tracks passing the fiducial cuts are matched to a CES cluster. The matched clusters are required to be consistent in size, shape and position with the expected electron shower. The CES electron energy is obtained by summing up the energy in the 5 strips (E_{s5}) and 5 wires (E_{w5}) around the extrapolated track position. To account for shower fluctuation in the calorimeter, which depends on momentum (p), we apply the following cuts on E_{s5} and E_{w5}:

- $E_{s5}/p > 0.24 + 0.003p$ for $p < 12$ GeV/c,
  $E_{s5}/p > 0.6 - 0.0125 \times (p - 12)$ for $12 < p < 20$ GeV/c,
  $E_{s5}/p > 0.5$ for $p > 20$ GeV/c,

- $E_{w5}/p > 0.24 + 0.003p$ for $p < 12$ GeV/c,
  $E_{w5}/p > 0.6 - 0.0125 \times (p - 12)$ for $12 < p < 20$ GeV/c,
  $E_{w5}/p > 0.5$ for $p > 20$ GeV/c,

where p is the track momentum in GeV/c. Figure 3.3 shows the E_{w5}/p and E_{s5}/p distributions for electrons from a conversion sample which is selected using cuts described in Section 3.3.6 and for background tracks from a hadron rich sample which is accumulated with the JET20 trigger. The JET20 trigger is an inclusive jet trigger with a transverse energy threshold of 20 GeV.

Next, the CES cluster positions in the r–ϕ and r–z planes are calculated by taking the energy-weighted mean of 3 wires and 3 strips respectively around the extrapolated track position. Then the distances Δx and Δz between the extrapolated track position and the cluster position are calculated and the following cuts are applied:

- $|\Delta x| <$ Max(0.7 cm, $1.82 - 0.1867p$ cm),

- $|\Delta z| < 2$ cm,

where p is the track momentum in GeV/c. The momentum dependent $|\Delta x|$ cut is adopted, since the $|\Delta x|$ distribution shows some variation with momentum due to shower fluctuations. Figure 3.4 shows $|\Delta x|$ and $|\Delta z|$ distributions for electrons from the photon conversion sample and for tracks in the JET20 data.

Finally the lateral shower shape of 7 channel CES clusters (χ^2_{wire} and χ^2_{strip}) is required to be consistent with the test beam data [45].

- $\chi^2_{wire}/6 \leq 16$

- $\chi^2_{strip}/6 \leq 16$

Figure 3.5 shows the $\chi^2_{wire}/6$ ($\chi^2_{strip}/6$) distributions for electrons from the photon conversion sample and for tracks in JET20 data.

3.3.3 CPR requirements

The preradiator energy for a track is calculated by extrapolating the CTC track to the CPR and summing the charges in the 3 adjacent CPR wires. Tracks at large $|\eta|$ (small $\sin\theta$) have a longer path length through the solenoid coil than tracks at low $|\eta|$ (large $\sin\theta$), causing the CPR response to vary with the polar angle. Thus the tracks at small $\sin\theta$ interact with more material to produce more secondary particles which deposit more charge in the CPR. The CPR threshold contains an angular dependence (p/p_T) to correct for this effect and the cut employed is:

- $Q_{CPR} > 4744 - 11592(p/p_T) + 7923\,(p/p_T)^2$,

where Q_{CPR} is the charge measured in the CPR and has unit of fC. The minimum threshold corresponds to four minimum ionizing particles. Figure 3.6 shows the Q_{CPR} distributions for electrons from the photon conversion sample and for tracks in JET20 data.

3.3.4 dE/dX requirements

The specific ionization (dE/dX) measured in the CTC is required to be consistent with the electron hypothesis. The charge collected in a CTC sense wire, which is proportional to the energy loss per sense wire spacing, is stored as the pulse width between the leading edge and the trailing edge of a CTC pulse. The mean charge Q_{CTC} in suprelayers 3 through 8 is used as a dE/dX quantity. Figure 3.7 shows the Q_{CTC} as a function of momentum. The Q_{CTC} plotted for electrons, pions, muons and protons, exhibits the expected dE/dX behavior. The Q_{CTC} distribution is essentially independent of momentum for electrons, but depends strongly on momentum for the other particles. To see how well the Q_{CTC} describes the dE/dX for a specific particle, we define the following S_i:

$$S_i \equiv \frac{Q_{CTC} - Q_i}{\sigma}, \quad i = e, \pi, p \tag{3.1}$$

p range	S_e cut
$3 > p > 2$ GeV/c	$S_e > -0.9$
$5 > p > 3$ GeV/c	$S_e > -1.1$
$6 > p > 5$ GeV/c	$S_e > -1.3$
$8 > p > 6$ GeV/c	$S_e > -1.5$
$10 > p > 8$ GeV/c	$S_e > -1.9$
$p > 10$ GeV/c	not applied

Table 3.3: The dE/dX cuts for the electron selection.

where i denotes the particle, Q_{CTC} is the measured dE/dX in CTC, Q_i is the expected dE/dX for the specific particle i and σ is the resolution of Q_{CTC}. In Figure 3.8, we show the S_e distribution for electrons, the S_π distribution for pions and the S_p distribution for protons. They were represented by a Gaussian with mean 0 and standard deviation 1.

The dE/dX requirements are determined so as to optimize $\varepsilon^2 R$ as a function of momentum, where ε is an efficiency for electrons and R is a rejection factor $R = 1/\varepsilon_{bkg}$ for backgrounds. To calculate $\varepsilon^2 R$, tracks of the conversion electron sample and tracks in the JET20 trigger data are used for electrons and for backgrounds, respectively. Figure 3.9 shows the S_e distribution for the electrons from the photon conversion and that for tracks in the JET20 data. The S_e cuts employed for the electron selection are listed in Table 3.3.

3.3.5 E/p and E_{had}/E_{EM} requirements

The E/p is defined as the electromagnetic energy measured in the CEM divided by the track momentum measured in the CTC, and the E_{had}/E_{EM} as the ratio of the hadronic energy to the electromagnetic energy. To calculate the calorimeter energy associated with a track, the candidate track is extrapolated to a tower in the central calorimeter. The calorimeter energy is given by the energy deposited in the tower to which the track points. However, if the track is extrapolated to within 2 cm from a tower boundary, the energy of the neighbor tower is also included. In the electron selection, the following E/p and E_{had}/E_{EM} cuts are applied:

- $0.7 < E/p < 1.5$,
- $E_{had}/E_{EM} < 0.1$.

3.3.6 Conversion removal

Photons are produced largely from the decay of neutral pions. These photons can convert in the detector to e^+e^- pairs which may be identified as electrons. Also 1.2% of the neutral pions produce a pair of electrons directly by decaying to a photon and an e^+e^- pair (the "Dalitz decay", $\pi^0 \rightarrow \gamma e^+e^-$) [32] .

In order to minimize these backgrounds, a conversion veto is incorporated into the SLT algorithm. A conversion electron candidate is identified by finding its conversion partner track which satisfies the following requirements:

- the electron candidate and a track have opposite charge,
- $|\Delta \cot \theta| < 0.06$,
- $|\Delta S| < 0.3$ cm,
- Mass$(e^+e^-) < 500$ MeV/c^2,
- $R_{conv} < 50$ cm,

where ΔS is the distance in the $r - \phi$ plane between the electron and positron tracks at the point where they are parallel (conversion point). R_{conv} is the radius of the conversion point. If the conversion partner track is not reconstructed because of its low p_T, the conversion electron fails these requirements and it may be identified as a signal by the SLT algorithm.

3.4 J/ψ + electron events

By applying the SLT algorithm to the J/ψ sample, electron candidates are identified in 418 events. The p_T distribution for the electron candidates is shown in Figure 3.10.

For the $B_c^+ \to J/\psi(\to \mu^+\mu^-)e^+X$ signal events, the dimuon and the electron come from a common vertex since the J/ψ immediately decays into $\mu^+\mu^-$. Therefore, a vertex constraint fit of 3 leptons is preformed. In this fit, the mass of the muon pair is also constrained to the world average mass of the J/ψ ($m(J/\psi) = 3.0968$ GeV/c^2 [32]). The following requirements are additionally applied in order to confirm that the J/ψ and the electron come from the same parent B meson.

- The J/ψ and the electron are in the same hemisphere, *i.e.*, $\Delta\phi(J/\psi, e) < \frac{\pi}{2}$.
- The probability of the 3 track vertex fit χ^2 is greater than 1%, *i.e.*, Prob(vertex fit χ^2) > 1%.

When the mass of the charged kaon ($m(K^+) = 493.7$ MeV/c^2 [32]) is assigned to a track and the invariant mass of the three tracks distributes around the charged B meson mass ($m(B_u^+) = 5.278$ GeV/c^2 [32]), these three tracks are considered to come from the $B_u^+ \to J/\psi K^+$ decay, with the K^+ misidentified as an e^+. To remove these contributions, we require that the three track invariant mass $m(\mu^+\mu^-K^+)$ satisfies that $|m(B_u^+) - m(\mu^+\mu^-K^+)| > 50$ MeV/c^2.

The p_T distribution for the electrons and the J/ψ + electron invariant mass distribution are shown in Figure 3.11. We find 70 J/ψ + electron candidates in the mass region $m(J/\psi e) < 15$ GeV/c^2.

3.4.1 $J/\psi + e$ mass distribution for Monte Carlo signal events

For the $B_c^+ \to J/\psi e^+ X$ decay mode, we cannot fully reconstruct the momentum and mass of the B_c meson, due to the missing particles (ν etc.). We can know only the momenta of the J/ψ and the electron. Therefore we define a signal region using the invariant mass of the J/ψ plus electron system. We naively expect that the mass of the J/ψ plus electron system lies in a range between the J/ψ mass and the B_c mass. In order to study the signal mass distribution of the J/ψ plus electron system, a Monte Carlo simulation is used. We generate the B_c mesons according to the B_c meson p_T spectrum of the α_s^4 calculation [11], shown in Figure 1.5. The η distribution is flat in the range $|\eta| < 1.2$. We let the B_c mesons decay into $J/\psi e^+\nu$ with the

$V - A$ matrix elements. The event undergoes the CDF detector simulation. Then the simulated events are processed with the same reconstruction programs as used for real data. Finally, the events pass through the trigger simulation [40]. Figure 3.12 shows the J/ψ + electron invariant mass distribution for the Monte Carlo simulation. From the figure, we define the signal mass region to be between 4 GeV/c^2 and 6 GeV/c^2, *i.e.*, $4 < m(J/\psi e) < 6$ GeV/c^2.

3.4.2 $J/\psi + e$ mass distribution for data

As mentioned in Chapter 1, the lifetime of the B_c meson is not exactly known. It would be better if we could select the B_c signal sample without any cuts depending on the lifetime. However there exist a lot of prompt J/ψ events in the J/ψ sample (about 80% of the J/ψ's are prompt J/ψ events [46]). Therefore, we use the decay length cut with a cut value set as low as possible.

As we cannot fully reconstruct the momentum and mass of the B_c meson, the pseudo-proper decay length x, defined below, is used instead of the true proper decay length. First we calculate the transverse decay length L_{xy} between the primary vertex and the secondary vertex, measured in the r–ϕ plane. The L_{xy} is defined by

$$L_{xy} \equiv \frac{\left(\vec{V}_{SV} - \vec{V}_{PV}\right) \cdot \vec{p}_T\left(J/\psi e\right)}{\left|\vec{p}_T\left(J/\psi e\right)\right|}, \tag{3.2}$$

where $\vec{p}_T\left(J/\psi e\right)$ is the transverse momentum of the $J/\psi + e$ system, $\vec{V}_{PV}$ is a primary vertex and $\vec{V}_{SV}$ is a secondary vertex of the J/ψ and the electron. These vectors are two dimensional. Then we correct the L_{xy} accounting for the Lorentz boost to obtain the pseudo-proper decay length x:

$$x \equiv \frac{m\left(J/\psi e\right)}{\left|\vec{p}_T\left(J/\psi e\right)\right|} L_{xy}. \tag{3.3}$$

These variables are described in detail in Chapter 6.

The minimum cut value on x is set to 60 μm which corresponds to 1.5 times the secondary vertex resolution (1.5σ). We look at the mass distribution of the J/ψ plus electron system with various x cuts. The $J/\psi + e$ mass distributions for $x > 60$ μm, 85 μm, 100 μm, and 150 μm are shown in Figure 3.13. The numbers of the $J/\psi + e$

x cut threshold	$N_{J/\psi+e}$ in $m < 15$ GeV/c^2	$N_{J/\psi+e}$ in $4 < m < 6$ GeV/c^2
60 μ m	23 events	19 events
85 μ m	17 events	13 events
100 μ m	15 events	12 events
150 μ m	11 events	10 events

Table 3.4: Number of $J/\psi + e$ candidates for $m(J/\psi e) < 15$ GeV/c^2 and for $4 < m(J/\psi e) < 6$ GeV/c^2. The data of 105 pb^{-1} were used.

candidates are listed in Table 3.4. In the signal region $4 < m(J/\psi e) < 6$ GeV/c^2 with the $x > 60$ μm cut, we find 19 $J/\psi + e$ candidates, of which 9 are $J/\psi + e^+$ and 10 are $J/\psi + e^-$.

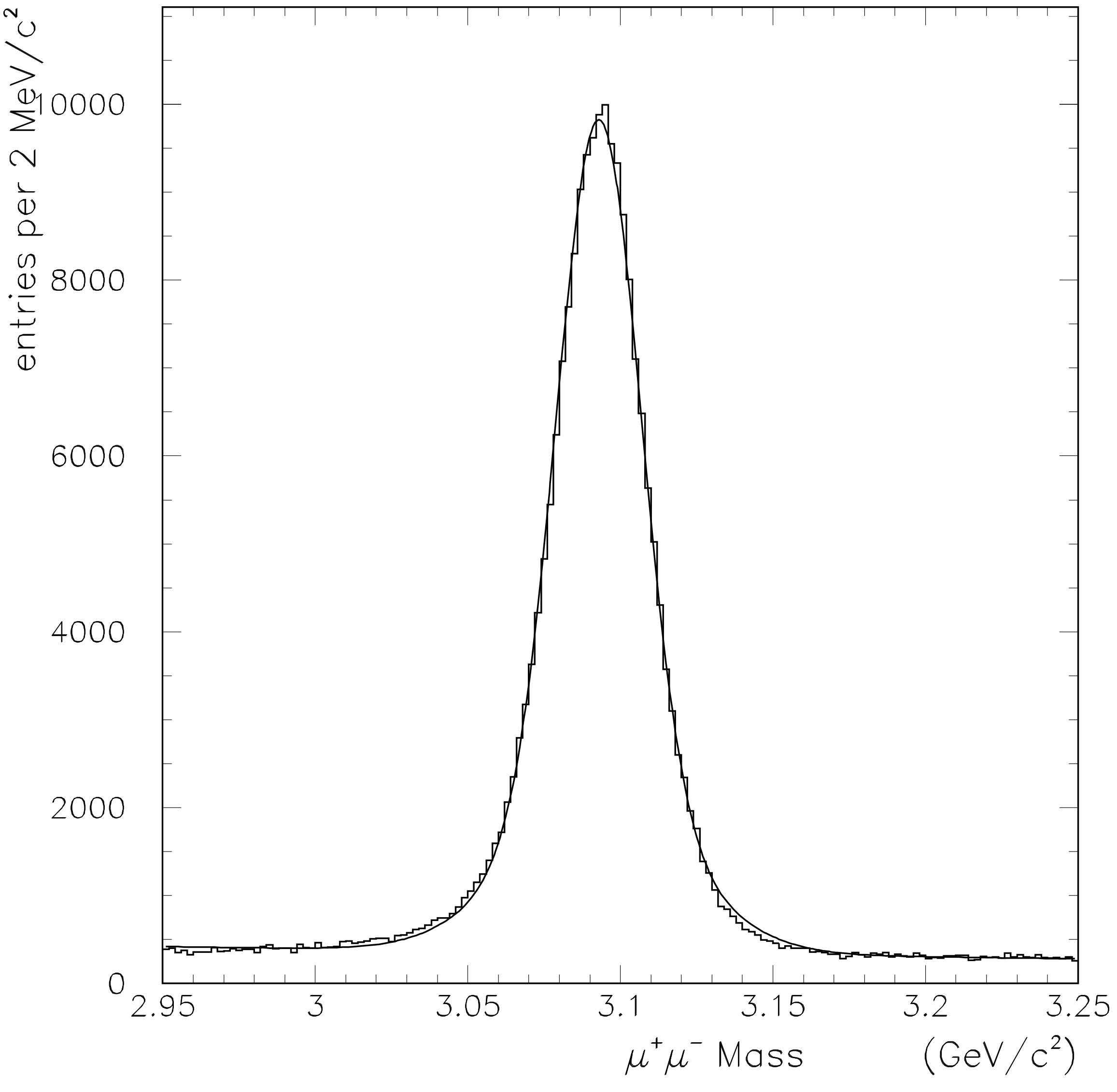

Figure 3.1: The invariant mass distribution of the dimuon pairs for Run I.

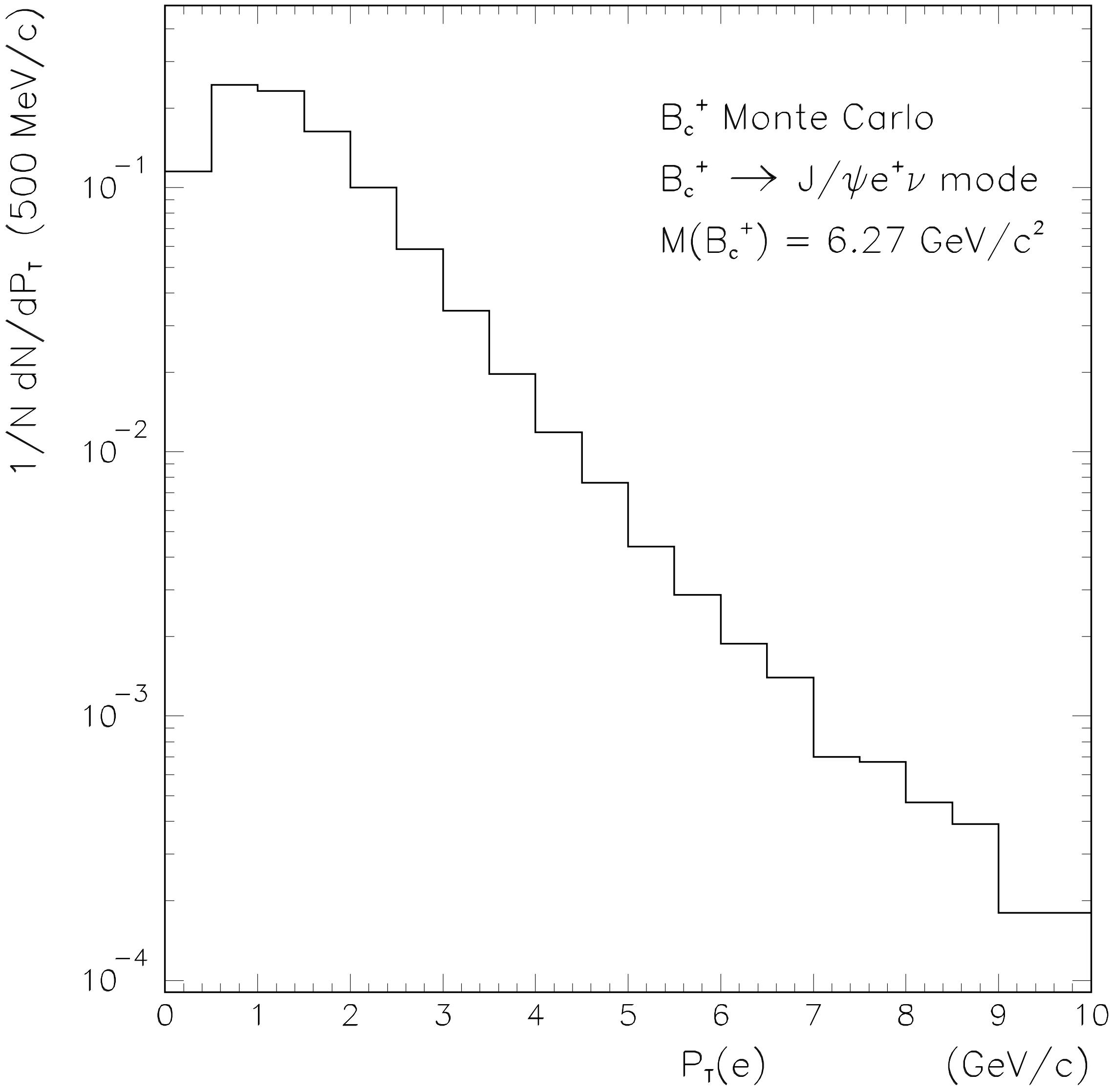

Figure 3.2: The electron p_T distribution for the Monte Carlo simulation. No cuts are applied.

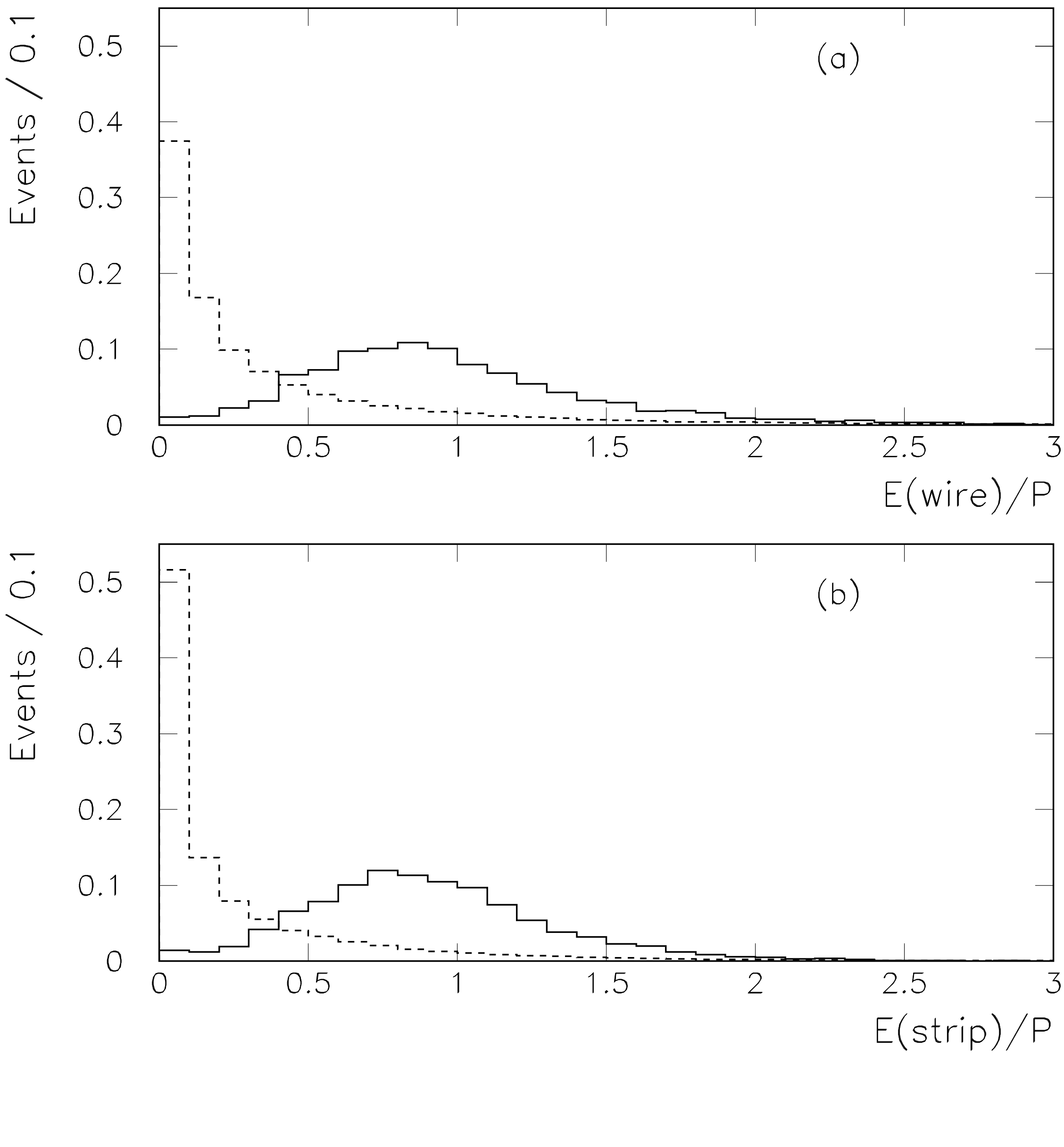

Figure 3.3: E_{CES}/p distributions for electrons from the photon conversion sample (solid line) and for tracks in the JET20 data (dashed line): (a) E_{w5}/p and (b) E_{s5}/p. The distributions are normalized to unit area.

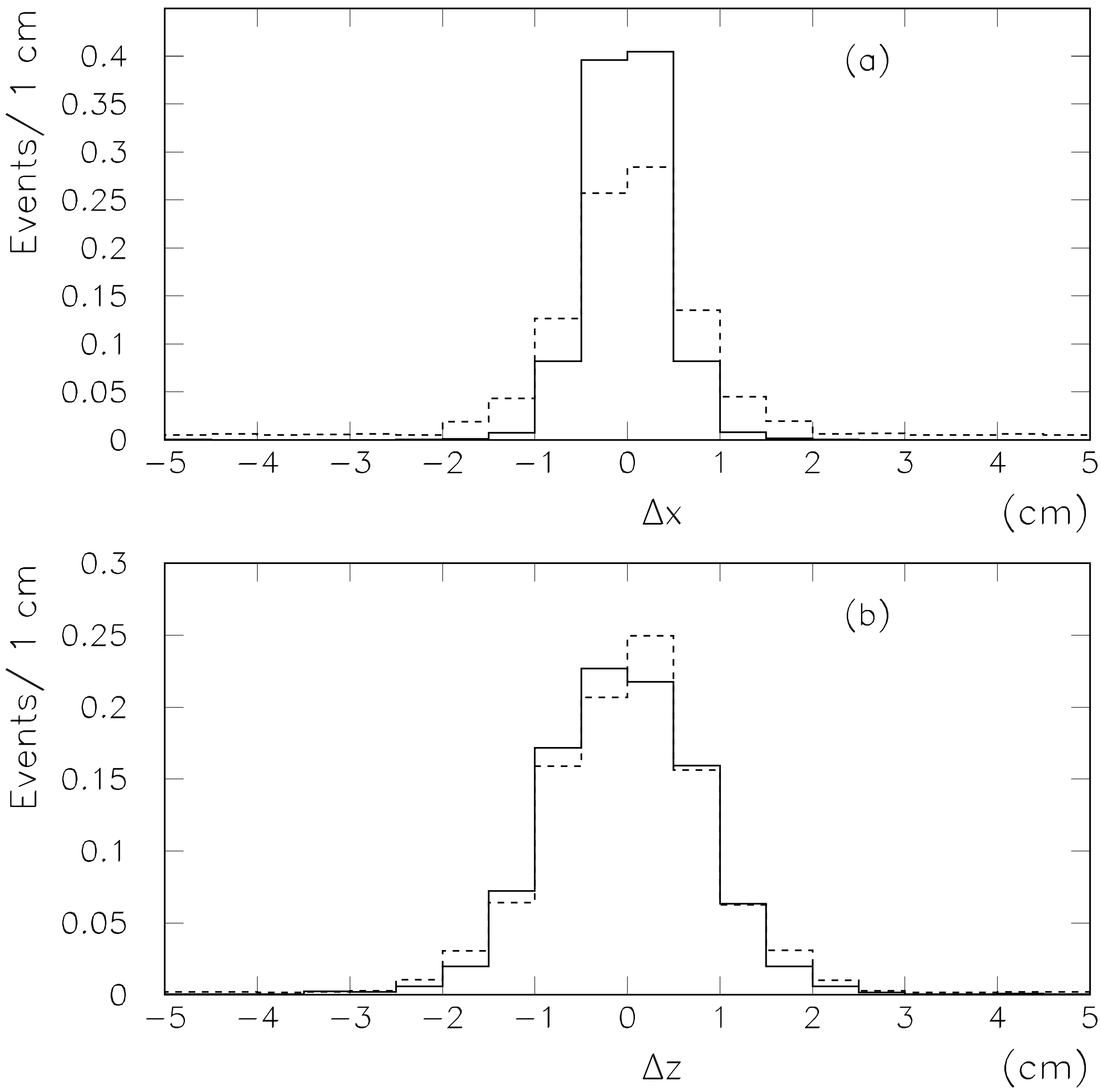

Figure 3.4: (a) ΔX and (b) ΔZ distributions for electrons from the photon conversion sample (solid line) and for tracks in the JET20 data (dashed line). The distributions are normalized to unit area.

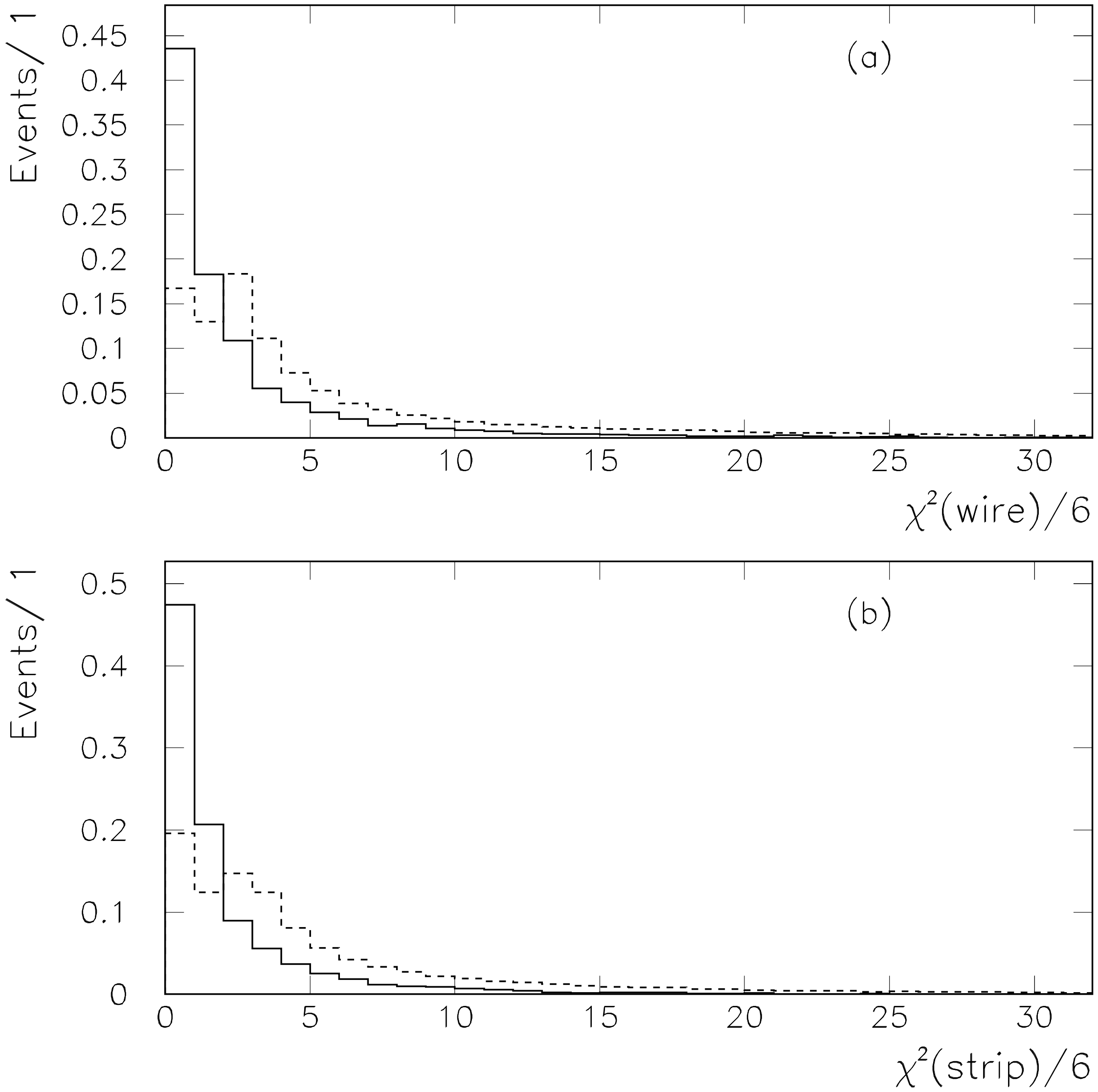

Figure 3.5: The χ^2 distributions for electrons (solid line) from the photon conversion sample and for tracks in the JET20 data (dashed line): (a) $\chi^2(wire)/6$ and (b) $\chi^2(strip)/6$. The distributions are normalized to unit area.

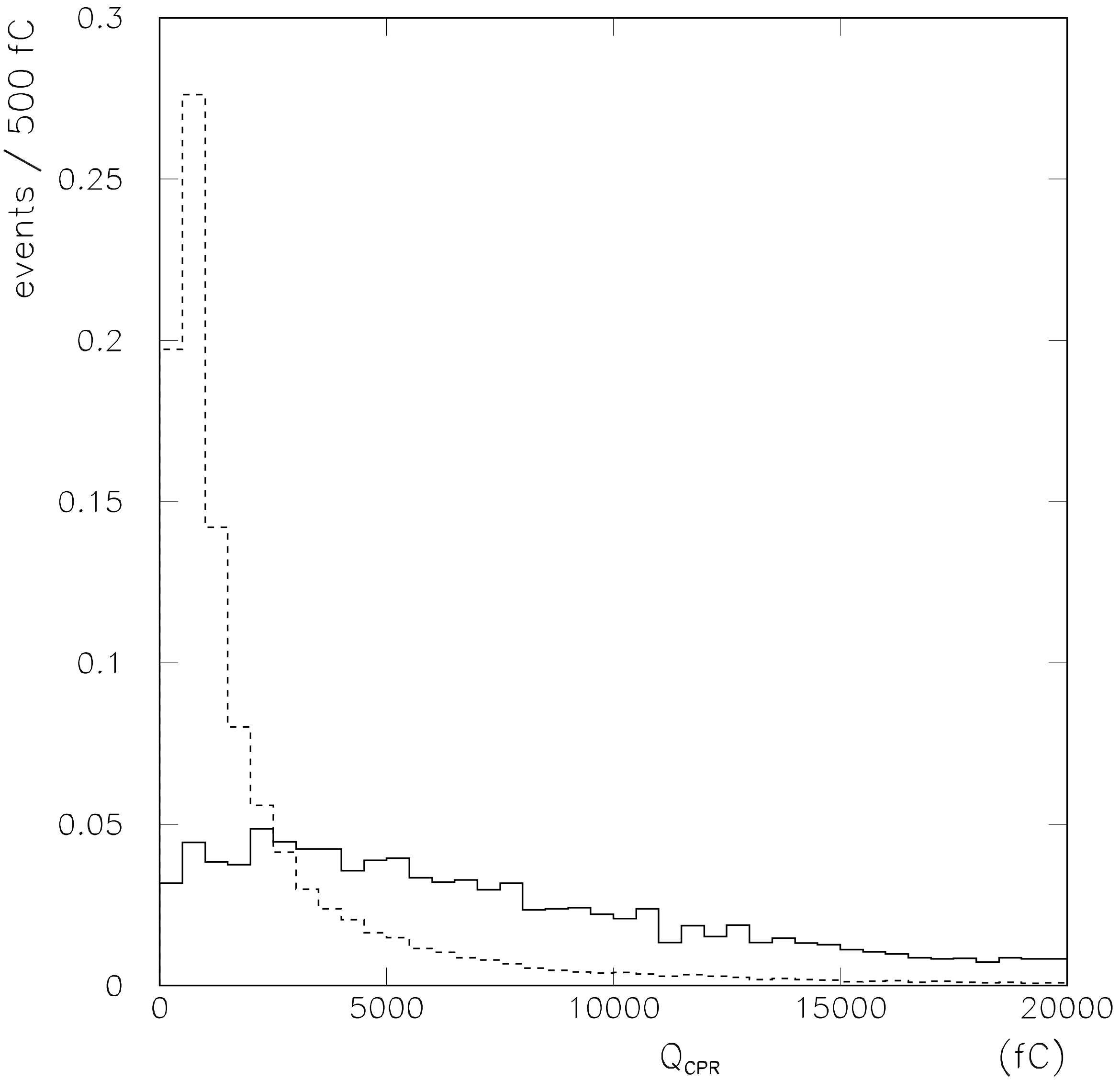

Figure 3.6: The Q_{CPR} distributions for electrons from the photon conversion sample (solid line) and for tracks in the JET20 data (dashed line). The distributions are normalized to unit area.

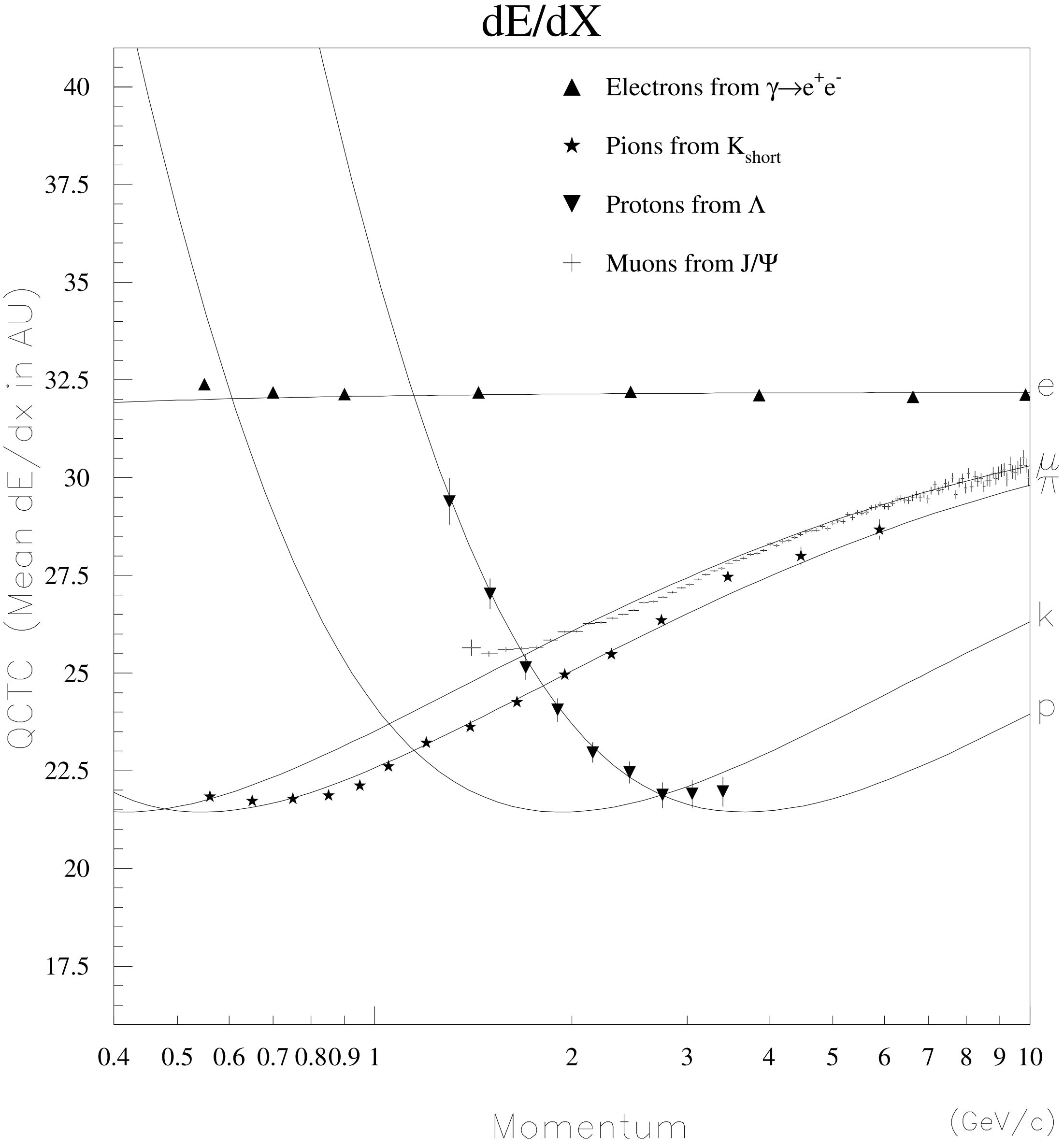

Figure 3.7: The Q_{CTC} (dE/dX) as a function of momentum for electrons, pions, protons and muons from the data. The predicted curve for kaons is also shown.

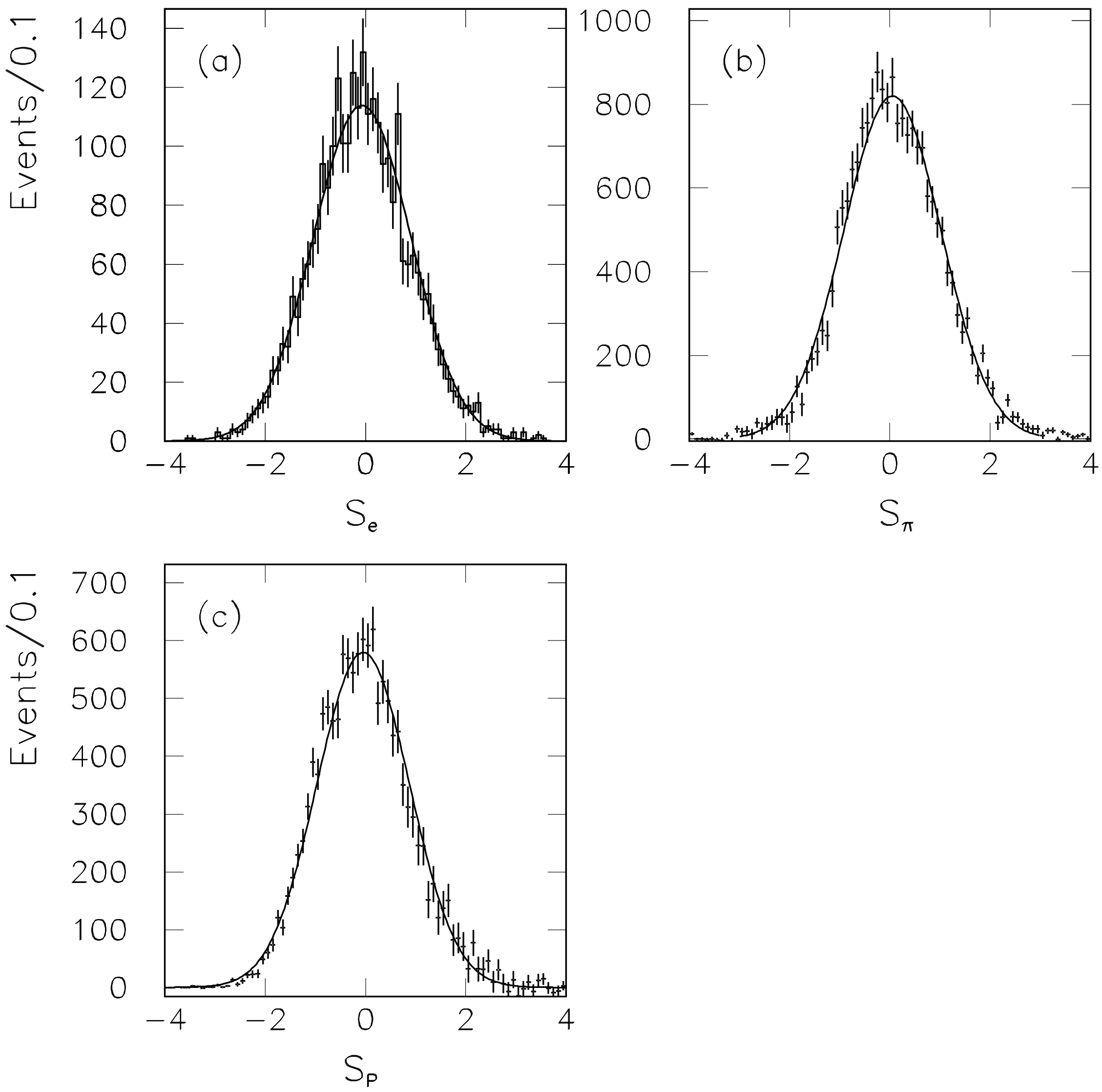

Figure 3.8: The S_i distributions superimposed with a Gaussian with mean 0 and standard deviation 1. (a) S_e for electrons from the conversion sample. (b) S_π for pions from the $K_s^0 \rightarrow \pi^+\pi^-$. (c) S_p for protons from $\Lambda \rightarrow p\pi^-$.

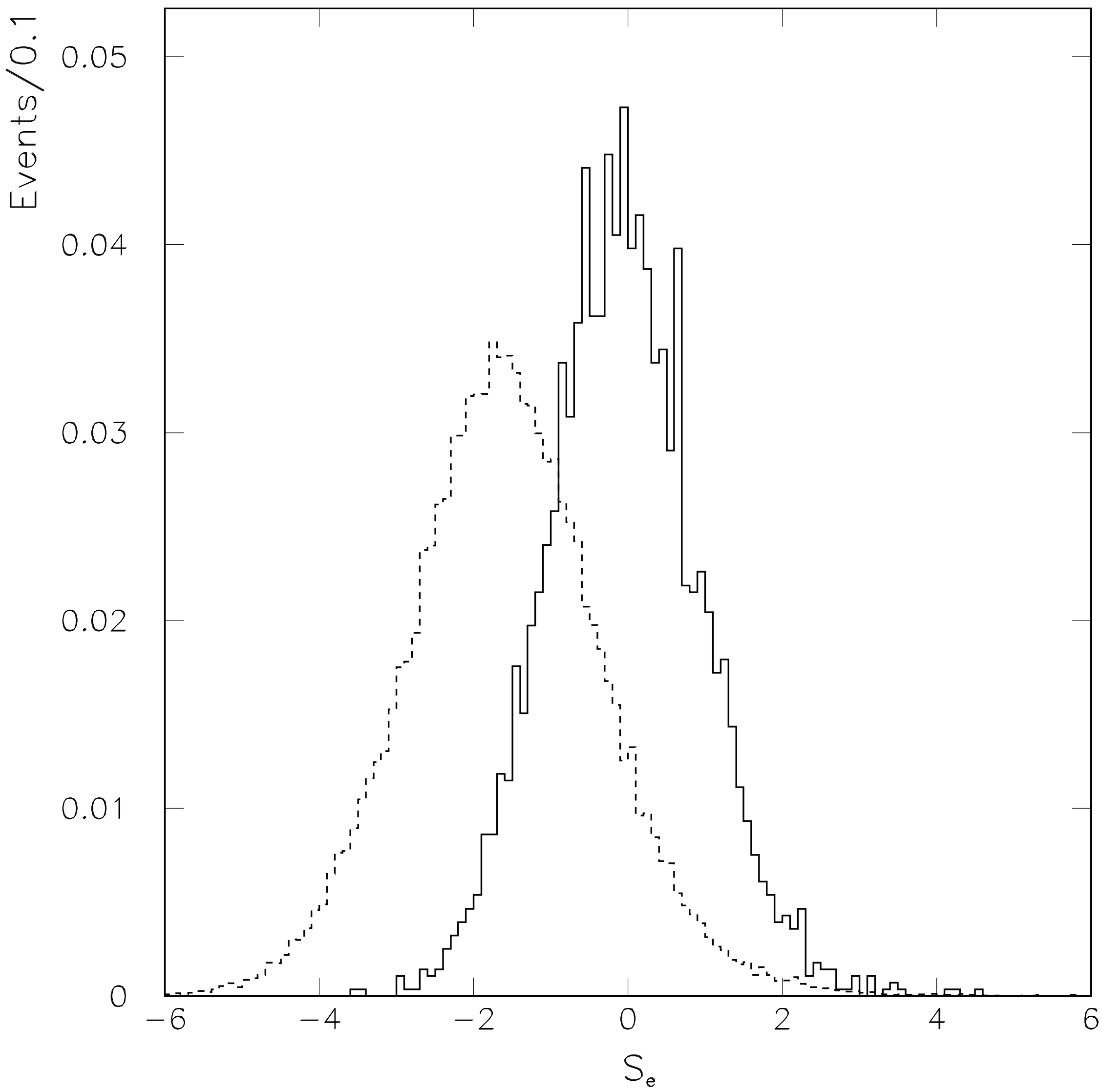

Figure 3.9: The S_e distribution for electrons from the photon conversion sample (solid line) and for tracks in the JET20 data (dashed line). The distributions are normalized to unit area.

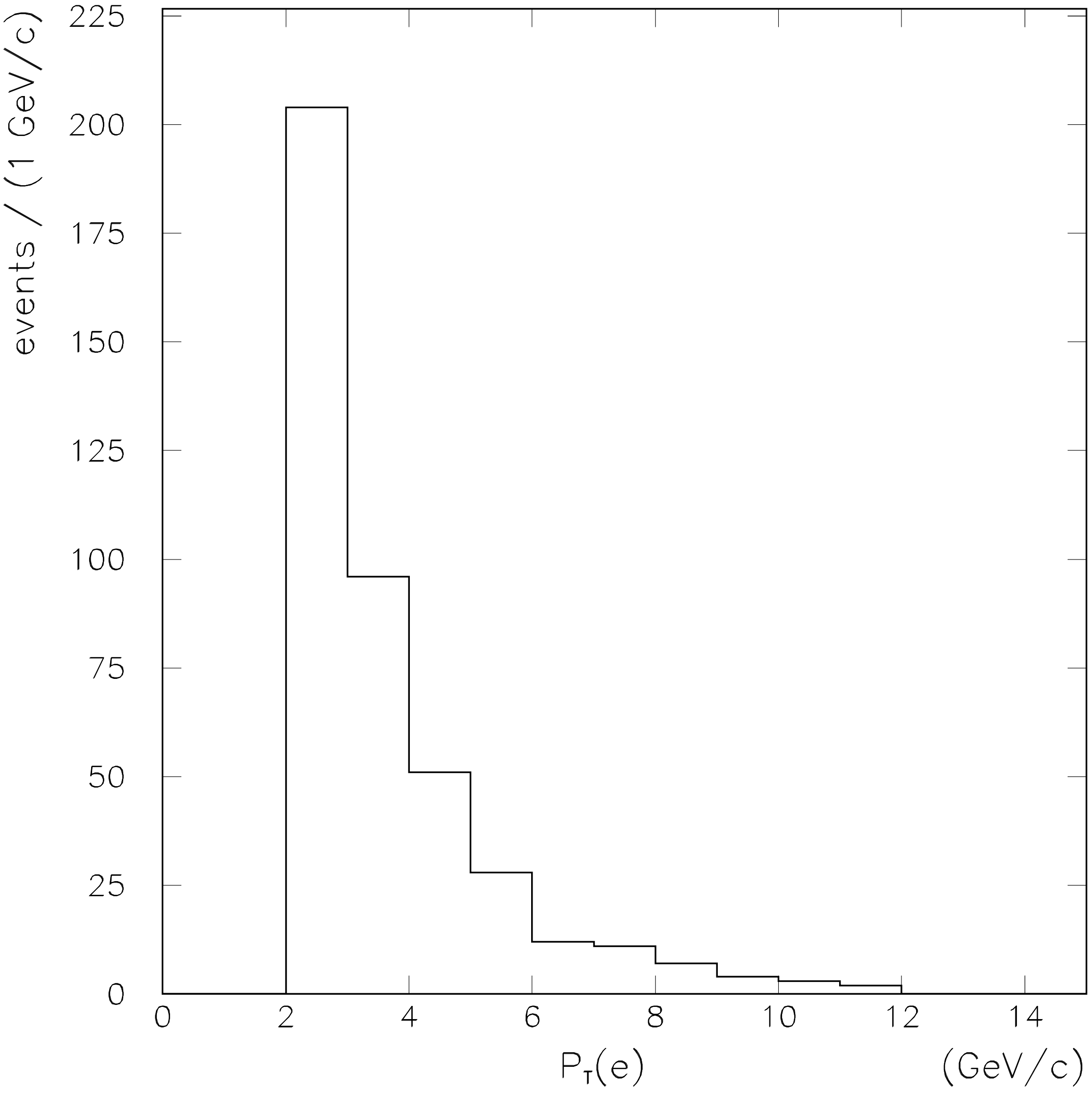

Figure 3.10: The transverse momentum distribution for the electron candidates in the J/ψ sample.

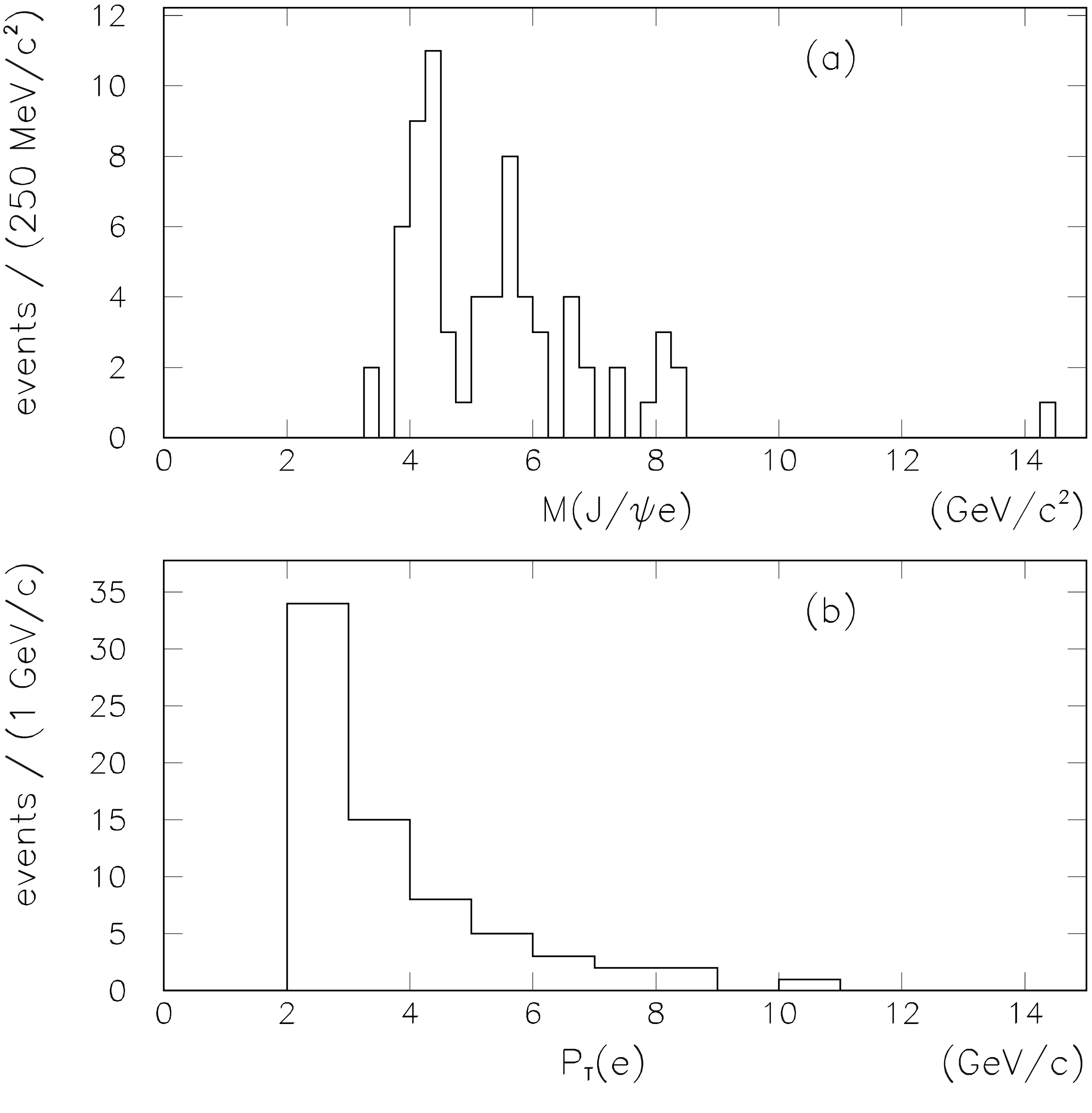

Figure 3.11: (a) The J/ψ + electron invariant mass distribution. (b) The p_T distribution of the electron candidates. These are distributions before the decay length cut is applied.

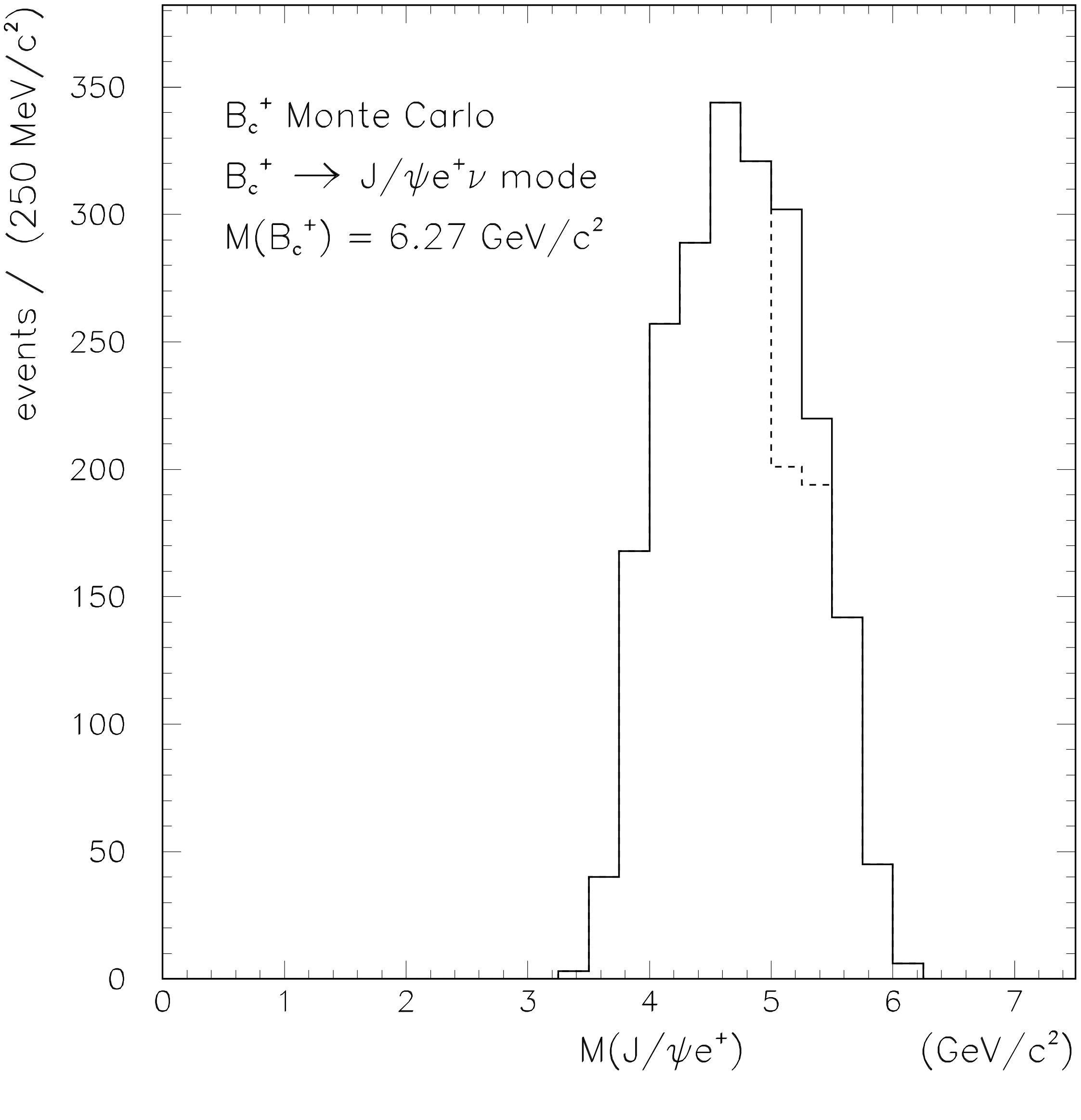

Figure 3.12: The $J/\psi + e$ invariant mass distribution for the Monte Carlo simulation. The solid line histogram shows the mass distribution without the $J/\psi K^+$ veto. The dashed line histogram shows that with the $J/\psi K^+$ veto.

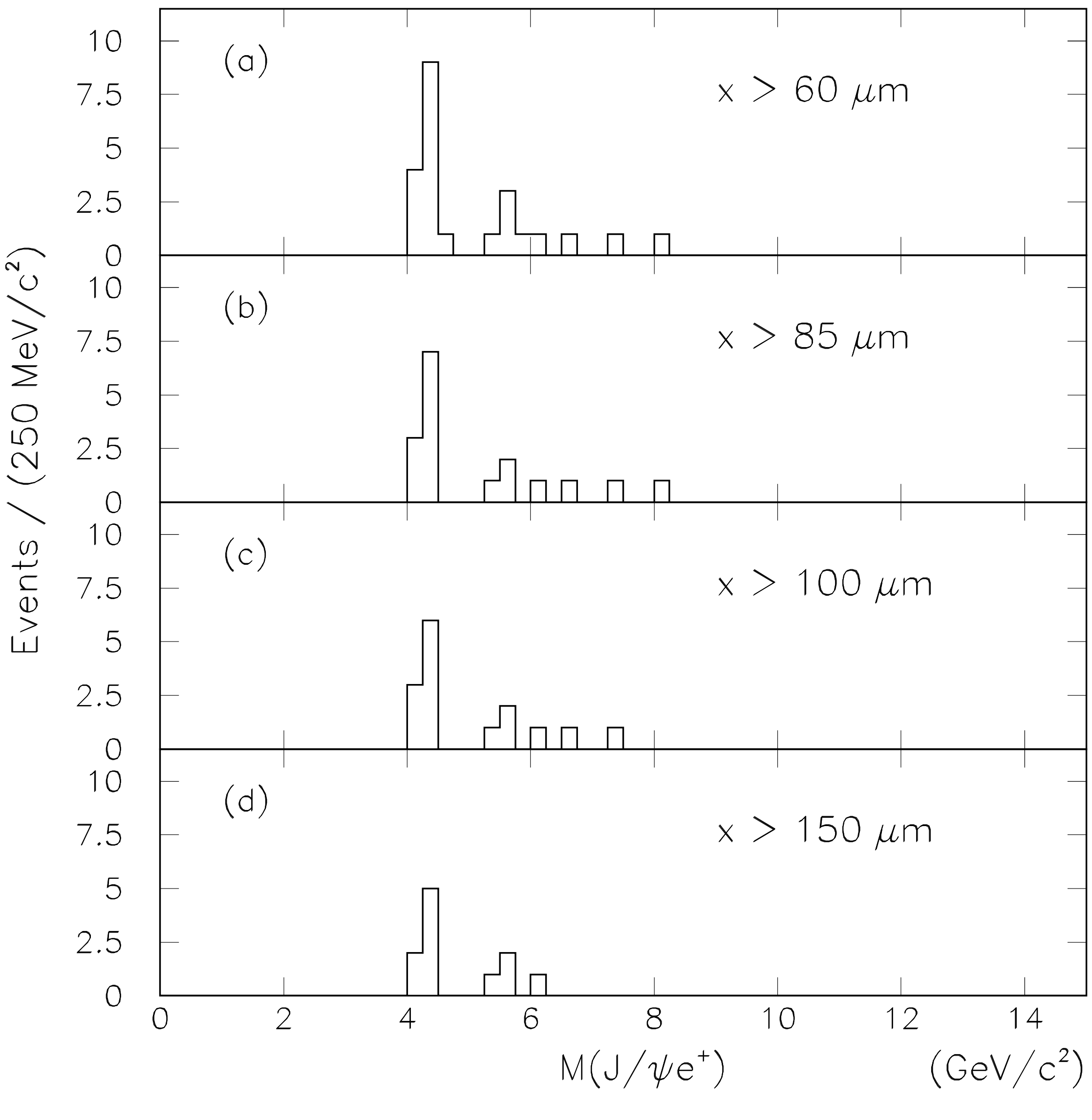

Figure 3.13: The $J/\psi e^+$ invariant mass distribution with different x cuts. (a) $x > 60$ μm. (b) $x > 85$ μm. (c) $x > 100$ μm. (d) $x > 150$ μm.

Chapter 4

Background Estimation

In Chapter 3, we selected the B_c candidates for the final state of tri-lepton (μ^+, μ^- and e). Possible sources of background events in the $J/\psi + e$ candidates can be classified into four categories:

- real J/ψ + fake e

  This background arises from misidentification of a hadron as an electron and is referred to as "fake electron background". If a hadron track in $B \rightarrow J/\psi$ + hadron decays is identified as an electron, the hadron track and the two muon tracks appear to come from a common vertex, and mimics a signal event.

- real J/ψ + real e

  If, in a $b\bar{b}$ production, the b decays into J/ψ plus anything and the $\bar{b}$ semileptonically decays, there are a J/ψ and an electron in the final state. The three leptons which appear in the final states sometimes pass the selection cuts. This is called "$b\bar{b}$ background".

  Photons are mostly generated by the $\pi^0 \rightarrow \gamma\gamma$ decay and are converted to a pair of an electron and a positron in the detector. As described in Chapter 3, we reject a conversion electron by looking for its partner track. However, if the partner track is not reconstructed, the conversion electron is identified as an electron. Photon conversions usually occur at a point, very far from a J/ψ vertex. Most of the conversion electrons therefore do not make a common vertex with the J/ψ. However, a conversion electron and J/ψ accidentally form a good vertex and pass the selection criteria. In addition, the π^0 in the $B \to J/\psi\pi^0 X$ decays, can decay into $\gamma e^+ e^-$ (Dalitz decay). If one of the two electrons is not reconstructed, the other electron and the J/ψ come from a common secondary vertex and can be included in the signal sample. These backgrounds are called "residual conversion background".

- fake J/ψ + real e and fake J/ψ + fake e

  There are some background events under the J/ψ mass peak as shown in Figure 3.1. These background events come from the decay-in-flight and punch-through backgrounds (one or two muons are false), muon pairs produced by the Drell-Yang process, and dimuons from the double sequential semileptonic decays of a b hadron. These backgrounds are "fake J/ψ background".

In the following, we discuss these backgrounds.

4.1 Fake electron background

A hadron, usually a charged pion or kaon, is misidentified as an electron, if the hadron happens to shower in front of the CEM and mimics a signature of an electron. Using a hadron rich sample, we estimate the probability that a hadron satisfies the SLT electron requirements, where the probability is called "fake rate". Then we multiply the number of J/ψ + track combinations by the fake rate to obtain the number of fake electron backgrounds.

4.1.1 Fake electron rate

In order to estimate the fake rate, we study a large sample of tracks in jet events which are accumulated using an inclusive jet trigger with a transverse energy threshold of 20 GeV (JET20). The probability that a track satisfies the electron selection criteria depends on isolation, since nearby particles can deposit energy in the tower traversed by the particle, and this extra energy affects the E/p and E_{had}/E_{EM} measurements. Figure 4.1 (a) shows the p_T distributions for tracks in the J/ψ sample and in the JET20 sample. There is a difference between the p_T distribution in the J/ψ sample

	$N_{\rm tot}$	N_e	N_π	N_K
$I < 0.2$	976 events	527 ± 37 events	347 ± 54 events	101 ± 31 events
$I > 0.2$	1492 events	811 ± 48 events	513 ± 72 events	168 ± 40 events
all I bin	2468 events	1336 ± 61 events	864 ± 90 events	268 ± 50 events

Table 4.1: Sample composition of the identified electrons in the JET20 sample, estimated using dE/dX. The S_e cut is not applied.

and that in the JET20 sample. Therefore we parametrize the fake rate as a function of p_T and isolation I of the track. The isolation I is defined by $I = \sum p/p$, where p in the denominator is the momentum of the track of interest and $\sum p$ in the numerator is the scalar sum of momenta of all other tracks within a cone of radius 0.2 in the $\eta - \phi$ space. The isolation distribution for tracks in the J/ψ sample and that in the JET20 sample are shown in Figure 4.1 (b). For the J/ψ sample, most of the events are in the first bin ($I < 0.2$). Hence we obtain the fake rate for two I bins, $I < 0.2$ and $I > 0.2$. The fake rate is defined by

$$\text{fake rate } (p_t, I) = \frac{\#\text{ of tagged tracks}}{\#\text{ of tracks passing the fiducial cuts}} \times (1 - f_e(I)), \tag{4.1}$$

where f_e is a real electron fraction in the tagged tracks. We introduce f_e to account for a real electron content in the JET20 sample. The sources of real electrons are discussed in Appendix A. We estimate f_e using the dE/dX information. Figure 4.2 shows the S_e distribution in the JET20 data, where the tracks satisfy the electron requirements except for the dE/dX requirement. The dE/dX requirements are removed to measure the hadron components. In the S_e distribution, if all tracks were electrons, the shape would be a Gaussian centered at zero with standard deviation 1.0. To estimate the number of e, π and K events in the S_e distribution, we fit the S_e distribution using three Gaussians representing e, π and K. The fitted curves are shown in Figure 4.2. The fit results are listed in Table 4.1. From these, we calculate the real electron fraction $f_e(I)$. The $f_e(I)$ with the S_e cut is listed in Table 4.2, and that without the S_e cut is also listed for comparison.

The fake rate determined by the above method is shown in Figure 4.3 as a function of p_T and I.

	Real electron fraction $f_e(I)$	
	Without S_e cut	With S_e cut
$I < 0.2$	$54 \pm 4\%$	$76 \pm 5\%$
$I > 0.2$	$54 \pm 3\%$	$74 \pm 4\%$
all I bin	$54 \pm 2\%$	$74 \pm 2\%$

Table 4.2: Real electron fraction in the identified electrons in the JET20 sample.

x cut threshold	N_{fake} in $m < 15$ GeV/c^2	N_{fake} in $4 < m < 6$ GeV/c^2
60 μm	4.2 ± 0.1 events	2.6 ± 0.1 events
85 μm	3.9 ± 0.1 events	2.1 ± 0.1 events
100 μm	3.5 ± 0.1 events	2.0 ± 0.1 events
150 μm	2.8 ± 0.1 events	1.6 ± 0.1 events

Table 4.3: Number of fake electron backgrounds for $m(J/\psi e) < 15$ GeV/c^2 and for 4 $< m(J/\psi e) < 6$ GeV/c^2.

4.1.2 Number of fake electron backgrounds

To estimate the fake electron background in the $J/\psi + e$ sample, we first reconstruct a J/ψ + track invariant mass using tracks passing all the $J/\psi + e$ selection cuts except for the electron requirements. Figure 4.4 shows the J/ψ + track invariant mass distributions for various x cuts. We then apply the fake rate as a function of p_T and I to each track to obtain the number of fake electron backgrounds. The J/ψ + track mass distribution for the fake electron background is shown in Figure 4.5. The numerical values for the fake electron background are listed in Table 4.3.

4.1.3 Systematic uncertainty

In order to check the fake rate, we calculate the fake rate using tracks in the Minimum Bias (MB) trigger data. The MB trigger is intended to collect events without any physics requirement. The p_T and I distributions in the MB data are shown in Figure 4.1. They are different from those for the JET20 sample. We calculate the fake rate for the MB sample as a function of p_T and I, in a similar way as for the

JET20 data. For the real electron fraction $f_e(I)$ in the MB sample, we evaluate it without dividing into two I bins, since there are not enough tracks passing the electron requirements for $I > 0.2$. We fit the S_e distribution (Figure 4.6) with three Gaussians and obtain $f_e = 64 \pm 7$ %. The fake rate for MB sample is plotted in Figure 4.3. When we calculate the number of the fake electron background events using the fake rate from the MB sample, we find 2.9 ± 0.05 events for $x > 60$ μm in the B_c signal region between 4.0 and 6.0 GeV/c^2. The fake electron background with the MB fake rate is different from that with the JET20 fake rate by 10%. We assign this difference of 10% to the systematic uncertainty on the fake electron background estimate.

4.1.4 Cross checks of the fake electron background

Fake rate for a specific hadron

The tracks in the JET20 sample consist of a mixture of hadrons. We estimate the kaon fake rate and the pion fake rate, using kaon and pion tracks from charmed meson decays, where the charmed mesons are produced by b semileptonic decays. The following four decay modes are used:

- $\ell + D^{*+}$, $D^{*+} \to D^0\pi^+$, $D^0 \to K^-\pi^+$
- $\ell + D^{*+}$, $D^{*+} \to D^0\pi^+$, $D^0 \to K^-\pi^+\pi^+\pi^-$
- $\ell + D^+$, $D^+ \to K^-\pi^+\pi^+$
- $\ell + D^0$, $D^0 \to K^-\pi^+$.

Figure 4.7 (a) shows the invariant mass distribution for D^0 or D^+ candidates, where the kaon tracks satisfy the SLT fiducial requirements. We fit the mass distribution to a sum of a Gaussian and a linear function and calculate the number of events. Then we fit the mass distribution (Figure 4.7 (b)) in which the kaon tracks satisfy all the electron requirements, to a sum of a Gaussian and a linear function. In the second fit, the standard deviation of the Gaussian is fixed at a value determined in the first fit. The fit results are listed in Table 4.4. In the same way, we obtain the number of

	N_{fiducial}	N_{tagged}	fake rate
charged kaons	2469 ± 71 events	$1.3\ ^{+2.9}_{-2.3}$ events	$(0.5 \pm 1.2) \times 10^{-3}$
charged pions	3087 ± 97 events	$5.1\ ^{+7.9}_{-7.3}$ events	$(1.6 \pm 2.5) \times 10^{-3}$

Table 4.4: The numbers of fiducial tracks, the numbers of tagged tracks and the fake rates in $D^0 \to K^-\pi^+$, $D^0 \to K^-\pi^+\pi^+\pi^-$, and $D^+ \to K^-\pi^+\pi^+$ decays.

pion tracks passing the SLT fiducial cuts and the number of pion tracks passing all the electron cuts. See Figure 4.8. The fit results are listed in Table 4.4.

The fake rate is given by

$$\text{fake rate} = \frac{\#\text{ of tagged tracks}}{\#\text{ of tracks passing the fiducial cuts}}. \tag{4.2}$$

The fake rates for kaons and for pions are listed in Table 4.4. Because of the limited statistics, it is hard to see a difference between the kaon and the pion fake rates. But these fake rates are consistent with the fake rate obtained from the JET20 sample.

Hadron fraction using dE/dX

We see 19 events of $J/\psi + e$ candidates in the signal region $4 < m(J/\psi e) < 6$ GeV/c^2 with the $x > 60$ μm cut (see Table 3.4). In this section, we remove the S_e requirement and estimate a fraction of hadrons in the resulting 23 events. We use an un-binned likelihood method, because of the limited statistics. Assuming the Gaussian dE/dX (S_i) shapes, we can write the likelihood $\mathcal{L}$ as

$$\begin{aligned}\mathcal{L} = \frac{e^{-(\nu_e+\nu_\pi+\nu_K)}}{N!} \prod_{j=1}^{N} [& \frac{\nu_e}{\sqrt{2\pi}\sigma_{Qj}} \exp\left(-\frac{(Q_j - Q_{ej})^2}{2\sigma_{Qj}^2}\right) \\ & + \frac{\nu_\pi}{\sqrt{2\pi}\sigma_{Qj}} \exp\left(-\frac{(Q_j - Q_{\pi j})^2}{2\sigma_{Qj}^2}\right) \\ & + \frac{\nu_K}{\sqrt{2\pi}\sigma_{Qj}} \exp\left(-\frac{(Q_j - Q_{Kj})^2}{2\sigma_{Qj}^2}\right)],\end{aligned} \tag{4.3}$$

where Q_j is the measured dE/dX and σ_{Qj} is its uncertainty. Q_{ej}, $Q_{\pi j}$ or Q_{Kj} is the dE/dX expected for an electron, pion or kaon hypothesis. N is the number of total events ($N = 23$), and parameters ν_e, ν_π and ν_K are the numbers of electrons, pions and kaons. We minimize twice the negative log-likelihood $-2\ln\mathcal{L}$ and obtain ν_e, ν_π and ν_K. The fit result is shown in Figure 4.9. We obtain $\nu_e = 17.9\ ^{+5.3}_{-4.6}$, ν_π =5.1 $^{+4.0}_{-5.0}$ and $\nu_K = 0\ ^{+3.7}_{-0}$. From this the number of hadrons where the S_e cut is turned on is estimated to be 2.2 $\pm$ 1.5 events. This is consistent with our previous fake electron background estimate of 2.6 events.

4.2 Residual conversion background

In the electron requirements, conversion electrons are rejected by finding their conversion partner tracks satisfying the requirements: $|\Delta\cot\theta| < 0.06$, $|\Delta S| < 0.3$ cm, $m(e^+e^-) < 500$ MeV/c^2 and $R_{conv} < 50$ cm. This conversion removal algorithm is not perfect because the partner can fail the CTC track reconstruction when its transverse momentum is small. Therefore, a conversion electron can pass the cuts and appear as an electron candidate.

In the J/ψ + track data, 2 events of J/ψ + conversion electron are found after the vertex χ^2 cut and the pseudo-proper decay length $x > 60\ \mu$m cut are applied. These 2 events remain after the $x > 150\ \mu$m cut. The invariant mass distribution is shown in Figure 4.10 (b).

To estimate the background from the residual conversions when there are two identified conversion events, we have to know the conversion finding efficiency. For that end we first prepare a data sample of J/ψ + conversion electron events by turning off the vertex χ^2 cut and the decay length cut. We find 24 J/ψ + conversion electron events in our data. Figure 4.10 (a) shows the mass distribution for these events. Second, we generate Monte Carlo J/ψ + π^0 events and simulate $\pi^0 \to \gamma\gamma$ and $\pi^0 \to e^+e^-\gamma$ decays. Comparing the electron p_T spectra of the Monte Carlo simulation to the observed spectra of the J/ψ + conversion electron events, we estimate the conversion finding efficiency.

4.2.1 Conversion Monte Carlo

To model the kinematics correctly, we use a sample of J/ψ + track events from real data. These tracks should mostly be charged pions, and from isospin symmetry, the neutral pions should have identical kinematics. From the sample, we take the three-momenta of μ^+, μ^- and a track. We replace the identity of the track with π^0 and make 98.8% of the π^0's decay into $\gamma\gamma$ and 1.2% into γe^+e^- (Dalitz decay), according to the π^0 decay branching ratio [32]. Then the event is passed through a detector simulation, where a photon can convert to an e^+e^- pair according to the detector material in the geometry data base.

4.2.2 Conversion finding efficiency

We estimate the conversion finding efficiency ε_{id} by comparing the conversion partner p_T distribution of this Monte Carlo sample to that of the J/ψ + track events. Figure 4.11 (a) shows the p_T distribution of the conversion electron candidates for data and for Monte Carlo. The distributions are normalized to unit area. The track of a Monte Carlo conversion electron candidate is required to be reconstructed by the same track reconstruction program as used for real data. The Monte Carlo simulation reproduces the p_T distribution of the conversion electrons in the real data. Figure 4.11 (b) shows the p_T distribution of the conversion partners for data and for Monte Carlo. For the Monte Carlo events, the p_T distribution of the partners is obtained from the generator level output (not required to be reconstructed). If the conversion finding efficiency is unity in the entire p_T range, the partner p_T distribution for data would be peaked at the lowest bin, as in the Monte Carlo events. Assuming that the CTC tracking efficiency is flat for $p_T > 0.5$ GeV/c, we normalize the p_T distribution of the conversion partners for data to that for the Monte Carlo events in the range $p_T > 0.5$ GeV/c, and obtain $\varepsilon_{id} = (49 \pm 6)\%$.

4.2.3 Number of conversion backgrounds

To estimate how many events are in the signal region $4 < m(J/\psi e) < 6$ GeV/c^2, we calculate the mass distribution for Monte Carlo events. Here we reconstruct a common vertex of the three tracks, μ^+, μ^-, and an electron from a conversion or a Dalitz decay, and apply the Prob(vertex fit χ^2) > 1% and $x > 60$ μm cuts. Figures 4.12 (a) and (b) show the invariant mass distributions for the identified conversions and for the residual conversions, respectively. From Figure 4.12 (b), we evaluate the fraction of residual conversion events lying in the signal region as ε_{mass} = N(signal region)/N(whole mass region) $= 55 \pm 3\%$. The number of residual conversions in the signal region is calculated from the number of identified conversions N_{id}(whole mass region) in the real data by

$$\begin{aligned} N_{res} &= N_{id}(\text{whole mass region}) \times \frac{1-\varepsilon_{\text{id}}}{\varepsilon_{\text{id}}} \times \varepsilon_{\text{mass}} \\ &= 1.2 \pm 0.8, \end{aligned} \tag{4.4}$$

where the uncertainty is only due to the statistics of $N_{id} = 2$. The residual conversion background for the whole mass region is N_{res}(whole mass region) $= 2.1 \pm 1.5$.

Systematic uncertainty

The systematic uncertainties in the residual conversion background are caused by the following:

- the statistical uncertainty of the conversion finding efficiency (ε_{id}) produces a 28% uncertainty in the value of N_{res}.
- an uncertainty due to the J/ψ + residual conversion mass shape. We compare the J/ψ + residual conversion mass shape for photon conversions to that for Dalitz decays and assign 9% uncertainty.
- an uncertainty due to the difference between the p_T distribution of tracks in zero-lifetime J/ψ events and that in J/ψ events coming from b decays. The track p_T distribution for events passing the $x(J/\psi$ + track) > 60 μm cut and that for the $x(J/\psi$ + track) < 60 μm cut are shown in Figure 4.13 (a). For comparison, we show the p_T distributions for J/ψ + track system in Figure 4.13 (b). Using the distributions of Figure 4.13 (a), we recalculate ε_{id}, and obtain 52.0% for the $x(J/\psi$ + track) > 60 μm tracks and 45.7% for the $x(J/\psi$ + track) < 60 μm tracks. We calculate the number of residual conversion electrons with these efficiencies and take the larger difference from Eq. (4.4) of 13% as the systematic uncertainty.

Summing the above uncertainties in quadrature yields a systematic uncertainty in the N_{res} of 32%.

4.2.4 Check of the conversion finding efficiency

A check of the above estimate of the conversion finding efficiency ε_{id} is preformed using conversion electrons which are created at the VTX outer wall or at the CTC inner wall (20 cm $<$ conversion radius $R_{conv} < 30$ cm) [47]. Since these conversion electrons do not leave hits in the VTX, one can identify these conversion electrons by requiring the VTX hit occupancy to be low. The VTX hit occupancy is defined as

$$V_{res} = \frac{\#\text{ of active hits in VTX}}{\#\text{ of expected hits in VTX}}, \tag{4.5}$$

and is applied to those tracks which have the number of expected hits in the VTX greater than 10. We select low V_{res} electrons from the J/ψ + track sample using the SLT code. We turn off the conversion removal cut and the SVX hit requirement here. To demonstrate how this V_{res} variable works, we use the conversion electrons whose partners are identified and show in Figure 4.14 the conversion radius distribution without the V_{res} cut and with the $V_{res} < 0.4$ cut. We see that the $V_{res} < 0.4$ cut works well to remove the conversion pairs produced inside the VTX ($R_{conv} < 20$ cm).

We calculate the conversion finding efficiency $\varepsilon_{id}(VTX)$:

$$\varepsilon_{id}(VTX) = \frac{\#\text{ of low V}_{\text{res}}\text{ electrons with partner}}{\#\text{ of low V}_{\text{res}}\text{ electrons}} = 0.46 \pm 0.06. \tag{4.6}$$

Previously we estimated $\varepsilon_{id} = 49 \pm 6\%$ using the conversion partner p_T distribution, to which the $\varepsilon_{id}(VTX)$ agrees.

4.3 $b\bar{b}$ background

When in a $b\bar{b}$ production a b quark decays to $J/\psi X$ and a $\bar{b}$ quark to eX', there are a J/ψ and an electron in the final state as in the B_c semileptonic decay. If these J/ψ and electron make a good displaced vertex and the $J/\psi + e$ mass falls into the signal region $4 < m(J/\psi e) < 6$ GeV/c^2, they result in an irreducible background to the B_c signal. We estimate this $b\bar{b}$ background using a Monte Carlo simulation. The $b\bar{b}$ events are generated according to the next-to-leading order QCD calculation [8] with renormalization scale $\mu_0 = \sqrt{m_b^2 + p_t^2}$, where the b quark mass m_b is set to 4.75 GeV/c^2. The MRSD$_0$ parton distribution function [48] is used. The b quark is fragmented

x cut threshold	$N_{b\bar{b}}$ in $m < 15$ GeV/c^2	$N_{b\bar{b}}$ in $4 < m < 6$ GeV/c^2
60 μm	2.3 ± 0.8 events	1.2 ± 0.4 events
85 μm	1.8 ± 0.5 events	1.0 ± 0.3 events
100 μm	1.5 ± 0.4 events	1.0 ± 0.3 events
150 μm	0.7 ± 0.2 events	0.6 ± 0.2 events

Table 4.5: Number of $b\bar{b}$ backgrounds for $m(J/\psi e) < 15$ GeV/c^2 and for $4 < m(J/\psi e) < 6$ GeV/c^2.

into b hadrons according to the Peterson fragmentation model [9] with the Peterson fragmentation parameter $\epsilon_P = 0.006$. We let the b hadrons decay according to the CLEO decay model [49], in which we force the b hadron to decay into $J/\psi X$ and the J/ψ into $\mu^+\mu^-$, but the $\bar{b}$ decays are not forced. Then the $b\bar{b}$ events are processed by the CDF detector simulation and the trigger simulation [40].

The number of $B^+ \to J/\psi K^+$ decays observed in real data is used to normalize the Monte Carlo $b\bar{b}$ background events. The selection cuts used to obtain the $J/\psi K^+$ events are the same as for the $J/\psi + e$ events, except for the electron requirements. We find the normalization factor $R(\text{Data/MC}) = 0.19 \pm 0.02$. The number of $b\bar{b}$ backgrounds with different x cuts are listed in Table 4.5. The $b\bar{b}$ background mass distributions with different x cuts are shown in Figure 4.15.

The systematic uncertainties in the estimate of the $b\bar{b}$ background are listed in Table 4.6. The systematic uncertainty associated with the trigger simulation is determined by alternately requiring and then not requiring the dimuon triggers and taking the difference in the resulting $b\bar{b}$ backgrounds as the uncertainty. The uncertainty in the branching ratio for the $B^+ \to J/\psi K^+$ decay [32] contributes 14%. The Monte Carlo statistics (uncertainty on the normalization factor R) contributes 11%. The total uncertainty is 18%.

4.4 Background from fake J/ψ's

We calculate the contribution from fake J/ψ events using events in the J/ψ sideband defined as 100 MeV/c^2 $< |m(\mu^+\mu^-) - m(J/\psi)| <$ 200 MeV/c^2 (see Figure 3.1).

Source	Uncertainty (%)
Trigger Simulation	5
$\mathcal{B}(B^+ \to J/\psi K^+)$	14
Monte Carlo Statistics	11
Total	18

Table 4.6: Summary of the systematic uncertainties on the $b\bar{b}$ background

We reconstruct the J/ψ + track invariant mass for J/ψ sideband events and apply all the cuts employed in the signal selection, with one modification. When we reconstructed the 3 track vertex in the J/ψ signal selection, the dimuon mass was constrained to the world average mass of J/ψ. Here the dimuon mass is constrained to the center of each side-band region. We find that, out of 2952 J/ψ sideband + track events, 3 events remain after the cuts. Taking account of the fact that J/ψ sideband region is twice as large as the J/ψ signal region, we estimate the probability that a fake J/ψ + track event forms a common vertex to be $(0.05 \pm 0.03)\%$. From Figure 3.1, the background under the J/ψ mass peak is about 8%. Then we multiply the number of $J/\psi + e$ candidates by this fraction and the above probability, and obtain 10^{-3} events for $x > 60$ μm. The fake J/ψ background is negligibly small and is not included in the following analysis.

4.5 Other background

The following two sources can appear in the $J/\psi + \ell$ final states:

- $J/\psi + c\bar{c}$ production in which the charm decays semileptonically.
- decays of an as yet unobserved baryon which contains b and c quarks.

4.5.1 $J/\psi + c\bar{c}$ production

It is possible for an additional charm to be produced along with a prompt J/ψ via the same production mechanisms as for the B_c production. Figure 4.16 shows p_T spectra for inclusive c quark and b quark production in the next-to-leading order calculation [8]. In the next-to-leading order (α_s^3) calculation, the inclusive production cross section for the c quark (σ_c) is about twenty times as large as that for b quark (σ_b). Since the J/ψ must have $p_T > 4$ GeV/c to satisfy the trigger requirements, we calculate the cross section ratio for $p_T > 4$ GeV/c and obtain $\sigma_c/\sigma_b \simeq 5$. The J/ψ and lepton coming from $J/\psi + c\bar{c}$ production do not generally form a common vertex, as in the $b\bar{b}$ background. Assuming the efficiency that the J/ψ and lepton survive our cut is equal to that for the $b\bar{b}$ background, we can write the ratio of the number of the prompt J/ψ background to that of the $b\bar{b}$ background as

$$\frac{N_{c\bar{c}}}{N_{b\bar{b}}} = \frac{\sigma_{c\bar{c}}\, f(c \to J/\psi)\, \mathcal{B}(\bar{c} \to \ell X)}{\sigma_{b\bar{b}}\, \mathcal{B}(b \to J/\psi X)\, \mathcal{B}(\bar{b} \to \ell X)} = \frac{5 \times 10^{-3} \times 0.1}{0.01 \times 0.1} \simeq 0.5, \tag{4.7}$$

where we have assumed that the probability for a c quark to fragment into a J/ψ is $f(c \to J/\psi) \sim 10^{-3}$ ($= f(\bar{b} \to B_c^+)$ [11]) and have used $\mathcal{B}(b \to J/\psi X) \simeq 0.01$ and $\mathcal{B}(b, c \to \ell X) \sim 0.1$ from Ref. [32]. The J/ψ's in the $J/\psi + c\bar{c}$ production have zero lifetime, and the requirement of the $x > 60$ μm reduces the prompt J/ψ contribution, compared to the $b\bar{b}$ background. Hence the contribution from the prompt J/ψ background to the $J/\psi + e$ signal is estimated to be less than 0.6 events for $4 < m(J/\psi e) < 6$ GeV/c^2.

4.5.2 (bcq) baryon decay

The baryon which consists of b quark, c quark and a light flavor quark q has not been observed yet, but is expected to exist. The (bcq) baryon can decay into the J/ψ + ℓ final states.

The production ratio of the (bcq) baryon to the B_c meson is roughly estimated to be $\sigma_{bcq}/\sigma_{B_c^+} \simeq \sigma_{\Lambda_b}/\sigma_{B_u^+} = \frac{1}{3}$. We consider the ($bcq$) baryon decay in which the (bcq) decays into J/ψ and (csq), followed by (csq) $\to \ell X$. The branching ratio for (bcq) $\to J/\psi X$ is expected to be $\mathcal{B}((bcq) \to J/\psi X) \simeq \mathcal{B}(B \to J/\psi X) = 0.01$, where the $\mathcal{B}(B \to J/\psi X)$ is obtained from Ref. [32]. We assume $\mathcal{B}((csq) \to \ell X) \simeq 0.1$ [32]. For the $B_c^+ \to J/\psi \ell^+ X$ decay, the branching ratio is assumed to be about 2% (see Table 1.4). The $\sigma\mathcal{B}$ ratio is written as

$$\frac{\sigma_{bcq}\mathcal{B}((bcq) \to J/\psi X)\mathcal{B}((csq) \to \ell X)}{\sigma_{B_c^+}\mathcal{B}(B_c^+ \to J/\psi \ell^+ X)} = \frac{1}{3}\frac{0.01 \times 0.1}{0.02} \simeq 0.02 \tag{4.8}$$

x cut	N_{fake}	N_{conv}	$N_{b\bar{b}}$	N_{tot}
60 μm	$4.2 \pm 0.1 \pm 0.4$	$2.1 \pm 1.5 \pm 0.7$	$2.3 \pm 0.8 \pm 0.4$	$8.6 \pm 1.6 \pm 1.0$
85 μm	$3.9 \pm 0.1 \pm 0.4$	$2.1 \pm 1.5 \pm 0.7$	$1.8 \pm 0.5 \pm 0.3$	$7.8 \pm 1.6 \pm 0.9$
100 μm	$3.5 \pm 0.1 \pm 0.4$	$2.1 \pm 1.5 \pm 0.7$	$1.5 \pm 0.4 \pm 0.3$	$7.1 \pm 1.6 \pm 0.9$
150 μm	$2.8 \pm 0.1 \pm 0.3$	$2.1 \pm 1.5 \pm 0.7$	$0.7 \pm 0.2 \pm 0.1$	$5.6 \pm 1.5 \pm 0.8$

Table 4.7: Summary of background for $m(J/\psi e) < 15$ GeV/c^2.

x cut	N_{fake}	N_{conv}	$N_{b\bar{b}}$	N_{tot}
60 μm	$2.6 \pm 0.1 \pm 0.3$	$1.2 \pm 0.8 \pm 0.4$	$1.2 \pm 0.4 \pm 0.2$	$5.0 \pm 0.9 \pm 0.5$
85 μm	$2.1 \pm 0.1 \pm 0.2$	$1.2 \pm 0.8 \pm 0.4$	$1.0 \pm 0.3 \pm 0.2$	$4.3 \pm 0.9 \pm 0.5$
100 μm	$2.0 \pm 0.1 \pm 0.2$	$1.2 \pm 0.8 \pm 0.4$	$1.0 \pm 0.3 \pm 0.2$	$4.2 \pm 0.9 \pm 0.5$
150 μm	$1.6 \pm 0.1 \pm 0.2$	$1.2 \pm 0.8 \pm 0.4$	$0.6 \pm 0.2 \pm 0.1$	$3.4 \pm 0.9 \pm 0.4$

Table 4.8: Summary of background for $4 < m(J/\psi e) < 6$ GeV/c^2.

Therefore, we expect the contribution from the (bcq) baryon decay is small.

4.6 Total background

A summary of our background estimation is given in Table 4.7 for $m(J/\psi e) <$ 15 GeV/c^2 and in Table 4.8 for $4 < m(J/\psi e) < 6$ GeV/c^2. The total background is given by the sum of the fake electron background, the residual conversion background, and the $b\bar{b}$ background. We do not include the fake J/ψ background, the J/ψ + $c\bar{c}$ background, and the (bcq) baryon decay background, because they are negligibly small.

Our background estimation for fake electrons and residual conversions was performed using a variety of real data sample: the JET20 sample, the MB sample, the J/ψ sample, and the conversion sample. We made several cross checks to confirm our estimation. The $b\bar{b}$ background was estimated using a Monte Carlo simulation. Another check of the background estimation is possible by using an independent data sample of b decays. This is described in detail in Appendix B, which provides support for the validity of the background estimation described in this chapter.

In Figure 4.17 we show the observed $J/\psi + e$ invariant mass distribution, together with the expected background distribution. We see an excess of observed events in the signal region $4 < m(J/\psi e) < 6$ GeV/c^2. In parallel with the present analysis, a B_c meson search in the J/ψ + muon channel has been performed at CDF [50]. In the next chapter, we will combine the two channels and discuss the statistical significance of the B_c signal.

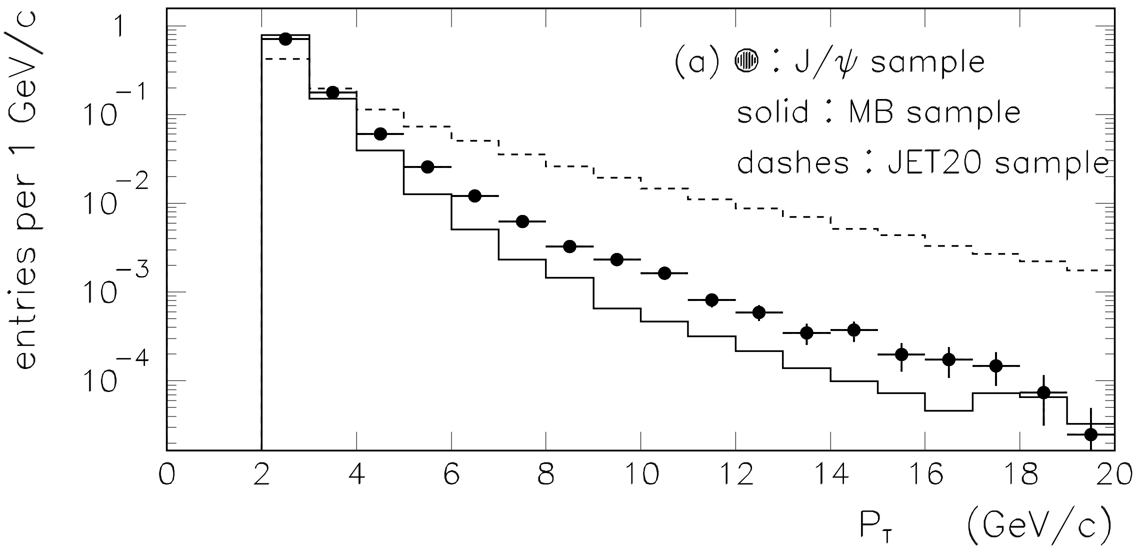

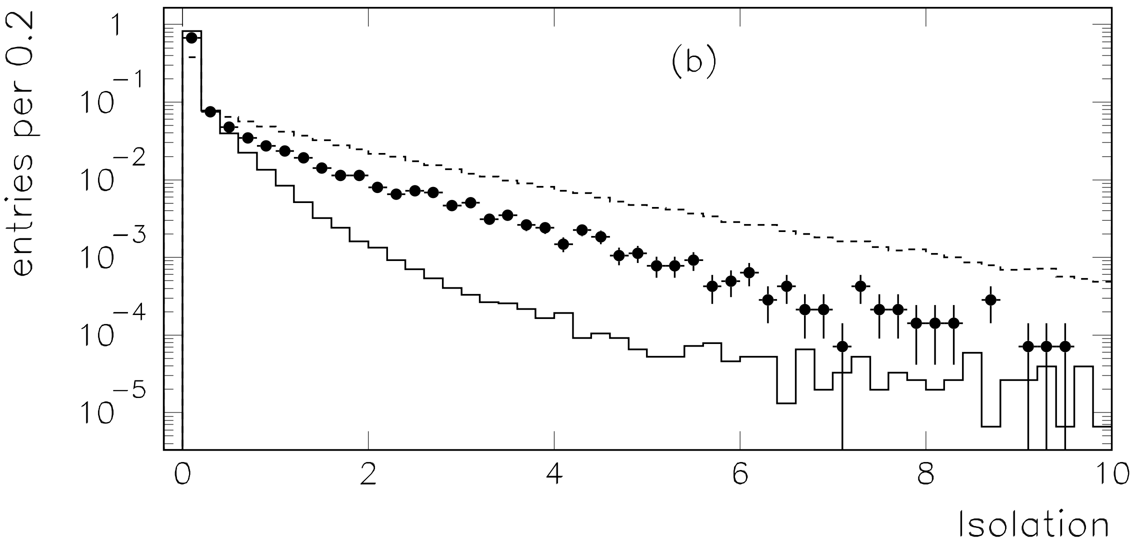

Figure 4.1: (a) The p_T distributions and (b) the I distributions for J/ψ, JET20 and MB data. The distributions are normalized to unit area.

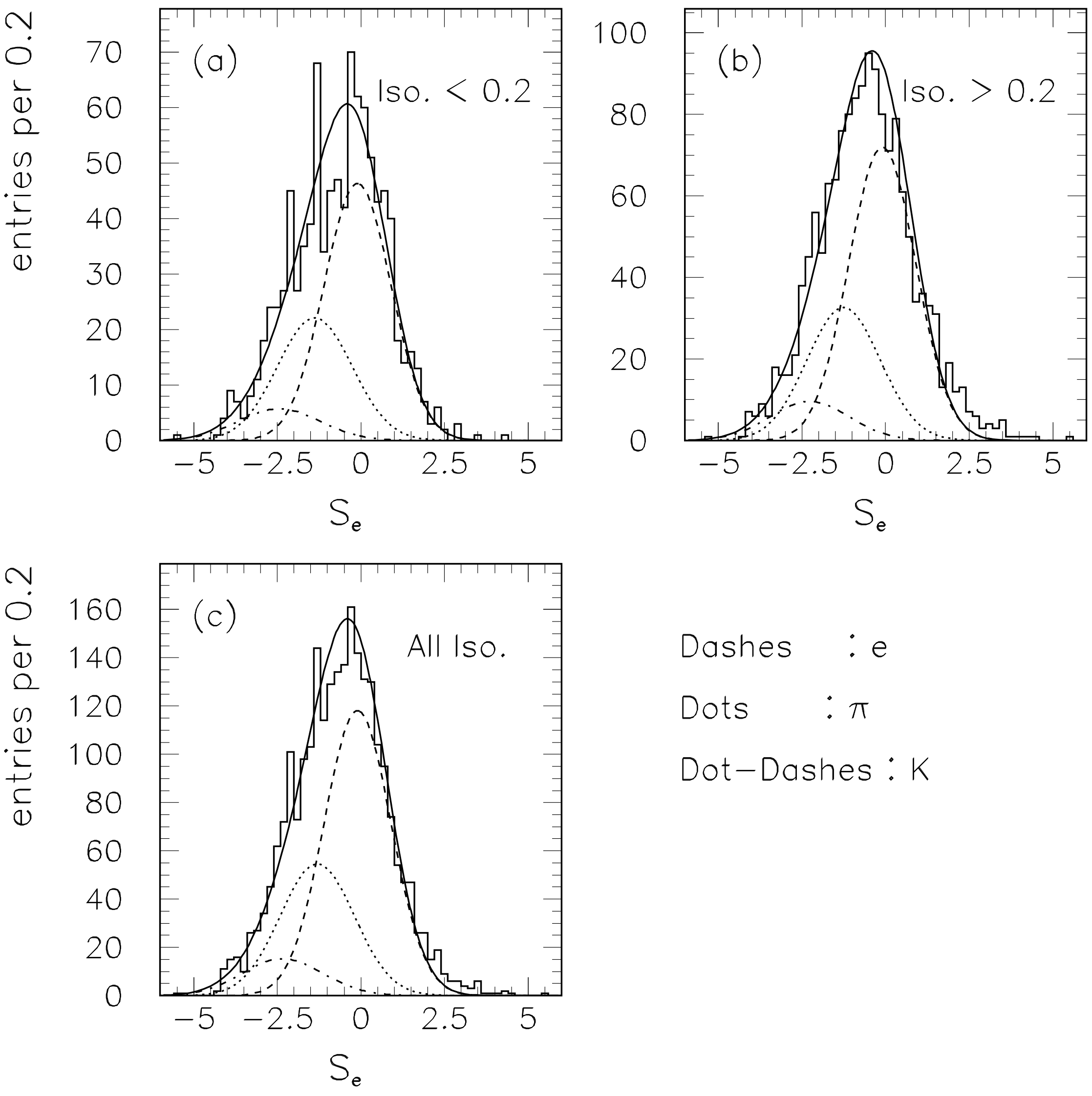

Figure 4.2: The S_e distribution for the tracks identified as electrons in the JET20 sample. (a) for $I < 0.2$, (b) for $I > 0.2$, and (c) all I.

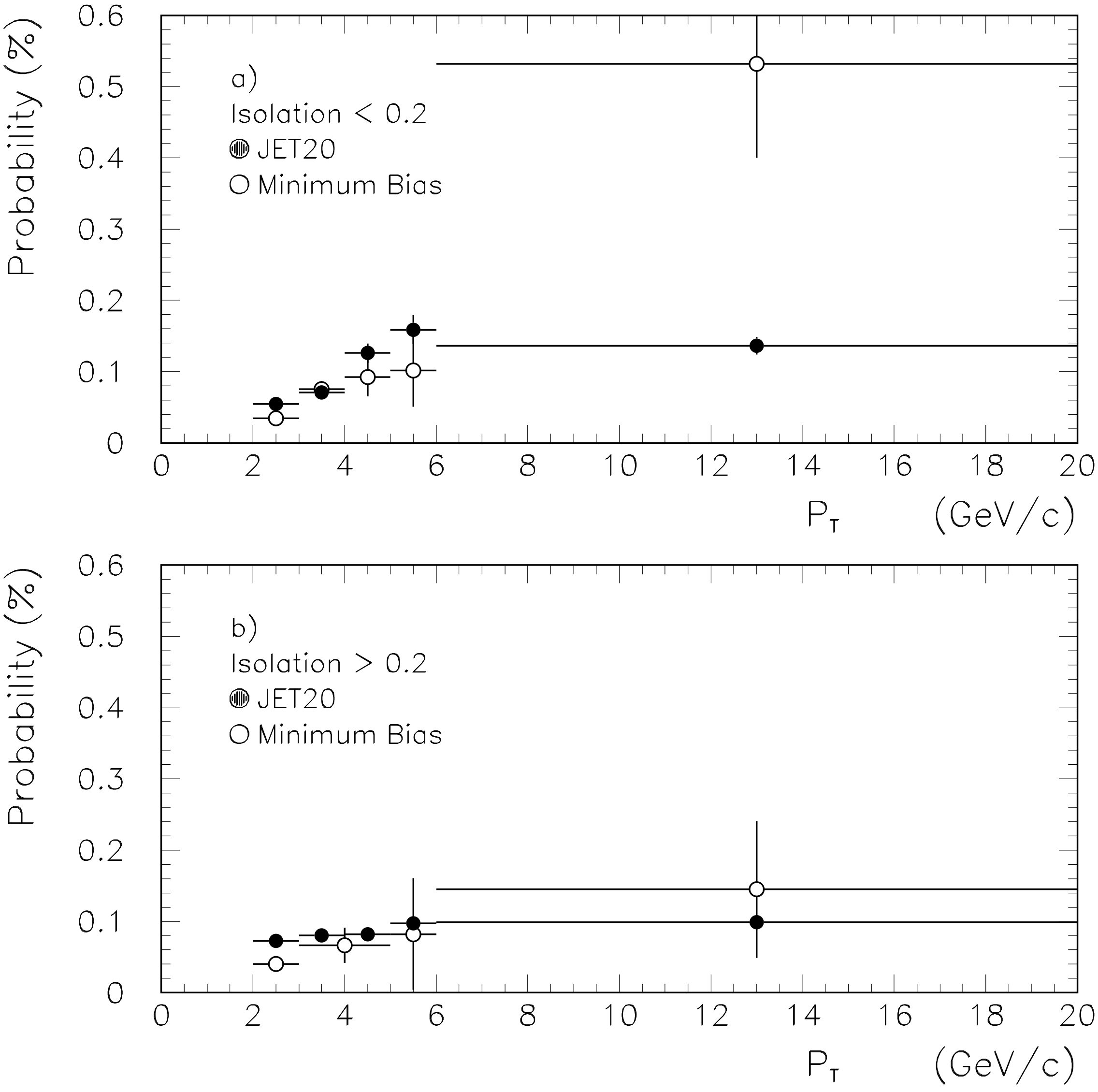

Figure 4.3: The fake rate determined by using JET20 data and MB data: (a) for $I < 0.2$ and (b) for $I > 0.2$.

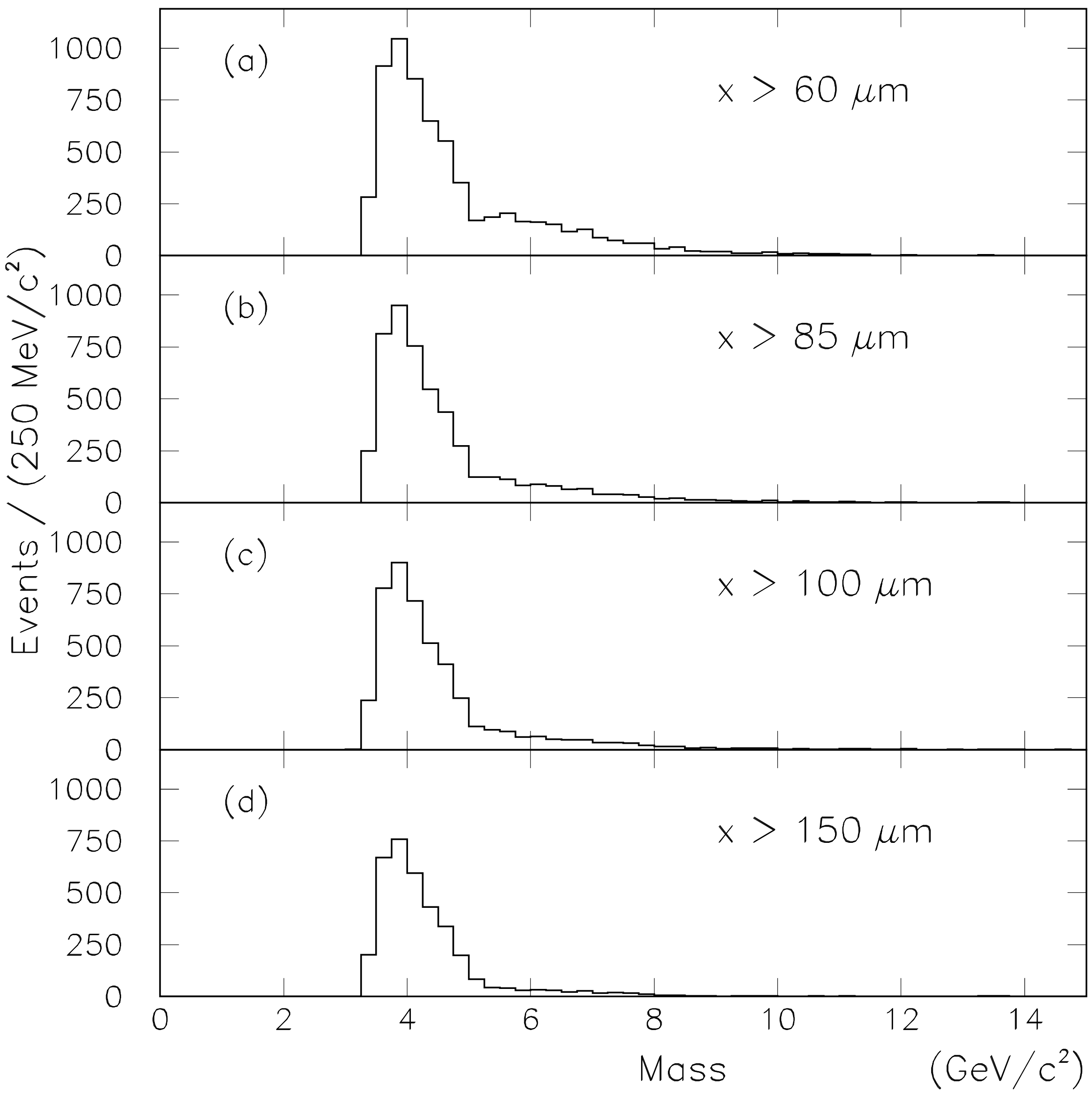

Figure 4.4: J/ψ + track invariant mass distributions. (a) $x > 60\ \mu$m, (b) $x > 85\ \mu$m, (c) $x > 100\ \mu$m, and (d) $x > 150\ \mu$m.

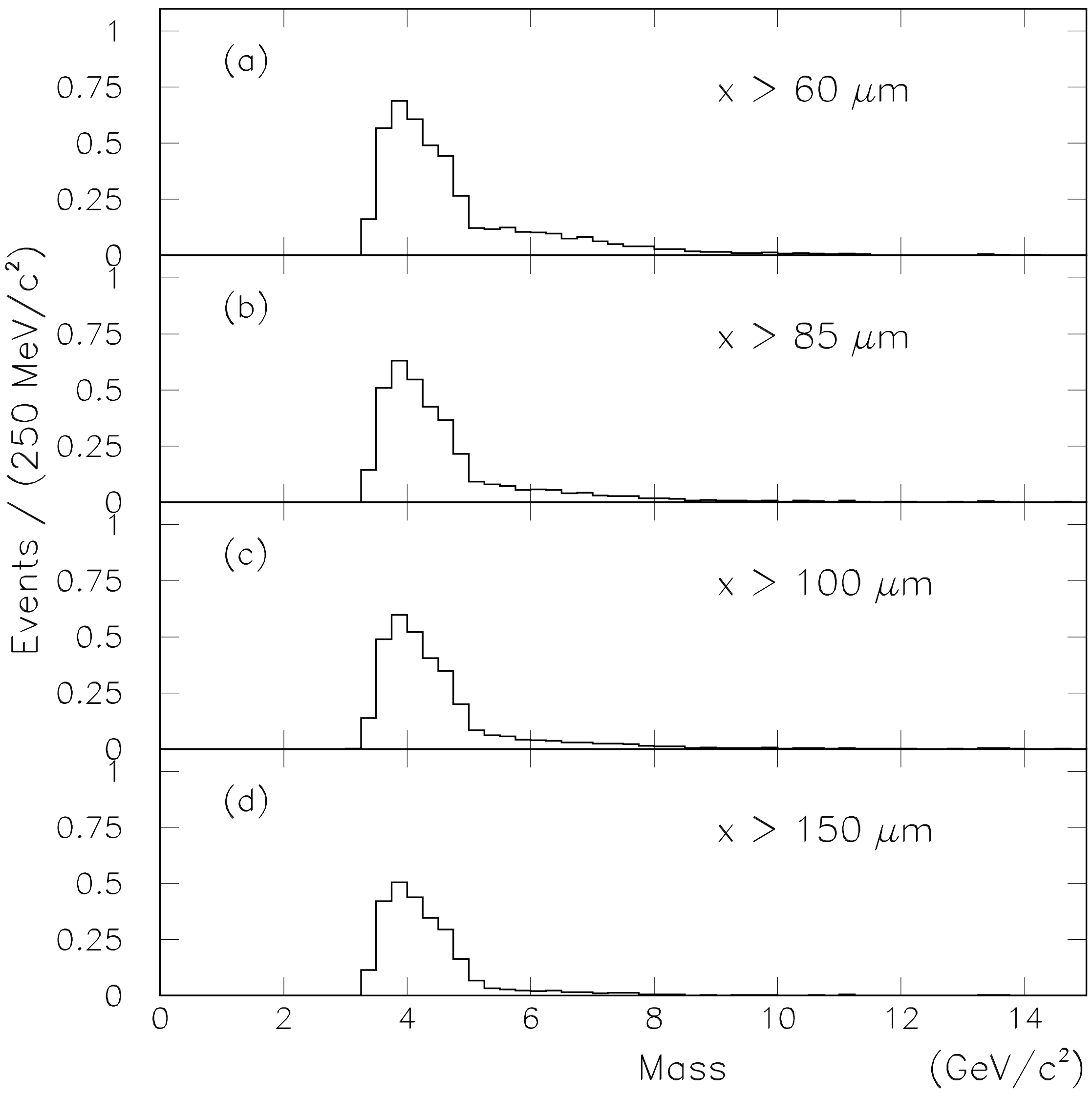

Figure 4.5: The fake electron background distributions. (a) $x > 60$ μm, (b) $x > 85$ μm, (c) $x > 100$ μm, and (d) $x > 150$ μm.

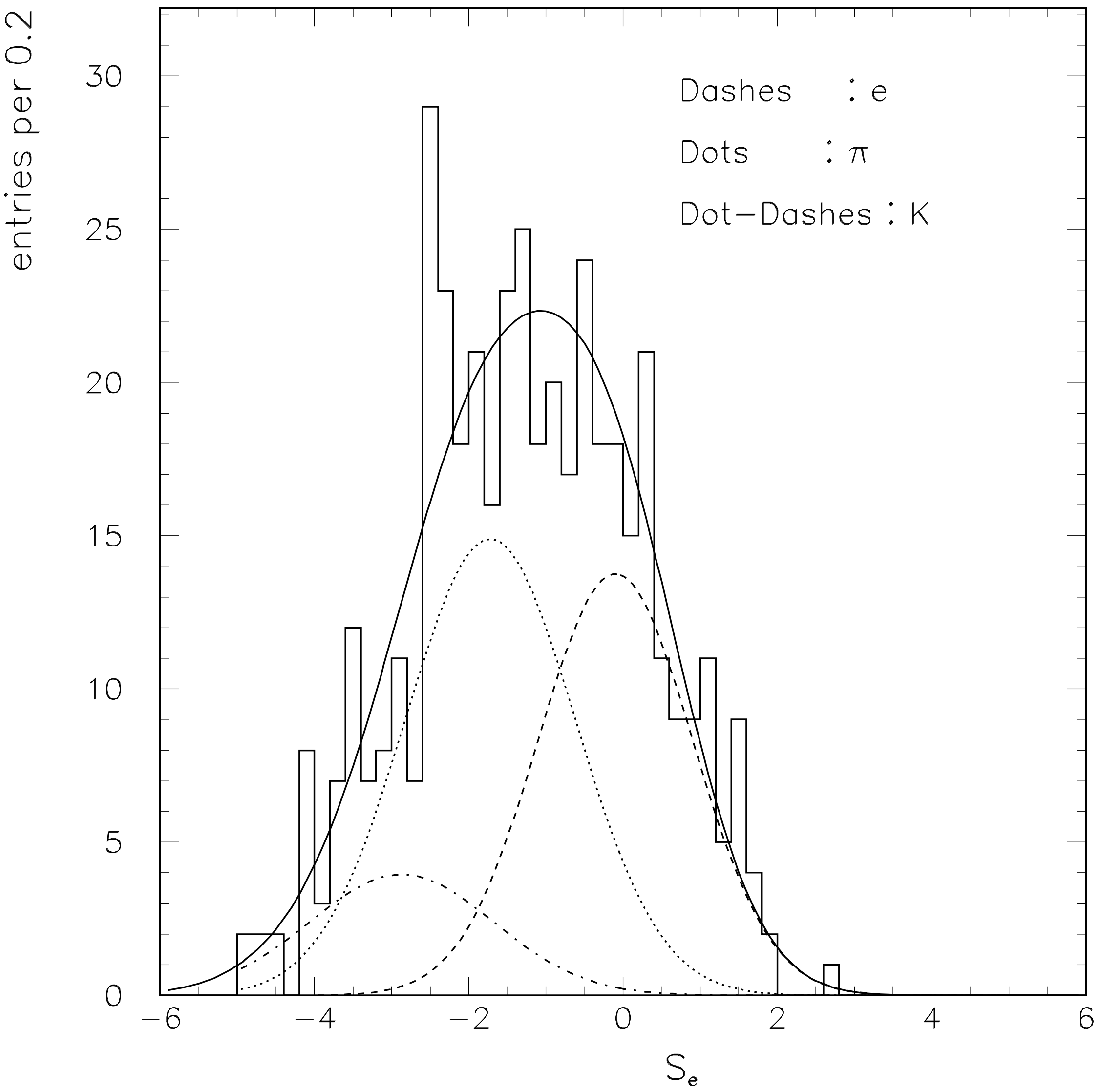

Figure 4.6: The S_e distribution for the tracks identified as electrons in the MB trigger data.

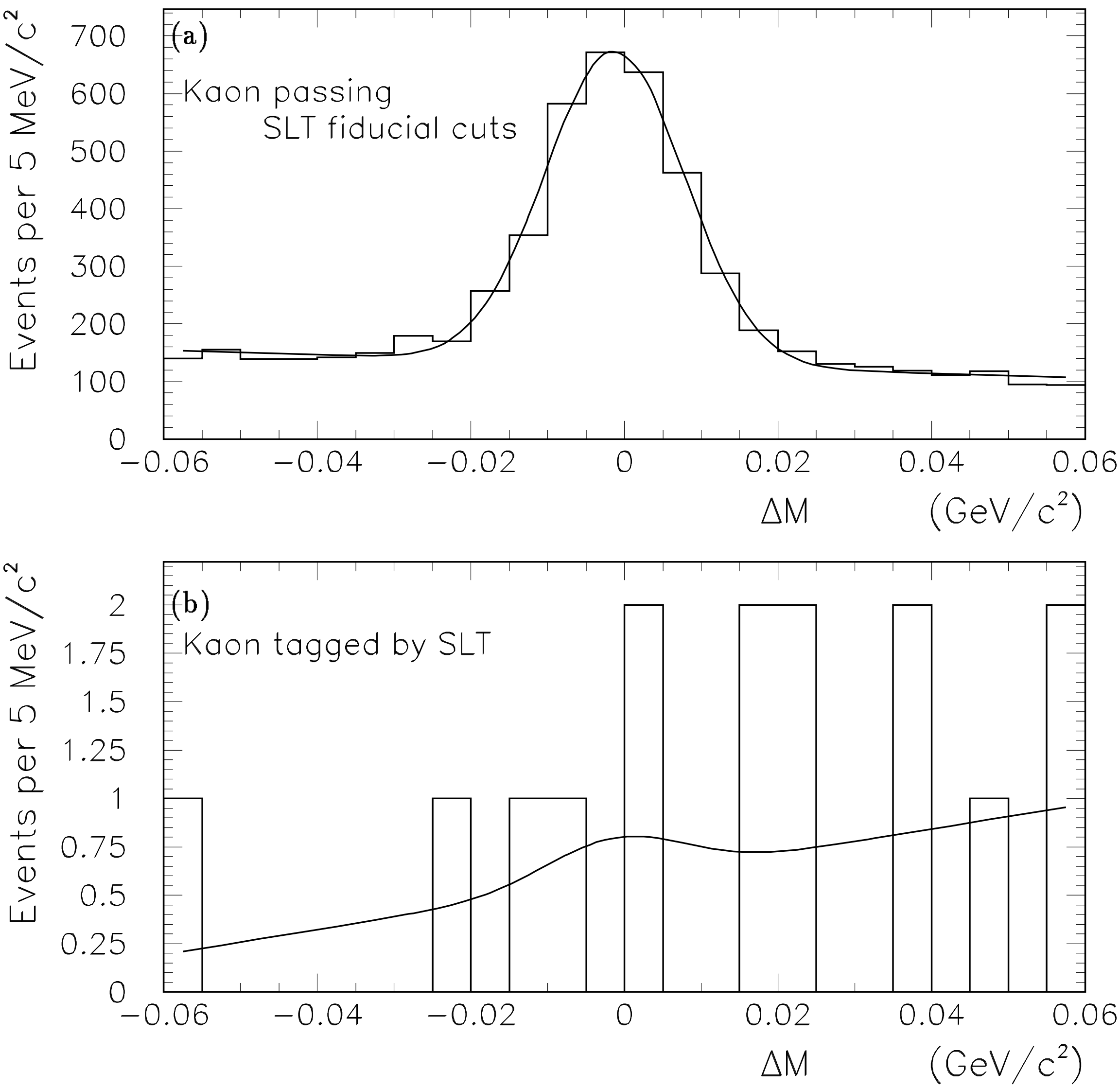

Figure 4.7: Invariant mass distribution for D meson candidates, where the ΔM is the difference between the reconstructed D^0 or D^+ mass and the world average D^0 or D^+ mass. (a) The K track is required to be a fiducial track. (b) The K track is identified as an electron.

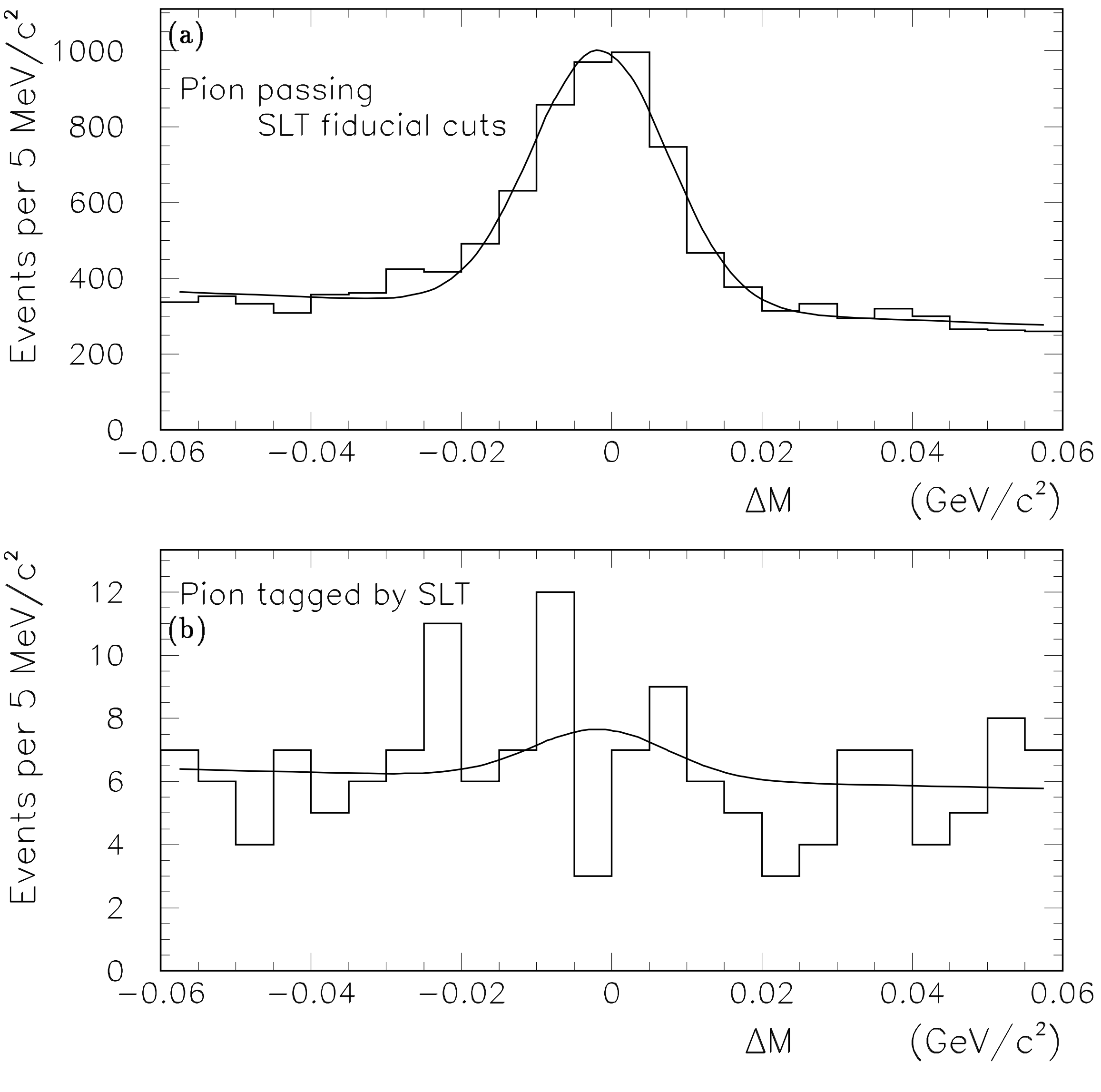

Figure 4.8: Invariant mass distribution for D meson candidates, where the ΔM is the difference between the reconstructed D^0 or D^+ mass and the world average D^0 or D^+ mass. (a) The π track is required to be a fiducial track. (b) The π track is identified as an electron.

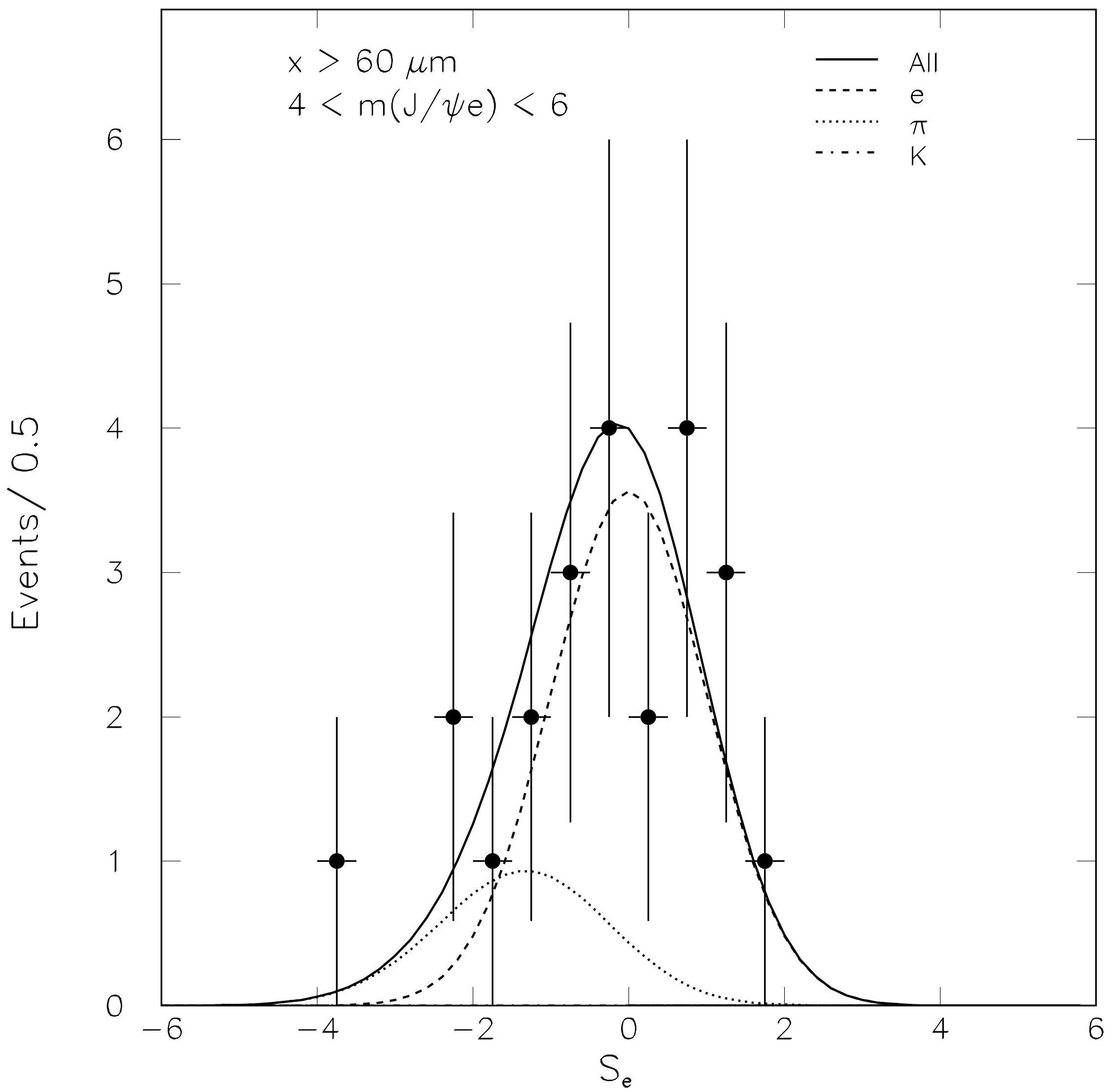

Figure 4.9: The S_e distribution for the $J/\psi + e$ candidates with the $x > 60$ μn cut, where the S_e requirement is removed.

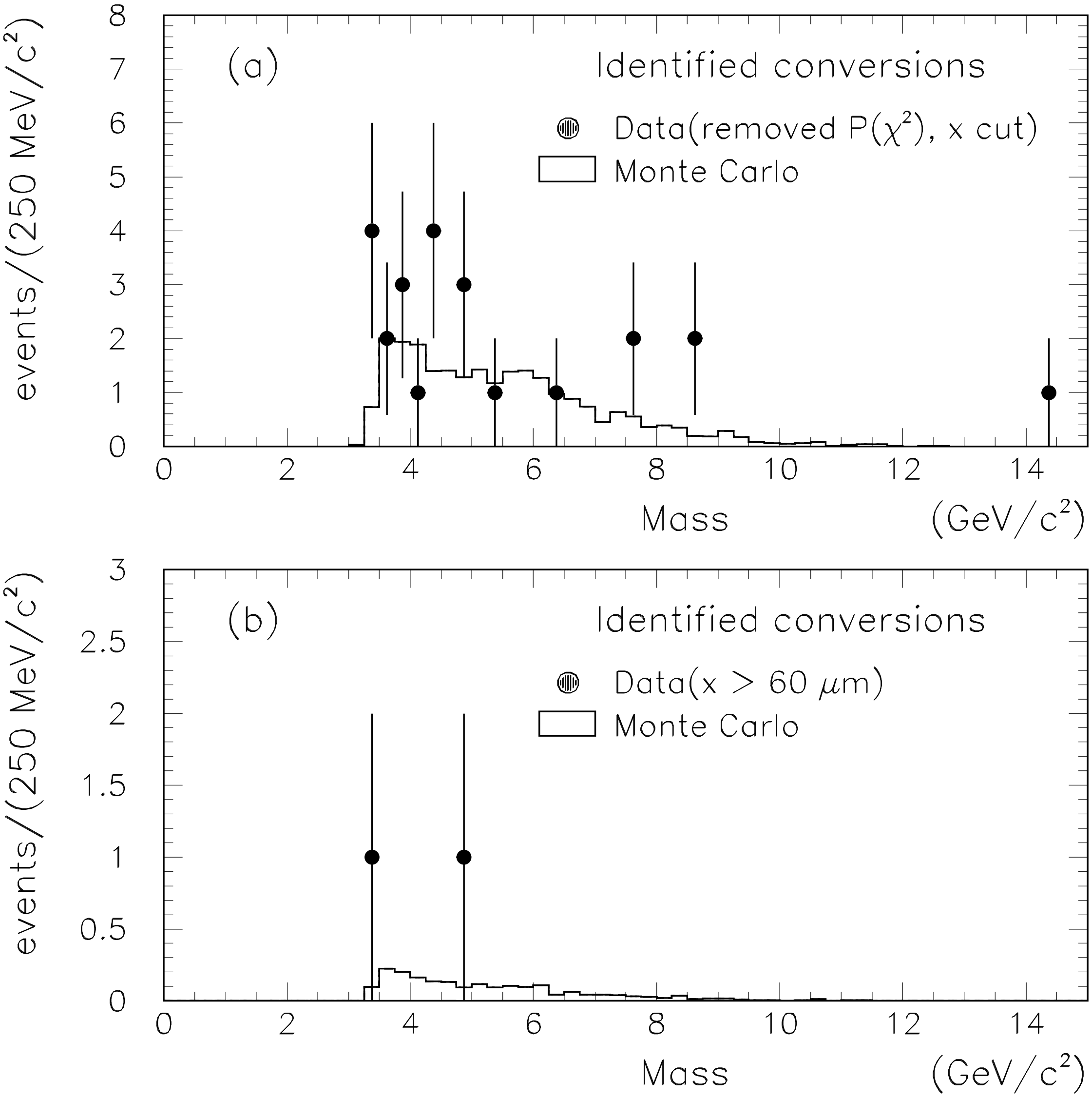

Figure 4.10: J/ψ + identified conversion mass distribution for data. (a) without the vertex χ^2 and the decay length (x) cuts. (b) with the P(χ^2) > 1% and the $x > 60$ μm cuts. The Monte Carlo simulation is described in section 4.2.1.

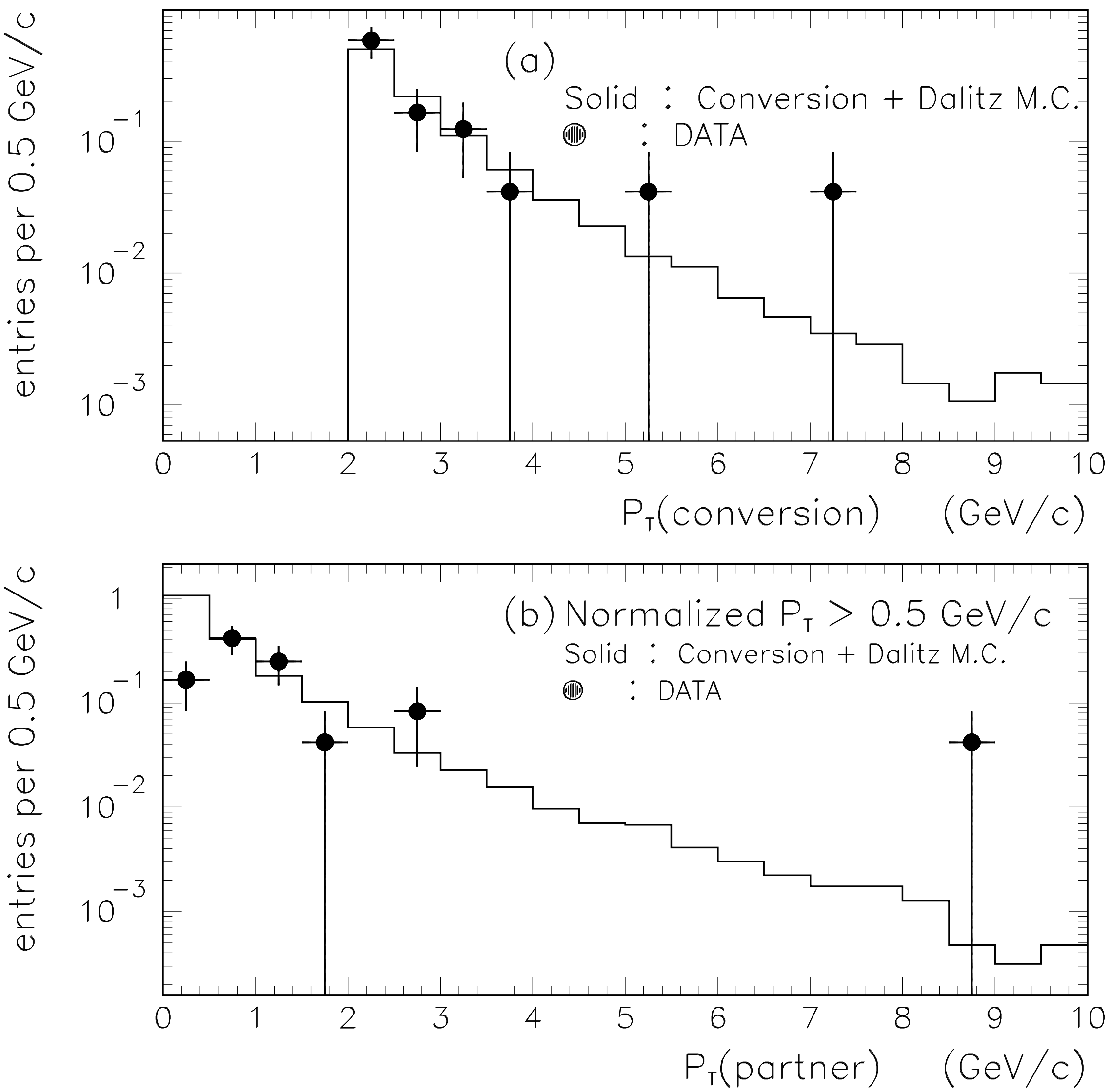

Figure 4.11: p_T distributions (a) for conversion electrons in the J/ψ + track sample and (b) for their partners. Here, the vertex fit χ^2 cut and the x cut are removed. In (a), the distributions are normalized to unit area. In (b), the data distribution is normalized to unit area. For the Monte Carlo sample, the distribution is normalized to the data in the range $p_T > 0.5$ GeV/c.

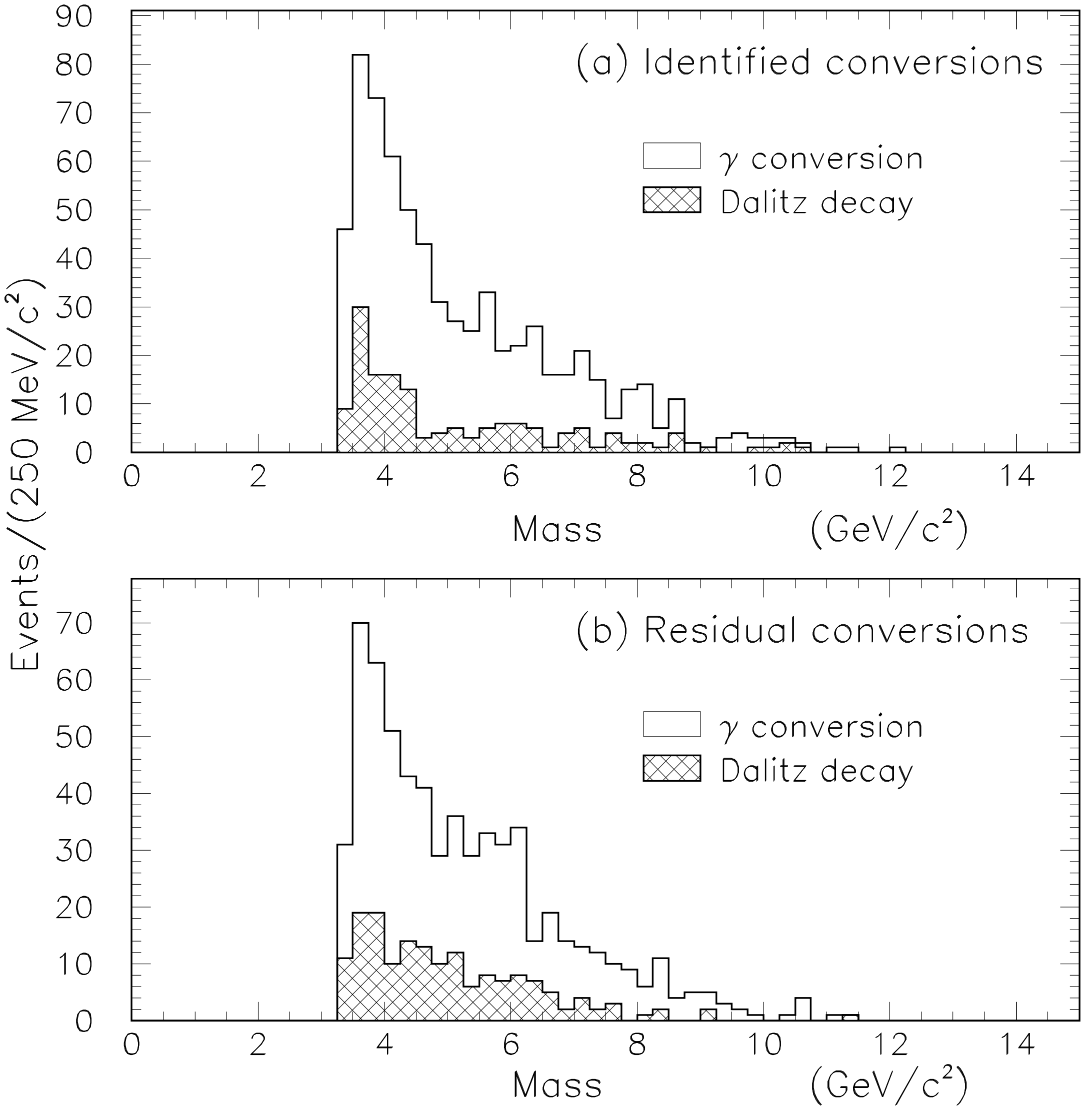

Figure 4.12: J/ψ + conversion mass distributions for Monte Carlo. (a) Identified conversions. (b) Residual conversions.

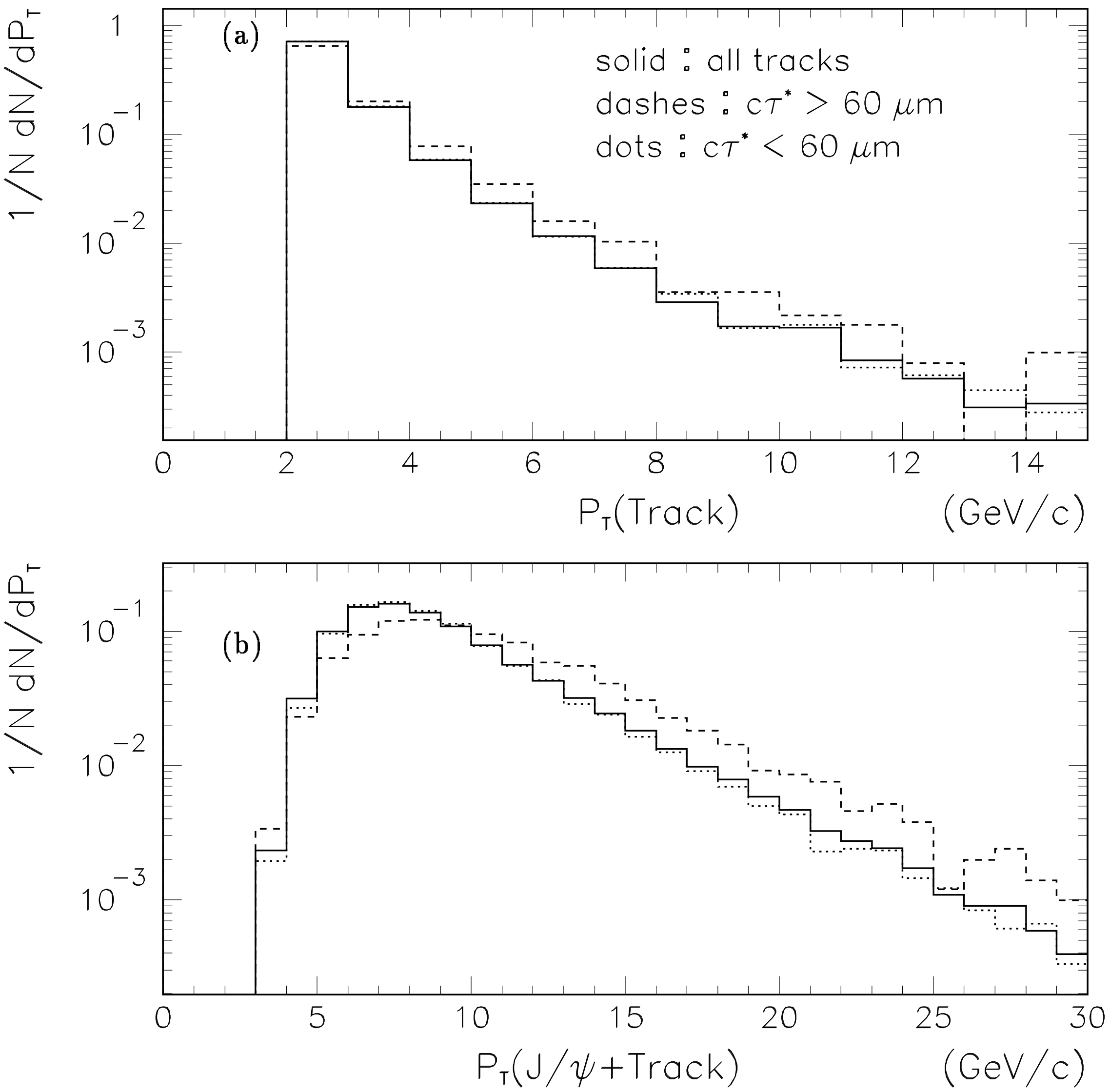

Figure 4.13: Pseudo-proper decay length dependence of the p_T shape in the J/ψ sample: (a) track p_T and (b) p_T of the J/ψ + track system.

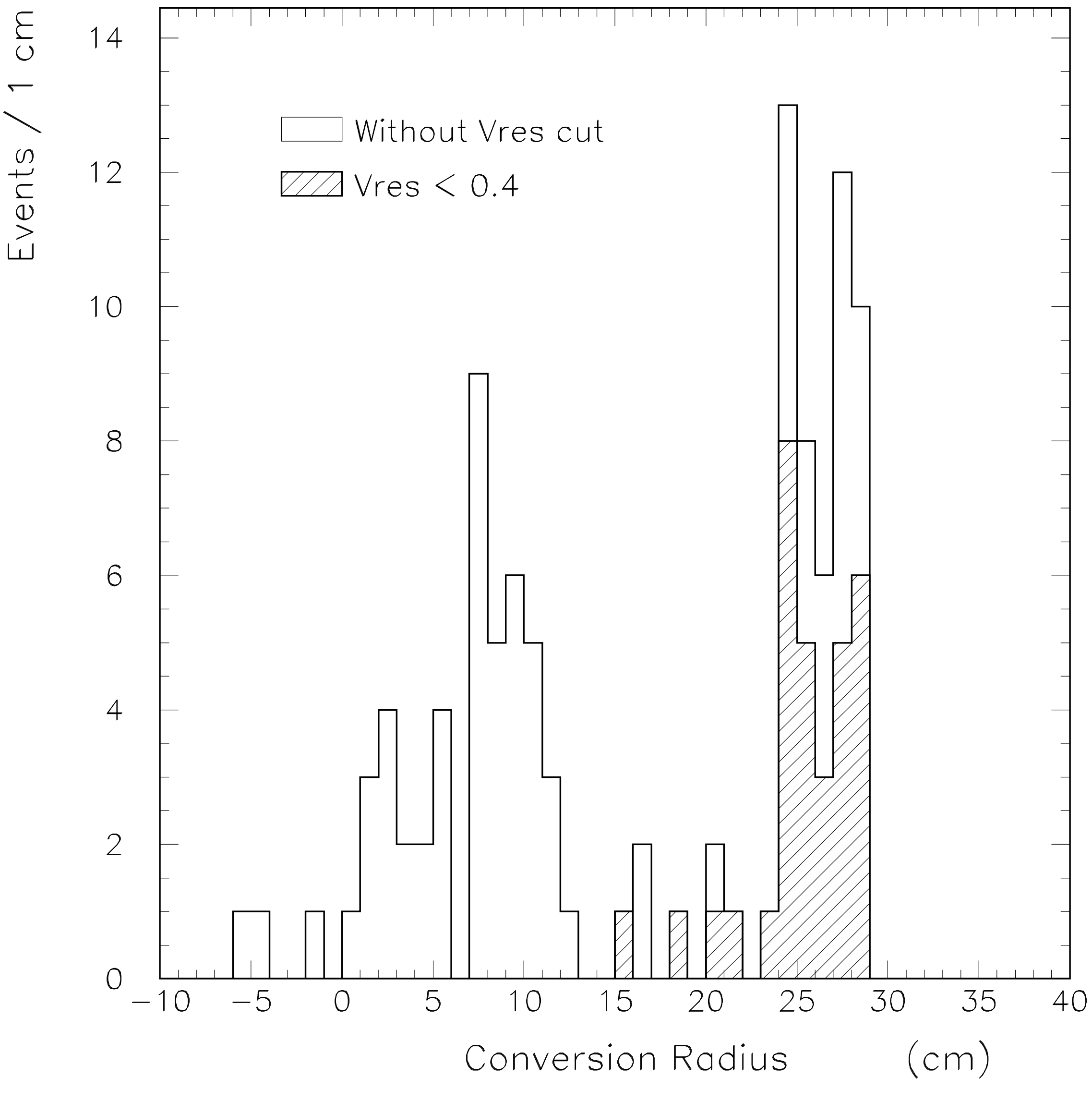

Figure 4.14: Conversion radius distributions without the V_{res} cut and with the $V_{res} <$ 0.4 cut.

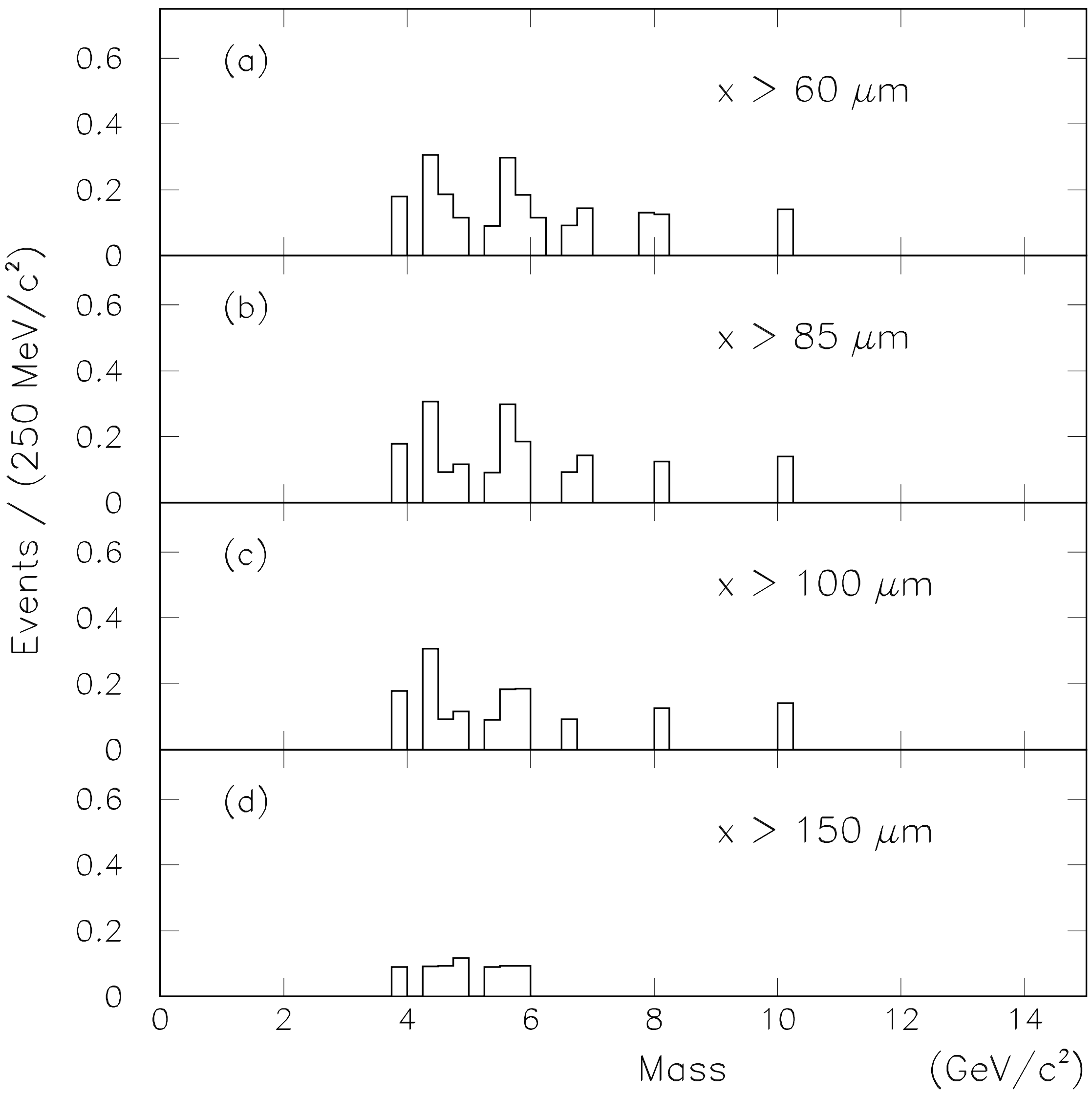

Figure 4.15: The $b\bar{b}$ background distributions for (a) $x > 60$ μm, (b) $x > 85$ μm, (c) $x > 100$ μm, and (d) $x > 150$ μm.

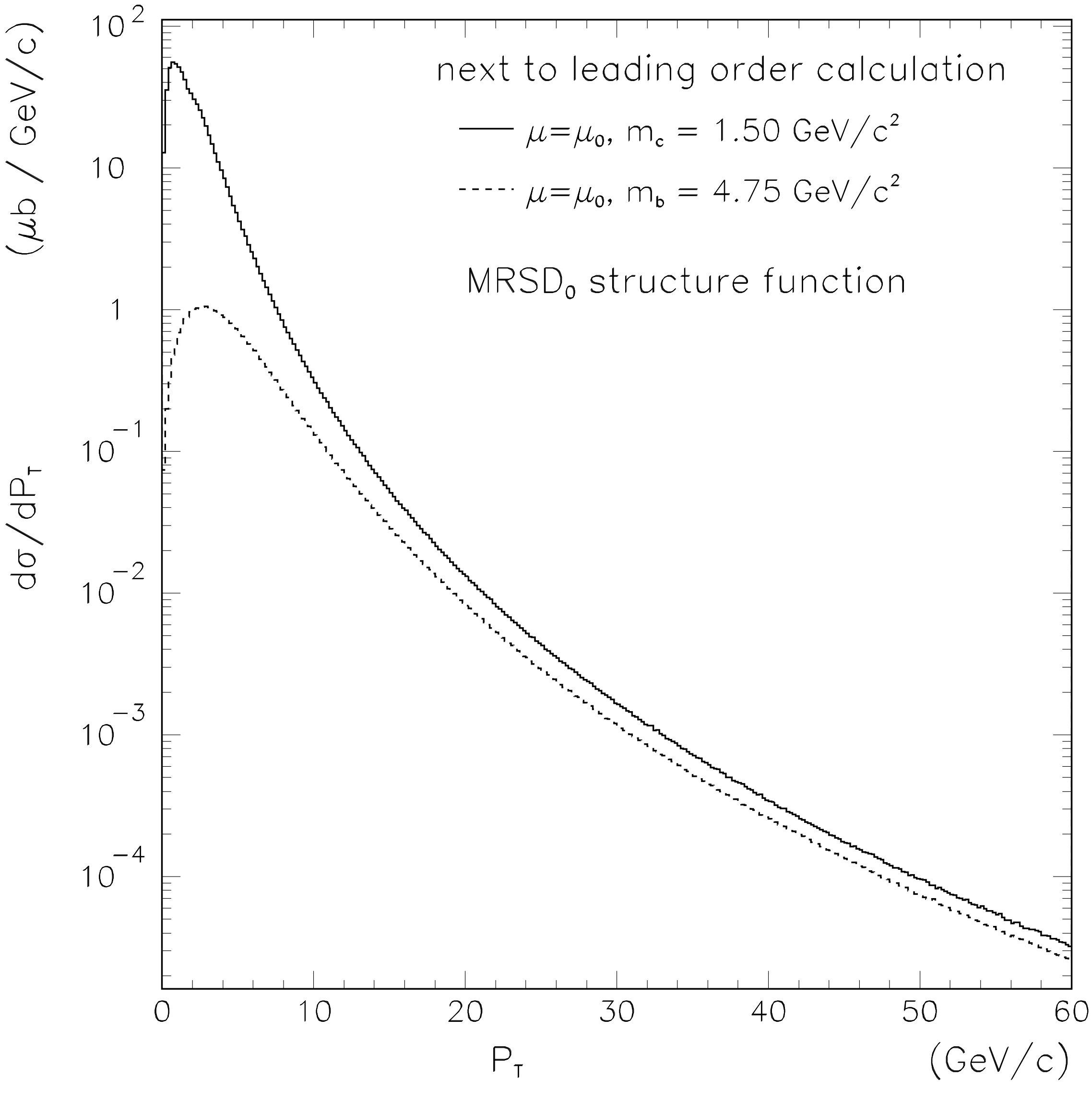

Figure 4.16: p_T distributions for inclusive c quark (solid) and b quark (dashed) production in the next-to-leading order calculation [6].

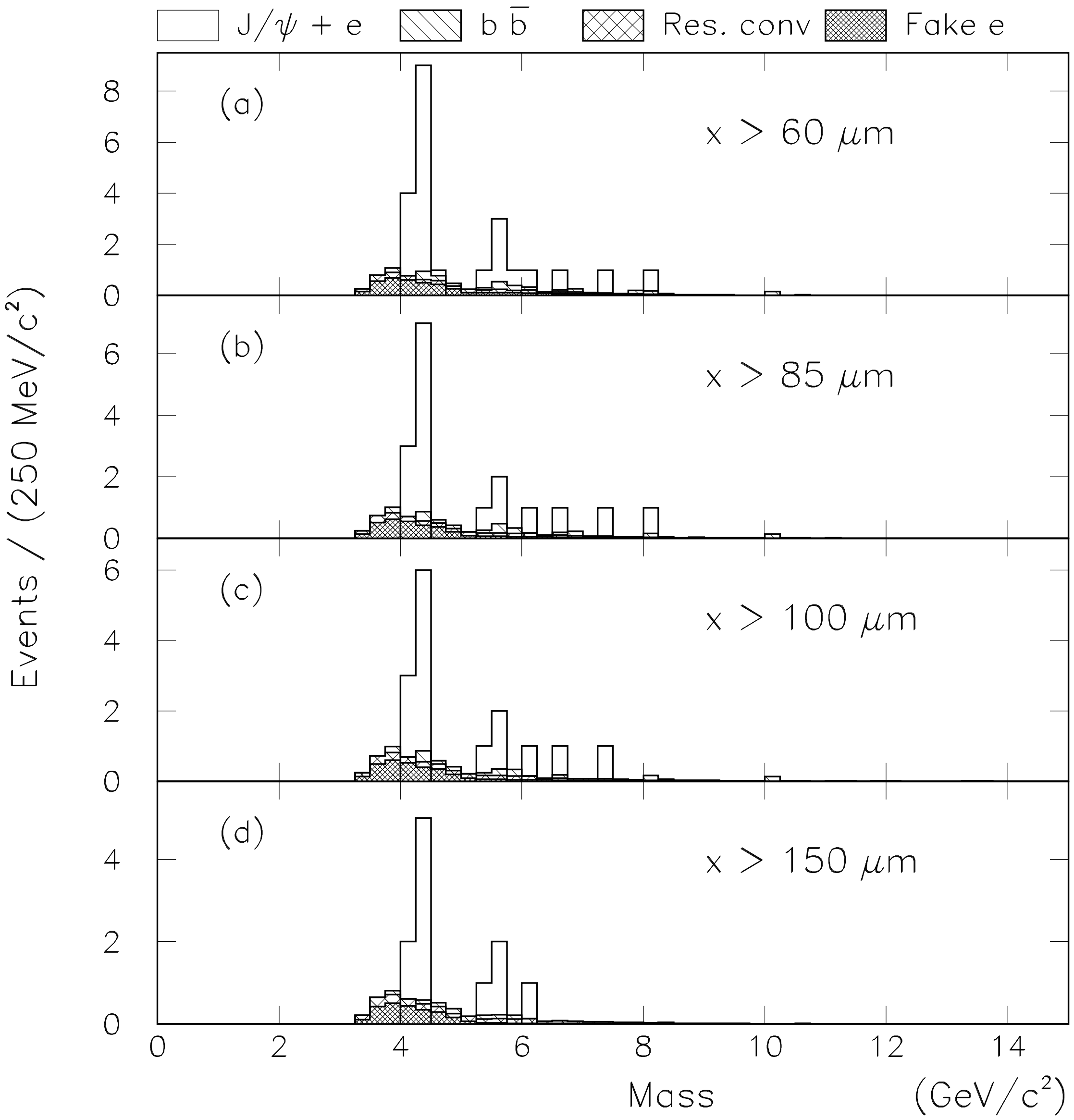

Figure 4.17: The $J/\psi + e$ mass distributions for (a) $x > 60$ μm, (b) $x > 85$ μm, (c) $x > 100$ μm, and (d) $x > 150$ μm. The shaded histograms represent the contributions from the fake electron background, the residual conversions, and the $b\bar{b}$ backgrounds.

Chapter 5

Statistical Significance of the B_c Signal

An excess of observed events over the expected background for the $B_c^+ \to J/\psi e^+ X$ mode is found in Chapter 4. At the CDF, the search for the $B_c^+ \to J/\psi \mu^+ X$ mode is also possible. In this chapter, we first introduce the $J/\psi + \mu$ analysis, which has been performed by other collaborators in CDF [50]. We then combine the $J/\psi + e$ analysis with the $J/\psi + \mu$ analysis. In order to test the excess statistically, we adopt the following two approaches: The first is a simple "counting experiment" based on the number of events in the J/ψ + lepton signal region, $4 < m(J/\psi \ell) < 6$ GeV/c^2. The second approach employs a binned likelihood method which includes the shape information from the mass distribution over the range $3.35 < m(J/\psi \ell) < 11$ GeV/c^2. In both approaches, we compute the probability that a random background fluctuation is consistent with the observed B_c candidates. This is the "null hypothesis".

5.1 $J/\psi + \mu$ analysis

For the $B_c^+ \to J/\psi\ \mu^+ X$ mode, the J/ψ's are selected using the same cuts for the electron mode (see Chapter 3). We require the following selection criteria on the third muon:

- The muon is found in both the CMU and CMP,
- $p_T(\mu) > 3$ GeV/c,

	$N_{J/\psi+\mu}$
Candidates	12 events
Punch-through background	0.88 $\pm$ 0.35 events
Decay-in-flight background	6.4 $\pm$ 2.0 events
$b\bar{b}$ background	0.7 $\pm$ 0.5 events
Total background	7.1 $\pm$ 1.5 events

Table 5.1: Number of $J/\psi + \mu$ candidates and backgrounds for $4 < m(J/\psi\mu) < 6$ GeV/c^2. The data of 105 pb^{-1} were used.

- χ^2 cuts on the position matching between the CTC and the muon chamber: Max(χ^2(CMU), χ^2(CMP)) $< 3\sigma$ in r–ϕ and χ^2(CMU) $< 3.5\sigma$ in z.

We reconstruct a vertex of three muons and require that the χ^2 probability of the vertex fit $> 1\%$, pseudo-proper decay length $x > 60$ μm, and $|m(B_u^+) - m(\mu^+\mu^-K^+)|$ > 50 MeV/c^2. There are fourteen J/ψ + μ candidates in the mass region $m(J/\psi\mu)$ < 15 GeV/c^2 and twelve events in the signal region $4 < m(J/\psi\mu) < 6$ GeV/c^2. The backgrounds for the J/ψ + μ modes are:

- punch-through background of the third muon.
- decay-in-flight background of the third muon.
- $b\bar{b}$ background.
- fake J/ψ background.

These backgrounds are discussed in detail in Ref. [50]. We refer to a combination of the punch-through and decay-in-flight background as the "false muon" background in the latter sections. The number of candidates and backgrounds are listed in Table 5.1. Figure 5.1 (b) shows the J/ψ + μ mass distribution together with the background distribution. We show the J/ψ + e invariant mass distribution in Figure 5.1 (a), for comparison.

	$J/\psi + e$ mode	$J/\psi + \mu$ mode	combined
Candidates	19 events	12 events	31 events
Total background	5.0 ± 1.1 events	7.1 ± 1.5 events	12.1 ± 1.9 events
Probability	2.1×10^{-5}	0.084	2.5×10^{-5} (4.1σ)

Table 5.2: Summary of the counting experiments.

5.2 Counting experiments

In the $J/\psi + \ell$ signal mass region, we find 19 $J/\psi + e$ candidates and 12 $J/\psi + \mu$ candidates. The expected total background is 5.0 ± 1.1 events for the $J/\psi + e$ mode and 7.1 ± 1.5 events for the $J/\psi + \mu$ mode. For each of the analysis, we calculate the probability P^e and P^μ that the background fluctuates up to the observed number of events. This calculation is done using Poisson statistics, where the mean of the distribution is given a Gaussian smearing in order to account for systematic uncertainty on the expected number of background events. We find $P^e = 2.1 \times 10^{-5}$ $(=P_0^e)$ and $P^\mu = 0.084$ $(=P_0^\mu)$. Since correlations between the $J/\psi + e$ and $J/\psi + \mu$ background estimates are negligibly small, we can regard P^e and P^μ as significance levels of two independent tests for the null hypothesis that a random background fluctuation is consistent with the observed B_c candidates. Then the combined probability that P^e and P^μ are such that $P^e P^\mu < P_0^e P_0^\mu$ is given by

$$P^{comb} = P_0^e P_0^\mu (1 - \ln(P_0^e P_0^\mu)) = 2.5 \times 10^{-5}. \tag{5.1}$$

The derivation of the formula for P^{comb} is described, for example, in Ref. [51]. Although P^{comb} is larger than P_0^e, we quote P^{comb} as the statistical significance of our counting experiment, since it is natural to treat the $J/\psi + e$ and $J/\psi + \mu$ modes statistically on an equal footing. The combined probability of 2.5×10^{-5} corresponds to 4.1 standard deviation for a Gaussian probability function. The results for the counting experiments are listed in Table 5.2.

5.3 Likelihood analysis

We use a binned likelihood method for testing and fitting the data and background estimates. It uses the shapes of the distributions over the mass range 3.35 to 11.0 GeV/c^2, and it includes as input all the information on the $J/\psi\ell$ mass distributions for signal and background discussed in earlier sections. The likelihood function has a necessary and sufficient set of parameters to fit these distributions to the observed data. It also allows constraints such as the expected fraction of events in the two decay channels.

5.3.1 Definition of likelihood

We define the input information and corresponding parameters along with the constraints and relationships among them and then we present the likelihood. Upper case letters represent input information, and lower case letters represent parameters of the fit. The superscript e (μ) refers to $J/\psi + e$ ($J/\psi + \mu$). We designate background types by additional superscript, fe for fake electrons, $f\mu$ for false muons, ce for conversion electrons, and Be ($B\mu$) for the $b\bar{b}$ contributions to electron (muon) backgrounds. We use λ_i^e (λ_i^μ) to represent a function of the parameters corresponding to the fitted number of signal plus background events in the i^{th} bin for the electron (muon) distribution. We use primes (N', n') for the number of events in the mass range 3.35 to 11.0 GeV/c^2, and elsewhere we use unprimed numbers (N, n) for the subset in the range between 4.0 and 6.0 GeV/c^2, where N' and N are the estimated numbers of events while n' and n are the fitting parameters of the number of events.

In order to propagate the uncertainties for various measured or calculated quantities, each item of input information has a corresponding parameter in the fit that we constrain to the measured value within its uncertainties. We include each such constraint as a Gaussian or Poisson factor in the likelihood. For quantities with both Poisson statistical uncertainties and Gaussian systematic uncertainties, we adopt a Gaussian approximation of the Poisson uncertainty and add them in quadrature.

Data

We show the input $J/\psi\ell$ mass distributions for the $J/\psi + e$ and $J/\psi + \mu$ modes in Figures 5.2 (a) and (b), respectively. For the histogram in Figure 5.2 (a), we represent the number of candidate $B_c^+ \to J/\psi e^+ X$ events in the i^{th} bin as D_i^e. These numbers contribute factors to the likelihood $\mathcal{L}$ according to the Poisson probabilities:

$$P(\lambda_i^e|D_i^e) = \frac{(\lambda_i^e)^{D_i^e}}{D_i^e!} e^{-\lambda_i^e}, \tag{5.2}$$

where the best estimate for the mean of D_i^e is represented by λ_i^e, the function that sums the signal and background contributions calculated in the fit. Each term in the sum is a product of parameters defined below. In like manner, we symbolize the bin-by-bin numbers of candidate $B_c^+ \to J/\psi\mu^+ X$ events (Figure 5.2 (b)) by D_i^μ, and the functions representing their means by λ_i^μ.

B_c signal

We obtain the signal $J/\psi\ell$ mass distribution using the same Monte Carlo simulation as described in Section 3.4.1. The mass of B_c is set to be 6.27 GeV/c^2. The signal $J/\psi\ell$ mass distributions are shown in Figures 5.2 (c) for the $J/\psi + e$ mode and in (d) for the $J/\psi + \mu$ mode, respectively. We generate the independent mass distributions for $J/\psi + e$ and $J/\psi + \mu$ and normalize each to unit area. Their contributions to the i^{th} bin are represented by S_i^e and S_i^μ, respectively. We symbolize the total number of $J/\psi + \ell$ events by n'^ℓ and the fraction of these in the $J/\psi + e$ channel by r^ε. For convenience, we express the numbers of events in the two decay channels as $n'^e = r^\varepsilon n'^\ell$ and $n'^\mu = (1 - r^\varepsilon)n'^\ell$, and we emphasize that these are derived from the fitted parameters. The contributions to λ_i^e and λ_i^μ are $n'^e S_i^e$ and $n'^\mu S_i^\mu$. The Monte Carlo simulation also determines the expected fraction of electron signal events, $R^\varepsilon = 0.58 \pm 0.04$ (see Section 7.3.2), which contributes to $\mathcal{L}$ as a constraining Gaussian probability factor.

$$G(r^\varepsilon|R^\varepsilon, \Delta R^\varepsilon) = \frac{1}{\sqrt{2\pi}\Delta R^\varepsilon} \exp\left(-\frac{1}{2}\left(\frac{r^\varepsilon - R^\varepsilon}{\Delta R^\varepsilon}\right)^2\right) \tag{5.3}$$

Fake electron background

The mass distribution for J/ψ + track events for the e mode is given in Figure 5.2 (e). The subset of these events which satisfy the fiducial requirement for third-track electrons is represented by J_i^{fe}. This sample forms the parent distribution for calculating the fake electron contribution. We show the mass shape for the fake electron background in Figure 5.2 (f) and normalize it to unit area. To allow for a shape difference from the parent distribution, we calculate the bin-by-bin fraction $F_i^{fe} \pm \Delta F_i^{fe}$ of the parent distribution. $N'^{fe} = 4.2 \pm 0.4$ is the total number of fake electron background events that satisfy all the electron identification criteria. In order to allow the fit to vary within the uncertainties in these measurements, we replace them by parameters. The fitted parameters j_i^{fe} are constrained to J_i^{fe} by Poisson contributions in $\mathcal{L}$. Similarly, the parameter n'^{fe} is constrained to N'^{fe} by a Gaussian factor in $\mathcal{L}$. The fitted parameters f_i^{fe} were constrained through Gaussian factors in $\mathcal{L}$. The contribution to λ_i^e from fake electron backgrounds is $n'^{fe} f_i^{fe} j_i^{fe}$.

Residual conversion background

We measure the number of identified conversion electron background events N'^{ce} to be 2. We represent this by a parameter n'^{ce} constrained to N'^{ce} by a Poisson factor in $\mathcal{L}$. With the Monte Carlo simulation described in Section 4.2, we determine the ratio of residual (not identified) conversions to identified conversions R^{ce} to be 1.06 ± 0.36, where $R^{ce} = (1 - \varepsilon_{id})/\varepsilon_{id}$ in Eq. (4.4). The corresponding fitted parameter r^{ce} is constrained by a Gaussian factor in the likelihood function. We normalize the mass distribution for residual conversions in Figure 5.3 (g) to unit area, which is represented by $J_i^{ce} \pm \Delta J_i^{ce}$. The corresponding parameters are j_i^{ce} with constraining Gaussian probability factors in $\mathcal{L}$. The contribution to λ_i^e from residual conversions is $n'^{ce} r^{ce} j_i^{ce}$.

$b\bar{b}$ background

We employ a Monte Carlo procedure described n Section 4.3 to calculate independently the $b\bar{b}$ background contributions to J/ψ + e and J/ψ + μ. In order to obtain the Monte Carlo sample with high statistics, we force b and $\bar{b}$ to decay to $J/\psi X$ and

ℓX, respectively. These shapes are found to be identical and a single parent distribution, $J_i^B \pm \Delta J_i^B$, normalized to unit area, is adopted for both. Figure 5.2 (h) shows the mass shape for the $b\bar{b}$ background. It is represented by the parameters j_i^B that are constrained by Gaussian terms in the likelihood function. The Monte Carlo results for total numbers of events are: $N'^{Be} = 2.3 \pm 0.9$ for $J/\psi + e$ and $N'^{B\mu} = 1.44 \pm 0.25$ for $J/\psi + \mu$. The corresponding parameters are n'^{Be} and $n'^{B\mu}$. The contributions to λ_i^e and λ_i^μ from $b\bar{b}$ background are $n'^{Be} j_i^B$ and $n'^{B\mu} j_i^B$, respectively.

False muon background

The false muon background is estimated using another subset of the J/ψ + track distribution that satisfies the purely geometric criteria for third-track muons. This sample forms the parent distribution (Figure 5.2 (i)) for calculating the false muon contributions from punch-through and decay-in-flight, and we combine these two sources of background into a single distribution (Figure 5.2 (j)). We normalize it to unit area. This parent distribution is $J_i^{f\mu}$. The remaining input information and parameters for the false muon background are formally identical to those for the fake electron background: $F_i^{f\mu}$, $f_i^{f\mu}$, $j_i^{f\mu}$, $N'^{f\mu} = 11.4 \pm 2.4$ and $n'^{f\mu}$. The contribution to λ_i^μ from false muon backgrounds is $n'^{f\mu} f_i^{f\mu} j_i^{f\mu}$.

Sums

We present here the two functions which, through their parameters, are adjusted for the best fit to the data distributions, D_i^e and D_i^μ.

$$\begin{aligned} \lambda_i^e &= r^\varepsilon n'^\ell S_i^e + n'^{fe} f_i^{fe} j_i^{fe} + n'^{ce} r^{ce} j_i^{ce} + n'^{Be} j_i^B \\ \lambda_i^\mu &= (1 - r^\varepsilon) n'^\ell S_i^\mu + n'^{f\mu} f_i^{f\mu} j_i^{f\mu} + n'^{B\mu} j_i^B \end{aligned} \tag{5.4}$$

The likelihood is written as

$$\mathcal{L} = G(r^\varepsilon | R^\varepsilon, \Delta R^\varepsilon) G(n'^{fe} | N'^{fe}, \Delta N'^{fe}) P(n'^{ce} | N'^{ce}) G(r^{ce} | R^{ce}, \Delta R^{ce}) \tag{5.5}$$

$$G(n'^{f\mu} | N'^{f\mu}, \Delta N'^{f\mu}) G(n'^{Be} | N'^{Be}, \Delta N'^{Be}) G(n'^{B\mu} | N'^{B\mu}, \Delta N'^{B\mu}) \tag{5.6}$$

$$\prod_{i=1}^{15} [P(\lambda_i^e | D_i^e) P(\lambda_i^\mu | D_i^\mu) P(j_i^{fe} | J_i^{fe}) G(f_i'^{fe} | F_i'^{fe}, \Delta F_i'^{fe}) G(j_i'^{ce} | J_i'^{ce}, \Delta J_i'^{ce}) \tag{5.7}$$

$$P(j_i^{f\mu} | J_i^{f\mu}) G(f_i'^{f\mu} | F_i'^{f\mu}, \Delta F_i'^{f\mu}) G(j_i'^B | J_i'^B, \Delta J_i'^B)], \tag{5.8}$$

where $G(x|\mu, \sigma)$ is the Gaussian function centered at μ with a width of σ and $P(\mu|n)$ is the Poisson function for a mean of μ. Lines (5.5) and (5.6) constrain the normalizations for the five background distributions, the Monte Carlo calculation of the expected ratio of electron to muon B_c events, and the calculated ratio of residual to identified conversion electron backgrounds. $P(\lambda_i^e|D_i^e)$ and $P(\lambda_i^\mu|D_i^\mu)$ in Line (5.7) are fit to the B_c candidate distributions. The other terms in Line (5.7) and Line (5.8) constrain the parent distributions for the various backgrounds and the shape-dependent fractions for the fake lepton distributions.

5.3.2 Mass distribution fit

In the likelihood $\mathcal{L}$, the only free parameter is the total number of B_c signal events, n'^{ℓ} $(= n'^{e} + n'^{\mu})$. All other parameters are constrained within uncertainties by information independent of the B_c candidate mass distribution. We minimize $-2\ln\mathcal{L}$ and obtain the number of B_c signals $n'^{\ell} = 20.4^{+6.2}_{-5.6}$ events in the fitting mass region, where the uncertainties of n'^{ℓ} are determined by allowing $-2\ln\mathcal{L}$ to increase 1. Since, of these events, 93.0 ± 0.6 % fall in the signal region $4 < m(J/\psi\ell) < 6$ GeV/c^2, we find $n^{\ell} = n^{e} + n^{\mu} = 19.0^{+5.8}_{-5.1}$ events in the signal region. This agrees with the counting experiment result. The other parameters are also listed in Table 5.3. Figure 5.3 shows the data $J/\psi\ell$ mass distribution together with the fit results.

We fit the mass shape with fixing the number of B_c signal n'^{ℓ}. For each value of n'^{ℓ}, $-2\ln\mathcal{L}$ is minimized as a function of other parameters. Figure 5.4 shows $\Delta(-2\ln\mathcal{L})$ as a function of the assumed number of B_c mesons in the data sample. The $\Delta(-2\ln\mathcal{L})$ is defined as the difference between the minimum $(-2\ln\mathcal{L})$ for a fixed number of B_c mesons and the minimum $(-2\ln\mathcal{L})$ for the data. The $\Delta(-2\ln\mathcal{L})$ shape is not parabola, because the number of observed events are statistically limited and the Poisson terms exist in the likelihood $\mathcal{L}$.

In order to check the likelihood fit, we generate a large number of "pseudo-experiments" as follows:

1. We generate each background according to the shapes shown in Figure 5.2, where the number of each background is fluctuated around the input value listed in

	Input Constraint	Results of fit
B_c signal	$\cdots$	$20.4^{+6.2}_{-5.6}$
B_c signal for e	$\cdots$	$12.0^{+3.8}_{-3.2}$
B_c signal for μ	$\cdots$	$8.4^{+2.7}_{-2.4}$
electron fraction for signal	0.58 ± 0.04	0.59 ± 0.04
fake electron background	4.2 ± 0.4	4.2 ± 0.4
identified conversion	2	2.2 ± 1.4
conversion ratio	1.06 ± 0.36	1.08 ± 0.35
residual conversion background	2.1 ± 1.7	2.4 ± 1.7
$b\bar{b}$ background for e	2.3 ± 0.9	2.6 ± 0.9
false muon background	11.4 ± 2.4	9.2 ± 2.3
$b\bar{b}$ background for μ	1.44 ± 0.25	1.42 ± 0.25

Table 5.3: Summary of the mass fit. The numbers are for the mass range $3.35 < m(J/\psi\ell) < 11.0$ GeV/c^2.

Table 5.3. We make one background histogram for each of the e and μ modes by summing the histograms from each source.

2. For each of the e and μ modes, we generate a signal distribution by fluctuating the number of events around the fitted value listed in Table 5.3.

3. We add the background distribution to the signal distribution, bin-by-bin, to get the number of entries for each bin, and we fluctuate it according to a Poisson distribution.

4. We fit the mass distributions for the e and μ mode simultaneously in the same way as for real data.

Figures 5.5 (a) and (b) show the $-2\ln\mathcal{L}$ distribution and the fitted number of B_c events for one thousand pseudo-experiments. From the data fit, we have found $-2\ln\mathcal{L}$ $= -671$. The probability of finding $-2\ln\mathcal{L} > -671$ is 13%.

5.3.3 Statistical significance of the mass distribution

In order to estimate the null hypothesis, *i.e.*, to evaluate the probability that a statistical fluctuation in the background can explain the observed excess of the data, we again perform pseudo-experiments. For the pseudo-experiments of the null hypothesis, we generate background events using the same method as described above, and we do not include the signal events. Figure 5.6 shows the number of B_c events returned by the mass distribution fit for 196750 pseudo-experiments. Since we set the lower limit of n'^{ℓ} to be zero, there is a peak at the lowest (zero) bin in Figure 5.6. None of the pseudo-experiment gave values of n'^{ℓ} exceeding 20.4. From this result, we conclude that the probability that a fluctuation of the background yields the observed distribution at 90 % confidence level is less than 1.1×10^{-5}, *i.e.*, the null hypothesis is rejected at the 4.1 standard deviation level.

As a check, we also perform an unbinned likelihood analysis. We obtain the signal and background shape from spline fits. Then the null hypothesis is tested in a same manner. The results are consistent with the binned likelihood analysis.

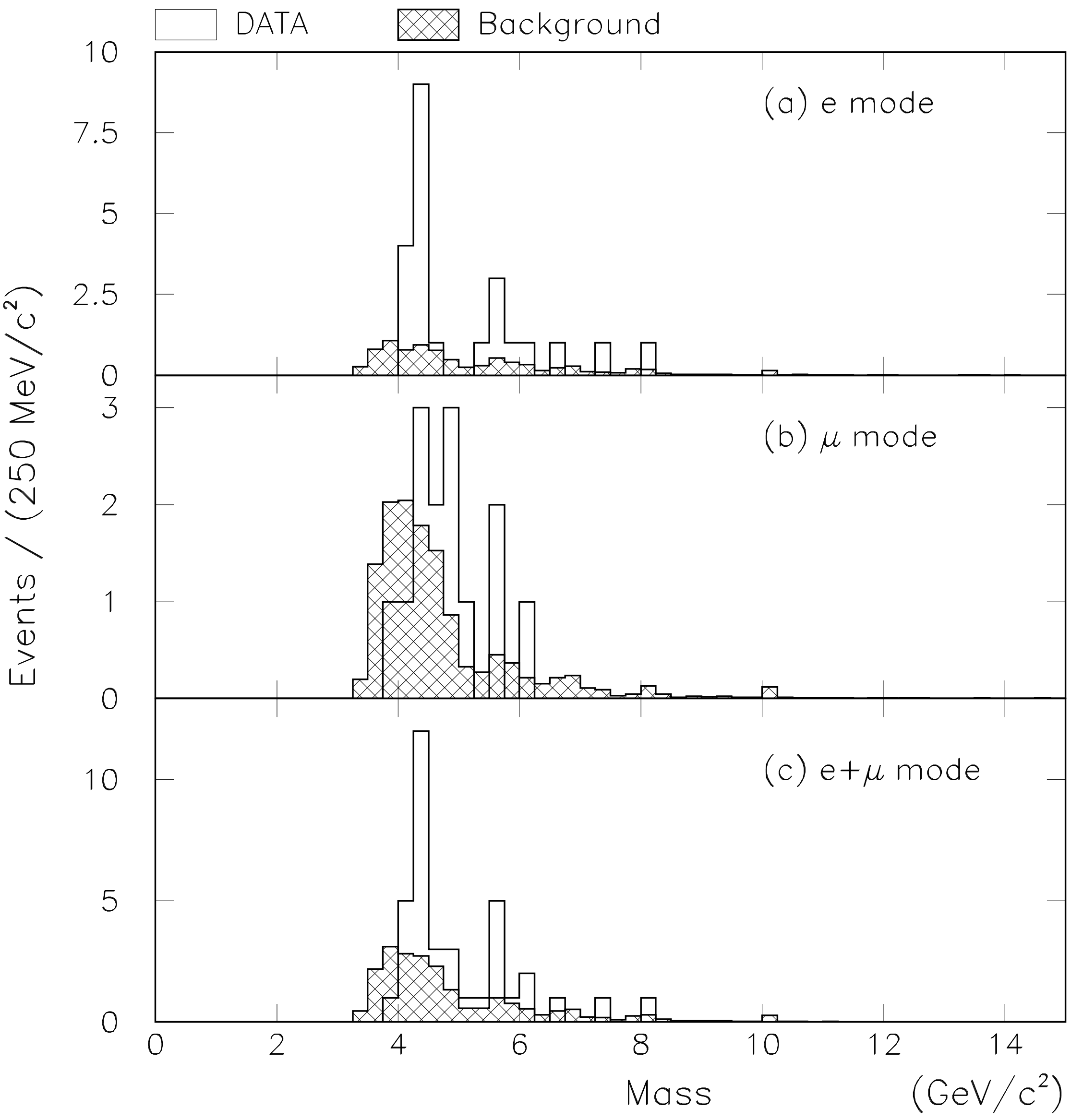

Figure 5.1: $J/\psi\ell$ mass distribution for $x > 60$ μm. (a) e mode. (b) μ mode. (c) $e + \mu$ mode.

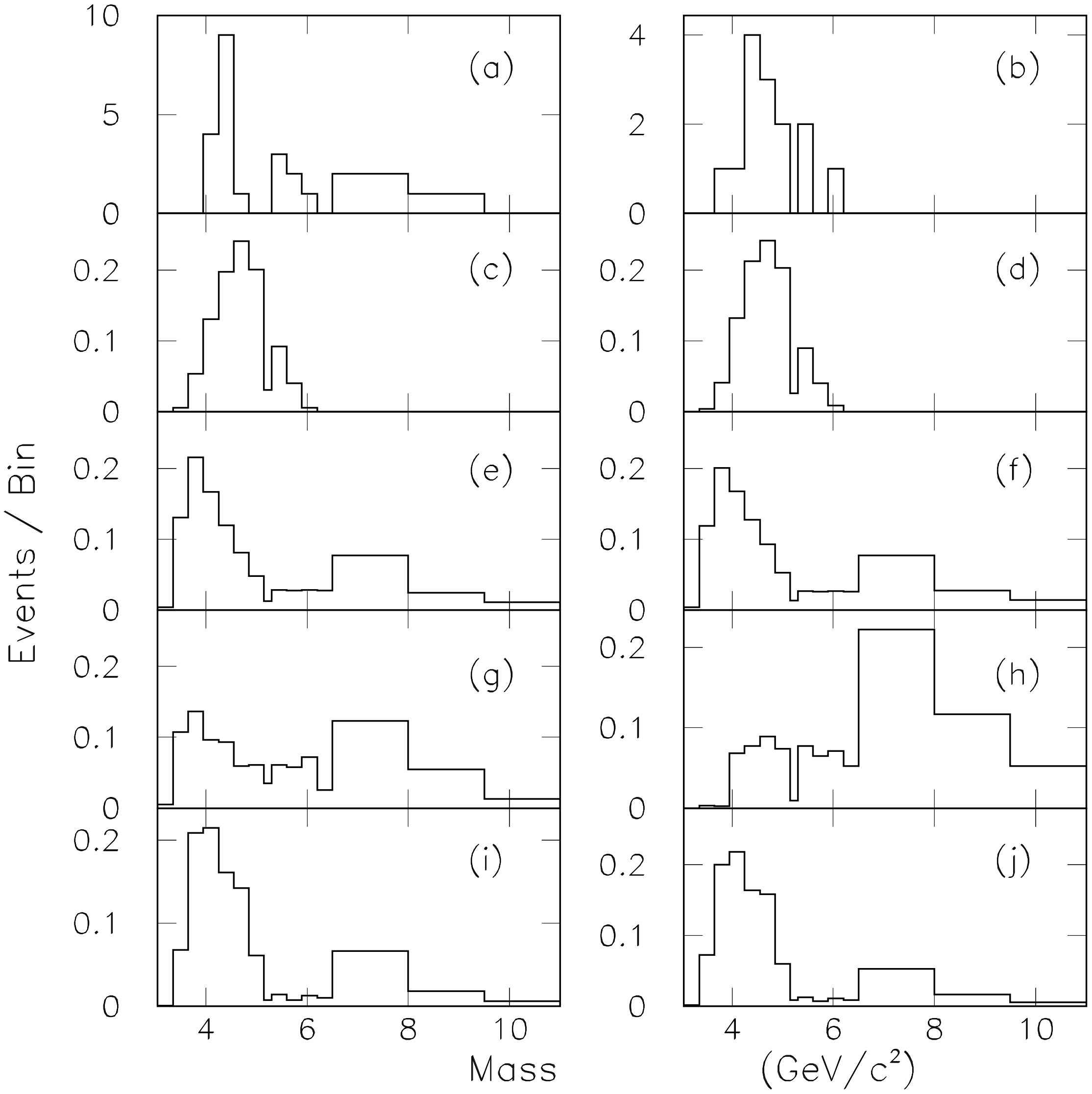

Figure 5.2: Input $J/\psi\ell$ mass distributions for the mass fit. (a) $J/\psi e$ data. (b) $J/\psi\mu$ data. (c) $J/\psi e$ signal. (d) $J/\psi\mu$ signal. (e) J/ψ + track for e mode. (f) fake e. (g) residual conversion. (h) $b\bar{b}$. (i) J/ψ + track for μ mode. (j) false μ.

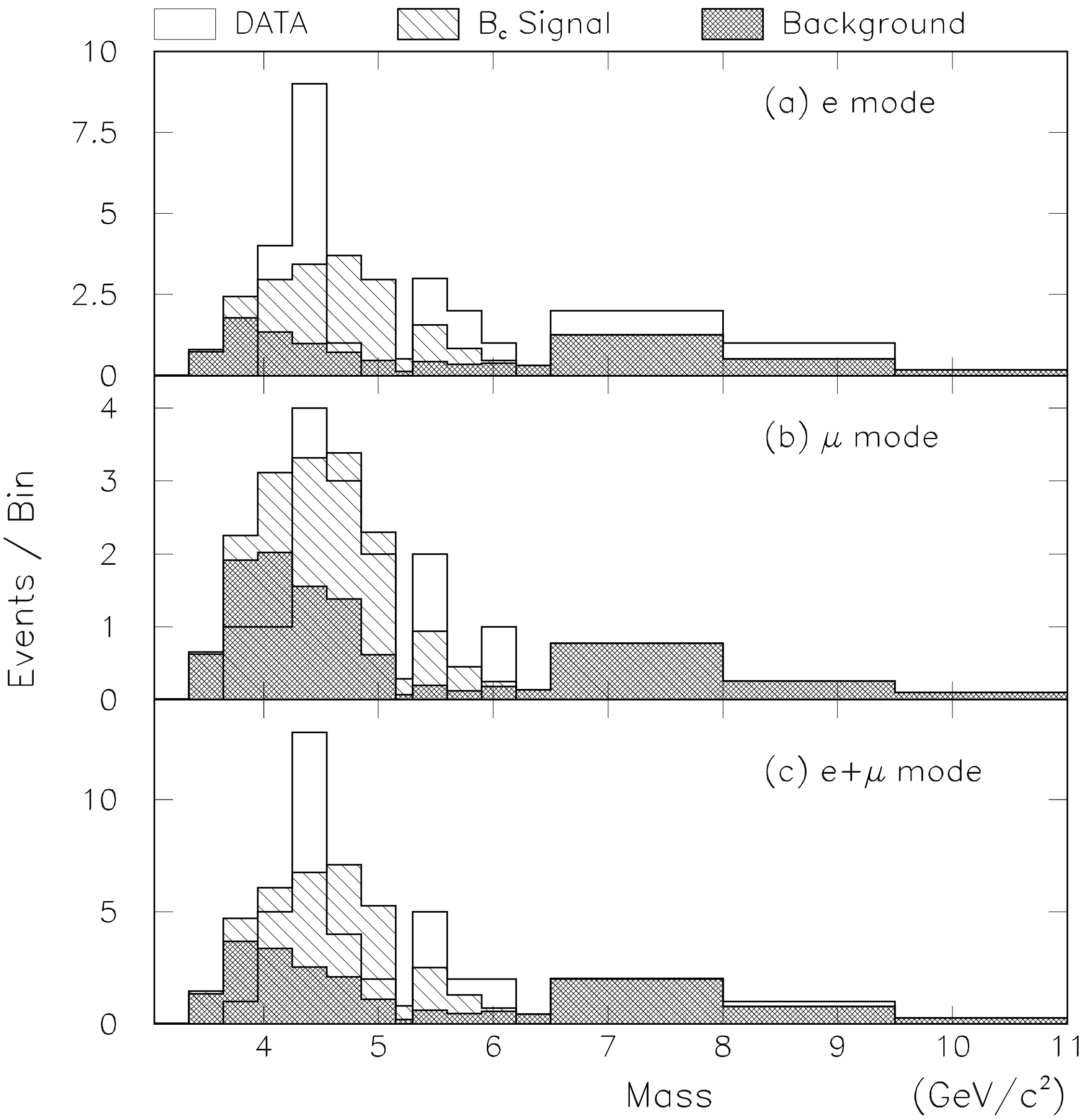

Figure 5.3: $J/\psi\ell$ mass distribution superimposed by the fit results. (a) e mode. (b) μ mode. (c) $e + \mu$ mode.

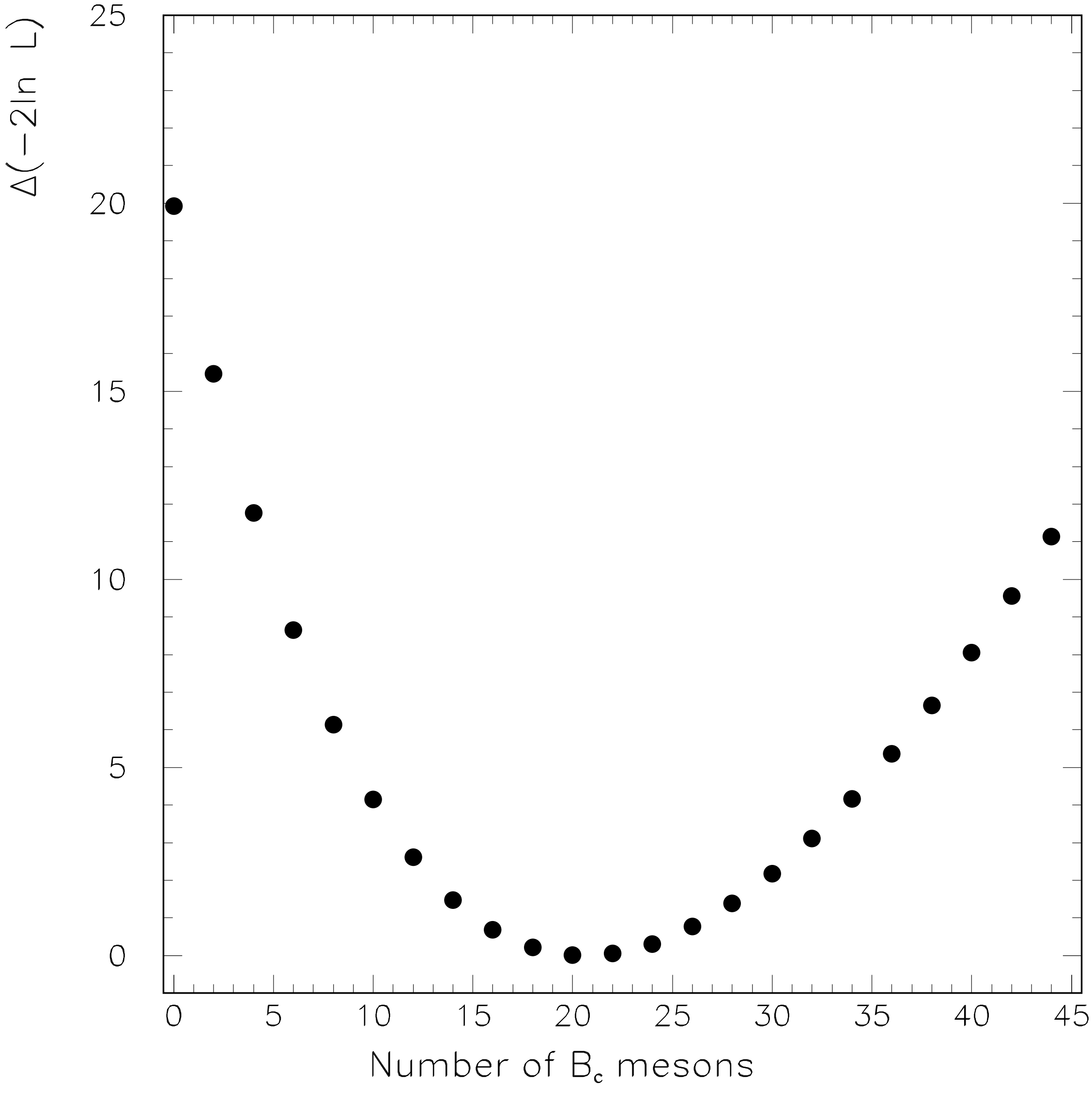

Figure 5.4: $\Delta(-2\ln\mathcal{L}) = -2\ln\mathcal{L} - (-2\ln\mathcal{L}_{min})$ as a function of the assumed number of B_c's.

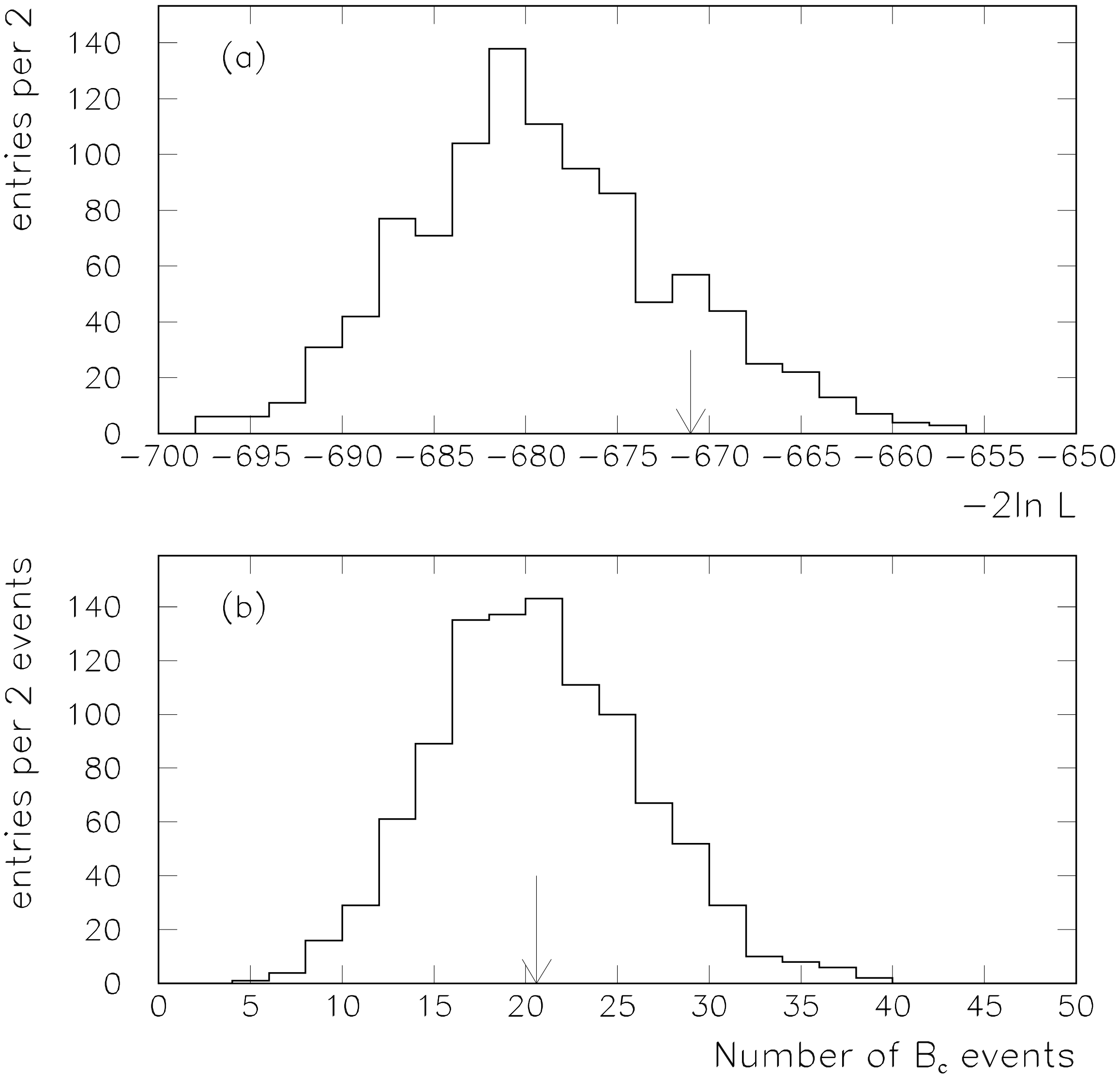

Figure 5.5: The results of pseudo-experiments for background plus B_c events. The arrow indicates the fit result for data. (a) $-2\ln\mathcal{L}$ distribution. (b) Fitted number of B_c events.

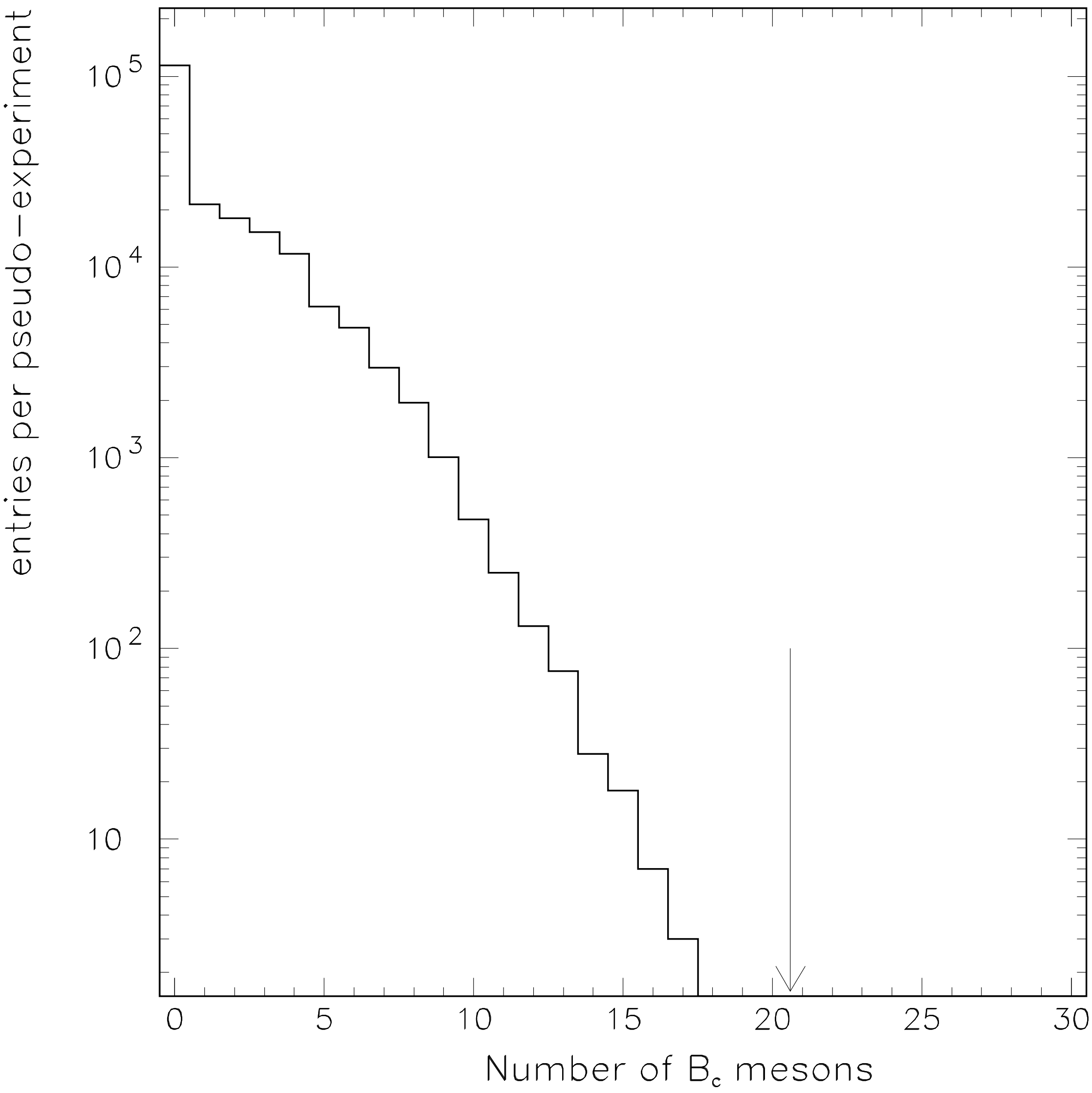

Figure 5.6: The number of B_c events for the pseudo-experiments for the null hypothesis. The arrow indicates the fit result for data.

Chapter 6

Measurement of the B_c Meson Lifetime

We have applied a decay length cut for $x > 60$ μm to search for the B_c signal. We have found a total of 31 candidates in the signal region $4 < m(J/\psi\ell) < 6$ GeV/c^2, 19 in the electron mode and 12 in the muon mode. We estimate a B_c signal of $20.4^{+6.2}_{-5.6}$ events using the mass shape fit, with an independent background estimate used as inputs. To measure the lifetime, we remove the above requirement on the decay length and find 74 candidates, 44 in the electron mode and 30 in the muon mode.

The theory predictions for the B_c lifetime lie in a rather wide range, between 0.40 ps and 1.44 ps as described in Section 1.3. The theoretical uncertainty on the B_c lifetime is larger than that on other B mesons.

CDF has measured the lifetimes of various b hadrons in semileptonic decays. In this Chapter, we will try to extract the B_c meson lifetime using the $B_c^+ \to J/\psi\ell^+X$ decay mode. To obtain the lifetime, we employ the procedure in Ref. [52].

6.1 Vertex and decay length

In the $B_c^+ \to J/\psi\ell^+\nu$, $J/\psi \to \mu^+\mu^-$ decay, three leptons (μ^+, μ^-, ℓ^+) come from a common secondary vertex, since the J/ψ decay occurs immediately. We reconstruct the vertex of the three leptons, where the $\mu^+\mu^-$ mass is constrained to the world average J/ψ mass. We require that all three tracks are reconstructed in SVX. The transverse decay length, measured between the primary vertex and the secondary vertex, is defined as

$$L_{xy} \equiv \frac{\left(\vec{V}_{SV} - \vec{V}_{PV}\right) \cdot \vec{p_T}\left(J/\psi\ell^+\right)}{p_T\left(J/\psi\ell^+\right)}, \tag{6.1}$$

where $\vec{V}_{SV}$ is the secondary vertex of three tracks and $\vec{p}_T\left(J/\psi\ell^+\right)$ is the transverse momentum vector of the $J/\psi\ell^+$ system. $\vec{V}_{PV}$ is the primary vertex and we use the average beam position. The vectors are two dimensional. The profile of the beam for a typical data acquisition run during Run Ib period is shown in Figure 6.1. The beam was roughly Gaussian and circular. The beam spot radius was roughly 35 μm in Run Ia and 25 μm in Run Ib.

The transverse decay length L_{xy} is related to the proper decay time t by the equation (with θ being the angle with respect to the beam line):

$$L_{xy} = ct\beta\gamma\sin\theta = ct\frac{p_T}{m}. \tag{6.2}$$

Then we define the proper decay length as

$$y \equiv L_{xy}\frac{m}{p_T} = ct. \tag{6.3}$$

This variable y should follow an exponential distribution $\exp(-\frac{y}{c\tau})$ defined for positive y, where τ is the lifetime. Due to the neutrino and other possible missing particles, we cannot fully reconstruct the semileptonic B_c decay. Therefore we use the mass and momentum of the J/ψ + lepton system to estimate the proper decay length of the B_c candidate. We define the "pseudo-proper decay length" x as follows:

$$\begin{aligned} x &\equiv L_{xy}\frac{m(J/\psi\ell^+)}{p_T(J/\psi\ell^+)} \\ &= y\frac{1}{K}, \end{aligned} \tag{6.4}$$

where K is a correction factor and is defined by

$$K = \frac{m(B_c^+)/p_T(B_c^+)}{m(J/\psi\ell^+)/p_T(J/\psi\ell^+)}. \tag{6.5}$$

As we shall see later, we construct a probability distribution function for the variable x, fit to a real data x distribution and extract the lifetime. The distribution of the variable K is derived using the same Monte Carlo calculation that is described in Section 3.4.1. The B_c mass is assumed to be 6.27 GeV/c^2. We apply the kinematic cuts (p_T cuts on dimuons from J/ψ and $p_T(e) > 2$ GeV/c or $p_T(\mu) > 3$ GeV/c) and a mass cut ($4 < m(J/\psi\ \ell) < 6$ GeV/c^2). Because the kinematic cuts are different for the electron and muon modes, we use different K distributions accordingly. Figure 6.2 shows the K distributions thus obtained. The K distribution has a mean value of 1.16 (1.18) with an r.m.s. width of 0.18 (0.17) for the electron (muon) mode.

We use only those events which satisfy

$$\begin{aligned} -0.05 \ <\ x \ <\ 0.15 \text{ cm}, \\ \sigma \ <\ 0.05 \text{ cm}, \end{aligned} \tag{6.6}$$

where σ is the estimated uncertainty in the pseudo-proper decay length x.

6.2 Background shape

In order to measure the B_c lifetime with our signal sample, we need to account for background events. We need to know their amount, and also their decay length distribution. We studied various backgrounds to $B_c^+ \to J/\psi\ \ell^+ X$ candidates. We will determine the proper decay length distributions of each background in this section.

6.2.1 Background shape for the electron mode

Fake electron background

The fake electron background shape is obtained from a J/ψ + track sample with $4 < m(J/\psi + \text{track}) < 6$ GeV/c^2. We apply the J/ψ selection cuts, the vertex cut (Prob(vertex fit χ^2) > 1%), and the fiducial cuts on the track with $p_T > 2$ GeV/c. In Section 4.1, we obtained the probability of hadron misidentification as a function of transverse momentum and isolation of the track. We apply the misidentification probability ("weights") to the J/ψ + track events to obtain the pseudo-proper decay length distribution for the fake electron background. The x distribution for the fake electron background thus obtained is shown in Figure 6.3 (a). The x distribution for unweighted J/ψ + track events is also shown for comparison. There is little difference between the weighted and unweighted distributions.

In order to obtain the background shape, we use a maximum likelihood method. We parameterize the fake background function with a sum of a Gaussian distribution centered at zero and two exponential functions on the positive and negative sides:

$$\begin{aligned}\mathcal{F}^e_{fake}(x) &= (1-f_+-f_-)G(x|s\sigma)\\ &+\frac{f_+}{\lambda_+}\theta(x)\exp\left(-\frac{x}{\lambda_+}\right)\otimes G(x|s\sigma)\\ &+\frac{f_-}{\lambda_-}\theta(-x)\exp\left(+\frac{x}{\lambda_-}\right)\otimes G(x|s\sigma),\end{aligned} \tag{6.7}$$

where $G(x|\sigma)$ is a Gaussian distribution with width σ, and an overall resolution scale factor s is introduced in order to account for a possible over- or under-estimate of the resolution. The symbol $\otimes$ denotes a convolution. The $\theta(x)$ is the step function defined as $\theta(x) = 1$ for $x \geq 0$ and $\theta(x) = 0$ for $x < 0$. The parameters $f_\pm$ are the fractions of the exponential functions, which are defined only for positive and negative x values, respectively.

The likelihood $\mathcal{L}^e_{fake}$ is written as

$$\mathcal{L}^e_{fake} = \prod_i^{J/\psi+track} \frac{\mathcal{F}_{fake}(x_i)}{W_i} N_{fake}, \tag{6.8}$$

where W_i is the fake rate, N_{fake} is a normalization factor of F_{fake}/W_i, $N_{fake} = 1/\sum W_i$. This normalization factor is needed to obtain the correct errors of the fitting parameters from $\mathcal{L}^e_{fake}$ [53]. We minimize twice the negative log-likelihood $-2\ln\mathcal{L}^e_{fake}$. The obtained background shape parameters are listed in Table 6.1, and the shape is shown in Figure 6.4(a).

Residual photon conversion background

In the data analysis, we have removed photon conversion electron candidates by looking for the conversion partner track which has small opening angle with the electron candidates. This conversion removal algorithm is not perfect because the partner can fail the CTC track reconstruction when its transverse momentum is small. Hence there exist residual conversion electrons in the signal sample.

	fake e background
s	1.39 ± 0.01
f_+	0.203 ± 0.004
λ_+	$328 \pm 8\ \mu$m
f_-	0.035 ± 0.003
λ_-	$94 \pm 7\ \mu$m

Table 6.1: Background shape parameters for fake e.

	residual conversion
s	1.410 ± 0.094
f_+	0.45 ± 0.02
λ_+	$382 \pm 28\ \mu$m
f_-	0.13 ± 0.02
λ_-	$115 \pm 16\ \mu$m

Table 6.2: Background shape parameters for residual conversion.

Using a Monte Carlo $J/\psi + \pi^0$ sample, we estimate the residual conversion background shape. This sample is also used to estimate the number of residual conversion backgrounds in Section 4.2. We require a $J/\psi \to \mu^+\mu^-$ candidate and an electron with p_T above 2 GeV/c. All three tracks should be reconstructed in SVX. Then we apply the photon conversion removal algorithm, just as in real data. Here we use those Monte Carlo events which have not been identified by the removal algorithm. The x distribution for J/ψ + residual conversions is shown in Figure 6.4 (b). We use the same parameterization as in the fakes. The obtained background shape parameters are listed in Table 6.2 and the shape is shown in Figure 6.4 (b).

$b\bar{b}$ background

When in a $b\bar{b}$ production, the b quark decays to $J/\psi X$ and the $\bar{b}$ quark to eX', there are a J/ψ and an electron in the final state as in the B_c semileptonic decay. The $J/\psi e$ mass of this background can fall into the signal region $4 < m(J/\psi e) < 6$ GeV/c^2. We obtain the decay length distribution for this $b\bar{b}$ background using Monte

	electron mode	muon mode
s	1.36 ± 0.20	1.21 ± 0.21
f_+	0.96 ± 0.01	0.98 ± 0.06
λ_+	$371 \pm 15\ \mu$m	$408 \pm 17\ \mu$m
λ_-	$37 \pm 15\ \mu$m	$35 \pm 17\ \mu$m

Table 6.3: $b\bar{b}$ background shape parameters.

Carlo events described in Section 4.3.

We reconstruct the vertex of three tracks, dimuons from the J/ψ decay and a track with $p_T > 2$ GeV/c that passes the fiducial cuts, where the J/ψ and the track come from different parent b. The pseudo-proper decay length distributions for the electron mode and for the muon mode are shown in Figures 6.5 (a) and (b), respectively. We parameterize the background distribution with two exponential functions on the positive and negative sides:

$$\begin{aligned} \mathcal{F}^e_{b\bar{b}}(x) &= \frac{f_+}{\lambda_+}\theta(x)\exp\left(-\frac{x}{\lambda_+}\right) \otimes G(x|s\sigma) \\ &+\frac{(1-f_+)}{\lambda_-}\theta(-x)\exp\left(+\frac{x}{\lambda_-}\right) \otimes G(x|s\sigma). \end{aligned} \tag{6.9}$$

We minimize $-2\ln\mathcal{L}^e_{b\bar{b}}$. The background shape parameters are listed in Table 6.3, and the fit result is shown in Figure 6.5.

Contribution from prompt J/ψ events

The background due to prompt J/ψ events is neglected in the mass fit, since we required the pseudo-proper decay length to be greater than 60 μm. We have to take account of this background in the lifetime measurement. We assume that the shape of this background is a Gaussian centered at zero:

$$\mathcal{F}^e_p(x) = \frac{1}{\sqrt{2\pi}s\sigma}\exp\left(-\frac{x^2}{2(s\sigma)^2}\right). \tag{6.10}$$

We incorporate the fraction of this background into the likelihood as an unconstrained parameter, since the amount is unknown.

	d-i-f background
s	1.434 ± 0.040
f_+	0.362 ± 0.011
λ_+	$354 \pm 15\ \mu$m
f_-	0.033 ± 0.007
λ_-	$94 \pm 15\ \mu$m

Table 6.4: Background shape parameters for decay in flight background.

6.2.2 Background shape for the muon mode

Decay-in-flight background

The muon background is dominated by pion and kaon decays in flight. For this background, we require a track pointing to the CMU/CMP fiducial region with $p_T >$ 3 GeV/c. The decay-in-flight background shape is obtained from J/ψ + track events in the same manner as obtained for the fake electron background. The p_T-dependent fake rate for decay-in-flight background is obtained in Ref. [50]. We multiply the decay rate to obtain the x distribution for this background. The weighted x distribution is shown in Figure 6.3 (b) together with the unweighted x distribution.

In order to obtain the background shape, we again employ a maximum likelihood method. We use the same parameterization as in the fake electron background,

$$\begin{aligned} \mathcal{F}^{\mu}_{d.i.f.}(x) &= (1 - f_+ - f_-)G(x|s\sigma) \\ &+ \frac{f_+}{\lambda_+}\theta(x)\exp\left(-\frac{x}{\lambda_+}\right) \otimes G(x|s\sigma) \\ &+ \frac{f_-}{\lambda_-}\theta(-x)\exp\left(+\frac{x}{\lambda_-}\right) \otimes G(x;s\sigma). \end{aligned} \tag{6.11}$$

The likelihood $\mathcal{L}^{\mu}_{dif}$ is written as

$$\mathcal{L}_{d.i.f.} = \prod_{i}^{J/\psi+track} \frac{\mathcal{F}_{d.i.f.}(x_i)}{W_i} N_{dif}, \tag{6.12}$$

where W_i is the fake rate for the muon. We minimize $-2\ln\mathcal{L}_{d.i.f.}$. The background shape parameters are listed in Table 6.4, and the fit result is shown in Figure 6.4(c).

Punch-through background

When a particle (π^+ or K^+) traverses the calorimeter and the CMP steel without interacting and forms a displaced vertex with a J/ψ, this event can appear in the J/ψ + μ signal sample. The fraction of the punch-through background is estimated to be about 10% of the total J/ψ + muon background in Ref. [50]. The pseudo-proper decay length distribution for the punch-through background is obtained in the same way as for the decay-in-flight background. For the punch-through background, the x distribution is identical to that for the decay-in-flight background. Therefore, we use the same parameterization as for the decay-in-flight background.

$b\bar{b}$ background

The $b\bar{b}$ background shape is obtained from a Monte Carlo simulation as in Section 6.1.3. The only difference is the p_T cut on the track. The background shape parameters are listed in Table 6.3, and the fit result is shown in Figure 6.5 (b).

Contribution from prompt J/ψ events

For the muon mode also, we assume that the shape of this background is a Gaussian. The fraction of this background is incorporated into the likelihood as an unconstrained parameter.

6.3 Lifetime fit

We use a maximum likelihood method to extract the lifetime. The probability distribution of the signal is given by an exponential function smeared with both the decay length resolution and the K distribution:

$$\mathcal{F}_{sig}(x) = \int dK\, H(K)\, \frac{K}{c\tau} \left[\theta(x) \exp\left(-\frac{Kx}{c\tau}\right) \otimes G(x|s\sigma)\right] \tag{6.13}$$

where σ is an estimated uncertainty in x, $G(x|\sigma)$ is a Gaussian with width σ, and s is an overall resolution scale factor to account for under- or over-estimate of the resolution. For the electron (muon) mode, the scale of $s = 1.39$ ($s = 1.43$) is used, as determined

	input	fit result
N(B_c)	$\cdots$	$19.0^{+5.8}_{-5.1}$
$\mathrm{N}_{fake\ e}$	2.6 ± 0.3	2.6 ± 0.3
$\mathrm{N}_{res.}$	1.2 ± 0.9	1.4 ± 0.9
$\mathrm{N}_{b\bar{b}}$(e)	1.2 ± 0.5	1.2 ± 0.5
$\mathrm{N}_{d.i.f.+P.T.}$	6.4 ± 1.4	5.2 ± 1.4
$\mathrm{N}_{b\bar{b}}(\mu)$	0.7 ± 0.3	0.7 ± 0.3

Table 6.5: The inputs and fit results in the mass fit for $x > 60$ μm. These numerical values are for the mass region $4 < m(J/\psi\ell) < 6$ GeV/c^2.

in the fake electron (decay-in-flight) background. $H(K)$ is a K distribution to correct for the missing momentum. The integration over K in Eq. (6.13) is in practice replaced with a finite sum:

$$\int dK H(K) \ \rightarrow \ \sum_i H(K_i), \tag{6.14}$$

where the K distribution $H(K_i)$ is provided as a normalized histogram with 25 bins in the range from 0.0 to 2.0, as shown in Figure 6.2.

In Section 5.3.2, we estimated the number of signal events and all backgrounds ($x > 60$ μm) using the $J/\psi\ell$ mass fit in the mass range $3.35 < m(J/\psi\ell) < 11$ GeV/c^2. The numerical values from the mass fit in the mass range $4 < m(J/\psi\ell) < 6$ GeV/c^2 are listed in Table 6.5.

Each background shape is determined in Section 6.2. Once we get the background shape, we can calculate the number of background events for $x < 60$ μm and the background fractions for the entire x region. The estimated number of background events for the entire x region is listed in Table 6.6 as well as the background fractions. These fractions are Gaussian constrained in the lifetime fit:

$$G(f|\langle f\rangle, \Delta f) = \frac{1}{\sqrt{2\pi}\Delta f} \exp\left(-\frac{1}{2}\left(\frac{f-\langle f\rangle}{\Delta f}\right)^2\right), \tag{6.15}$$

where $\langle f\rangle$ is a background fraction for input in the lifetime fit and Δf is its uncertainty.

The likelihood for the electron mode is defined as

$$\mathcal{L}^e = G(f_{fake})G(f_{res})G(f^e_{b\bar{b}}) \prod_i^{J/\psi+e} [(1 - f_{fake} - f_{res} - f^e_{b\bar{b}} - f^e_p)\mathcal{F}^e_{sig}(x_i)$$

	number of bkg.	fraction ($\langle f \rangle$)
fake e background	11.6 ± 1.2	0.27 ± 0.03
residual conversion background	3.9 ± 2.1	0.09 ± 0.05
$b\bar{b}$ background for e	1.29 ± 0.43	0.03 ± 0.01
decay-in-flight and punch-through background	14.7 ± 3.6	0.49 ± 0.12
$b\bar{b}$ background for μ	0.6 ± 0.3	0.02 ± 0.01

Table 6.6: Number of backgrounds and background fractions for the entire x region.

$$+f_{fake}\mathcal{F}_{fake}(x_i) + f_{res}\mathcal{F}_{res}(x_i) + f^e_{b\bar{b}}\mathcal{F}^e_{b\bar{b}}(x_i) + f^e_p\mathcal{F}^e_p(x_i)]. \tag{6.16}$$

The likelihood for the muon mode is defined as

$$\begin{aligned}\mathcal{L}^{\mu} = G(f_{dif})G(f^{\mu}_{b\bar{b}}) \prod_i^{J/\psi+\mu} [(1 - f_{dif} - f^{\mu}_{b\bar{b}} - f^{\mu}_p)\mathcal{F}^{\mu}_{sig}(x_i) \\ +f_{dif}\mathcal{F}_{dif}(x_i) + f^{\mu}_{b\bar{b}}\mathcal{F}^{\mu}_{b\bar{b}}(x_i) + f^{\mu}_p\mathcal{F}^{\mu}_p(x_i)].\end{aligned} \tag{6.17}$$

For the lifetime fit, we fix the parameters for the background shape. Therefore there are eight parameters in the lifetime fit. The lifetime $c\tau$ and two background fractions to account for the prompt component are the unconstrained parameters, while the five background fractions for the other backgrounds are Gaussian constrained. First, we minimize the individual $-2\ln\mathcal{L}^{\ell}$. We find $c\tau = 149.3\,^{+79.8}_{-62.5}$ μm for the electron mode and $c\tau = 191.1\,^{+118.2}_{-98.8}$ μm for the muon mode. The decay length distributions and the individual fit results are shown in Figure 6.6.

We then combine the electron and muon modes, and fit the signal distribution simultaneously. The combined likelihood is written as

$$\mathcal{L}^{comb} = \mathcal{L}^e\mathcal{L}^{\mu}. \tag{6.18}$$

The fit results are listed in Table 6.7, and the lifetime $c\tau$ is $164.3\,^{+64.3}_{-56.2}$ μm. The simultaneous fit results are shown in Figures 6.7 and 6.8. We also scan $-2\ln\mathcal{L}^{comb}$ from $c\tau(B_c^+) = 10$ μm to 500 μm. The result is shown in Figure 6.9.

6.4 Systematic uncertainties

In this section, we evaluate systematic uncertainties in the lifetime determination.

$c\tau$ (μm)	$164.3\,^{+64.3}_{-56.2}$
f_{fake}	0.27 ± 0.03
f_{res}	0.11 ± 0.05
$f^{e}_{b\bar{b}}$	0.03 ± 0.01
f^{e}_{p}	0.18 ± 0.12
f_{dif}	0.53 ± 0.11
$f^{\mu}_{b\bar{b}}$	0.02 ± 0.01
f^{μ}_{p}	0.06 ± 0.14

Table 6.7: Results of the lifetime fit.

6.4.1 Fitting procedure bias

The fitting procedure is tested by a simple Monte Carlo exercise. We generate one hundred samples each containing a mixture of signal and background events. Each sample consists of 74 events, 44 events of $J/\psi + e$ and 30 events of $J/\psi + \mu$ candidates. The number of each background is allowed to fluctuate according to the Poisson statistics, where the mean value of each background is set to the value determined from the B_c mass fit (Table 6.6). The decay length of the B_c signal is generated according to the lifetime of 165 μm. They are smeared with the K distribution and with the decay length resolution. The decay length of the background events is generated according to each probability density function, where the parameters are fixed to those determined earlier. The distributions of the fitted lifetime, its uncertainty and $-2\ln\mathcal{L}$ are shown in Figure 6.10. The mean of the fitted lifetime agrees with the input lifetime of 165 μm, and it is consistent with no bias. Since the statistical uncertainty on the mean of the fitted lifetime distribution (Figure 6.10 (b)) is 5.3 μm, we conservatively assign $\pm$ 5.3 μm as a systematic uncertainty due to the fitting bias.

6.4.2 Momentum correction

Since the semileptonic decays are used in this lifetime measurement, we can not fully reconstruct the B_c meson momentum and mass for each event. To correct for the missing momentum, we have used K distributions which are derived from a Monte Carlo calculation. This distribution is affected by both the production and the decay kinematics of the B_c meson.

Production spectrum

The b quark p_T spectrum is not exactly known, and different spectra give different K distributions. In Figure 6.11, the p_T distribution of the $J/\psi + \ell$ candidates is shown. We have used the p_T spectrum of Ref. [11] to generate the B_c Monte Carlo events. Although the data seems to agree with theory, it is very hard to quantitatively check the consistency between data and theory, because of the limited statistics. On the other hand, a lot of CDF measurements indicate that the b quark p_T spectrum is steeper than that of the theory. The b quark p_T spectra with different structure functions are shown in Figure 6.12, where the b quark p_T spectra are calculated to the next-to-leading order, with $m_b = 4.75$ GeV and renormalization scale $\mu_0 = \sqrt{m_b^2 + p_T(b)^2}$. The spectrum with CTEQ4M [54] is steeper than those with older structure functions (MRSD_0 [48] and CTEQ3M [16]). Using this CTEQ4M spectrum, b quarks are generated and are fragmented into B_c mesons according to the the fragmentation function given in Ref. [15]. We then obtain a new K distribution from this Monte Carlo sample. The new distribution is shown in Figure 6.13 (a). Then we refit the signal sample with the new K distribution. The obtained lifetime is $166.3^{+64.9}_{-56.6}$ μm. Therefore we assign $\pm$ 1.9 μm as a systematic uncertainty due to this source.

Mass of the B_c meson

We have assumed the mass of the B_c meson to be 6.27 GeV/c^2. The mass of B_c meson is theoretically predicted to be between 6.2 and 6.3 GeV/c^2. Therefore, we conservatively shift the B_c meson mass by $\pm$ 150 MeV/c^2 and derive new K distributions. The distributions are shown in Figures 6.13 (b). Then we refit the signal sample and obtain $162.4^{+63.4}_{-55.4}$ μm for -150 MeV/c^2 and $162.3^{+63.5}_{-55.2}$ μm for $+150$ MeV/c^2. We assign the maximum difference, ± 2.1 μm, as a systematic uncertainty due to this source.

	$\Gamma_{c\bar{c}}/\Gamma_{J/\psi}$	$\mathcal{B}((c\bar{c}) \to J/\psi X)$	$\Gamma_{c\bar{c}}/\Gamma_{J/\psi} \times \mathcal{B}((c\bar{c}) \to J/\psi X)$
$B_c^+ \to \chi_{c2}(1P)\ell^+\nu$	0.076	13.5 $\pm$ 1.1 %	0.0050
$B_c^+ \to h_c\ell^+\nu$	0.13	1.5 to 2.6%	0.0020 to 0.0034
$B_c^+ \to \chi_{c1}(1P)\ell^+\nu$	0.051	27.3 $\pm$ 1.8 %	0.0034
$B_c^+ \to \chi_{c0}(1P)\ell^+\nu$	0.025	6.6 $\pm$ 1.8 %	0.0017
$B_c^+ \to \psi(2S)\ell^+\nu$	0.18	57.0 $\pm$ 4.0 %	0.11

Table 6.8: Relative branching ratio expected by the ISGW model. $\Gamma_{c\bar{c}}/\Gamma_{J/\psi}$ is a ratio of $\Gamma(B_c^+ \to (c\bar{c})\ell^+\nu)$ to $\Gamma(B_c^+ \to J/\psi\ell^+\nu)$. For the $(c\bar{c}) \to J/\psi X$ decays, we obtain the branching ratio from Ref. [25]. For the $h_c \to J/\psi X$ decay, the branching ratio is predicted in Ref. [55]. $\mathcal{B}(h_c \to J/\psi\pi^0) = 0.5\%$ and $\mathcal{B}(h_c \to J/\psi\pi\pi)$=1.0% $\sim$ 2.1%.

Higher mass $c\bar{c}$ states

The B_c meson can decay to a $\ell^+\nu$ pair and a higher mass $c\bar{c}$ state, which in turn can decay to $J/\psi X$. A pair of J/ψ and ℓ^+ appears in the final states and this pair might be included in the signal $J/\psi\ell^+$ events. The $J/\psi\ell^+$ events coming from these higher mass $c\bar{c}$ states would have different K distributions than the $B_c \to J/\psi\ell^+\nu$ events. In Table 6.8, estimates on the relative branching ratios of $B_c^+ \to (c\bar{c})\ell^+\nu$ to $B_c^+ \to J/\psi\ell^+\nu$ are shown. These are predicted by the ISGW model [27].

The largest contribution comes from the decay $B_c^+ \to \psi(2S)\ell^+\nu$, which could add 11% to the $B_c^+ \to J/\psi\ell^+\nu$ mode. At the same time, $\psi(2S)$ is the heaviest $c\bar{c}$ meson in Table 6.8, and consequently, the K distribution for the $B_c^+ \to \psi(2S)\ell^+\nu X$ decay will be most different. We generate $B_c^+ \to \psi(2S)\ell^+\nu$, $\psi(2S) \to J/\psi X$ events and obtain a K distribution. This distribution is shown in Figure 6.13 (c). We refit the signal sample using this K distribution and find $c\tau = 161.9^{+62.5}_{-55.0}$ μm. The difference of ± 2.4 μm from the standard fit is conservatively assigned as a systematic uncertainty.

Decay model

For Monte Carlo events of the signal B_c meson decay, the B_c meson decays with a $V - A$ matrix element. Here we use a matrix element calculated by the ISGW model [27]. We generate $B_c^+ \to J/\psi\ell^+\nu$ events with this matrix element and obtain a new K distribution. This distribution is shown in Figure 6.13 (d). We refit the

	fitted $c\tau$ (μm)
λ_+ $+1\sigma$	$163.2^{+61.6}_{-52.3}$
λ_+ -1σ	$169.4^{+52.3}_{-65.5}$
λ_- $+1\sigma$	$164.5^{+64.3}_{-56.2}$
λ_- -1σ	$163.9^{+64.4}_{-56.3}$

Table 6.9: Lifetimes when the background shape is changed.

signal with this K distribution and obtain $168.6^{+66.7}_{-58.0}$ μm. Then we assign ± 4.3 μm as a systematic uncertainty due to the decay mode.

Trigger simulation

To test the effect of the level 2 trigger, we turn off the trigger simulation. But we apply the kinematical cuts and get a new K distribution. The lifetime with this K distribution differs by 1 μm. Then we assign ± 1 μm as a systematic uncertainty due to possible incompleteness in the trigger simulation.

6.4.3 Background shape

We have measured the decay length distribution of various backgrounds using the J/ψ + track and Monte Carlo samples. These samples have finite statistics, and the measured shapes are subject to statistical uncertainty. In order to estimate the effect on the lifetime, we shift λ_+ by $\pm 1\sigma$, where σ is the statistical uncertainty on the parameter determined from the fits (Tables 6.1, 6.2, 6.3 and 6.4). Since there are correlations between this parameter and others, we refit each background sample with the parameter λ_+ fixed to a new value but with all others floated. From this fit, we obtain a new background shape and refit the signal sample for the lifetime. The result is listed in Table 6.9. We also change λ_- by $\pm 1\sigma$ and obtain new background shapes in the same way. The result is shown in Table 6.9 as well and we assign ± 5.1 μm, which is the largest shift from the standard fit, as an uncertainty.

We assumed one exponential tail for the background shape and parameterized the background decay length distributions. Since this parameterization may not perfectly

	fake e	residual conv.	d.i.f.
s	1.31 ± 0.01	1.25 ± 0.09	1.35 ± 0.04
f_+	0.20 ± 0.07	0.32 ± 0.04	0.31 ± 0.03
λ_+ (μm)	409 ± 17	575 ± 96	425 ± 40
f'_+	0.10 ± 0.07	0.26 ± 0.04	0.11 ± 0.01
λ'_+ (μm)	48 ± 23	74 ± 18	80 ± 37
f_-	0.04 ± 0.003	0.15 ± 0.03	0.04 ± 0.009
λ_- (μm)	101 ± 12	117 ± 20	85 ± 14

Table 6.10: Background shape parameters for the fake e, residual conversion, and decay-in-flight backgrounds with 2 exponential tails.

describe the background shape, we consider another background parameterization, by adding a second exponential tail on the positive side. We fit the decay length distributions for the fake e, the residual conversion and the decay-in-flight backgrounds, with two positive exponential tails. The obtained parameters are listed in Table 6.10 and the fit results are shown in Figure 6.14. For the $b\bar{b}$ background shape, we use a parameterization of one exponential tail. We refit the signal sample using these new background parameterizations and find a lifetime of $181.7^{+65.9}_{-54.1}$ μm. The lifetime is shifted by ± 17.4 μm from the standard fit.

Adding the above two uncertainties in quadrature, we assign ± 18.1 μm as a systematic uncertainty.

6.4.4 Background fraction

The background fractions f are determined by the $J/\psi\ell$ mass fit for the pseudo-proper decay length above 60 μm. It is subject to some uncertainty. So we change the background fractions by $\pm 1\sigma$. We change the fractions of all background sources simultaneously by the same amount. We then refit the pseudo-proper decay length distribution, where the background fractions are fixed. We obtain a lifetime of $168.7^{+87.2}_{-65.3}$ μm for $+1\sigma$ and $150.5^{+43.5}_{-39.1}$ μm for -1σ. Then the uncertainty of ± 13.8 μm is assigned. This is probably an overestimate, but we choose to be conservative.

6.4.5 Decay length resolution

The resolution scale factor s of the vertex determination is obtained from the fake background fit for each mode (Table 6.1 and Table 6.4). We change this factor to 1.0 and 1.8, fix it and refit the background shape. Then we fit the pseudo-proper decay length distribution of the signal sample using the same scale factor and obtain a lifetime of $176.7^{+74.0}_{-63.0}$ μm for s=1.8 and $150.5^{+56.7}_{-50.0}$ μm for s=1.0. The lifetime shift of ± 13.8 μm is assigned as a systematic uncertainty.

6.4.6 Prompt J/ψ events

To estimate systematic uncertainty due to the prompt J/ψ background, we preform the lifetime fit without the prompt component. We remove the prompt component from the likelihood and fit the pseudo-proper decay length distribution, where only $c\tau$ is unconstrained parameter while the five background fractions are Gaussian constrained. We obtain $c\tau = 122.4^{+48.2}_{-42.5}$ μm and show the fit result in Figure 6.15. The difference between this fit and the standard fit is 41.9 μm. Assuming that the probability for this background is uniform between zero and twice the fitted value, we multiply 41.9 μm by a factor of $\frac{2}{\sqrt{12}}$. We assign 24.2 μm as a systematic uncertainty.

6.4.7 Detector alignment

For this source we borrow the result used in the B-hadron lifetime analysis using the $B \rightarrow J/\psi X$ mode. From Ref. [56], we assign ± 2.0 μm.

6.4.8 Total uncertainty

We add all the contributions in quadrature and obtain a total systematic uncertainty of ± 36.8 μm. A summary is given in Table 6.11.

Source	uncertainty (μm)
Fitting procedure	± 5.3
Momentum correction	
Production spectrum	± 1.9
B_c mass	± 2.1
Higher $c\bar{c}$ states	± 2.4
Decay model	± 4.3
Trigger simulation	± 1.0
Background shape	± 18.1
Background fraction	± 13.8
Prompt J/ψ background	± 24.2
Decay length resolution	± 13.8
Detector alignment	± 2.0
Total	± 36.8

Table 6.11: A summary of systemic uncertainties in the B_c lifetime measurement.

6.5 Summary

We have measured the B_c meson lifetime using the semileptonic decay $B_c^+ \to J/\psi \ell^+ X$. The lifetime is

$$c\tau = 164 \ ^{+64}_{-56} \ \pm 37 \ \mu\text{m}, \tag{6.19}$$

or

$$\tau = 0.55 \ ^{+0.21}_{-0.19} \ \pm 0.12 \ \text{ps}, \tag{6.20}$$

where the first uncertainty is statistical and the second is systematic.

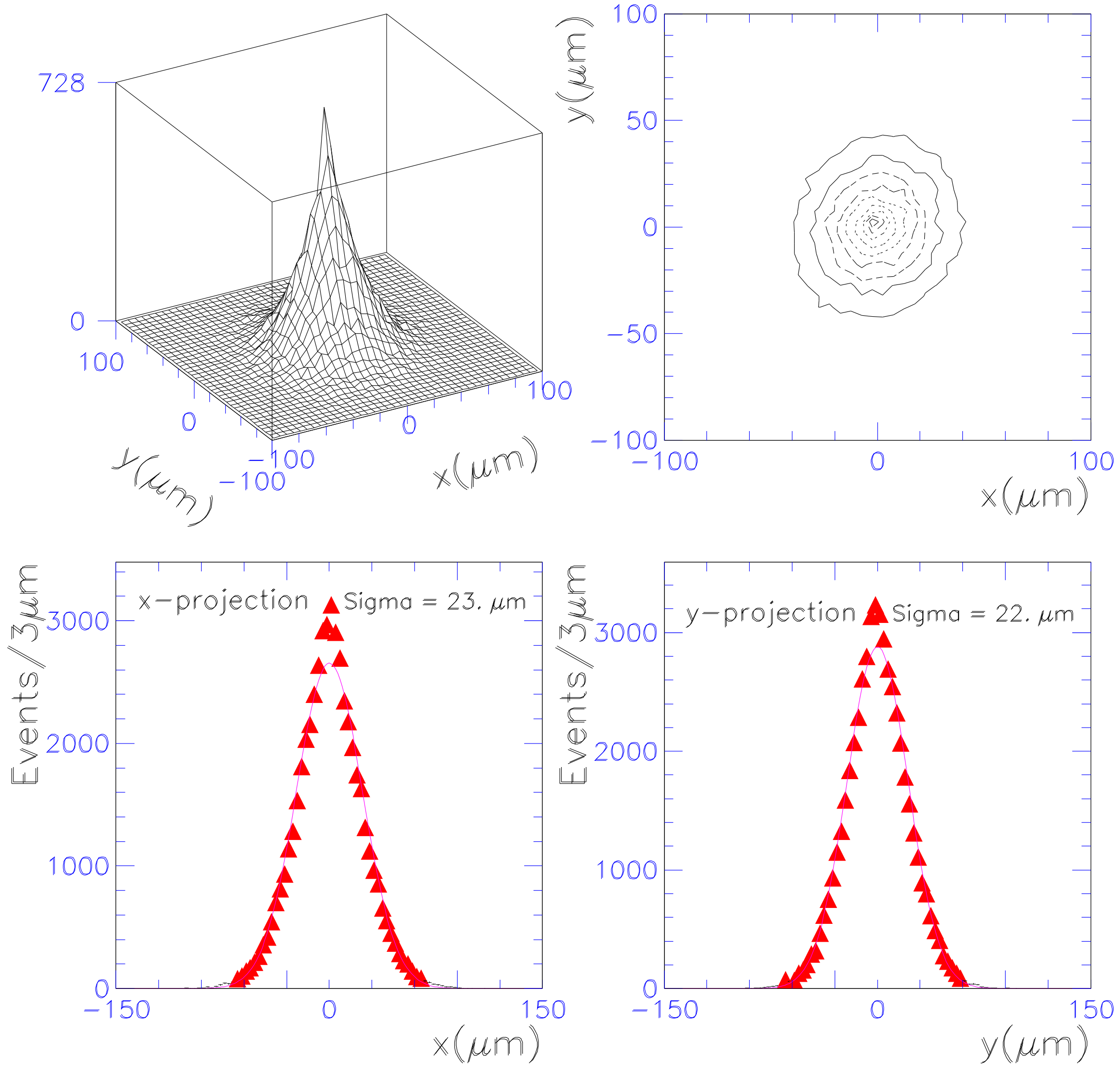

Figure 6.1: The two-dimensional beam profile for a typical data aquisition run during Run Ib is shown in the upper two plots. The x and y projections are shown in the lower two plots.

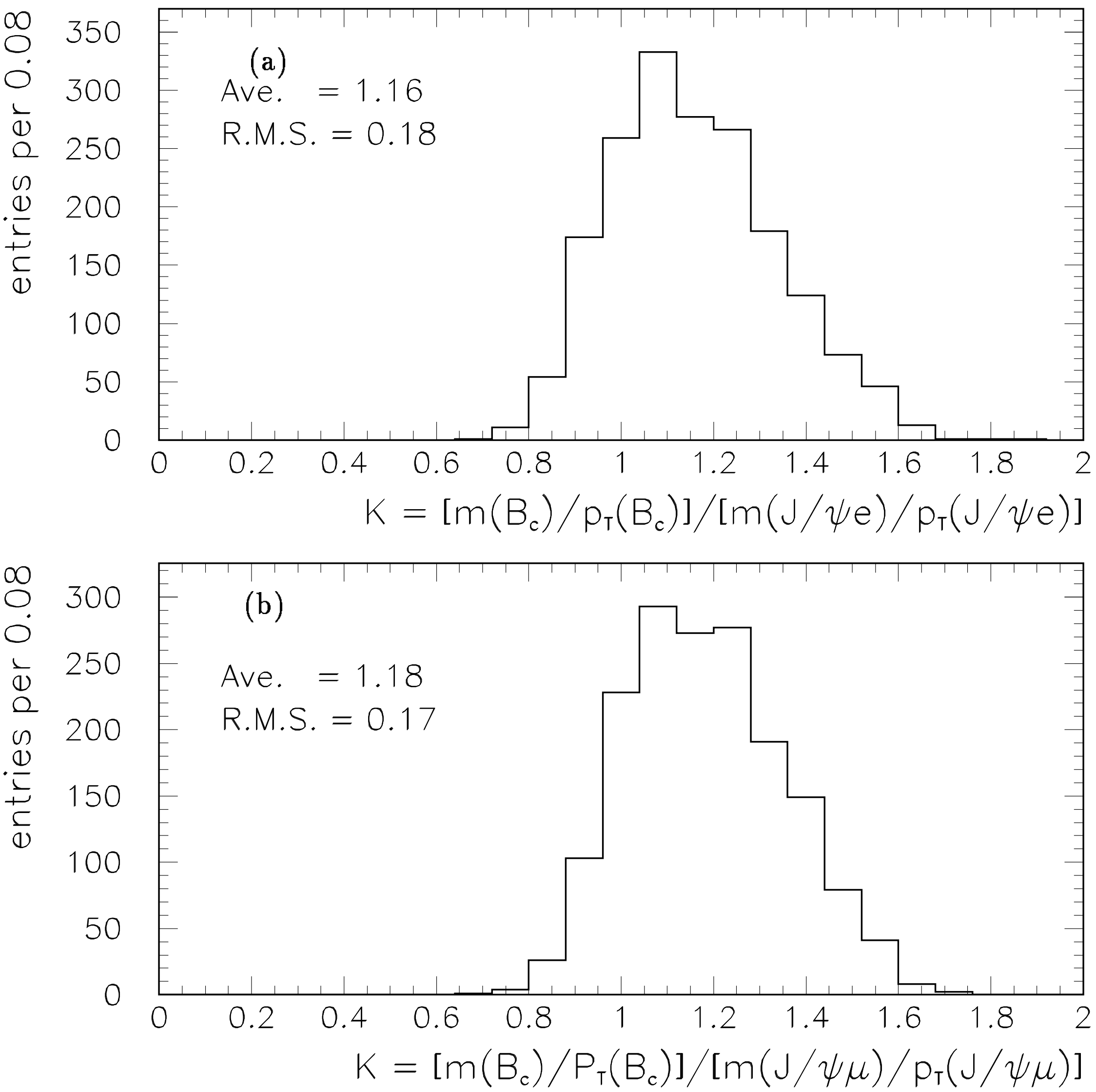

Figure 6.2: $K = [m(B_c)/p_T(B_c)]/[m(J/\psi\ell)/p_T(J/\psi\ell)]$ distributions using Monte Carlo, (a) for the electron channel and (b) for the muon channel.

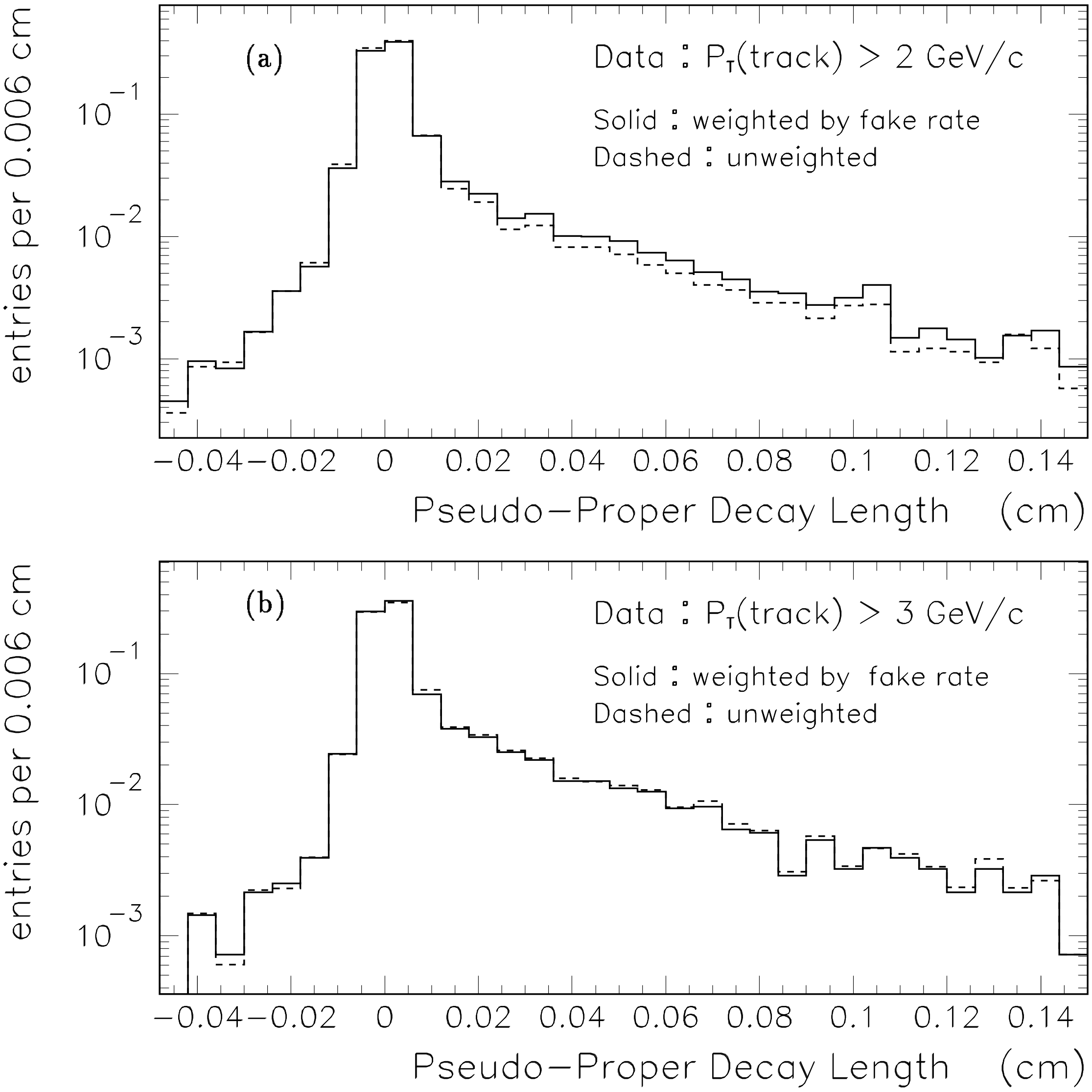

Figure 6.3: Pseudo-proper decay length distributions for J/ψ+ track events. The distributions are normalized to unit area. (a) track passing the fiducial cuts and $p_T >$ 2 GeV/c. (b) track pointing to CMU/CMP region and $p_T >$ 3 GeV/c.

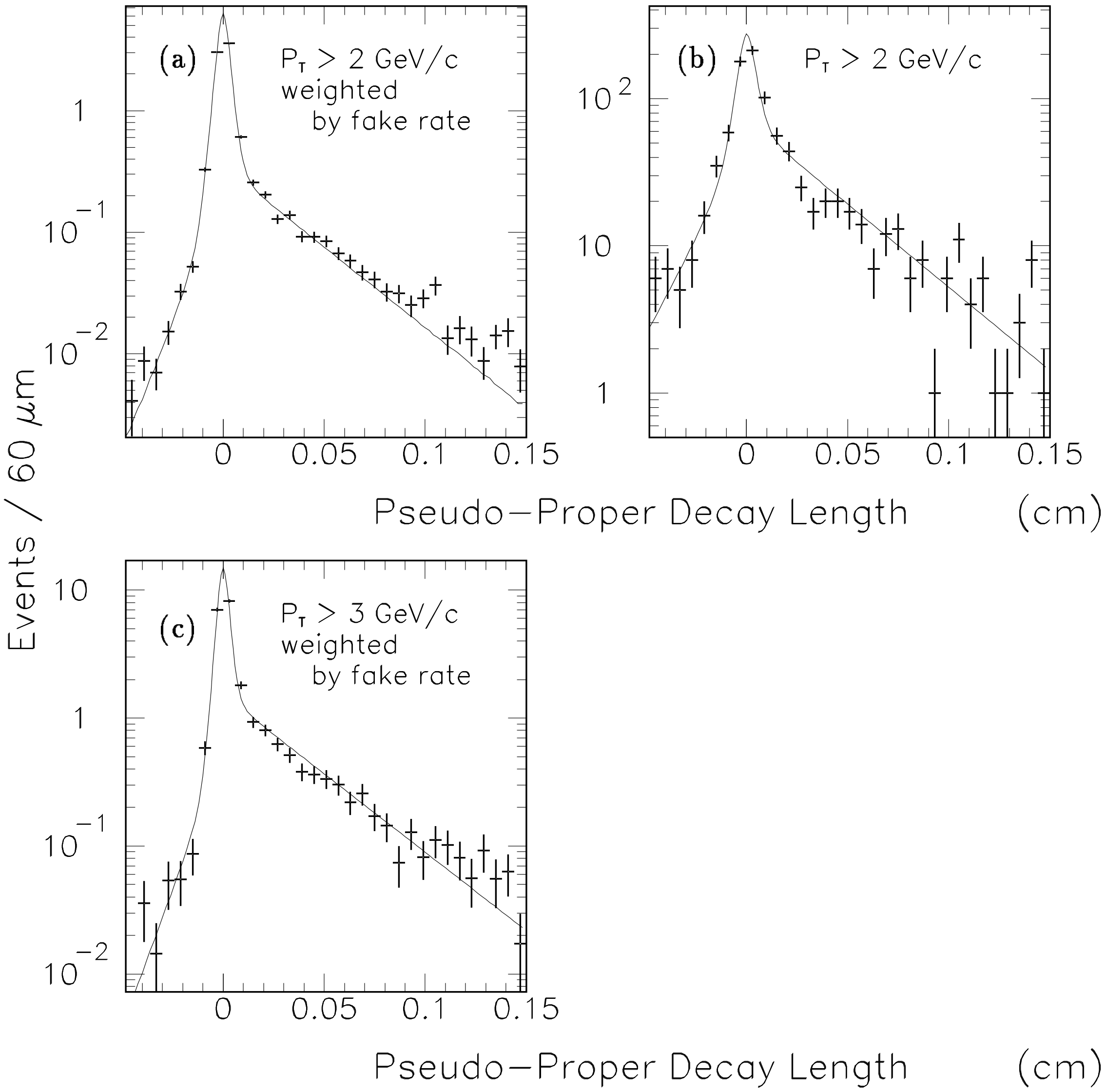

Figure 6.4: Pseudo-proper decay length distributions for J/ψ + track with the fitted curve: (a) Fake electron background. Weighted by fake rate. (b) Residual conversion background using Monte Carlo. (c) False muon (Decay-in-Flight) background. Weighted by fake rate.

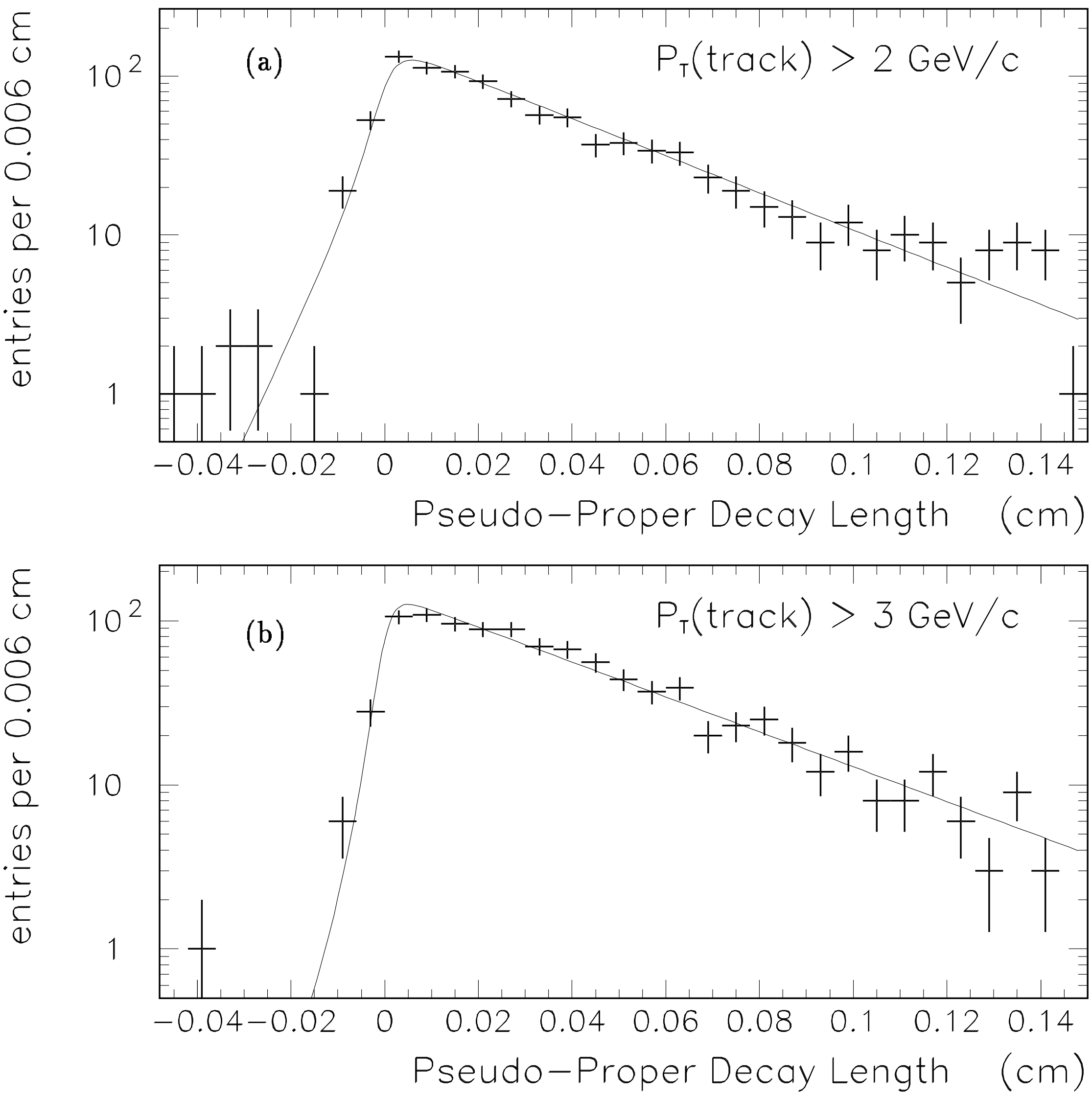

Figure 6.5: Pseudo-proper decay length distributions for $b\bar{b}$ events. (a) for the electron mode. (b) for the muon mode.

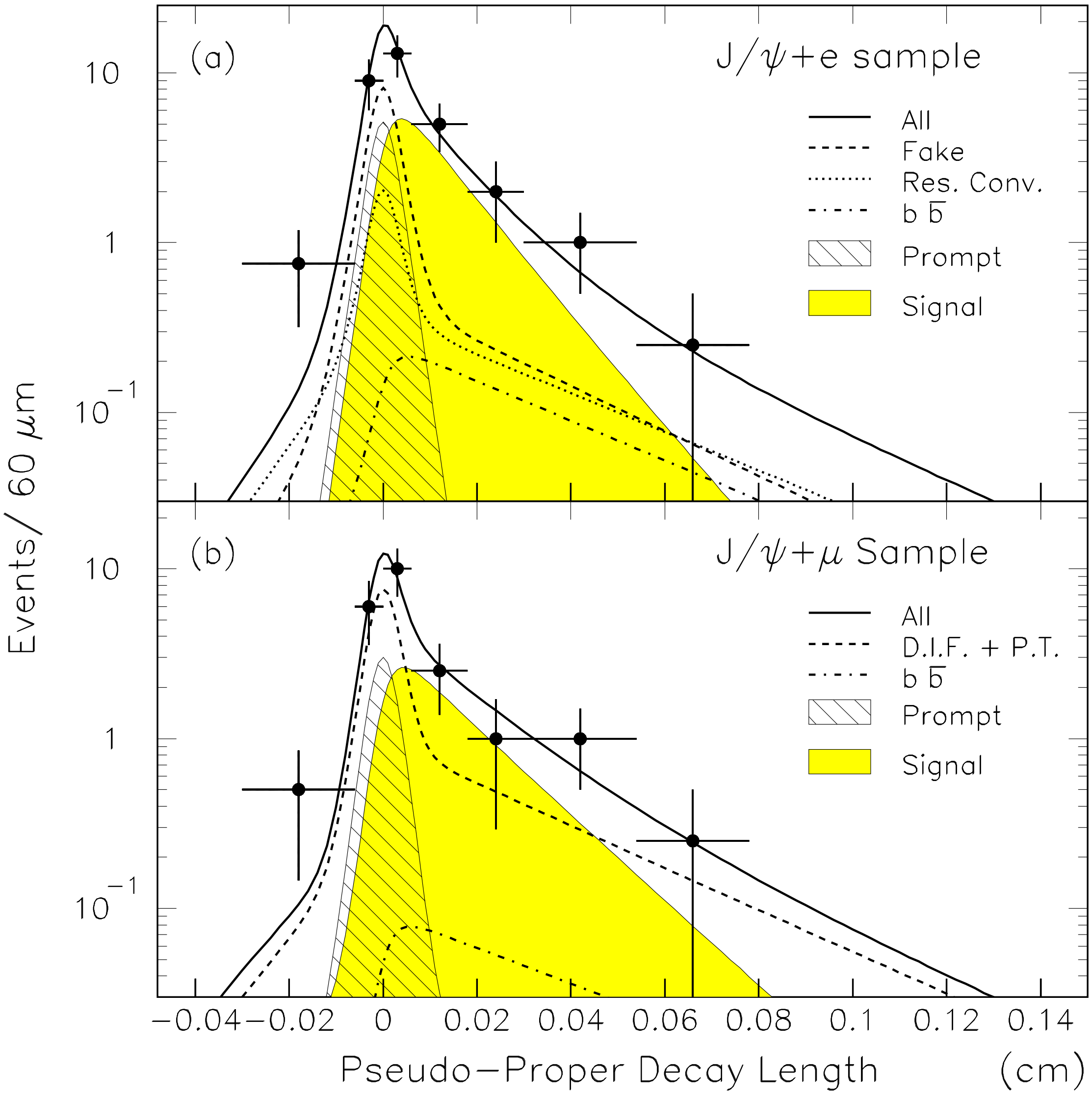

Figure 6.6: Pseudo-proper decay length distributions for data and fit results from the individual fit. (a) the electron channel. (b) the muon channel.

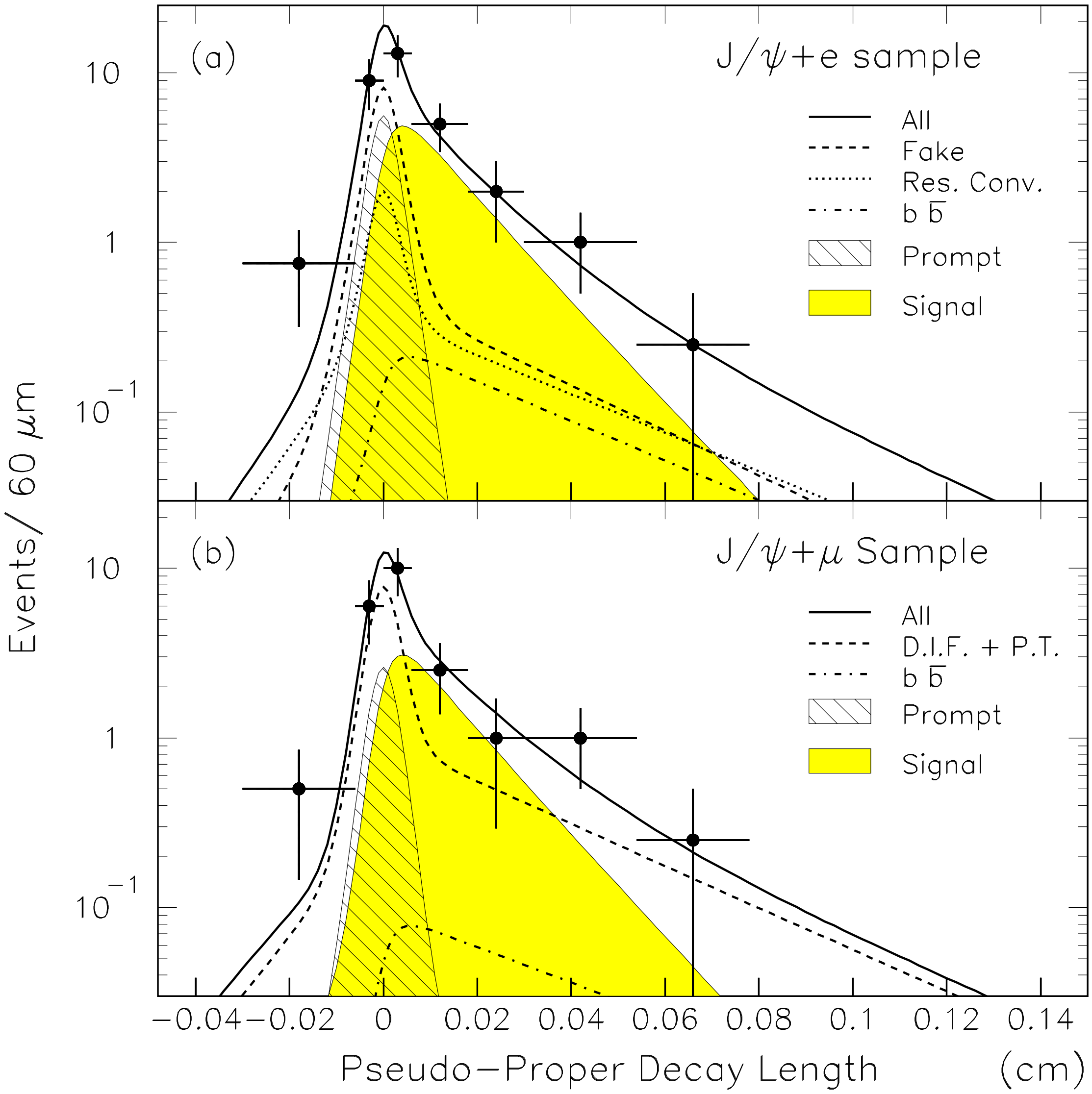

Figure 6.7: Pseudo-proper decay length distributions for data and fit results from the simultaneous fit. (a) the electron channel. (b) the muon channel.

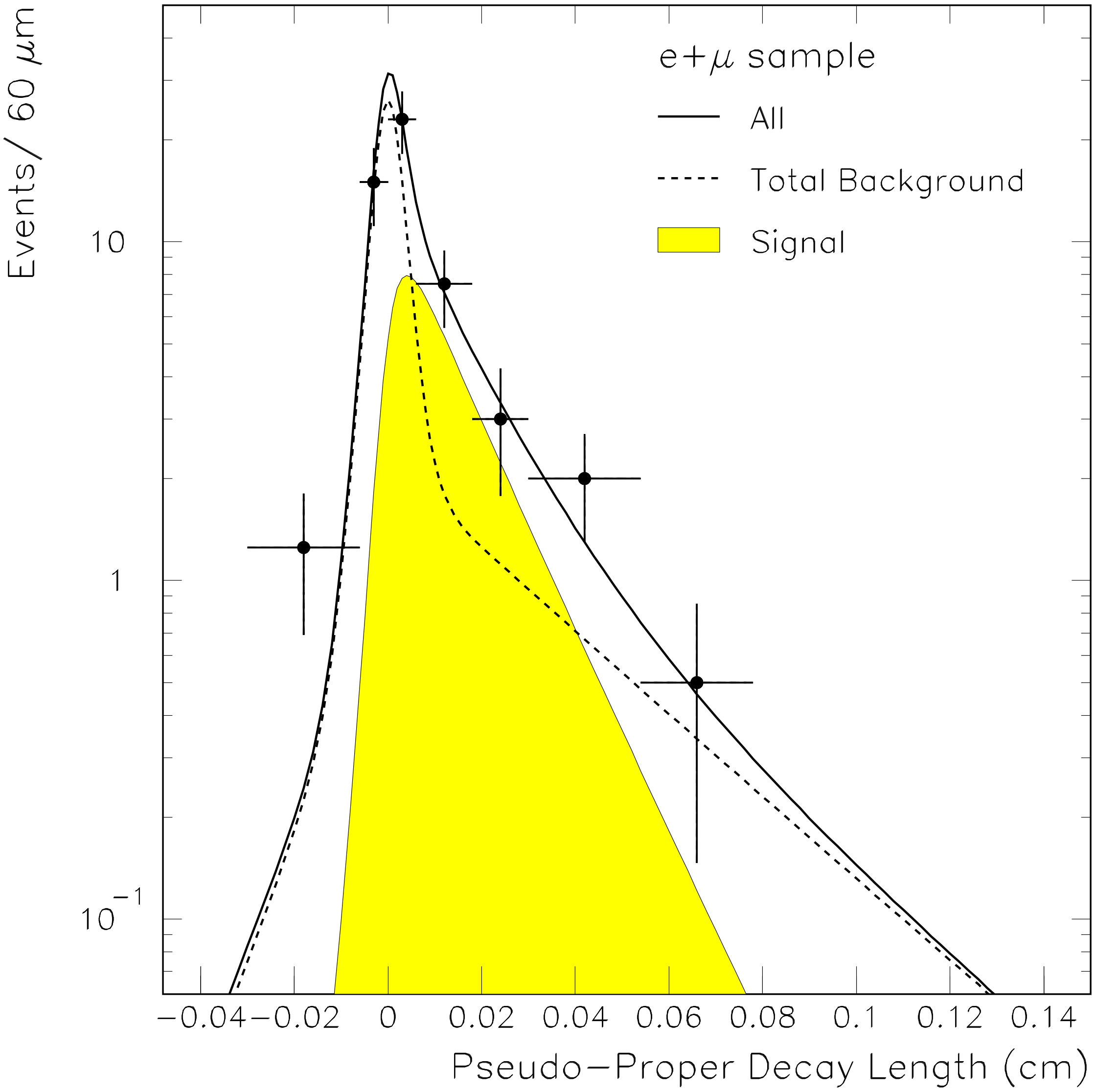

Figure 6.8: Pseudo-proper decay length distribution for the combined $e + \mu$ sample and fit results from the simultaneous fit.

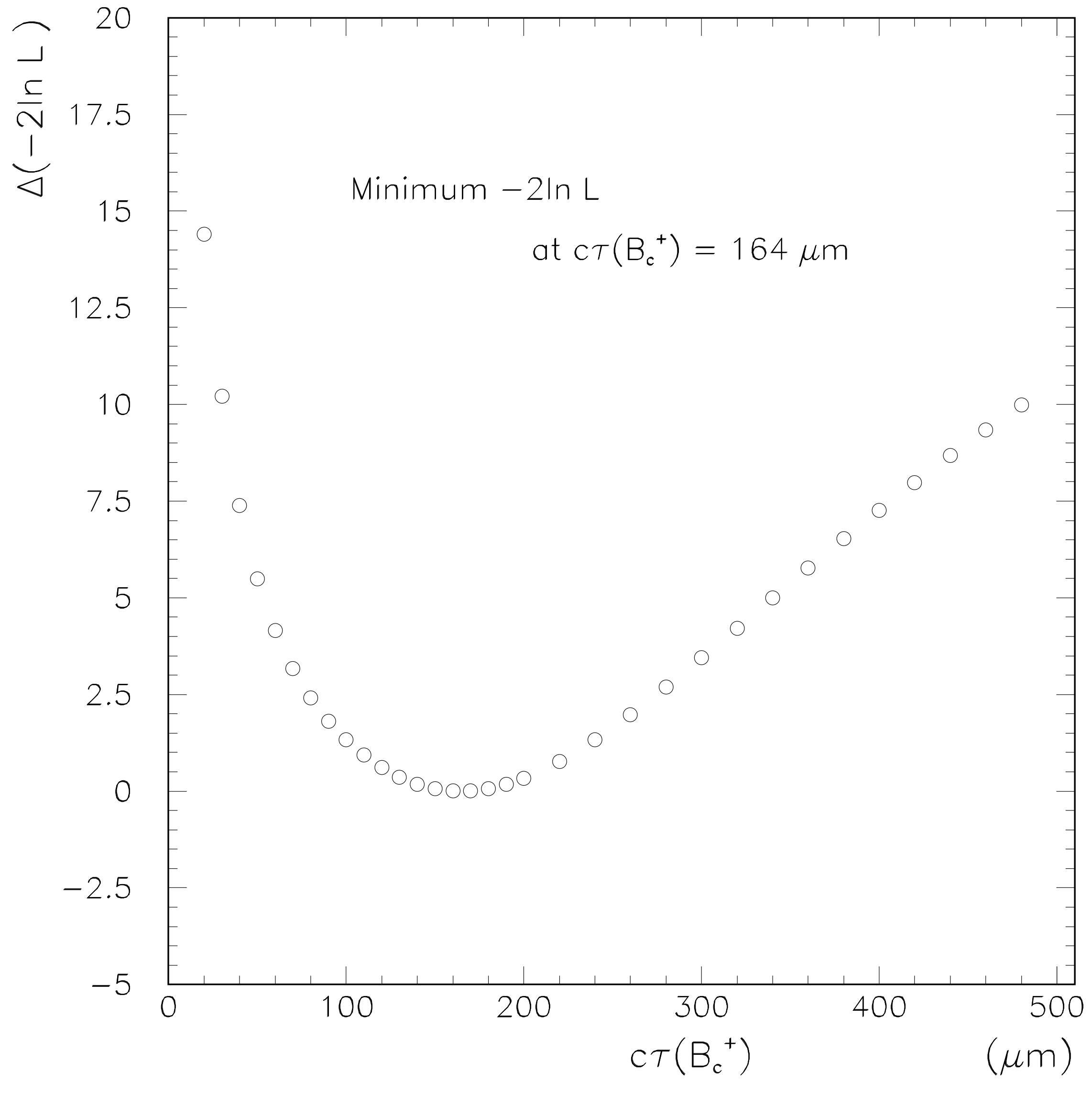

Figure 6.9: $\Delta(-2\ln\mathcal{L}) = -2\ln\mathcal{L} - (-2\ln\mathcal{L})_{min}$ as a function of $c\tau(B_c)$.

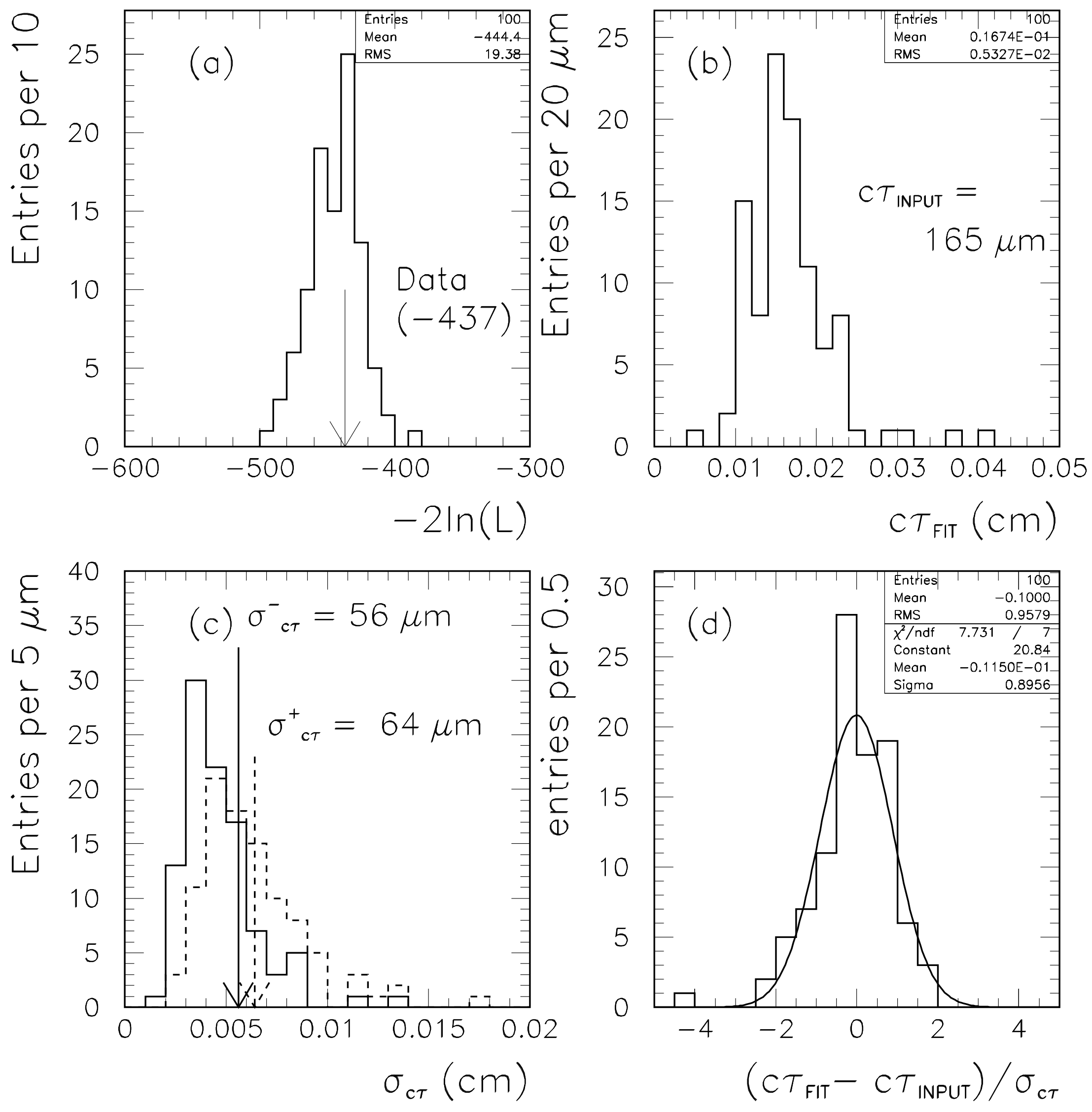

Figure 6.10: Results of the fitting test. (a) $-2\ln\mathcal{L}$. (b) Fitted lifetime. (c) Its uncertainty. solid line for the error for negative side. dashed line for that for positive side.(d) $(c\tau_{FIT} - c\tau_{INPUT})/\sigma_{FIT}$. The positive (negative) uncertainty is used if the fitted lifetime is smaller (larger) than the input lifetime.

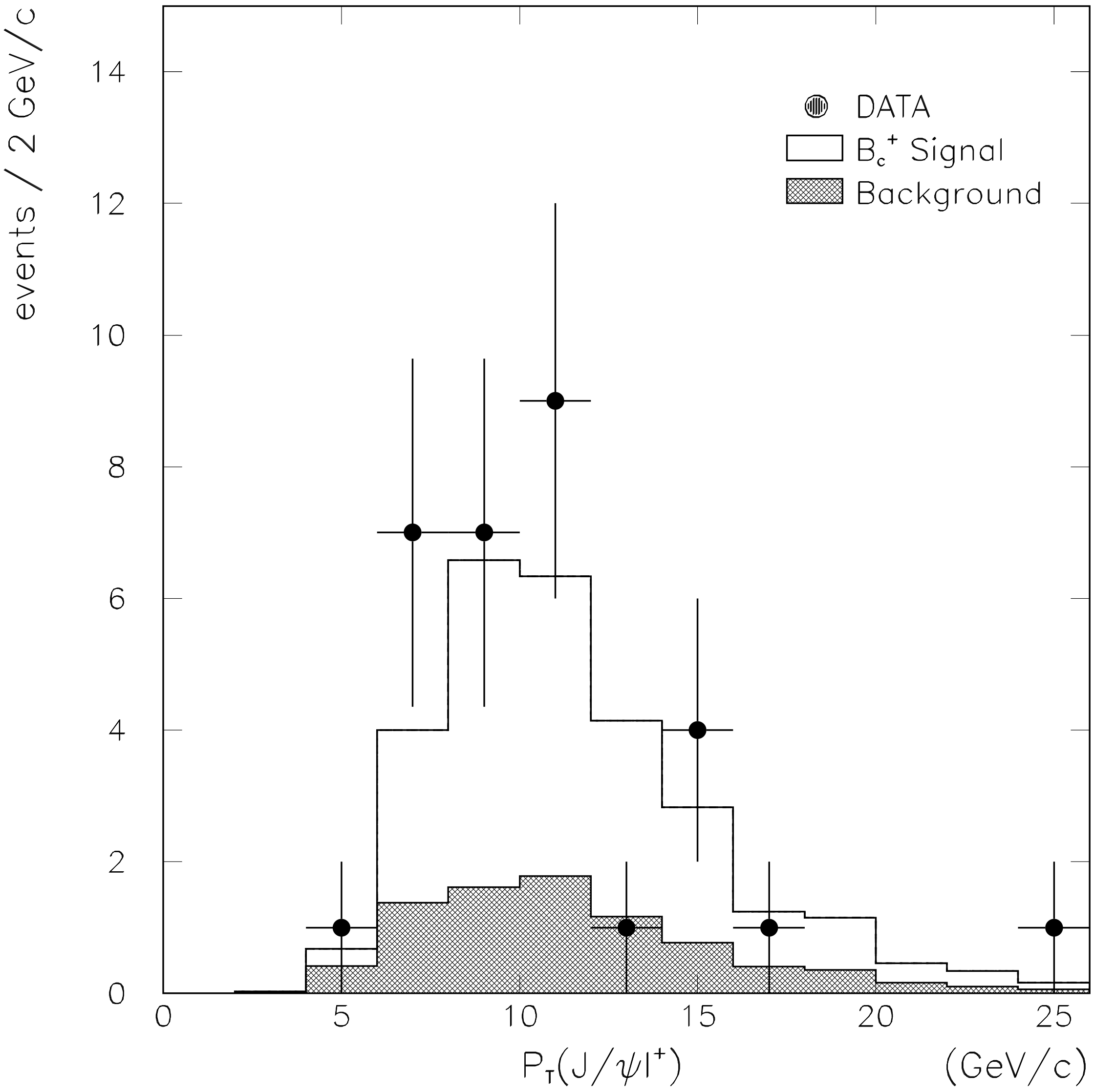

Figure 6.11: p_T distribution of the $J/\psi + \ell$ sample with $x > 60$ μm. The Monte Carlo distribution for the B_c signal is calculated using the b quark p_T spectrum in Ref. [11]. The background distribution consists of the fake e, residual conversion, $b\bar{b}$ for e, and decay-in-flight, punch-through, $b\bar{b}$ for μ backgrounds.

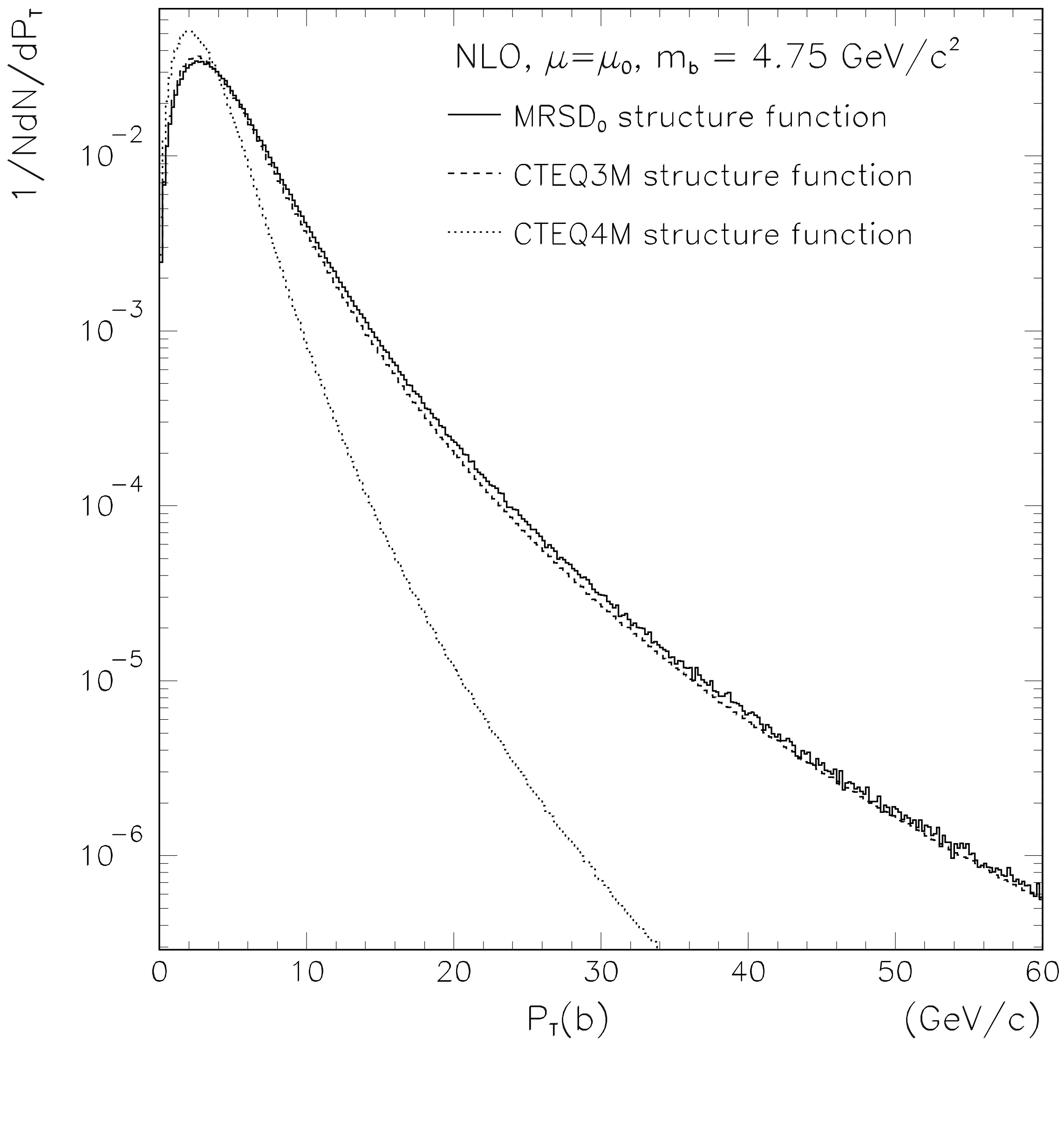

Figure 6.12: b quark p_T spectra. They are normalized to unit area.

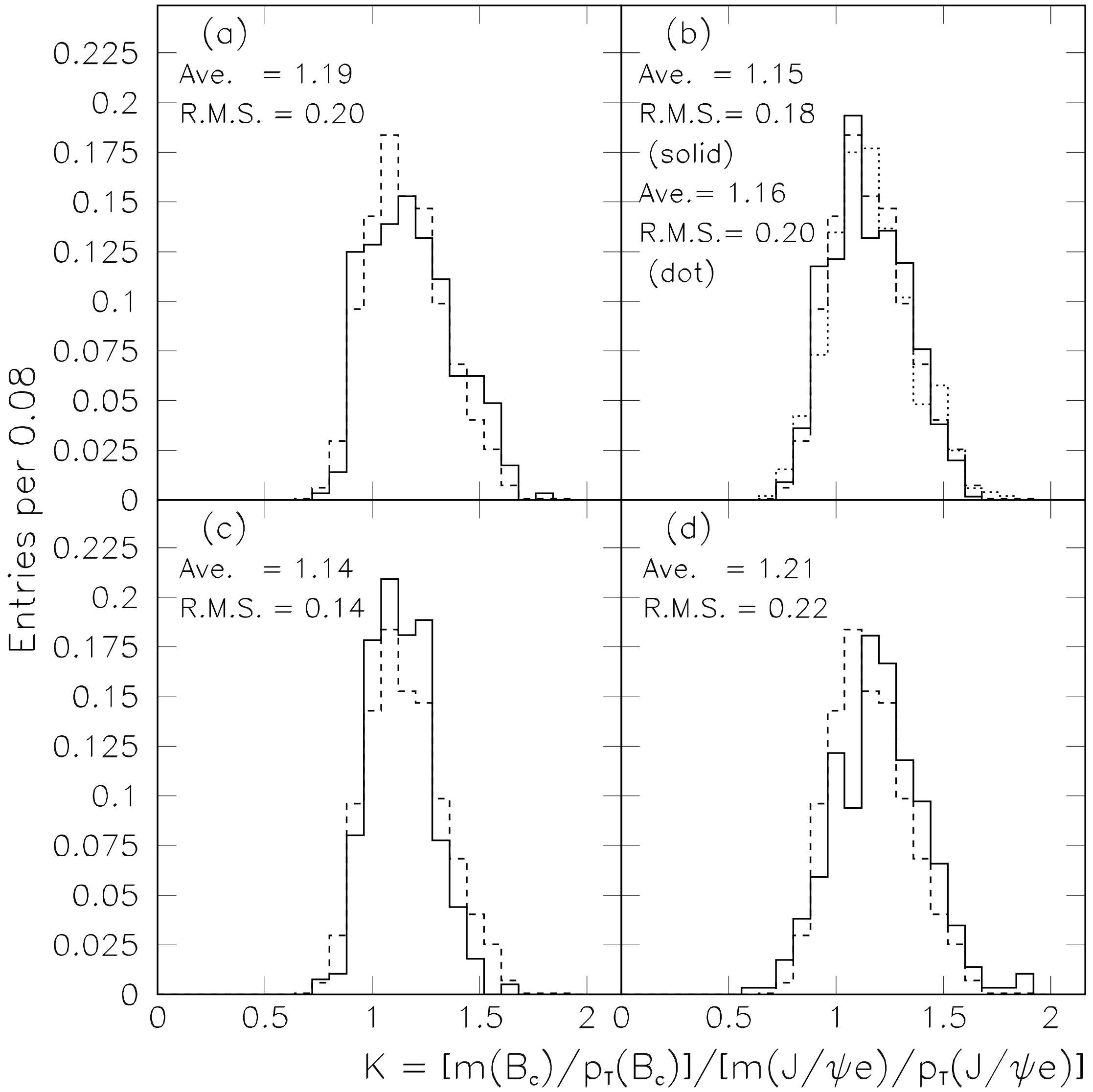

Figure 6.13: Variations in K distributions caused by various sources. (a) Different b quark spectrum. (b) Uncertainties in the B_c mass: $m(B_c) - 150$ MeV (solid) and $m(B_c) + 150$ MeV (dots). (c) $B_c^+ \to \psi(2S)\ell^+\nu$, $\psi(2S) \to J/\psi X$. (d) Different decay model. The dashed histograms show the default distribution in Figure 6.2 (a).

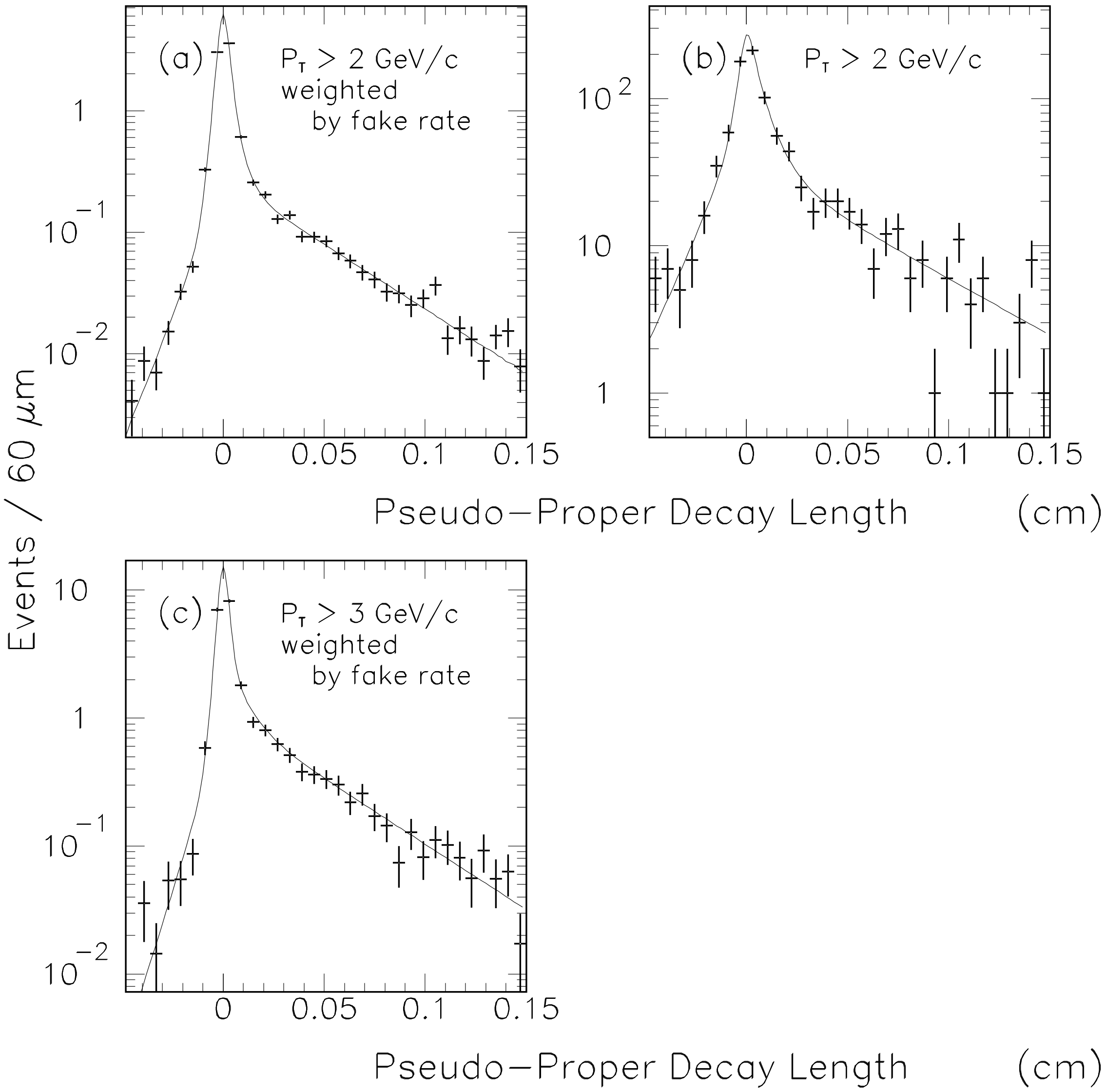

Figure 6.14: Pseudo-proper decay length distributions for J/ψ + track fitted with an alternative parameterization. (a) Fake electron background. Weighted by fake rate. (b) Residual conversion background using Monte Carlo. (c) False muon (decay-in-flight) background. Weighted by fake rate.

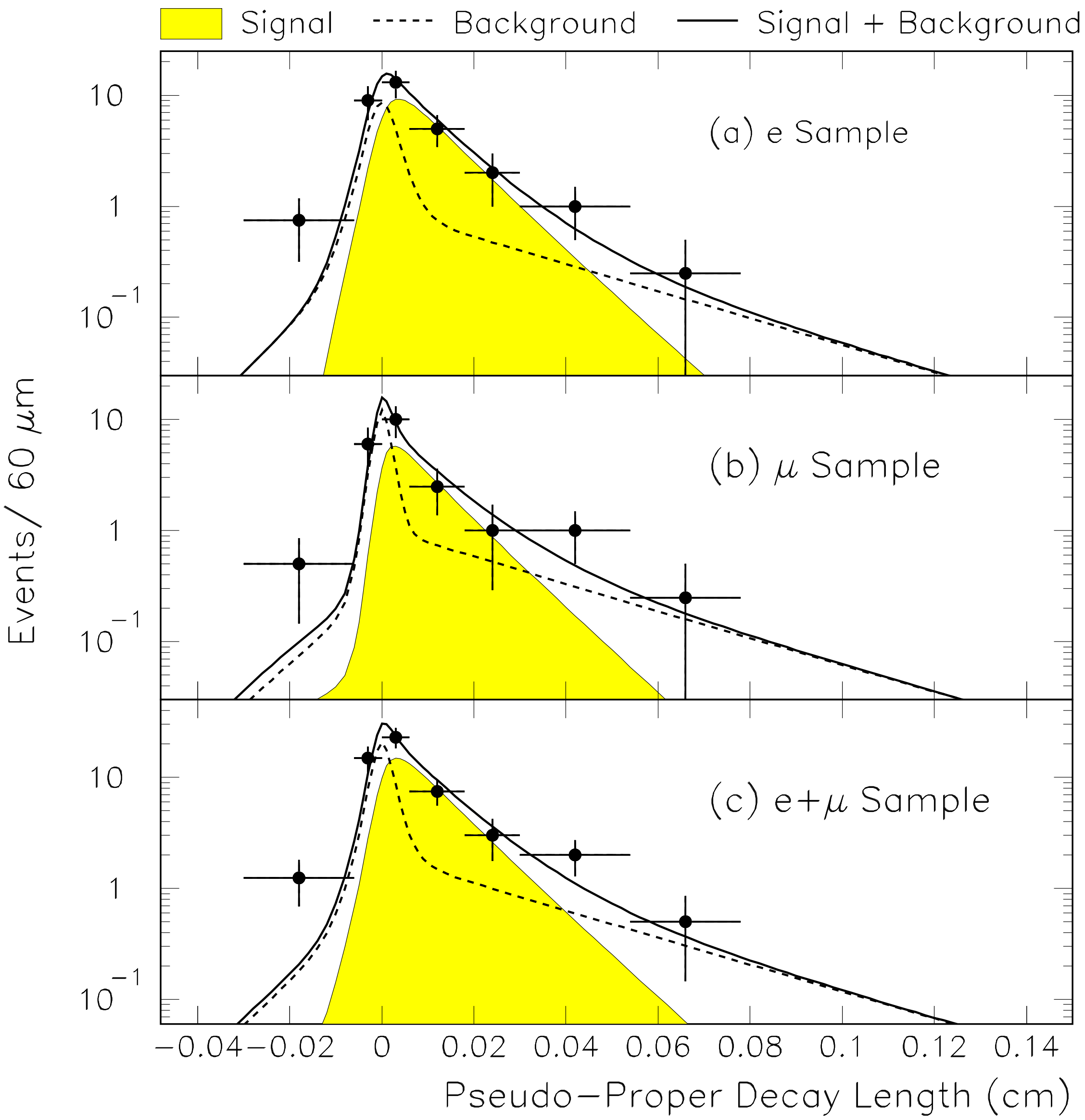

Figure 6.15: Pseudo-proper decay length distributions with fit results for the simultaneous fit, without the prompt J/ψ component. (a) e mode. (b) μ mode. (c) $e + \mu$ mode.

Chapter 7

The B_c Production Cross Section

We present the B_c meson production cross section in terms of the ratio to the $B_u^+ \to J/\psi K^+$ production cross section, $\sigma_{B_c^+}\mathcal{B}\left(B_c^+ \to e^+ J/\psi X\right)/\sigma_{B_u^+}\mathcal{B}\left(B^+ \to J/\psi K^+\right)$. This quantity is chosen because the systematic effects of the J/ψ trigger and the CTC track finding efficiency will cancel in the ratio.

7.1 Expressions for the cross section ratio

In Chapter 5, we determined the number of signal $B_c^+ \to J/\psi \ell^+ X$ events in the observed mass distribution. We derive the cross section ratio using the fit result of the mass distribution. The ratio $\sigma_{B_c^+}\mathcal{B}(B_c^+ \to J/\psi \ell^+ X)/\sigma_{B_u^+}\mathcal{B}(B_u^+ \to J/\psi K^+)$ is given by,

$$\frac{\sigma_{B_c^+}\mathcal{B}\left(B_c^+ \to J/\psi \ell^+ X\right)}{\sigma_{B_u^+}\mathcal{B}\left(B_u^+ \to J/\psi K^+\right)} = \frac{1}{2} \times \frac{\frac{N(B_c^+)}{\varepsilon(B_c^+)L}}{\frac{N(B_u^+)}{\varepsilon(B_u^+)L}}, \tag{7.1}$$

where $N(B_c^+)$ is the number of $B_c^+ \to J/\psi \ell^+ X$ events determined as $N(B_c^+) = n'^{\ell} = 20.4^{+6.2}_{-5.6}$ in the mass distribution fit in Section 5.3.2, N(B_u) is the number of $B_u^+ \to J/\psi K^+$ events, $\varepsilon(B_c^+)$ and $\varepsilon(B_u^+)$ are the detection efficiencies including kinematic and geometric acceptances and cut efficiencies, and L is the integrated luminosity which cancels out in the ratio. The factor of 1/2 is needed, since we are using the combined electron and muon yield to calculate the cross section.

The $N(B_c^+)$ contains both $J/\psi + e$ and $J/\psi + \mu$ events with a ratio of $r^{\varepsilon} : (1 - r^{\varepsilon})$, where r^{ε} is the fraction of the $J/\psi + e$ mode, determined as $r^{\varepsilon} = 0.59 \pm 0.04$ in the mass distribution fit in Section 5.3.2. We consequently can rewrite $N(B_c^+)/2\varepsilon(B_c^+)$ as

$$\frac{N(B_c^+)}{2\varepsilon(B_c^+)} = \frac{r^\varepsilon N(B_c^+)}{\varepsilon^e} = \frac{(1-r^\varepsilon)N(B_c^+)}{\varepsilon^\mu}, \tag{7.2}$$

where ε^e and ε^μ are the detection efficiencies for the $B_c^+ \to J/\psi e^+ X$ mode and for the $B_c^+ \to J/\psi \mu^+ X$ mode, respectively. In what follows, we use ε^K for $\varepsilon(B_u^+)$, *i.e.*, the detection efficiency for the $B_u^+ \to J/\psi K^+$ is denoted by ε^K.

Then the cross section ratio can be written as

$$\frac{\sigma_{B_c^+}\mathcal{B}(B_c^+ \to J/\psi \ell^+ X)}{\sigma_{B_u^+}\mathcal{B}(B_u^+ \to J/\psi K^+)} = \frac{r^\varepsilon N(B_c^+)}{N(B_u^+)}\varepsilon^r, \tag{7.3}$$

where $\varepsilon^r = \varepsilon^K/\varepsilon^e$.

To obtain the cross section ratio $\sigma_{B_c^+}\mathcal{B}(B_c^+ \to J/\psi \ell^+ X)/\sigma_{B_u^+}\mathcal{B}(B_u^+ \to J/\psi K^+)$, we estimate the number of $B_u^+ \to J/\psi K^+$ events and the relative efficiency ε^r.

7.2 Selection of $B_u^+ \to J/\psi K^+$ events

We select $B_u^+ \to J/\psi K^+$ events by applying the following cuts:

- the same J/ψ selection cuts as described in Section 3.1.
- kaon track satisfies the same fiducial requirements as electrons.
- J/ψ and kaon are in the same hemisphere.
- three track vertex fit χ^2 probability is greater than 1%.
- "proper decay length" > 60 μm. For the $B_u^+ \to J/\psi K^+$ mode, we can fully reconstruct the B_u^+ meson. Therefore we can calculate the "proper decay length".

Except for the cuts for the electron selection, these cuts are identical to those for the $J/\psi + e$ combination. We fix the proper decay length cut threshold to 60 μm for the B_u meson. The $J/\psi K^+$ invariant mass distribution is shown in Figure 7.1.

We fit the $J/\psi K^+$ invariant mass distribution to a sum of a Gaussian and a flat background distribution. We find (290 ± 19) events of the $B_u^+ \to J/\psi K^+$ decay in 105 pb^{-1} data.

7.3 Relative efficiency

We estimate the relative efficiency $\varepsilon^r = \varepsilon^K/\varepsilon^e$. The ε^e and ε^K are written as

$$\varepsilon^e \equiv \varepsilon_{\rm trig}\,\varepsilon_{J/\psi}\varepsilon_{ele}\,\varepsilon_{J/\psi+e}, \tag{7.4}$$

$$\varepsilon^K \equiv \varepsilon_{\rm trig}\,\varepsilon'_{J/\psi}\,\varepsilon'_K\,\varepsilon'_{J/\psi+K}, \tag{7.5}$$

where $\varepsilon_{\rm trig}$ is the dimuon trigger efficiency (common to the $B_c^+ \to J/\psi e^+ X$ and $B_u^+ \to J/\psi K^+$ decays), $\varepsilon^{(\prime)}_{J/\psi}$ is the detection efficiency for J/ψ, $\varepsilon_{ele}(\varepsilon'_K)$ is the efficiency for the electron (kaon) identification, and $\varepsilon_{J/\psi+e}$ $(\varepsilon'_{J/\psi+K})$ is the efficiency for the Prob(vertex fit χ^2) $> 1\%$ and (pseudo-) proper decay length > 60 μm cuts.

We estimate ε^e and ε^K using Monte Carlo simulation.

7.3.1 Efficiency (ε^e) for the $B_c^+ \to J/\psi e^+ X$ decay

To evaluate ε^e, we generate $B_c^+ \to J/\psi e^+ \nu$ events in the same way as described in Section 3.4.1. The B_c meson mass is set to 6.27 GeV/c^2. The generated Monte Carlo events are simulated by the CDF detector simulation, processed using the same reconstruction code as used for real data, and passed through the trigger simulation. First we select $J/\psi \to \mu^+\mu^-$ events from the Monte Carlo sample.

As dsecried in Section 3.3, we apply many cuts for the electron selection to obtain a high purity electron sample. The electron identification efficiency ε_{ele} is given by

$$\varepsilon_{ele} = \varepsilon_{fid}\,\varepsilon_{CES}\,\varepsilon_{CPR}\,\varepsilon_{S_e}\,\varepsilon_{conv}\,\varepsilon_{E/p}\,\varepsilon_{Had/Em}, \tag{7.6}$$

where ε_{fid} is the efficiency for the fiducial cut, ε_{CES} is the efficiency for the CES cuts, ε_{CPR} is the efficiency for CPR minimum charge deposition cut, ε_{S_e} is the efficiency for the CTC dE/dX cut, ε_{conv} is the efficiency for the conversion removal cut, $\varepsilon_{E/P}$ is the efficiency for the E/p cut, and $\varepsilon_{Had/Em}$ is the efficiency for the E_{had}/E_{EM} cut. Among these efficiencies, ε_{CES}, ε_{CPR} and ε_{S_e} do not depend on the isolation of an electron track, because of the fine segmentation of the CES, CPR and CTC. On the other hand, $\varepsilon_{E/P}$ and $\varepsilon_{Had/Em}$ depend on the isolation. Therefore we do not apply all electron selection criteria for the analysis of Monte Carlo events. We look for an electron track which is matched to an electron at the generator level. Then we apply only the fiducial, conversion removal, E_{had}/E_{EM} and E/p cuts to the electron track, and account for the efficiencies for the CES, CPR and S_e cuts by multiplying the measured efficiency numbers by hand. The CES and CPR efficiencies are measured as a function of p_T, using conversion electrons in the real data [44]. Figure 7.2 (a) shows the CES and CPR cut efficiencies as a function of p_T. Since the S_e cut depends on the track momentum, we show the S_e cut efficiency as a function of p in Figure 7.2 (b).

We reconstruct a common vertex of 3 leptons applying the Prob(vertex fit χ^2) $> 1\%$ cut, form an invariant mass of the $J/\psi + e$, and apply the pseudo-proper decay length cut of $x > 60$ μm. Dividing the number of $J/\psi + e$ events in the mass range $3.35 < m(J/\psi e) < 11.0$ GeV/c^2 by the number of events which pass the trigger simulations, we obtain $\varepsilon^e/\varepsilon_{trig}$. For convenience, we calculate $\varepsilon^e/\varepsilon_{trig}$ for the B_c lifetimes of 0.25, 0.50, 0.75, 1.00, 1.25 and 1.55 ps. Figure 7.3 (a) shows the efficiency for the $B_c^+ \rightarrow J/\psi e^+ \nu$ decay mode as a function of the assumed B_c lifetime. We parameterize it as

$$\varepsilon^e/\varepsilon_{trig} = P_1(1 - \exp(P_2 \tau(B_c)), \tag{7.7}$$

where $\tau(B_c)$ is the B_c lifetime. The parameters P_1 and P_2 are determined by fitting the ε^e plot. The fit result is superimposed in Figure 7.3 (a). At the B_c lifetime of 0.55 ps, we find $\varepsilon^e/\varepsilon_{trig}$ = (2.54 $\pm$ 0.14) %, where the uncertainty is due to Monte Carlo statistics.

7.3.2 Efficiency (ε^μ) for the $B_c^+ \rightarrow J/\psi \mu^+ X$ decay and R^ε

We also estimate the $B_c^+ \rightarrow J/\psi \mu^+ X$ detection efficiency ε^μ. We generate $B_c^+ \rightarrow J/\psi \mu^+ \nu$ events using the Monte Carlo simulation, like the $B_c^+ \rightarrow J/\psi e^+ \nu$ events. We reconstruct $J/\psi + \mu$ events in the same way as for the real data, and obtain $\varepsilon^\mu/\varepsilon_{trig}$ = (1.82 $\pm$ 0.09) % at the B_c lifetime of 0.55 ps.

Using $\varepsilon^e \varepsilon_{trig}$ and $\varepsilon^\mu/\varepsilon_{trig}$ at $\tau(B_c) = 0.55$ ps, we estimate the fraction of $J/\psi + e$ events in the B_c signal, R^ε. The R^ε is given by

$$R^\varepsilon = \frac{n^e}{n^e + n^\mu} = \frac{1}{1 + \dfrac{n^\mu}{n^e}} = \frac{1}{1 + \dfrac{\varepsilon^\mu}{\varepsilon^e}} = 0.58 \pm 0.04. \tag{7.8}$$

The above value for R^{ε} was used as an input in the fit of the mass distribution in Section 5.3.

7.3.3 Efficiency (ε^K) for the $B_u^+ \to J/\psi K^+$ decay

We generate inclusive $\bar{b}$ events according to the next-to-leading order QCD calculation [8] with renormalization scale $\mu_0 = \sqrt{m_b^2 + p_T(b)^2}$, where the b quark mass m_b is set to 4.75 GeV/c^2 , and the MRSD$_0$ parton distribution functions [48] are used. The $\bar{b}$ quark is hadronized into a B_u^+ meson according to the Peterson fragmentation model [9] using the Peterson fragmentation parameter $\epsilon_P = 0.006$. The B_u^+ is decayed into $J/\psi K^+$, followed by the $J/\psi \to \mu^+\mu^-$ decay, according to the CLEO decay model [49]. Then the event is processed by the CDF detector simulation and the trigger simulation [40]. Finally, the event undergoes the same reconstruction code as real data.

We select $J/\psi K^+$ events by applying the same cuts as for the data and obtain the detection efficiency $\varepsilon^K/\varepsilon_{trig}$ of $(9.5 \pm 0.3)\%$.

7.3.4 Relative efficiency ε^r

The relative efficiency $\varepsilon^r = \varepsilon^K/\varepsilon^e$ is obtained as a function of the assumed B_c lifetime and is shown in Figure 7.3 (b). In Chapter 6, we have measured the B_c lifetime to be 0.55 $^{+0.21}_{-0.19}$ ± 0.12 ps. From Figure 7.3 (b), we find $\varepsilon^r = 3.75 \pm 0.22$ at the B_c lifetime of 0.55 ps, where the uncertainty is due to Monte Carlo statistics.

7.4 Uncertainties on the efficiency ε^r

In this section, we estimate the systematic uncertainties on ε^r.

- Production spectrum
  In the efficiency calculation for the $B_c^+ \to J/\psi \ell^+ X$, we employed the B_c meson p_T spectrum of the α_s^4 calculation [13]. Here we generate inclusive $\bar{b}$ quark events using the next-to-leading order calculation [8] with renormalization scale $\mu_0 = \sqrt{m_b^2 + p_T(b)^2}$ ($m_b = 4.75$ GeV/c^2) and the structure function MRSD$_0$. The $\bar{b}$ quark is fragmented into the B_c meson according to the fragmentation function

of Ref. [15]. To see an uncertainty on ε^K, we generate B_u^+ events by changing the parameter set (μ_0, m_b) from ($\mu_0 = \sqrt{m_b^2 + p_T(b)^2}$, $m_b = 4.75$ GeV/c^2) to ($\mu_0 = \frac{1}{2}\sqrt{m_b^2 + p_T(b)^2}$, $m_b = 4.5$ GeV/c^2) and ($\mu_0 = 2\sqrt{m_b^2 + p_T(b)^2}$, $m_b = 5.0$ GeV/c^2). We calculate ε^r using these Monte Carlo samples and find 5.0% difference. To estimate a systematic uncertainty on ε^K due to the Peterson fragmentation parameter ϵ_P, we change ϵ_P from 0.006 to 0.003 and 0.009, and find 2.3% uncertainty. Calculating a quadrature sum of these two sources, we assign 5.5% as a systematic uncertainty due to the production spectrum.

- Difference between Run Ia and Run Ib

  Since 80% of events come from Run Ib data, we determined the relative efficiency ε^r using the Monte Carlo simulation which was set to the Run Ib condition. The SVX was replaced by the SVX′ at the beginning of Run Ib. The dimuon trigger is different in Run Ia from Run Ib. We simulate the $B_c^+ \to J/\psi e^+ \nu$ and $B_u^+ \to J/\psi K^+$ events using the detector simulation under the Run Ia condition and the trigger simulation [40] for Run Ia. We find 5% difference between ε^r for Run Ib and that for Run Ia, and assign 5% to this systematic uncertainty.

- Trigger simulation

  To estimate the uncertainty coming from the dimuon trigger simulation, we turn off the trigger simulation for the B_c and B_u Monte Carlo and obtain the relative efficiency. We find a difference of 4% and assign the 4% as a systematic uncertainty.

- Electron identification efficiency

  We assign 10% as a systematic uncertainty on the electron identification efficiency, taken from Ref. [44].

- Monte Carlo statistics

  The statistical uncertainty on the relative efficiency due to the finite Monte Carlo statistics is 4%.

Adding these uncertainties in quadrature, we obtain a total uncertainty of 14%. A summary of the uncertainties on the ε^r ($=\varepsilon^K/\varepsilon^e$) is given in Table 7.1.

Production spectrum	5.5%
Run Ia/Ib difference	5%
Trigger simulation	4%
Electron ID efficiency	10%
Monte Carlo statistics	4%
Total	14%

Table 7.1: Uncertainties on the relative efficiency ε^r.

7.5 The cross section ratio

The product of the production cross section times branching ratio for $B_c^+ \to J/\psi \ell^+ X$ at the measured value of the lifetime relative to the cross section times branching ratio for $B_u^+ \to J/\psi K^+$ is calculated as

$$\begin{aligned}\frac{\sigma_{B_c^+}\mathcal{B}(B_c^+ \to J/\psi \ell^+ X)}{\sigma_{B_u^+}\mathcal{B}(B_u^+ \to J/\psi K^+)} &= \frac{r^\varepsilon N(B_c^+)}{N(B_u^+)}\varepsilon^r \\ &= 0.155\,^{+0.047}_{-0.043} \pm 0.027, \end{aligned} \tag{7.9}$$

where the first uncertainty is statistical and the second is systematic. In this calculation, the following values are used:

- $r^\varepsilon = 0.59 \pm 0.04$ (Section 5.3.2),
- $N(B_c^+) = n'^\ell = 20.4\,^{+6.2}_{-5.6}$ (Section 5.3.2),
- $N(B_u^+) = 290 \pm 19$ (Section 7.2),
- $\varepsilon^r = 3.75 \pm 0.22 \pm 0.53$ (Section 7.3.4 and Section 7.4).

The statistical uncertainty in the $\sigma\mathcal{B}$ ratio, Eq. (7.9), contains only that on $N(B_c^+)$. The systematic uncertainty comes from the statistical uncertainty on $N(B_u^+)$, the uncertainty on r^ε, and the statistical and systematic uncertainties on ε^r. The total systematic uncertainty on the $\sigma\mathcal{B}$ ratio is 17%.

In Chapter 6, we determined the B_c lifetime:

$$\tau = 0.55\,^{+0.21}_{-0.19} \pm 0.12 \text{ ps},$$

where the first uncertainty is statistical and the second is systematic. From the B_c lifetime $\tau(B_c)$ ($= 1/\Gamma_{\mathrm{tot}}$) and the partial width $\Gamma(B_c^+ \to J/\psi\ell^+\nu)$, one can calculate the branching ratio $\mathcal{B}(B_c^+ \to J/\psi\ell^+\nu)$:

$$\mathcal{B}(B_c^+ \to J/\psi\ell^+\nu) \quad = \quad \frac{\Gamma(B_c^+ \to J/\psi\ell^+\nu)}{\Gamma_{\mathrm{tot}}}. \tag{7.10}$$

If we assume a theoretical estimate of the partial width $\Gamma(B_c^+ \to J/\psi\ell^+\nu) = (5.9 \pm 2.4) \times 10^{-2}\ \mathrm{ps}^{-1}$ [21], we find $\mathcal{B}(B_c^+ \to J/\psi\ell^+\nu) = 0.032\ ^{+0.014}_{-0.013}\ \pm 0.016$, where the first uncertainty comes from the total uncertainty on the lifetime measurement, and the second is from the theoretical uncertainty in the partial width [21].

Since the contribution from the higher mass $c\bar{c}$ states to the $J/\psi + \ell$ mode is expected to be small as shown in Table 6.8, we can neglect the contribution from the higher mass $c\bar{c}$ states and make an approximation on that $\mathcal{B}(B_c^+ \to J/\psi\ell^+X) \simeq \mathcal{B}(B_c^+ \to J/\psi\ell^+\nu)$. Once the branching ratio $\mathcal{B}(B_c^+ \to J/\psi\ell^+X)$ is given, one can extract the ratio of the production cross sections $\sigma_{B_c^+}/\sigma_{B_u^+}$ from the $\sigma\mathcal{B}$ ratio as

$$\frac{\sigma_{B_c^+}}{\sigma_{B_u^+}} = \left(4.9\ ^{+1.5}_{-1.4}\ ^{+2.3}_{-2.2}\ \pm 2.1\right) \times 10^{-3}, \tag{7.11}$$

where we have used the branching ratio $\mathcal{B}(B_u^+ \to J/\psi K^+) = (1.01 \pm 0.14) \times 10^{-3}$ [32]. The first uncertainty in $\sigma_{B_c^+}/\sigma_{B_u^+}$ is statistical, and the second is systematic where anything related to branching ratios is excluded. The third uncertainty is associated with the branching ratios and contains the contributions from $B_u^+ \to J/\psi K^+$ (14%) and from $B_c^+ \to J/\psi\ell^+\nu$ (40%).

The $\sigma\mathcal{B}$ ratio can be rewritten as

$$\begin{aligned}\frac{\sigma_{B_c^+}\mathcal{B}(B_c^+ \to J/\psi\ell^+X)}{\sigma_{B_u^+}\mathcal{B}(B_u^+ \to J/\psi K^+)} &= \frac{\sigma_{\bar{b}} f_{\bar{b}\to B_c^+}\mathcal{B}(B_c^+ \to J/\psi\ell^+X)}{\sigma_{\bar{b}} f_{\bar{b}\to B_u^+}\mathcal{B}(B_u^+ \to J/\psi K^+)} \\ &\simeq \frac{\sigma_{\bar{b}} f_{\bar{b}\to B_c^+}\mathcal{B}(B_c^+ \to J/\psi\ell^+\nu)}{\sigma_{\bar{b}} f_{\bar{b}\to B_u^+}\mathcal{B}(B_u^+ \to J/\psi K^+)},\end{aligned} \tag{7.12}$$

where $\sigma_{\bar{b}}$ is the $\bar{b}$ quark production cross section, $f_{\bar{b}\to B_c^+}$ ($f_{\bar{b}\to B_u^+}$) is the probability that a $\bar{b}$ quark fragments into the B_c^+ (B_u^+) meson. Here we assume $f_{\bar{b}\to B_c^+} = 10^{-3}$ [11] and $f_{\bar{b}\to B_u^+} = 0.375$ [57]. Then, for a given prediction of $\Gamma(B_c^+ \to J/\psi\ell^+\nu)$, the right-hand side of Eq. (7.12) is calculable as a function of the B_c lifetime. In Figure 7.4, we compare our result of the $\sigma\mathcal{B}$ ratio to the theoretical calculation using the $\Gamma(B_c^+ \to J/\psi\ell^+\nu)$

$= (5.9 \pm 2.4) \times 10^{-2}$ ps^{-1} of Ref. [21]. We note that the theoretical uncertainty in Figure 7.4 is due to the uncertainty in $\Gamma(B_c^+ \to J/\psi \ell^+ \nu)$ only and does not include other uncertainties associated with $f_{\bar{b}\to B_c^+}$, $f_{\bar{b}\to B_u^+}$, nor $\mathcal{B}(B_u^+ \to J/\psi K^+)$.

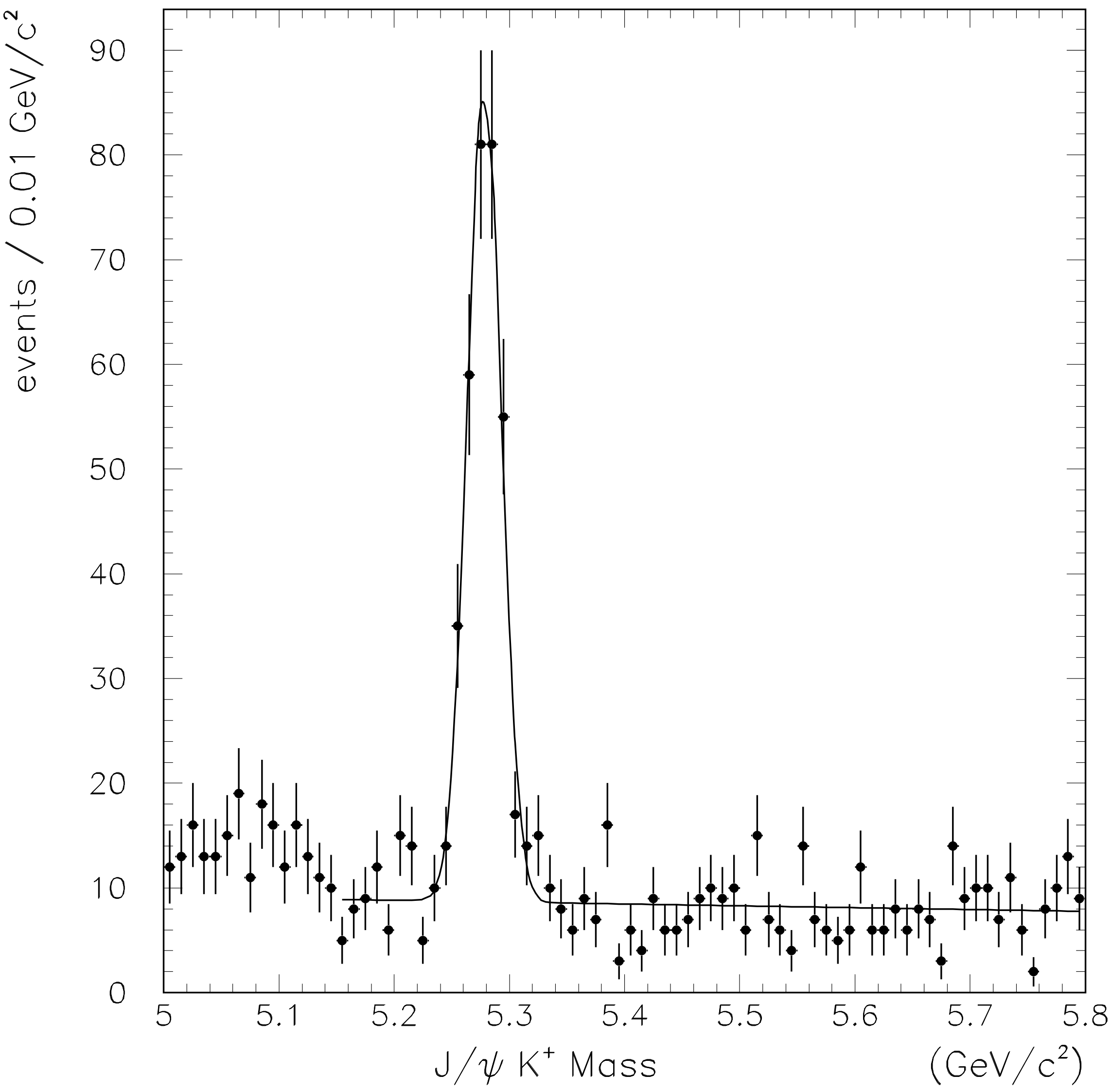

Figure 7.1: The $J/\psi K^+$ invariant mass distribution with a cut on proper decay length $> 60\ \mu$m.

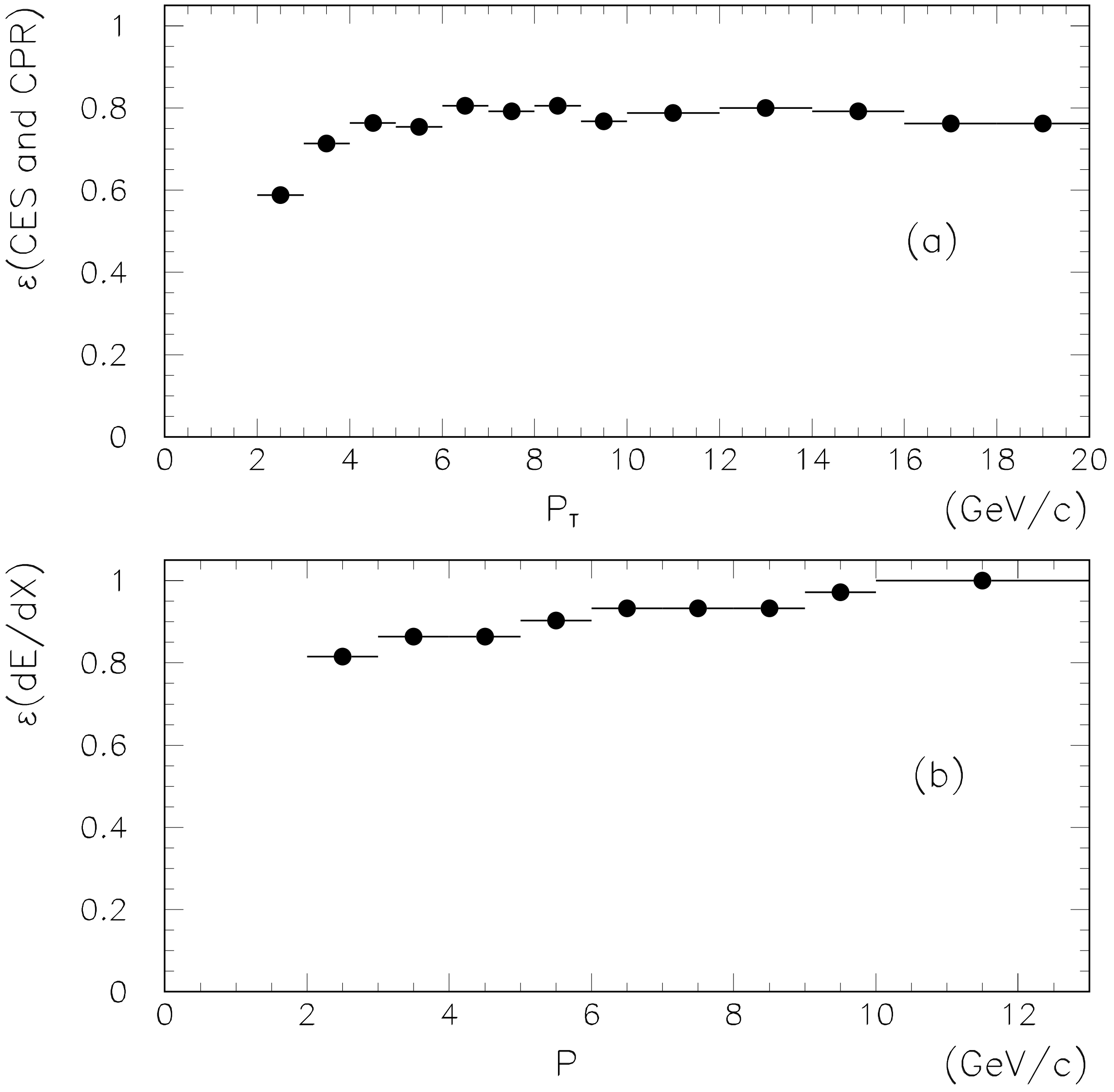

Figure 7.2: Electron selection efficiencies. (a) CES and CPR cut efficiency as a function of p_T. (b) S_e cut efficiency as a function of p.

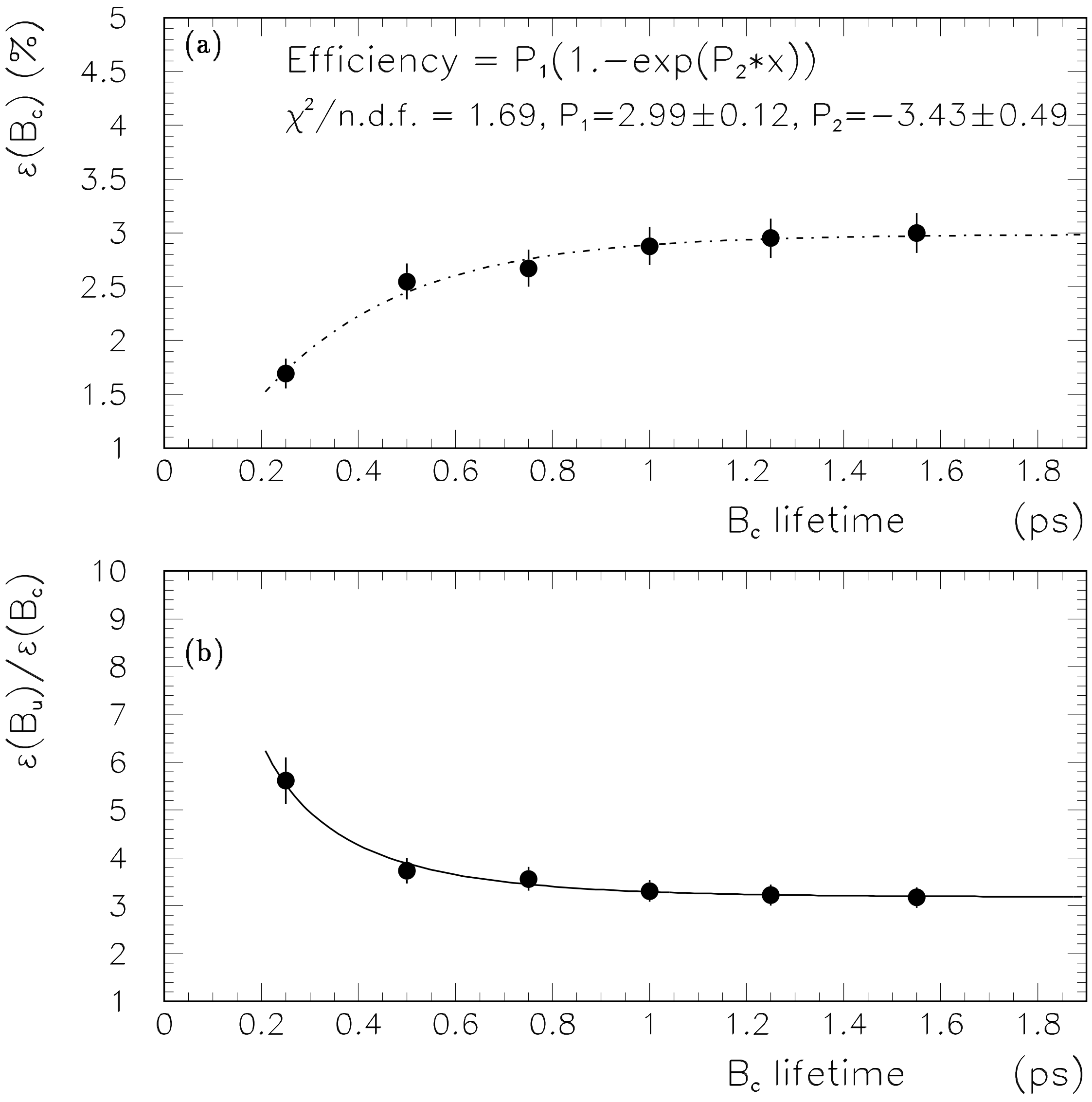

Figure 7.3: Signal detection efficiency for the $B_c^+ \to J/\psi e^+ \nu$ mode as a function of the B_c lifetime. (a) $\varepsilon^e/\varepsilon_{trig}$. (b) Relative efficiency $\varepsilon^r = \varepsilon^K/\varepsilon^e$.

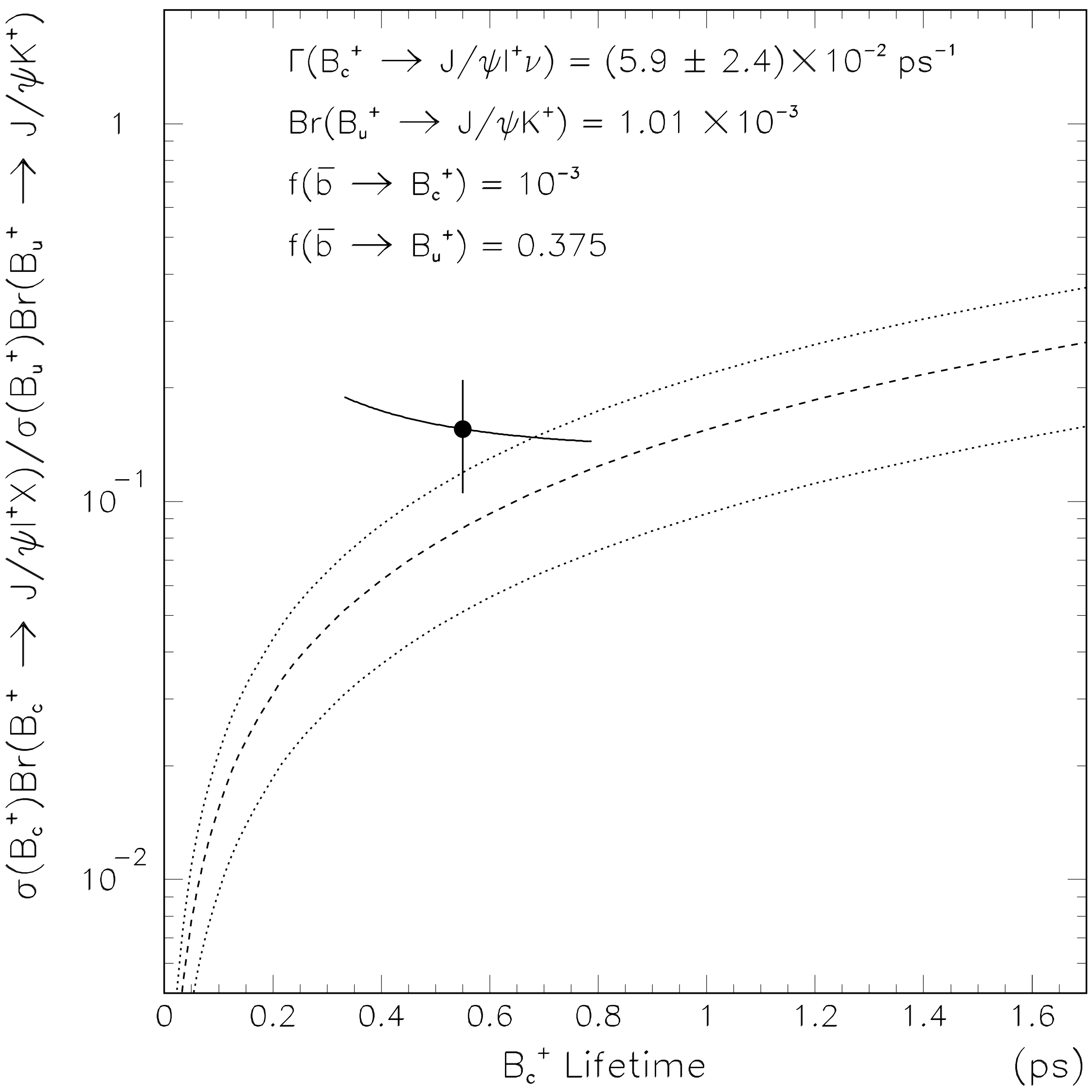

Figure 7.4: The ratio of $\sigma\mathcal{B}(B_c^+ \to J/\psi\ell^+X)/\sigma\mathcal{B}(B_u^+ \to J/\psi K^+)$ as a function of B_c lifetime. The dashed line is the theoretical calculation using the $B_c^+ \to J/\psi\ell^+\nu$ partial width in Ref. [21]. We assume $f_{\bar{b}\to B_c^+}$ $=10^{-3}$, and $f_{\bar{b}\to B_u^+} = 0.375$, and $\mathcal{B}(B_u^+ \to J/\psi K^+)$ $= 1.01 \times 10^{-3}$. The dotted line is a theoretical uncertainty due to the uncertainty on $\Gamma(B_c^+ \to J/\psi\ell^+\nu)$ only.

Chapter 8

Conclusion

Using 105 pb^{-1} of data collected by the CDF detector, we search for the B_c meson using the $B_c^+ \to J/\psi e^+ X$ decay mode. We observe 19 $B_c^+ \to J/\psi e^+ X$ candidate events in the signal mass region, $4 < m(J/\psi e) < 6$ GeV/c^2, with the pseudo-proper decay length cut of $x > 60$ μm. We study the expected background in detail, and estimate 5.0 $\pm$ 1.1 background events in the signal mass region for $x > 60$ μm. Then we combine the result from the search in the $B_c^+ \to J/\psi \mu^+ X$ mode [50]. There are 12 $B_c^+ \to J/\psi \mu^+ X$ candidate events for $4 < m(J/\psi \mu) < 6$ GeV/c^2, while 7.1 $\pm$ 1.5 background events are expected. Assuming a Gaussian fluctuation for the background events, the probability that all 31 events are background is calculated to be 2.5×10^{-5}. Using the $J/\psi \ell$ mass shape in the region $3.35 < m(J/\psi \ell) < 11$ GeV/c^2, we fit the $J/\psi \ell$ mass to the sum of the B_c signal shape and background shape and find 20.4 $^{+6.2}_{-5.5}$ events of the B_c signal. We also calculate the probability that the observed mass distributions are due to background only and determine it to be less than 1.1×10^{-5}.

We measure the B_c meson lifetime from the pseudo-proper decay length distribution to be

$$\tau = 0.55\ ^{+0.21}_{-0.19}\ \pm 0.12\ \text{ps}, \tag{8.1}$$

where the first uncertainty is statistical and the second is systematic. Although the measurement is limited by statistics, the B_c meson has a significantly shorter lifetime than other B mesons.

Finally, we estimate the product of the production cross section times branching ratio for $B_c^+ \to J/\psi \ell^+ X$ at the above value of the lifetime relative to the cross section times branching ratio for $B_u^+ \to J/\psi K^+$. Our estimation for this ratio is:

$$\frac{\sigma_{B_c^+}\mathcal{B}(B_c^+ \to J/\psi \ell^+ X)}{\sigma_{B_u^+}\mathcal{B}(B_u^+ \to J/\psi K^+)} = 0.155\,^{+0.047}_{-0.043} \pm 0.027, \quad (8.2)$$

where the first uncertainty is statistical and the second is systematic.

Appendix A

Electron Fractions in JET20

In Chapter 4, we found from the analysis of the dE/dX distributions that about 2/3 of SLT tagged tracks in the JET20 data were real electrons. In this appendix, we assume two sources of the real electron: real electrons from heavy flavor decays and residual conversion electrons. We estimate these fractions by an independent method and compare the result with that from the dE/dX analysis.

A.1 Real electrons from heavy flavor decays

In order to estimate the fraction of real electrons coming from the heavy flavor decays, we use information on the impact parameter with respect to the primary vertex. The impact parameter distributions for tracks satisfying the fiducial requirements and for tracks identified as electrons are shown in Figure A.1 (a) and Figure A.1 (b), respectively. The impact parameter distribution is broader for tagged tracks, which most probably is due to heavy flavor decays. Assuming that the background shape in the tagged track distribution is identical with the fiducial track distribution, we fit the distribution in Figure A.1 (a) by a Gaussian centered at zero and two exponential tails:

$$\begin{aligned} F_{BG}(d) = N_g \Delta_{bin} G(d|\sigma) &+ \frac{N_{\lambda_1}\Delta_{bin}}{2\lambda_1} \exp\left(-\frac{|d|}{\lambda_1}\right) \otimes G(d|\sigma) \\ &+ \frac{N_{\lambda_2}\Delta_{bin}}{2\lambda_2} \exp\left(-\frac{|d|}{\lambda_2}\right) \otimes G(d|\sigma), \end{aligned} \tag{A.1}$$

where d is the impact parameter, N's are number of events for each component, Δ_{bin} is a bin width, $G(d|\sigma)$ is a Gaussian distribution with a width σ, and the symbol "$\otimes$" denotes the convolution. The fitted curve is shown in Figure A.1 (a).

Next we fit the impact parameter distribution for tagged tracks to a sum of the background shape parameterized by F_{BG} and an exponential tail from heavy flavor decays:

$$F(d) = N_t(1 - f_e)\Delta_{bin}F'_{BG}(d) + \frac{N_t f_e \Delta_{bin}}{2\lambda} \exp\left(-\frac{|d|}{\lambda}\right) \otimes G(d|\sigma), \qquad \text{(A.2)}$$

where $F'_{BG}(d)$ is the normalized distribution of F_{BG}. The σ is fixed to the value obtained in the background fit. The fit results are shown in Figure A.1 (b). From this, we obtain $f_e = 31 \pm 1$ %.

A.2 Residual conversions

The SLT code rejects conversion electron candidates by identifying a conversion partner track which satisfies $|\Delta \cot\theta| < 0.06$, $|\Delta S| < 0.3$ cm, $m(e^+e^-) < 500$ MeV/c^2 and $R_{conv} < 50$ cm (see Section 3.3.6).

Electrons are not identified as a conversion electron if the track of the conversion partner is not reconstructed. We estimate the residual conversion contribution using a same Monte Carlo simulation as used in Section 4.2. We generate π^0 events using the three-momenta of tracks in the JET20 data and simulate $\pi^0 \to \gamma\gamma$ and $\pi^0 \to e^+e^-\gamma$ decays.

The solid circles in Figure A.2 (a) and (b) show the p_T distribution of the conversion electrons and their partners in the JET20 data. The distributions are normalized to unit area. The solid lines in Figure A.2 show the p_T distributions of the Monte Carlo conversion electrons (that are required to be SVX tracks) and their partners obtained from the generator level (not required to be reconstructed). The p_T distribution of the Monte Carlo conversion partners is normalized to the data distribution in the region p_T > 1 GeV/c. From these partner p_T distributions, the finding efficiency ε_{id} is estimated to be (47 ± 4) %.

The number of residual conversions (N_{res}) is calculated by

$$N_{res} = \frac{1 - \varepsilon_{id}}{\varepsilon_{id}} \times N_{id}, \tag{A.3}$$

where N_{id} (=554) is the number of identified conversion electrons. Then we obtain N_{res} = 625 $\pm$ 93. As the total number of JET20 tracks tagged by SLT is 1617, the fraction of residual conversions is 39 $\pm$ 6 %.

A.3 Real electrons in SLT tagged JET20 tracks

The real electron fraction was estimated to be 74 $\pm$ 2 % by the dE/dX analysis in Section 4.1. This agrees with "the heavy flavor fraction 31 $\pm$ 1 %" plus "the residual conversion fraction 39 $\pm$ 6 %". The real electrons from heavy flavor decays and residual conversion electrons can explain the real electrons in SLT tagged tracks in the JET20 data.

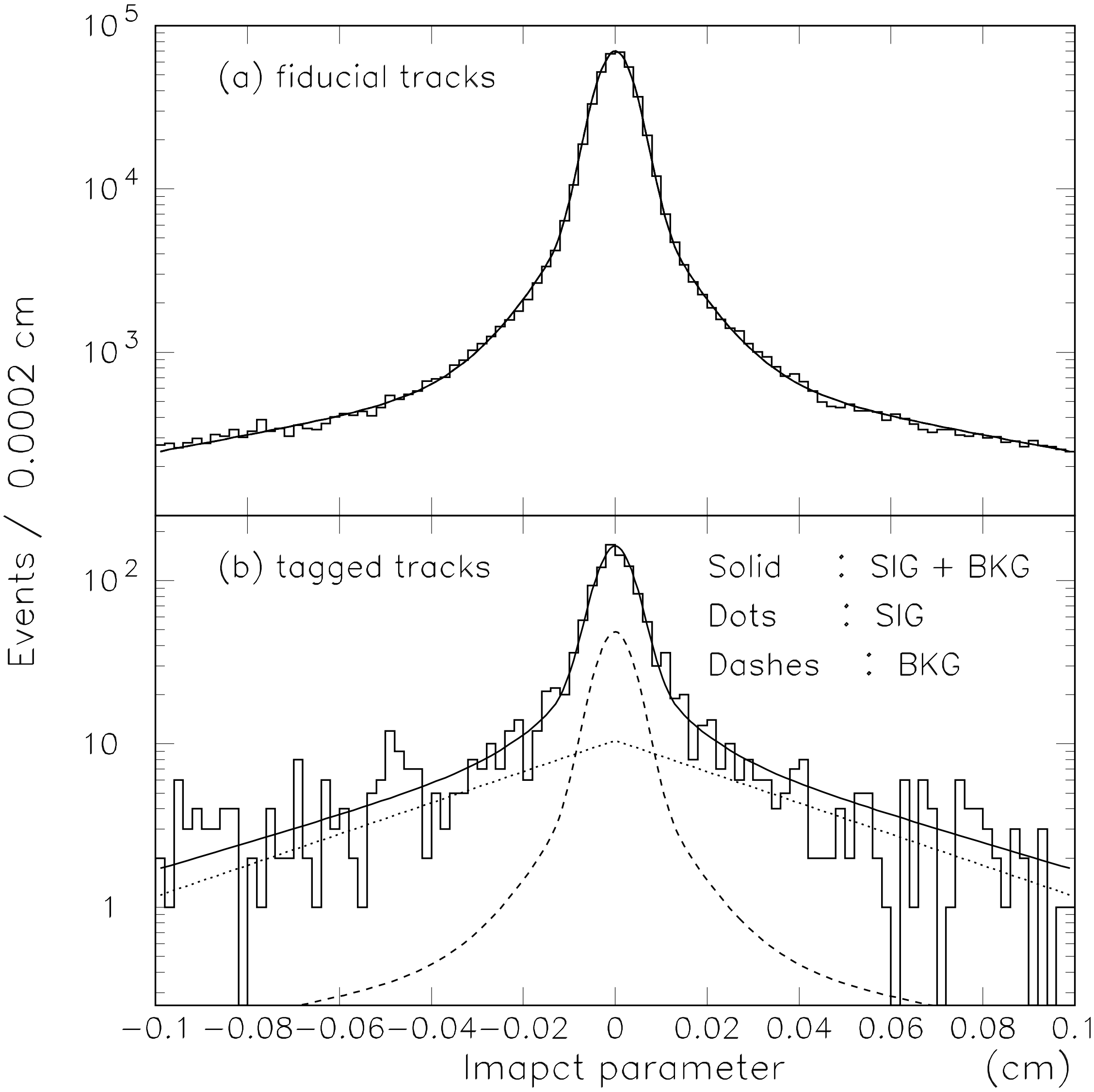

Figure A.1: Impact parameter distributions for JET20 data. (a) fiducial tracks and (b) tracks satisfying the electron requirements.

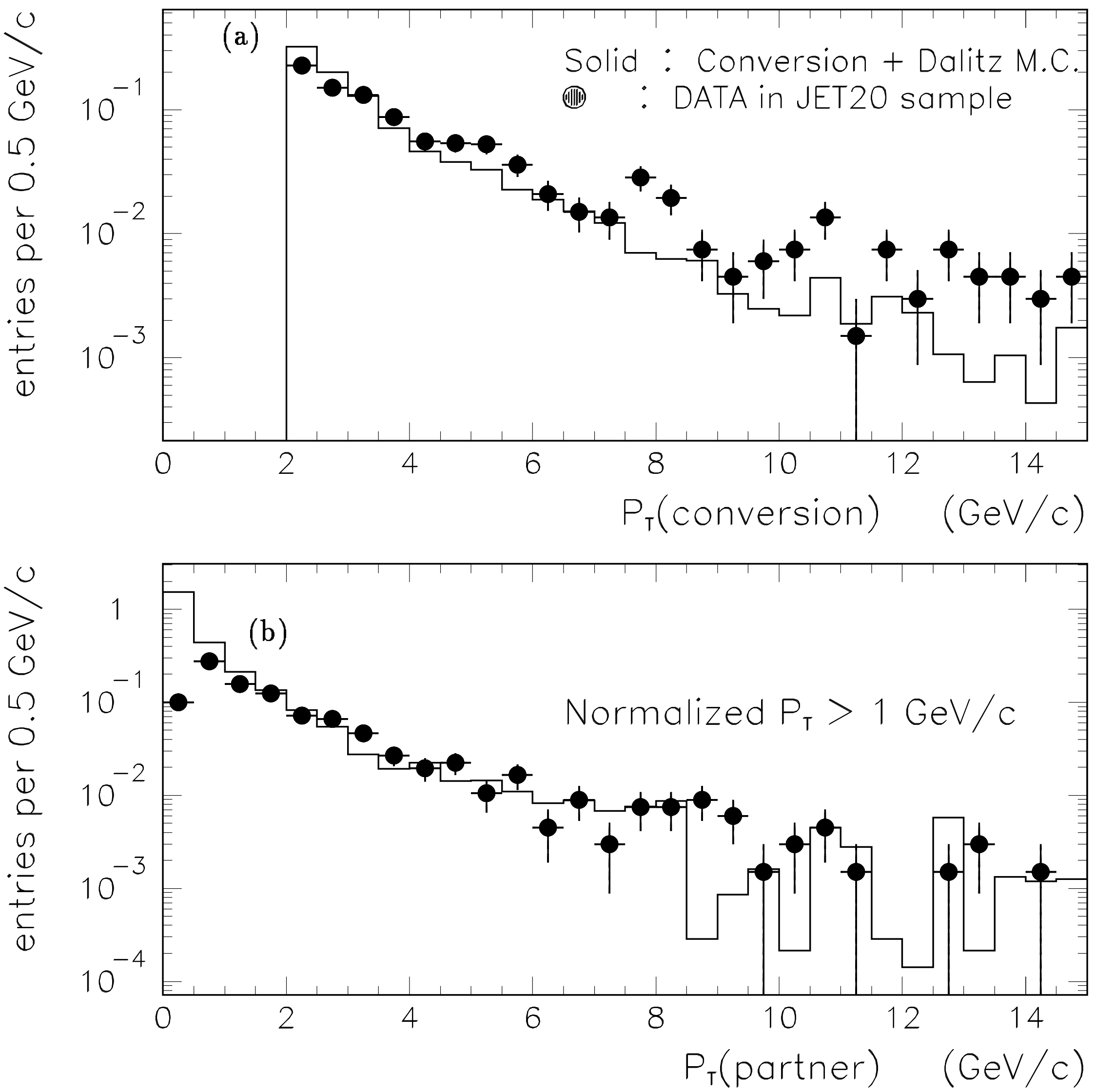

Figure A.2: p_T distributions for the conversion electrons and their partners in the JET20 data sample. The p_T distribution for the Monte Carlo conversion partners is normalized to data in the range $p_T > 1$ GeV/c.

Appendix B

Background Validation

To confirm the background estimation, we perform a check using the process of the b semileptonic decay to c followed by the semileptonic decay of the c,

$$b \rightarrow c\ell_1^- X, \; c \rightarrow s\ell_2^+ X. \tag{B.1}$$

These two leptons $\ell_1^- \ell_2^+$ must have opposite charge. If we see the same charge lepton pair, then one of the leptons has most probably been misidentified due to the same background processes that have been described in Chapter 4.

The data which is accumulated with the single lepton (both e and μ) trigger is used. The p_T of the trigger electron (muon) is required to be greater than 6 GeV/c (8 GeV/c). In order to obtain high purity $b\bar{b}$ sample, we require that the trigger lepton track and tracks within the cone 0.7 in η–ϕ space form a displaced vertex with $L_{XY}/\sigma_L > 2$, where L_{XY} is a distance between the primary vertex and the secondary vertex and σ_L is its uncertainty. The algorithm that finds a secondary vertex is called "SECVTX" [58]. The b purity in the sample for e trigger is about 86% and that for μ trigger is about 82%. Ref. [59] describes in detail the sample composition. This sample is called a SECVTX lepton sample.

B.1 Mass of the trigger lepton and the second electron

We look for a second electron using the same method as described in Section 3.3. We reconstruct an invariant mass of the trigger lepton and the second electron. The

	same side				opposite side			
	tag	fake	conv.	bb	tag	fake	conv.	bb
$e^{\pm}e^{\pm}$	67	16.3 ± 1.6	21.4 ± 9.4	25.6 ± 6.8	312	26.5 ± 2.7	29.8 ± 8.8	250 ± 21
$e^{\pm}e^{\mp}$	915	21.5 ± 1.7	32.2 ± 11.5	839 ± 32	545	28.0 ± 2.8	36.6 ± 10.2	485 ± 30
$\mu^{\pm}e^{\pm}$	99	19.6 ± 2.0	20.6 ± 4.7	56.0 ± 7.4	247	25.0 ± 2.5	44.6 ± 7.7	179 ± 13
$\mu^{\pm}e^{\mp}$	627	26.1 ± 2.6	30.3 ± 6.8	478 ± 22	365	25.9 ± 2.6	39.8 ± 7.1	297 ± 17

Table B.1: Number of tags, number of expected fake electrons, number of residual conversions and number of $b\bar{b}$ events in the SECVTX e and μ samples.

trigger electron and second electron mass distribution for the same-sign pairs is shown in Figure B.1 (a) and the mass distribution for the opposite-sign pairs is shown in Figure B.1 (b). Figures B.2 (a) and (b) show the mass distribution for the same-sign pairs of trigger muon and tagged electron, and that for the opposite-sign pairs, respectively.

When a track and a trigger lepton come from the same parent b decay, it is called "same-side". When a trigger lepton comes from a b decay and a track comes from other parent $\bar{b}$, it is called "opposite-side". If a trigger lepton is a same-side pair, the invariant mass of the track and the trigger lepton must be less than the b hadron mass. Hence we define the same-side and the opposite-side pairs as follows,

- Same side: mass (trigger ℓ + second e) < 5 GeV/c^2.
- Opposite side: mass (trigger ℓ + second e) > 5 GeV/c^2.

The numbers of second electron tags are listed in Table B.1 for the SECVTX e and μ sample.

B.1.1 Fake electron background

The mass distribution of the trigger lepton and the fake electron is obtained by pairing the trigger lepton with an SVX track in the event which passes the fiducial cut. The entry for such a pair in the mass plot is weighted by the fake rate depending on p_T and I of the track. The fake rate is identical to the one obtained in Section 4.1.1. Table B.1 lists the number of expected fake events for the SECVTX e and μ

samples. Figure B.1 and Figure B.2 show the contribution of fake tagged electron to mass spectrum of the ee or the μe pairs.

B.1.2 Residual conversion background

The contribution due to the residual conversion is estimated using the same method as described in Section 4.2.1. We generate π^0 events using three-momenta of tracks in the SECVTX lepton sample and simulate $\pi^0 \to \gamma\gamma$ and $\pi^0 \to e^+e^-\gamma$ decays.

We find the conversion electron candidates in the SECVTX sample with the conversion removal algorithm as described in Section 3.3.6. The p_T distributions of the conversion electrons and their partners in the SECVTX sample are shown in Figure B.3 for the same-sign, same-side pairs. We calculate the conversion finding efficiency (ε_{id}) using the p_T distribution of the partner. Then we obtain the number of residual conversions using this ε_{id}. The numbers of residual conversion backgrounds are listed in Table B.1.

B.1.3 Contribution from $b\bar{b}$ production

When $\Delta\phi$ between b and $\bar{b}$ is small, tracks which come from other b decay are included in the cone 0.7 in η–ϕ around the trigger lepton and are used in the SECVTX tag. We estimate this contribution using the Monte Carlo simulation. We generate the $b\bar{b}$ events with the same strategy in Section 4.3. Here we do not force any b nor $\bar{b}$ decays. The events which have leptons (e or μ) undergo the trigger simulation to reproduce the level 2 CFT efficiency. The $b\bar{b}$ Monte Carlo was normalized to data using the number of trigger leptons. The numbers of $b\bar{b}$ backgrounds are listed in Table B.1. The invariant mass distributions are shown in Figures B.1 and B.2.

B.1.4 Comparison

The predicted number of the lepton pairs for each data set is obtained by adding the fake electrons, residual conversions, and the $b\bar{b}$ predictions for that set. The same-side pairs in Figures B.1 (a) and B.2 (a) show that the number of predicted pairs is consistent with the number of observed pairs, implying that the calculated electron

	SECVTX e sample		SECVTX μ sample	
	tag	Total background	tag	Total background
same sign	67	63.6 ± 11.7	99	96.2 ± 8.9
opposite sign	915	893 ± 41	627	535 ± 23

Table B.2: The number of same-side trigger lepton and tagged e pairs and the number of expected total background (fake e + residual conversions + $b\bar{b}$).

backgrounds are consistent with what we see in the data. The numbers of tags and expected events from the fake electrons, residual conversions, and $b\bar{b}$ for the same-side pairs are listed in Table B.2.

In Figures B.1 (b) and B.2 (b), the data for same-side, opposite-sing pair is slightly higher than the prediction. This is due to incompleteness of the $b\bar{b}$ Monte Carlo and impurities in the trigger leptons since about 20% of the trigger leptons in SECVTX data are not coming from b hadron decays.

B.2 Both leptons in the SECVTX tag

To reduce the contribution from opposite side B meson, we require that the second electron is a part of the SECVTX tag. In this section, we look at such lepton pairs. The dilepton invariant mass distributions are shown in Figure B.4 for SECVTX e sample and in Figure B.5 for SECVTX μ sample. The numbers of tags and expected events from the fake electrons, residual conversions, and $b\bar{b}$ for same-side pairs are listed in Table B.3. The sum of each background is listed in Table B.4. The observed same-sign dilepton pairs are consistent with the expected background. This supports the validity of the background calculation in the B_c analysis.

B.3 Check using dE/dX

In the previous sections, we have checked the electron backgrounds comparing the number of second leptons to the number of predictions Here we present another test for the fake electron background using the dE/dX. We fit the dE/dX distribution for

	same side			
	tag	fake	conv.	bb
$e^{\pm}e^{\pm}$	33	10.0 ± 1.0	6.6 ± 2.9	12.2 ± 4.6
$e^{\pm}e^{\mp}$	755	13.3 ± 1.3	18.1 ± 8.0	735 ± 35
$\mu^{\pm}e^{\pm}$	37	9.5 ± 1.0	7.4 ± 3.0	20.4 ± 4.5
$\mu^{\pm}e^{\mp}$	439	13.9 ± 1.4	19.0 ± 8.6	329 ± 18

Table B.3: The number of tags and the number of events from fake electrons, residual conversions, and $b\bar{b}$ events in the SECVTX e and μ samples. These results are for the case where the two leptons come from the same tagged jet.

	SECVTX e sample		SECVTX μ sample	
	tag	Total background	tag	Total background
same sign	33	28.8 ± 5.5	37	37.3 ± 5.5
opposite sign	755	766 ± 36	439	362 ± 20

Table B.4: The number of same-side trigger lepton and tagged electron pairs and the number of expected total background (fake e + residual conversion + $b\bar{b}$). These results are for the case where the two leptons come from the same tagged jet.

the second electrons and compare the number of hadrons to the number of predictions. We employ a maximum likelihood method as described in Section 4.1.4.

Figure B.6 (a) shows the dE/dX distribution for same-side, same-sign in SECVTX e sample, where the second electron is not required to be a part of SECVTX tag. The fitted curves are also superimposed in Figure B.6 (a). Figure B.6 (b) is the dE/dX distribution for the SECVTX μ sample. Using the fit results, we calculate the number of π's and K's with the S_e cut. The results are listed in Table B.5. We also fit the dE/dX distribution for the same-sign, same-side electrons in the case where the second electron is a part of the SECVTX tags. We show the fit curves in Figure B.7 and list the fit results in Table B.5.

Comparison of Table B.5 to Tables B.1 and B.3 shows that, in either case, the number of hadrons obtained from the dE/dX fit agrees with the number of fake electrons calculated using the fake rate.

	SECVTX e sample			SECVTX μ sample		
	N_π	N_K	N_{had}	N_π	N_K	N_{had}
(a)	16.4 ± 5.5	2.4 ± 0.9	18.8 ± 5.6	19.3 ± 5.9	1.6 ± 1.0	20.9 ± 6.0
(b)	11.0 ± 4.6	1.2 ± 0.7	12.2 ± 4.7	9.0 ± 4.4	0.6 ± 0.6	9.6 ± 4.5

Table B.5: The number of hadrons (pion and kaon) in the same-side, same-sign tags, determined from the dE/dX fit. (a) For all second electrons and (b) for the case where second electron is a part of the SECVTX tag.

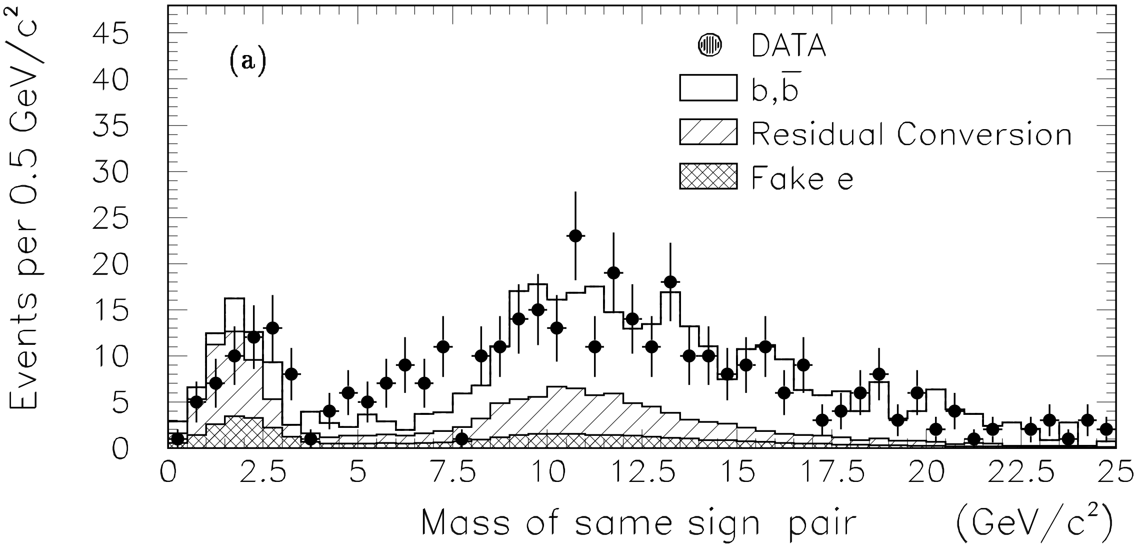

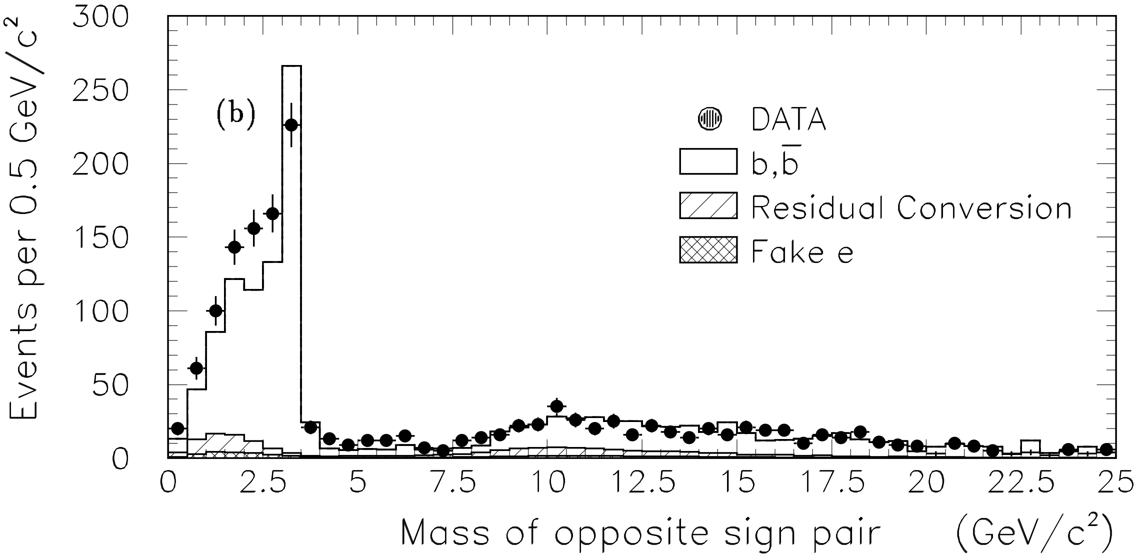

Figure B.1: Mass distribution of the trigger lepton (e) + tagged electron in SECVTX e sample together with each background. (a) for same-sign pair. (b) for opposite-sign pair.

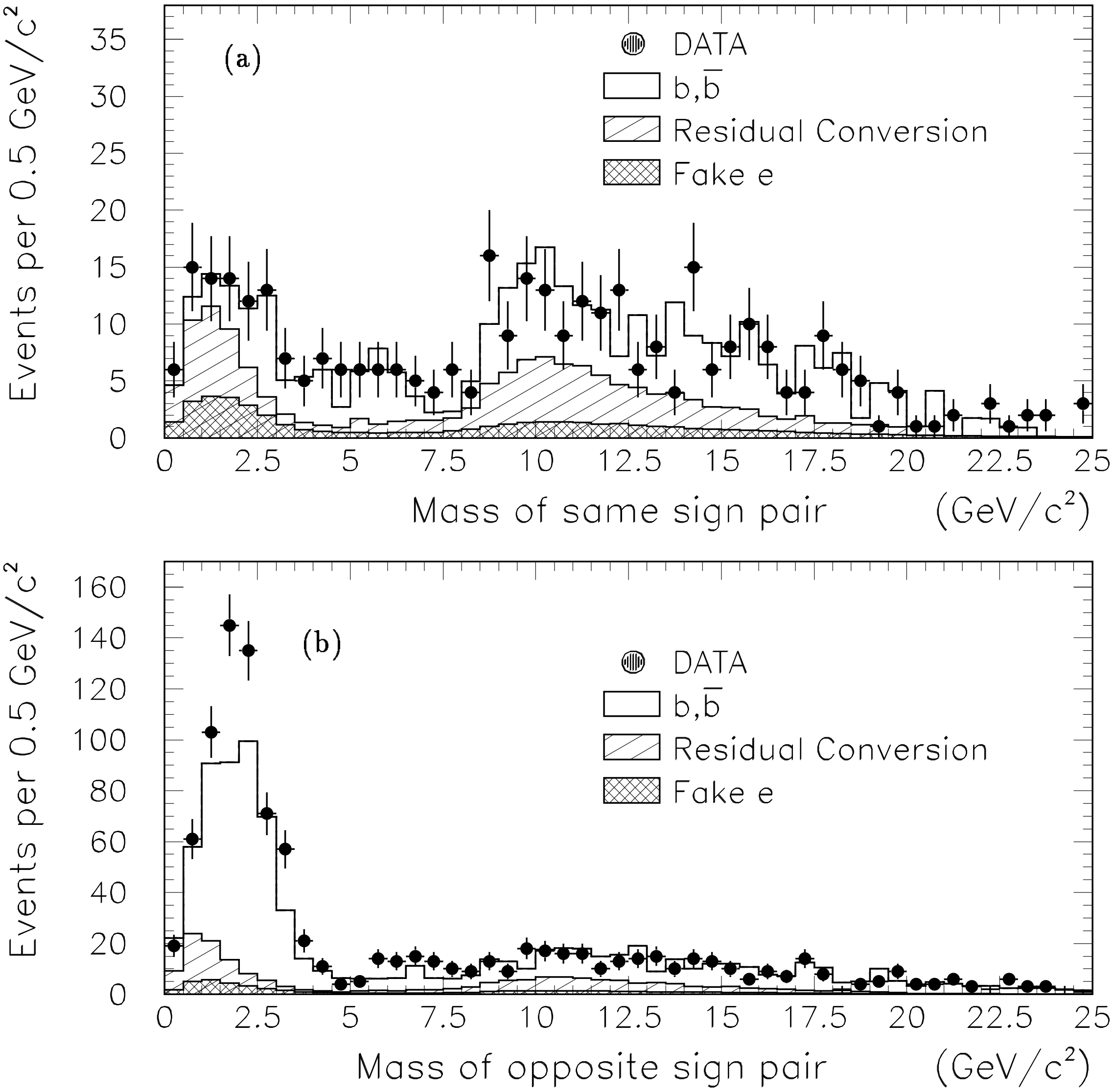

Figure B.2: Mass distribution of the trigger lepton (μ) + tagged electron in SECVTX μ sample together with each background. (a) for same-sign pair. (b) for opposite-sign pair.

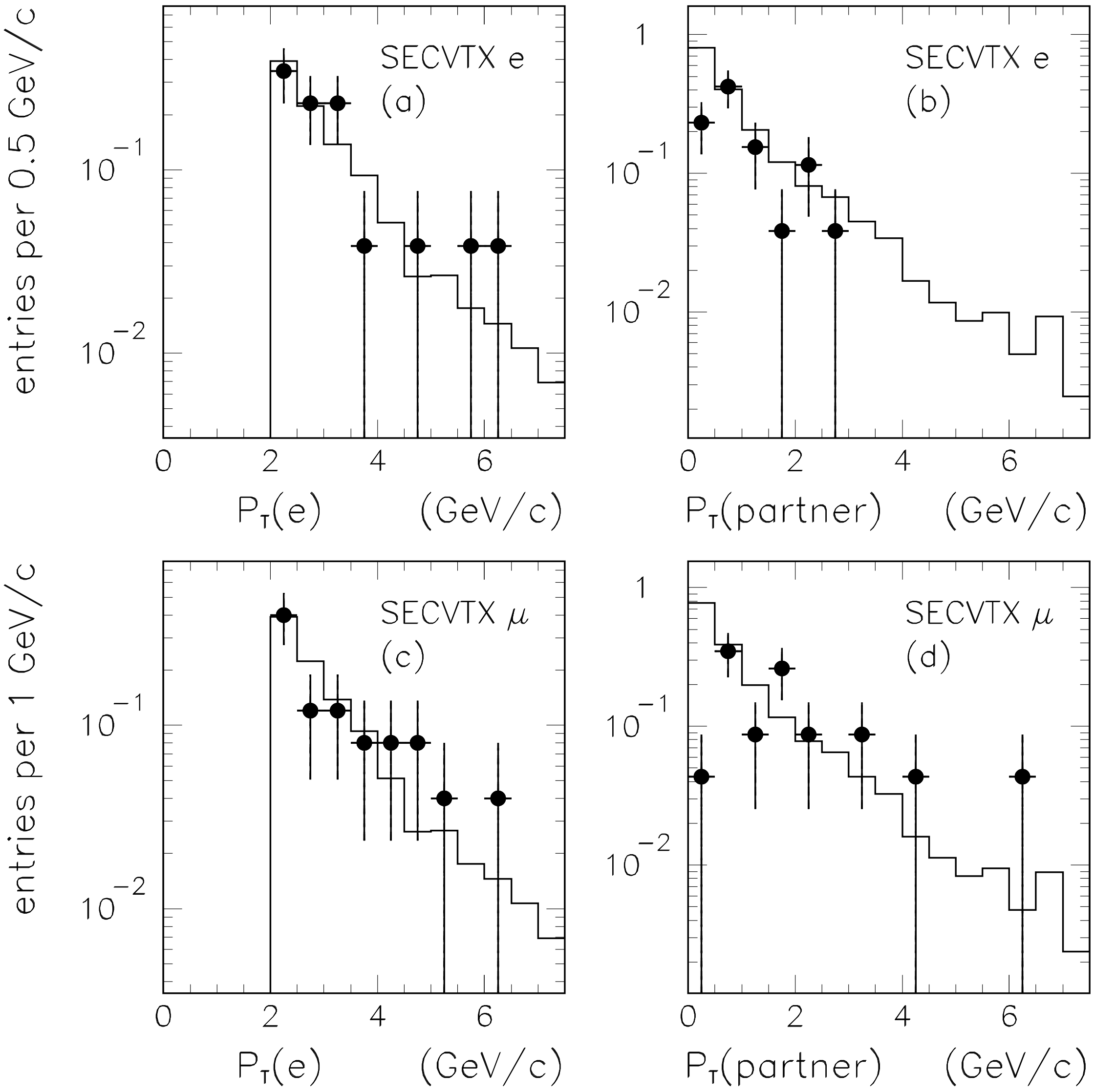

Figure B.3: p_T distributions for the conversion electrons and their partners. (a) for the conversion electron in the SECVTX e sample. (b) for the conversion partner in the SECVTX e sample. (c) for the conversion electron in the SECVTX μ sample. (d) for the conversion partner in the SECVTX μ sample.

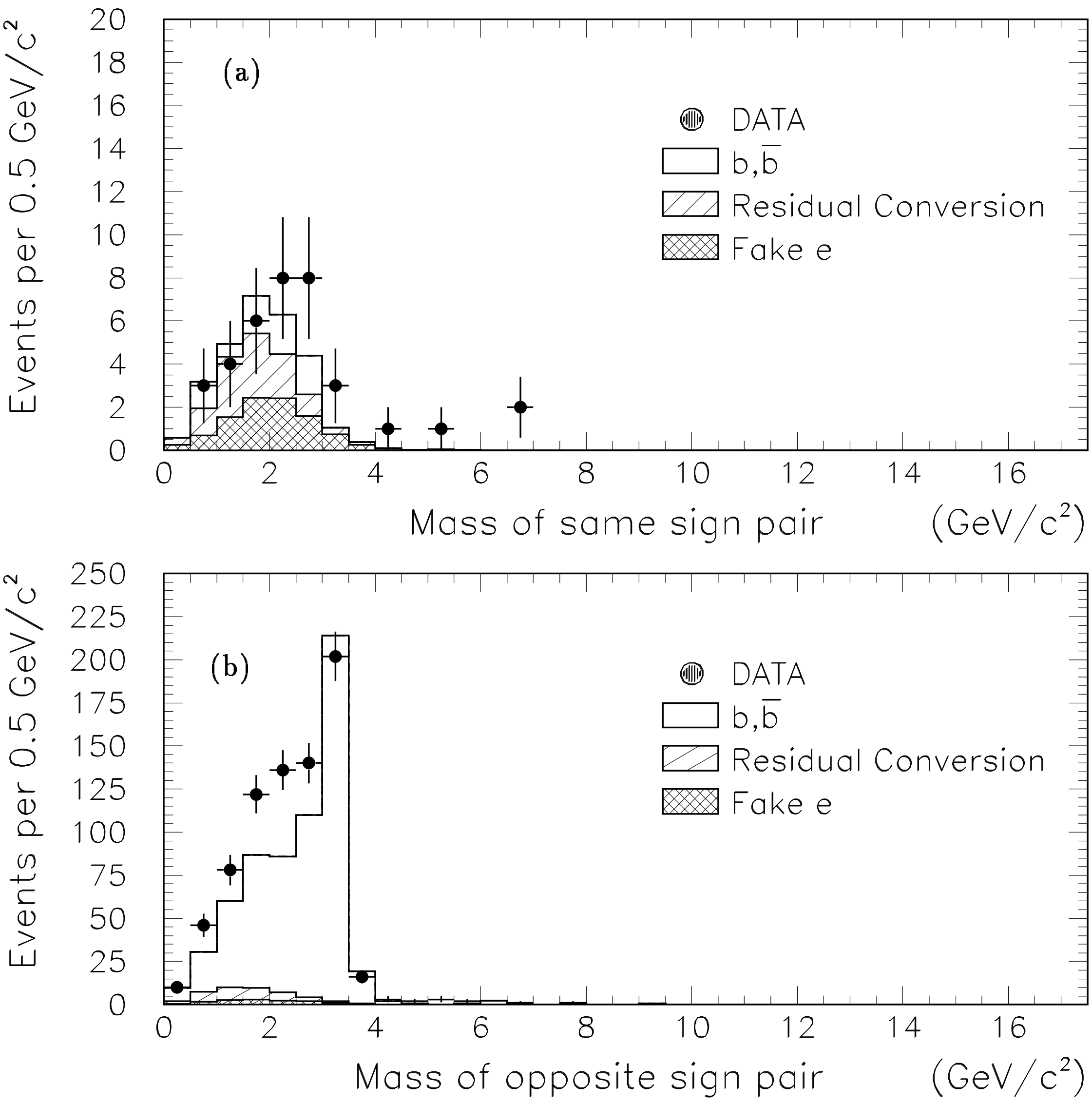

Figure B.4: Invariant mass distribution of trigger lepton (e) + electron in SECVTX electron sample together with each background. Both leptons are a part of the SECVTX tag. (a) for same-sign pair. (b) for opposite-sign pair.

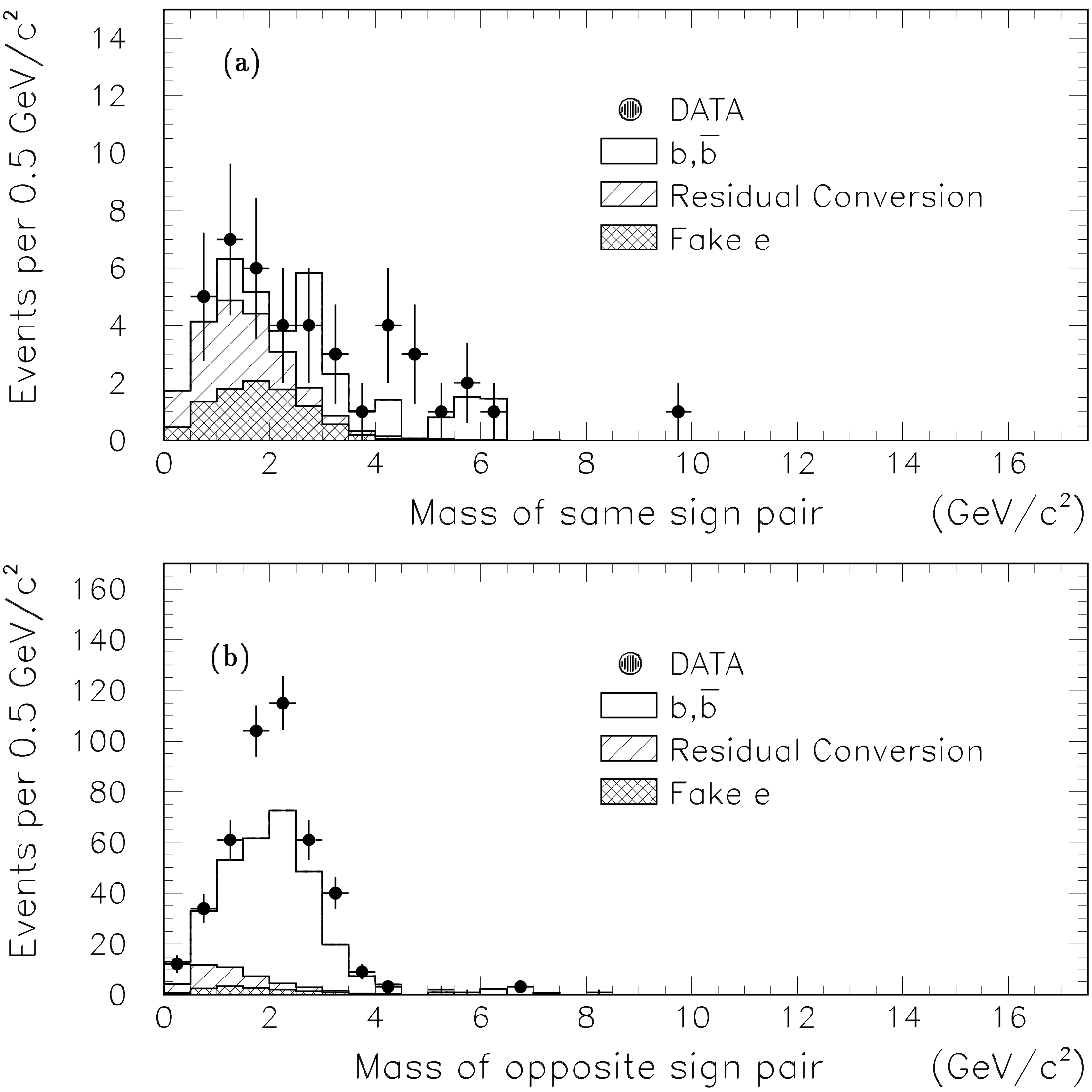

Figure B.5: Invariant mass distribution of trigger lepton (μ) + electron in SECVTX muon sample together with each background. Both leptons are a part of the SECVTX tag. (a) for same-sign pair. (b) for opposite-sign pair.

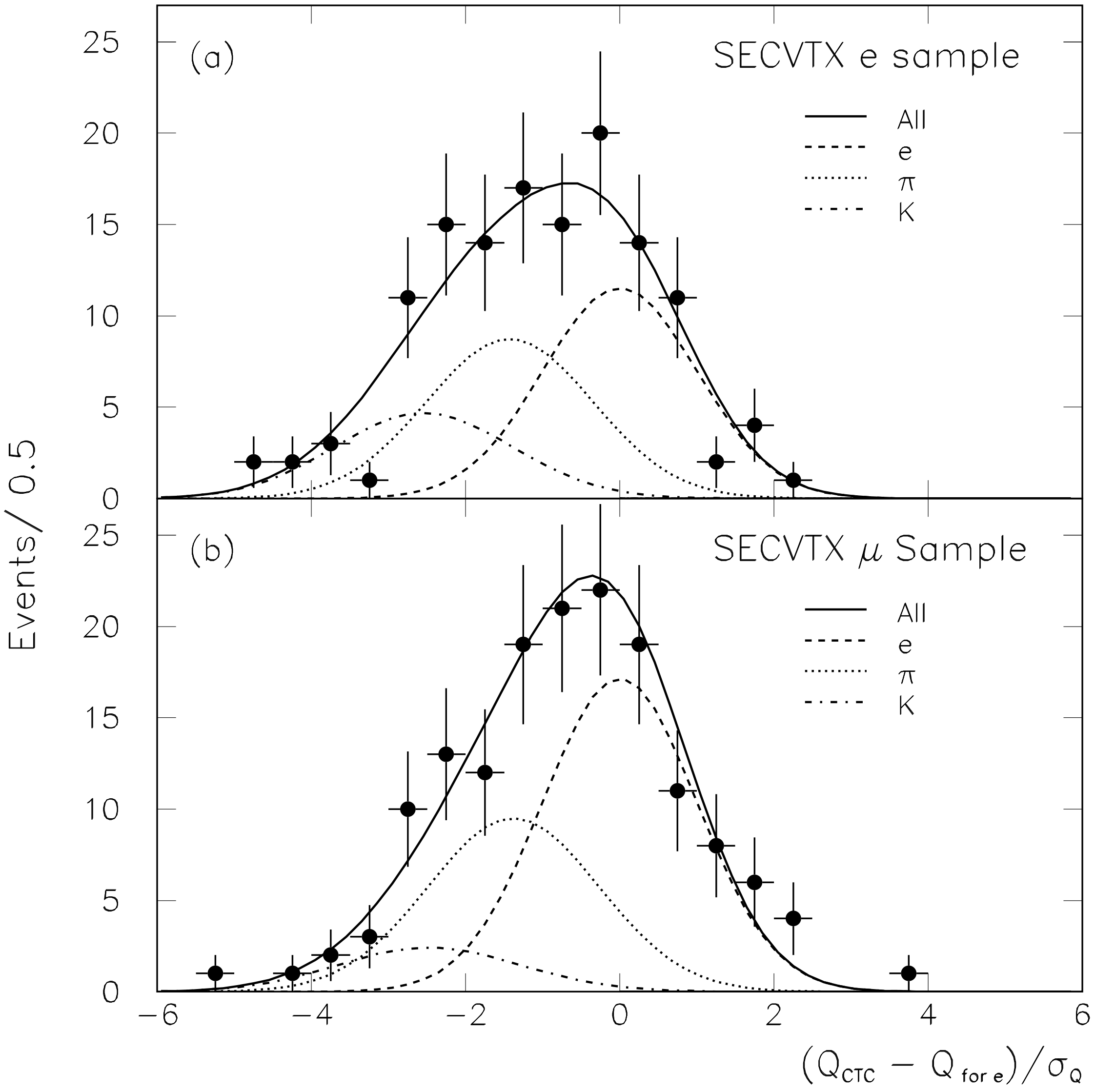

Figure B.6: S_e distribution for the same-sign, same-side tracks identified as electrons without the S_e cut. (a) SECVTX e sample. (b) SECVTX μ sample.

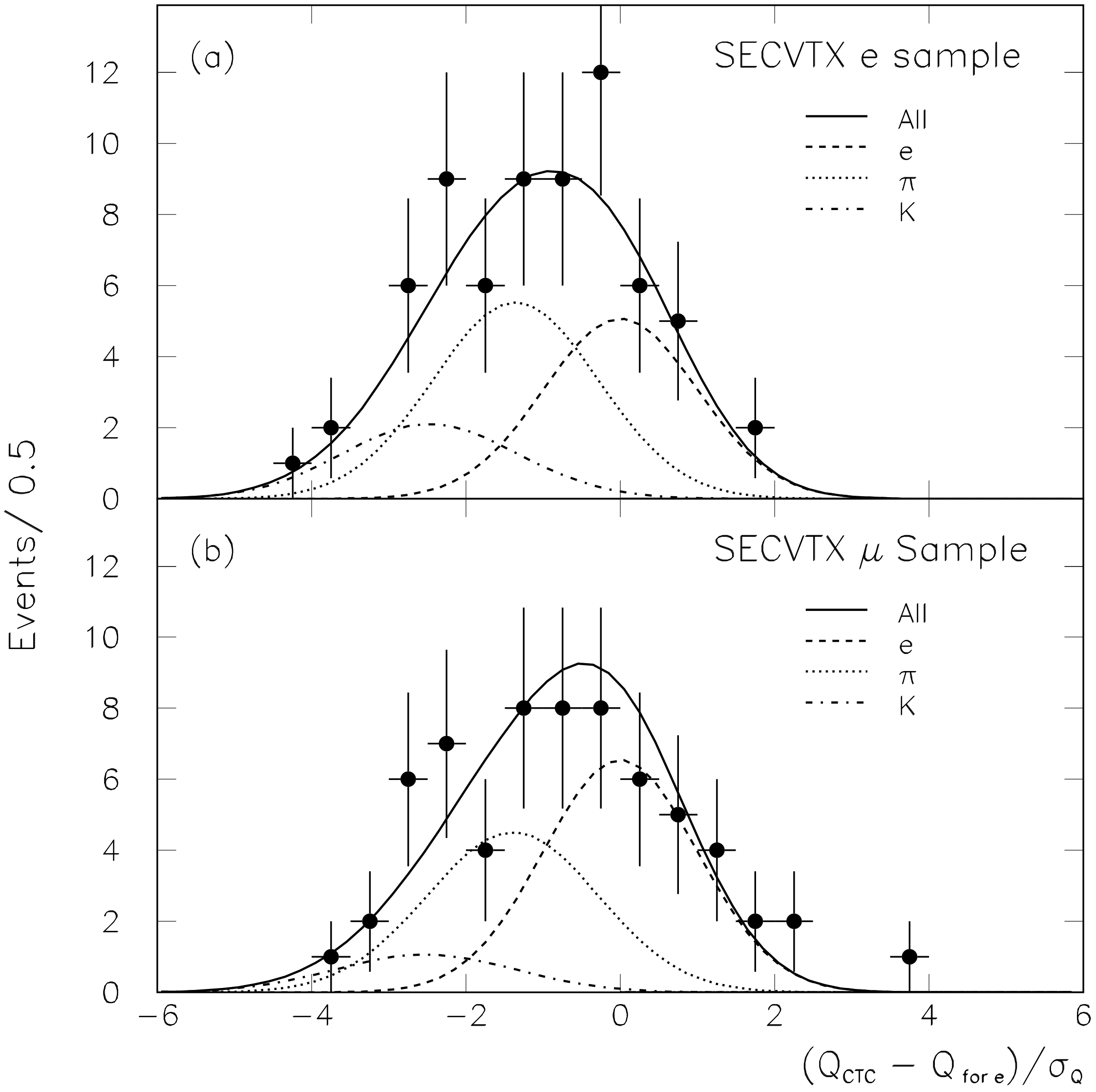

Figure B.7: S_e distribution for the same-sign, same-side tracks identified as electrons without the S_e cut. The second electrons are required to be a part of the SECVTX tag. (a) SECVTX e sample. (b) SECVTX μ sample.

Bibliography

[1] S.W. Herb *et al.*, Phys. Rev. Lett. 39 (1977) 252.

[2] C. Berger *et al.*, Phys. Lett. B 76 (1978) 243.;
C.W. Darden *et al.*, Phys. Lett. B 76 (1978) 246.;
J.K. Bieenlein it et al., Phys. Lett. B 78 (1978) 360.;
C.W. Darden *et al.*, Phys. Lett. B 78 (1978) 364.;
D. Andrews *et al.*, Phys. Rev. Lett. 44 (1980) 1108.;
T. Böhringer *et al.*, Phys. Rev. Lett. 44 (1980) 1111.;
D. Andrews *et al.*, Phys. Rev. Lett. 45 (1980) 219.;
G. Finocchiaro *et al.*, Phys. Rev. Lett. 45 (1980) 222.

[3] S. Behrends *et al.*, Phys. Rev. Lett. 50 (1983) 881.

[4] P. Abreu *et al.*, Phys. Lett. B 289 (1992) 199.;
D. Buskulic *et al.*, Phys. Lett. B 294 (1992) 145.

[5] P. D. Acton *et al.*, Phys. Lett. B 312 (1993) 503.;
P. Abreu *et al.*, Z. Phys. C 61 (1994) 407.;
D. Buskulic *et al.*, Phys. Lett. B 322 (1994) 275.

[6] F. Abe *et al.*, Phys. Rev. D 53 (1996) 3496.;
F. Abe *et al.*, Phys. Rev. Lett. 74 (1995) 4988.

[7] F. Abe *et al.*, Phys. Rev. Lett. 75 (1995) 1452.

[8] P. Nason, S. Dawson, R.K. Ellis, Nucl. Phys. B 327 (1989) 49.;
M.L. Mangano, P. Nason, G. Ridolfi, Nucl. Phys. B 373 (1992) 295.

[9] C. Peterson *et al.* Phys. Rev. D 27 (1983) 105.

[10] B. Andersson *et al.*, Phys. Rep. 97 (1983) 31.

[11] C. Chang *et al.*, Phys. Rev. D 54 (1996) 4344.

[12] C. Chang *et al.*, Phys. Lett. B 364 (1995) 78.

[13] A.V. Berezhnoy, A.K. Likhoded and O.P. Yushuchenko, Phys. of At. Nucl. 59 (1996) 709.

[14] K. Kolodziej, A. Leike and R. Rükel, Phys. Lett. B 355 (1995) 337.

[15] E. Braaten, K. Cheung and T. Yuan, Phys. Rev. D 48 (1993) R5049.

[16] H.L. Lai *et al.*, MSU-HEP-41024 (1994).

[17] E.J. Eichten and C. Quigg, Phys. Rev. D 49 (1994) 5485.

[18] S. Godfrey and N. Isgur, Phys. Rev. D 32 (1985) 189.

[19] M. Baker, J.S. Ball and F. Zachariasen, Phys. Rev. D 45 (1992) 910.

[20] S.S. Gershteĭn *et al.*, Sov. J. Nucl. Phy. 48 (1988) 327.

[21] M. Lusignoli and M. Msetti, Z. Phys. C 51 (1991) 549.

[22] C. Chang and Y. Chen, Phys. Rev. D 49 (1994) 3399.

[23] C. Quigg, FERMILAB-CONF-93/265-T.

[24] I.I. Bigi, Phys. Lett. B 371 (1996) 105.

[25] M. Beneke and G. Buchalla, Phys. Rev. D 53 (1996) 4991.

[26] "Semileptonic Hadron Decay in the Quark Potential Model", D. J. Scora, Ph. D. Thesis, University of Tront (1992).

[27] D.J. Scora and N. Isgur, CEBAF-TH-94-14.

[28] R. Barate *et. al.*, Phys. Lett. B 402 (1997) 213.

[29] P. Abreu *et. al.*, Phys. Lett. B 398 (1997) 207.

[30] G. Alexander *et. al.*, CERN-PPE/97-137, to be submitted to Phys. Lett. B.

[31] F. Abe *et. al.*, Phys. Rev. Lett. 77 (1996) 5176.

[32] R.M. Barnett *et al.*, Phys. Rev. D 54 (1996) 1.

[33] F. Abe *et al.*, Nucl. Instrum. Methods Phys. Res., Sect. A 271 (1988) 327, and references therein.

[34] D. Amidei *et al.*, Nucl. Instrum. Methods Phys. Res., Sect. A 350 (1994) 73.

[35] S. Cihangir *et al.*, FERMILAB-Conf-94/205-E.

[36] K. Biery *et al.*, CDF internal note 2223.

[37] R. Blair *et al.*, CDF internal note 760.

[38] J.D. Lewis *et al.*, CDF internal note 2858, to be submitted to Nucl. Instrum. Methods.

[39] G.W. Foster *et al.*, Nucl. Instrum. Methods Phys. Res., Sect. A 269 (1988) 93.

[40] S.P. Pappas and J. D. Lewis, CDF internal note 4076.

[41] D. Frei, CDF internal note 1430.

[42] J. Marriner, CDF internal note 1996.

[43] F. Abe *et al.*, Phys. Rev. Lett. 71 (1993) 500.

[44] F. Abe *et al.*, Phys. Rev. D 50 (1994) 2966.;
C. Campagnari and D. Kestenbaum, CDF internal note 3682.

[45] R.M. Harris, R. Blair and S. Kuhlmann, CDF internal note 1432.

[46] F. Abe *et al.*, Phys. Rev. Lett. 79 (1997) 578.

[47] "Bottom quark production in 1.8-TeV Proton-Antiproton Collisions", F. Ukegawa, Ph. D. Thesis, University of Tsukuba (1991).

[48] A. Martin, R. Roberts, J. Stirling Phys. Rev. D 47 (1993) 867.

[49] P. Avery, K. Read and G. Thrahern, Cornell Internal Note CSN-112

[50] F. Abe *et al.*, "Observation of the B_c meson in 1.8 TeV $\bar{p}p$ Collisions", to be submitted to Phys. Rev. D.

[51] "Statistical Methods in Experimental Physics", by W.T. Eadie *et al.*, North-Holland, 1971, p.282.

[52] F. Abe *et al.*, Phys. Rev. Lett. 76 (1996) 4462.

[53] "Statistics for nuclear and particle physicists", by L. Lyons, Cambridge University Press, 1971, p.272.

[54] H.L. Lai *et al.*, MSU-HEP-60426 (1996).

[55] Y.P. Kaung *et al.*, Phy. Rev. D37 (1988) 1210.

[56] H. Wenzel *et al.*, CDF internal note 4227, to be submitted to Phys. Rev. D.

[57] F. Abe *et al.*, Phys. Rev. D 54 (1996) 6596.

[58] D. Glenziniki *et al.*, CDF internal note 2925 (1995).

[59] M. Paulini *et al.*, CDF internal note 3757 (1996).